MAX-PLANCK-INSTITUT FÜR PHYSIK KOMPLEXER SYSTEME DRESDEN

Interfaces between Competing Patterns in Reaction-diffusion Systems with Nonlocal Coupling

Dissertation
zur Erlangung des
Doktorgrades der Naturwissenschaften
(*Doctor rerum naturalium* - Dr. rer. nat.)

vorgelegt
der **Fakultät Mathematik und Naturwissenschaften**
der **Technischen Universität Dresden**

von

Ernesto M. Nicola

geboren am 16. August 1971 in Concordia (Entre Rios), Argentinien

DRESDEN 2001

Eingereicht am 25. September 2001

1. Gutachter: Prof. Dr. P. Fulde
2. Gutachter: Prof. Dr. U. Bahr
3. Gutachter: Prof. Dr. H. Engel

Abstract

In this thesis we investigate the formation of patterns in a simple activator-inhibitor model supplemented with an inhibitory nonlocal coupling term. This model exhibits a wave instability for slow inhibitor diffusion, while, for fast inhibitor diffusion, a Turing instability is found. For moderate values of the inhibitor diffusion these two instabilities occur simultaneously at a codimension-2 wave-Turing instability. We perform a weakly nonlinear analysis of the model in the neighbourhood of this codimension-2 instability. The resulting amplitude equations consist in a set of coupled Ginzburg-Landau equations. These equations predict that the model exhibits bistability between travelling waves and Turing patterns. We present a study of interfaces separating wave and Turing patterns arising from the codimension-2 instability. We study theoretically and numerically the dynamics of such interfaces in the framework of the amplitude equations and compare these results with numerical simulations of the model near and far away from the codimension-2 instability. Near the instability, the dynamics of interfaces separating small amplitude Turing patterns and travelling waves is well described by the amplitude equations, while, far from the codimension-2 instability, we observe a locking of the interface velocities. This locking mechanism is imposed by the absence of defects near the interfaces and is responsible for the formation of drifting pattern domains, *i.e.* moving localised patches of travelling waves embedded in a Turing pattern background and vice versa.

Contents

Chapter 1

Introduction

The formation of spatio-temporal patterns is a very common feature of natural systems. In the last few decades a lot of work has been done in the study of pattern forming processes in nonequilibrium systems. Some representative reviews and introductory books that treat this topic can be found in [1, 2, 3, 4, 5, 6, 7].

The variety of different spatio-temporal patterns seen in nature is very vast. It has been recognised, however, that these patterns very often arise in situations where a previously stable homogeneous state becomes unstable to small perturbations. In such a situation, pattern forming systems can be classified according to the primary instability of the spatially homogeneous state. Three basic types of instabilities in unbounded systems can be distinguished [1]. In these three different cases the new solutions are:

1. spatially periodic and stationary in time,
2. spatially periodic and oscillatory in time and
3. spatially homogeneous and oscillatory in time.

This leads to a classification of pattern forming systems into a few different cases. Furthermore, a universal description of patterns arising near these instabilities is achieved within the framework of the so called amplitude equations (see *e.g.* Ref. [1, 5, 7, 8, 9, 10]). These universal equations play a fundamental rôle in the field of pattern formation.

Pattern forming systems in nature are extended in space and often evolve in time. Very often these systems can be described by some set of deterministic partial differential equations [1, 2, 5]. These equations are usually nonlinear.

Some types of pattern formation processes in nature have been studied extensively. Probably the best studied cases of pattern formation come from the field of fluid dynamics [1, 7]. The Navier-Stokes equations typically provide the starting point of these studies. The formation of patterns in chemical reactions has also received a lot of attention [5, 11, 12, 14]. A family of models that have been extensively used to analyse patterns observed in chemical processes are *reaction-diffusion systems* [5, 11, 12, 13]. These models consist of a reaction part describing the chemical kinetics and a diffusion part representing transport processes. Within the reaction-diffusion literature, the characteristic instabilities mentioned before are known as *Turing*, *wave* and *Hopf bifurcation*, respectively [14]. Reaction-diffusion models have been also applied to other fields like, for example, biology [2, 15, 16] and ecology [2].

A well studied subgroup of reaction-diffusion models are *activator-inhibitor* systems. These simple models capture many features observed in numerous chemical and biological patterns [2, 3]. They consist of two diffusing components with a characteristic temporal dynamics [3]. In such two component reaction-diffusion models only Turing and Hopf instabilities are possible [14]. A particular type of simple activator-inhibitor systems, the so called FitzHugh-Nagumo dynamics, has been successfully used to model a broad array of pattern forming processes [2, 3, 12].

Recently, there has been an increasing interest in reaction-diffusion models related with activator-inhibitor systems but consisting of more than two components. These studies address typically reaction-diffusion systems with *three components* [17, 18, 19, 20, 21, 22, 23, 24]. An interesting feature observed in some of these models is that, beside the Turing and Hopf instabilities, also a wave instability may occur [17].

In this thesis we will study a simple activator-inhibitor model supplemented with an *inhibitory nonlocal coupling* term. The model follows a FitzHugh-Nagumo type dynamics. The nonlocal coupling term will naturally arise if we consider a limiting case of a three component reaction-diffusion system consisting of one activator and two inhibitors.

The instabilities of the reaction-diffusion model with nonlocal coupling will be studied extensively in this thesis. We will see that for slow inhibitor diffusion (compared to the activator diffusion), the model exhibits a wave instability, while, for fast inhibitor diffusion, a Turing instability is found. These two instabilities can occur simultaneously at a *codimension-2 wave-Turing bifurcation*. Such a situation has been found earlier within some models of convection [25, 26, 27, 28] and is a generalisation of the well investigated Turing-Hopf instability in two component reaction-diffusion systems [29]. Basic properties of such coexisting instabilities have been studied theoretically in amplitude equations [30] as well as experimentally in a one-dimensional gas-discharge system [31].

We will see that, near the codimension-2 instability, the model may have

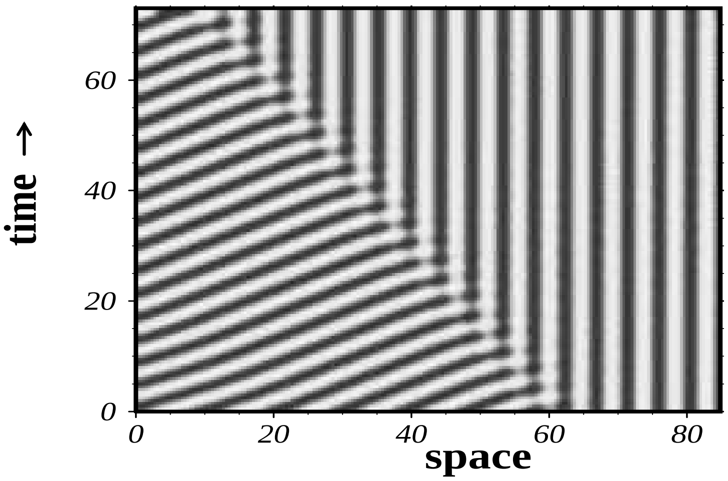

Figure 1.1: In this figure we show a typical example of an interface separating a right-travelling wave and a Turing pattern in the reaction-diffusion model with nonlocal coupling. In this grey scale plot the colour black corresponds to big concentrations of the activator and withe to low. The model numerically integrated is given by Eqs. (2.13,2.14) and the parameters are the same than in Fig. 6.1(b) (for more details see the caption of this figure).

a region of bistability between Turing and travelling wave patterns. In this bistability region both patterns exist.

Many systems in nature show competition between periodic patterns [29, 32, 33, 34]. As a result of this competition, interfaces separating different patterns may arise. In our model these interfaces will separate travelling waves and Turing patterns. An typical example of such an interface is presented in Fig. 1.1.

In this thesis we present a general study of interfaces near and far from codimension-2 instabilities. Near such a codimension-2 instability the dynamics of such interfaces is analysed in a set of coupled amplitude equations. We compare these theoretical results with numerical simulations of the model, near and far away from the codimension-2 wave-Turing instability. The dynamics of interfaces separating small amplitude patterns is well described by the result of the coupled amplitude equations.

For large amplitude patterns, we observe a locking of interface velocities, which is imposed by the absence of defects near the interfaces. This mechanism is responsible for the formation of drifting pattern domains, *e.g.* travelling waves embedded in a Turing pattern background and vice versa. These patches have constant width and move (drift) with constant speed. They exist in a broad region of the parameter space embedded in the bistability region between travelling waves and Turing patterns.

- Organisation and outline of this Thesis

After accomplished a short motivation and introduction to the main topics of this thesis, let us now give some hints about its organisation.

This thesis is divided in two parts:

1. In the first part we will introduce the model, study its linear stability, derive the corresponding amplitude equations and study their constant amplitude solutions.

2. In the second part we will concentrate our attention on the study of interfaces separating competing patterns.

Let us now describe the chapters of this thesis and their relationship. Each chapter begins with a brief introduction and has a short description of its organisation.

The first part is composed of four chapters. The model will be introduced and motivated in Chapter 2. In Chapter 3 we will study the spatially homogeneous solutions of the model and perform a linear stability analysis of these solutions. Chapter 4 will begin with an introduction to the derivation of amplitude equations and continue with the derivation of these equations in the model near the Turing, wave and codimension-2 wave-Turing instabilities. We will finish this chapter with a preliminary analysis of the behaviour of the amplitude equations. In Chapter 5, the last chapter of the first part, we will study simple solutions of the amplitude equations. These solutions correspond to constant amplitude patterns. We will compare quantitatively these solutions with numerical simulations of the model.

The second part of the thesis is composed of four chapter plus a summary. In the first section of Chapter 6 we will motivate the study of interfaces separating constant amplitude patterns. A classification of the possible interfaces will follow. Chapter 6 will end with a introduction to the theoretical tools that we will use to study the interfaces in the next two chapters. In Chapters 7 and 8 we will perform an extensive study of the dynamics of interfaces near the codimension-2 instability. To achieve this, in Chapter 7, we will apply a coherent structure approach to the amplitude equations. The resulting ordinary differential equations will be analysed in detail in Chapter 8. We will compare the outcome of this approach with the dynamics of interfaces in numerical simulations of the model. In this chapter we will also study the the shape and size (*i.e.* the scaling properties) of the interfaces near the codimension-2 wave-Turing instability. In Chapter 9 we will study interfaces separating Turing and wave patterns at a substantial distance from the instability thresholds.

Finally, in Chapter 10 we will provide a short summary of the main results of this thesis and give a brief overview of the principal open issues.

Part I

The model and its instabilities

Chapter 2

The Model: Reaction-Diffusion System with Nonlocal Coupling

In this chapter we will introduce and motivate the model that we will analyse through this thesis. The model consists in a reaction-diffusion system supplemented with a nonlocal spatial coupling term. The model has two variables; an activator and an inhibitor. The dynamics of these variables is of the FitzHugh-Nagumo type. We will see that a spatial nonlocal coupling term can naturally arise as a limiting case of a three variable reaction-diffusion system.

2.1 Introduction

The main aim of this chapter is to present a simple reaction-diffusion model with nonlocal coupling. This model describes the interaction of an activator and an inhibitor.

We will motivate the introduction of the (spatial) nonlocal coupling as a limiting case of an extended three variable reaction-diffusion system consisting of one activator and two inhibitors. This limiting case arrises when the dynamics of one of the inhibitors is much faster that the other. In this situation, the fast inhibitor can be eliminated adiabatically, resulting in a two variable activator-inhibitor model with nonlocal coupling.

The dynamics of the model is of the FitzHugh-Nagumo type. Although systems with this kind of dynamics are typically used to model the dynamics of excitable media [2, 3, 12, 36], here we will put the emphasis in the onset of pattern formation resulting from destabilisation of an homogeneous steady state.

- Organisation of this chapter

This chapter is divided in two sections. In Section 2.2 we will give a brief introduction to reaction-diffusion systems. In particular we will discuss the activator-inhibitor dynamics, including the FitzHugh-Nagumo class. We will also discuss three variable systems. In Section 2.3 the model to be discussed in this Thesis will be introduced. Some interesting limits of this model will be considered.

2.2 Introduction to Reaction-Diffusion Systems

2.2.1 Generalities

In the introduction of this Thesis we mentioned that models of reaction-diffusion type have received a lot of attention in the literature. This has been reflected in a deep knowledge of the subject and in an overwhelming quantity of papers. Some representative reviews and introductory books that treat this topic are [2, 3, 4, 5, 6, 8, 12]. In the following we will give a brief description of this type of models.

Reaction-diffusion models are systems of coupled partial differential equations (**PDEs** in the following) that can be written in the following way:

$$\partial_t \mathbf{X}(\mathbf{x};t) = \underbrace{\boldsymbol{g}(\mathbf{X}(\mathbf{x};t))}_{\text{reaction}} + \underbrace{\boldsymbol{D}\nabla^2\mathbf{X}(\mathbf{x};t)}_{\text{diffusion}}, \tag{2.1}$$

where $\mathbf{X}$ is a (column) vector field. In the context of chemical reactions, the elements of this field represent the concentrations of different reactants. The functions in the vector $\boldsymbol{g}(\mathbf{X}(\mathbf{x};t))$ are typically nonlinear. This portion of the equation (2.1) is usually called the *reaction part*. The *diffusion matrix* $\boldsymbol{D}$ is square and typically diagonal. This last portion of the equation (2.1) is called the *diffusion part* and accounts for the diffusion of the reactants.

In this Thesis we will concentrate on cases where the physical space on which the reactants diffuse is *one-dimensional*[1]. Consequently, in the following we will substitute the Laplacian operator ∇^2 by a one dimensional spatial (second) derivative ∂_x^2.

---

[1] Many examples of real physical system of interest are one dimensional or quasi-one dimensional (see *e.g.* [1, 12]).

2.2.2 Activator-Inhibitor Systems

A well studied subgroup of reaction-diffusion systems are the so called activator-inhibitor models [2, 3, 4, 5, 14]. As we mentioned in the introduction, these models have been used in many different pattern forming systems ranging from chemical reactions [5, 14, 35] to biological problems [2, 16] (such as population dynamics, epidemic spreading, and many others).

The *activator-inhibitor models* consist of *two variables* (*i.e.* $\mathbf{X} = (u, v)^{\mathrm{Tr}}$ in Eq. (2.1)) which diffuse in the medium. The first variable, u, called *activator* and the second, v, *inhibitor*. The field u is auto-catalytic. A small amount of its concentration triggers the production of more of it. The growth of u is inhibited by the presence of a second field v.

The dynamics of the inhibitor v is such that the presence of a nonzero concentration of activator u stimulates the v production, *i.e.* u acts as a *catalysator* for the v production. On the other hand a nonzero quantity of this second field v induces its decrease.

Consequently a nonzero quantity of u *activates* the production of both u and v and, conversely, a nonzero quantity of v halts and reverses (*i.e. inhibits*) the production of both. This is the reason why the fields u and v are called *activator* and *inhibitor* respectively.

So far this description corresponds to the linear behaviour. Typically (saturating) nonlinearities are introduced to limit the unbounded catalytic process.

- FitzHugh-Nagumo System

A paradigmatic example of an activator-inhibitor model is the so called *FitzHugh-Nagumo* system (FHN) [2, 3, 5, 15, 36, 37]. This model was initially proposed independently by R. FitzHugh [38] and Nagumo *et al.* [39] as a mathematically tractable model for propagation of electrical signals in neurons (for a short introduction to this topic see Section 6.5 in [2] and references therein). The FHN model represents one of the simplest descriptions of an excitable media, consequently it has been used as simplified or toy model in many other areas (see *e.g.* [3, 36, 37]).

A crucial feature that distinguishes the FHN model is that nonlinearities appear *only* in the dynamics of the activator field u. This saturating nonlinearity term has the form of a cubic function in u. A generic FHN model is given by:

$$\partial_t u = au - bv + \alpha u^2 - \beta u^3 + D_u \partial_x^2 u \tag{2.2}$$

$$\partial_t v = cu - dv + m + D_v \partial_x^2 v, \tag{2.3}$$

where D_u and D_v are the diffusion coefficients (consequently they are assumed to be always positive quantities). The coefficients a, b, c, d are typically positive in order to preserve the activator-inhibitor interpretation[2]. In order to get the nonlinear saturation the the cubic coefficient β should be always positive. Finally, the constant m and the quadratic coefficient α can be either positive, zero or negative.

Let us remark that in the literature there are many different ways of writing FHN-like systems. Typically they can be mapped one into the other (see Ref. [37] for a discussion of this topic). In Eqs. (2.2,2.3) we chose a very general form in order not to introduce unnecessary constraints.

2.2.3 Three variable activator-inhibitor model

A natural extension of the standard FHN model is to consider the case where a second inhibitor comes into play. Such kind of models have been scarcely studied in the literature. Some examples, known to us, of fields where these three variable activator-inhibitor models have been used to describe the formation of pattern are in sea shells [22], in cell biology [23], in interacting biological populations [40], in spot dynamics in gas discharges devices [18, 19, 20, 21] and in concentration patterns appearing in heterogeneous catalysis [41, 42]. In these cases the models are typically under bistable conditions. In [17] a related three variable model has been studied numerically.

Let us consider the following extention of FHN model in Eqs. (2.2,2.3):

$$\begin{aligned}
\partial_t u &= au - bv + \alpha u^2 - \beta u^3 - gw + D_u \partial_x^2 u && (2.4)\\
\partial_t v &= cu - dv + m + D_v \partial_x^2 v && (2.5)\\
\partial_t w &= eu - fw + n + D_w \partial_x^2 w, && (2.6)
\end{aligned}$$

where w is the new inhibitor. The new constants g, e and f are positive quantities and n can assume any value. Note that the activator has similar impact in the dynamics of both inhibitors.

As we already mentioned in the introduction of this chapter, our studies will be directed upon the stability analysis of spatially homogeneous solutions. Therefore here we will assume that Eqs. (2.4,2.5,2.6) admit such a solution for $u = u_0$, $v = v_0$ and $w = w_0$. In this case we can rewrite the model using new field variables: $u \rightarrow u - u_0$, $v \rightarrow v - v_0$ and $w \rightarrow w - w_0$.

---

[2] It is interesting to note that the case when $a, d > 0$ and $b, c < 0$ is called *activation-depletion model* and has a dynamics very similar to the activator-inhibitor model. Activation-depletion systems have been used to model, for instance, the formation of dunes by action of the wind in deserts [16].

The new system has a homogeneous trivial solution at $u = 0, v = 0$ and $w = 0$. Performing a convenient change of the units of space and time, the system of Eqs. (2.4,2.5,2.6) reduces to:

$$\begin{aligned} \partial_t u &= au - bv + \alpha u^2 - \beta u^3 - gw + \partial_x^2 u & (2.7)\\ \tau\partial_t v &= cu - dv + \delta\partial_x^2 v & (2.8)\\ \varpi\partial_t w &= eu - fw + \gamma\partial_x^2 w, & (2.9) \end{aligned}$$

where $\delta = D_v/D_u$ and $\gamma = D_w/D_u$ are the ratios between the inhibitor and activator diffusion coefficients and τ and ϖ are two new time scales indicating how fast is the dynamics of each inhibitor respect to the activator[3].

2.3 Two variable model with nonlocal coupling

- Adiabatic elimination of one inhibitor

In many practical situations the time evolution of the two inhibitors is governed by *well separated time scales* [43, 44, 45].

Here we will concentrate on the case where the inhibitor w has a much faster dynamics than v (*i.e.* $\tau \gg \varpi$). In particular we will consider a situation where the time constant ϖ is so small that can be considered equal to zero. Consequently the time derivative in the evolution equation (2.9) for the fast inhibitor w can be neglected. The resulting equation:

$$eu = fw - \gamma\partial_x^2 w, \tag{2.10}$$

is *linear*. Therefore we can solve it using the *Green's Function Method*. In Appendix A we show that this method allows us to write the inhibitor concentration w as a *functional* of the activator concentration u; namelly:

$$w(x;t) = \frac{\mu}{g}\int_{-\infty}^{+\infty} e^{-\sigma|x-x'|}u(x';t)dx' \overset{\text{def}}{=} \frac{\mu}{g}\int_{-\infty}^{+\infty} \Sigma(x,x')u(x';t)dx', \tag{2.11}$$

where:

$$\sigma = \sqrt{f/\gamma} \quad \text{and} \quad \mu = g\sqrt{e^2/4\gamma f}. \tag{2.12}$$

$\Sigma(x,x') \overset{\text{def}}{=} e^{-\sigma|x-x'|}$ is the Green's function of the convolution integral.

Setting $\tau = 1$ and inserting the functional of Eq. (2.11) in Eq. (2.7) we get the following two variable system:

---

[3] Note that, due to the change of variables and units, the constants $a, b, c, d, e, f, g, \alpha$ and β in Eqs. (2.7,2.8,2.9) are not the same than in Eqs. (2.4,2.5,2.6).

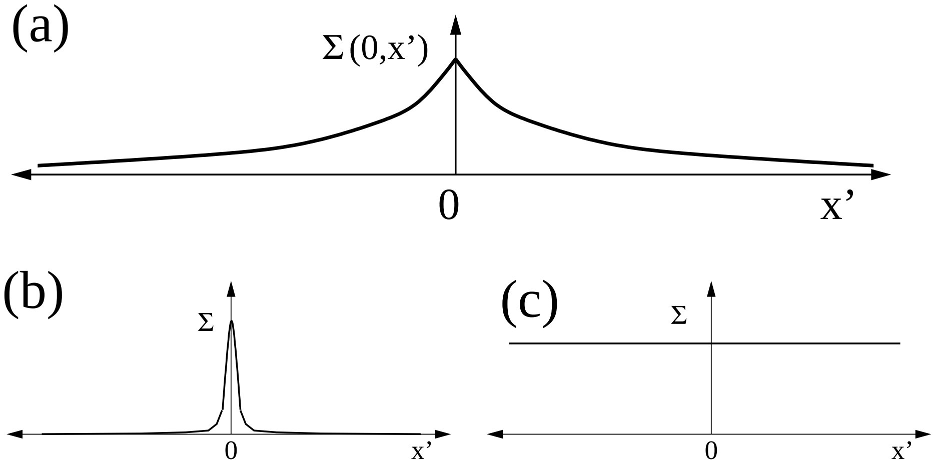

Figure 2.1: Sketches of the nonlocal coupling kernel $e^{-\sigma|x-x'|}$. *Normal case* in (a), *diffusive limit* (*i.e.* σ large) in (b) and *global coupling limit* (*i.e.* $\sigma \to 0$) in (c) .

$$\partial_t u = au - bv + \alpha u^2 - \beta u^3 + \partial_x^2 u - \mu \int_{-\infty}^{+\infty} e^{-\sigma|x-x'|} u(x',t)dx' \quad (2.13)$$

$$\partial_t v = cu - dv + \delta \partial_x^2 v. \quad (2.14)$$

In the rest of this Thesis we will refer to this *reaction-diffusion system with nonlocal coupling* as the **RDNC model**.

- Inhibitory nonlocal coupling

Note that the new integral term in Eqs. (2.13,2.14) acts as a *inhibitory nonlocal coupling* for the u-field. The Green's function $e^{-\sigma|x-x'|}$ can be interpreted now as a *nonlocal kernel* which acts as a "weight factor" for the influence of the value of the field in the position x' (*i.e.* $u(x')$) on $u(x)$. In Fig. 2.1(a) a schematic plot of this Nonlocal Kernel is shown (in Figs. 2.1 (b) and (c) two limit cases of this kernel are also shown). Note that since $\Sigma(x,x')$ depends only on the difference $x - x'$ (*i.e.* $\Sigma(x,x') \equiv \Sigma(|x-x'|)$), the nonlocal coupling is *isotropic*. The new parameters σ and μ are respectively the *inverse of the coupling range* and the *strength of the nonlocal coupling* (see Eq. (2.12) for their relation to the original parameters of the three variable model (2.7,2.8,2.9)).

Finally, we want to mention that some cases reaction-diffusion systems with nonlocal coupling terms have been studied in [41, 42, 45, 46].

2.3.1 Interesting limits of the nonlocal coupling

Let us discuss some important limits of the RDNC model when the coupling range σ^{-1} is varied.

- Case $\sigma \to \infty$: Diffusive Coupling

A particularly interesting case can be recovered from Eqs. (2.13,2.14) when the coupling range is very short (*i.e.* σ large). The nonlocal kernel becomes nonzero only very near the origin (see Fig. 2.1 (b)). If we expand $u(x-y)$ in a Taylor series around x, the nonlocal coupling term becomes:

$$\begin{aligned}\int_{-\infty}^{+\infty} e^{-\sigma|x-x'|}u(x')dx' &\equiv \int_{-\infty}^{+\infty} e^{-\sigma|y|}u(x-y)dy \\ &= \int_{-\infty}^{+\infty} e^{-\sigma|y|}\Big\{u(x) - y\partial_x u(x) \\ &\quad + \frac{y^2}{2}\partial_x^2 u(x) - \frac{y^3}{6}\partial_x^3 u(x) \\ &\quad + \cdots + (-1)^n \frac{y^n}{n!}\partial_x^n u(x) + \cdots\Big\}dy. \qquad (2.15)\end{aligned}$$

Using that $\int_0^\infty y^n e^{-\sigma y}dy = \frac{n!}{\sigma^{n+1}}$ if n is even and $\int_0^\infty y^n e^{-\sigma y}dy = 0$ if n is odd, we get:

$$\begin{aligned}\int_{-\infty}^{+\infty} e^{-\sigma|x-x'|}u(x')dx' &= m_0 u(x) + m_2\partial_x^2 u(x) \\ &\quad + \cdots + m_{2n}\partial_x^{2n}u(x) + \cdots \qquad (2.16)\end{aligned}$$

where $m_0 = 2/\sigma$, $m_2 = 4/\sigma^3$ and in general $m_{2n} = 2(2n)!/\sigma^{2n+1}$. Since σ is big the constants m_{2n} get progressively smaller as n increases. If we truncate this series to include only two terms, we get a standard two variable FHN as in Eqs. (2.2,2.3) with an effective $a' = a - 2\mu/\sigma$ and diffusion constant for the activator equal to $D_u' = 1 - 4\mu/\sigma^3$. Consequently, in the σ large limit, the inhibitory nonlocal coupling reduces to an effective diffusion operator.

- Case $\sigma \to 0$: Global Coupling

Another interesting case is when the coupling range goes to infinity (*i.e.* $\sigma \to 0$). In this case the nonlocal kernel becomes flat ($\equiv 1$); see Fig. 2.1 (c). This case corresponds to a *global coupling* where the coupling term is given by:

$$\mu \int_{-\infty}^{+\infty} u(x',t)dx'.$$

Reaction-diffusion systems with global coupling have been fairly well studied in the literature. Some references, between many, are [41, 42, 43, 44, 46, 47, 48, 49, 50].

2.3.2 Alternative interpretation of the nonlocal coupling: Feedback

Let us briefly mention that the nonlocal coupling term in the RDNC model can alternatively considered as an externally imposed *feedback* in a reaction-diffusion model. An example of this feedback mechanism has been realized in the light-sensitive Belousov-Zhabotinskii media.

The Belousov-Zhabotinskii (BZ) reaction is one of the best studied cases of pattern forming chemical reactions (see *e.g.* [2, 11, 12]). In the last years there has been an increasing interest in the BZ reaction using Ruthenium as the catalyst. In this variant of the BZ reaction the properties of the media depend on the light intensity [51]. A mathematical model for this reaction has been introduced in [52]. This model has been contrasted with experiments in the case where the light intensity is kept constant (see [24, 53] and references therein). In recent experiments, information about the patterns of the system has been included in the intensity of the projected light [54]. This nonhomogenous light intensity acts as a nonlocal coupling feedback.

2.3.3 Notation for the RDNC model

In the progress of this thesis we will study in detail the system defined by Eqs. (2.13,2.14). Thus, it will be useful to introduce the following, more compact, notation the RDNC model:

$$\partial_t \mathbf{X} = \mathbf{\Lambda}[\mathbf{X}] \overset{\text{def}}{=} \mathbf{\Lambda}_H \mathbf{X} + \mathbf{\Lambda}_D \partial_x^2 \mathbf{X} + \mathbf{\Lambda}_{NC} \int_{-\infty}^{+\infty} \Sigma(|x - x'|)[\mathbf{X}(x')]dx' + \mathbf{h}(\mathbf{X}), \quad (2.17)$$

where the operator $\mathbf{\Lambda}[\circ]$ acts over the state vector:

$$\mathbf{X}(x;t) \overset{\text{def}}{=} \begin{pmatrix} u(x;t) \\ v(x;t) \end{pmatrix}, \quad (2.18)$$

and includes the following square matrices: $\mathbf{\Lambda}_H$, $\mathbf{\Lambda}_D$ and $\mathbf{\Lambda}_{NC}$. The *homogeneous matrix* $\mathbf{\Lambda}_H$ correspond to the linear homogeneous part of the system and is given by:

$$\mathbf{\Lambda}_H \overset{\text{def}}{=} \begin{pmatrix} a & -b \\ c & -d \end{pmatrix}. \quad (2.19)$$

The *diffusion matrix* $\mathbf{\Lambda}_D$ is given by:

$$\mathbf{\Lambda}_D \overset{\text{def}}{=} \begin{pmatrix} 1 & 0 \\ 0 & \delta \end{pmatrix}. \tag{2.20}$$

The *nonlocal coupling matrix* $\mathbf{\Lambda}_{NC}$ is given by:

$$\mathbf{\Lambda}_{NC} \overset{\text{def}}{=} \begin{pmatrix} -\mu & 0 \\ 0 & 0 \end{pmatrix}, \tag{2.21}$$

and the scalar function:

$$\Sigma(|x - x'|) \overset{\text{def}}{=} e^{-\sigma|x-x'|}, \tag{2.22}$$

is the *nonlocal coupling kernel*. Finally, $\mathbf{h}(\mathbf{X})$ is the nonlinear function defined by:

$$\mathbf{h}(\mathbf{X}) \overset{\text{def}}{=} \begin{pmatrix} +\alpha u^2 - \beta u^3 \\ 0 \end{pmatrix}. \tag{2.23}$$

Chapter 3

Linear Stability Analysis

The RDNC model possesses, for any value of the parameters , a solution which is uniform in space and time. In this chapter we will analyse the stability of this solution. We will see that, as the parameters of the model vary, this solution can become unstable against small perturbations in space and/or in time. New stable space and/or time periodic solutions arise after these instabilities of the uniform solution. The dynamics and competition of such solutions will be studied in the rest of this thesis.

3.1 Introduction

In this chapter we will analyse the stability of the homogeneous solutions of the RDNC model. Depending on the values of the parameters of the model, there can be one or more of these homogeneous solutions. Here we will concentrate on the analysis of the patterns resulting from destabilisation of a unique homogeneous solution.

In order to analyse these instabilities we will span the parameter space using mainly two characteristic parameters: a and δ. The "driving force" a takes into account the "reaction" part of the RDNC model and the diffusion ratio δ the "diffusion" part.

We will see that all three basic types of instabilities mentioned in the introduction of this thesis (*cf.* Turing, homogeneous Hopf and wave instability) are found in the RDNC model. Moreover, instabilities where two different patterns become unstable simultaneously (*i.e.* codimension-2 instabilities) may occur for special values of the control parameters.

- Organisation of this chapter

This chapter is organised as follows. In the next section we will study all the homogeneous solutions possible in the RDNC model. In Section 3.3 we will give a brief introduction to the concepts of bifurcation and instability. The analysis of the instabilities of the uniform solution in the RDNC model will be addressed in Section 3.4. Further investigations of these instabilities, including the exploration of the parameter space of the model, will be done in Section 3.5. In this last section we will analyse in detail the most important instabilities possible: Turing, wave and Codimension-2 wave-Turing.

3.2 Spatially homogeneous solutions

The fist step in our study of the RDNC model is to find its spatially homogeneous solutions. Inserting $\mathbf{X}(t) = (u(t), v(t))^{\mathrm{Tr}}$ in Eqs. (2.13,2.14) we get the following set of ordinary differential equations (ODE) [1]:

$$\begin{aligned} \partial_t u &= (a - \frac{2\mu}{\sigma})u - bv + \alpha u^2 - \beta u^3 \overset{\text{def}}{=} g(u,v) && (3.1)\\ \partial_t v &= cu - dv \qquad\qquad\qquad\qquad \overset{\text{def}}{=} h(u,v). && (3.2) \end{aligned}$$

The points in the space u vs. v where $\partial_t u = 0$ and $\partial_t v = 0$ are called the *fixed points* of Eqs. (3.1,3.2). They correspond to solutions of the RDNC model which are uniform in space and in time.

- Trivial fixed point of Eqs. (3.1,3.2)

Eqs. (3.1,3.2) have a trivial fixed point solution at:

$$\mathbf{X}_0 \overset{\text{def}}{=} \begin{pmatrix} 0 \\ 0 \end{pmatrix}. \tag{3.3}$$

The existence of this solution is just a result of the selection of the variables done in Section 2.2.3. Although this solution exists always and does not depend on the value of the parameters of Eqs. (2.13,2.14), its *stability may change*. This last issue will be analysed through this chapter.

---

[1] Notice that, even for a spatially homogeneous solution, the nonlocal coupling term *does* contribute to the homogeneous problem with the term $-\frac{2\mu}{\sigma}u$ (this is because $-\mu\int_{-\infty}^{+\infty} e^{-\sigma|x'|}dx' = -\frac{2\mu}{\sigma}$).

- Other fixed points of Eqs. (3.1,3.2)

Since the RDNC model is nonlinear, the ODE (3.1,3.2) may have *more than one* fixed point solution. Since Eq. (3.2) is linear, these solutions satisfy that $v = \frac{c}{d}u$. Using this feature, and that the function $g(u, v)$ is cubic, we can find the fixed points analytically. They are the roots of the cubic equation $g(u, \frac{c}{d}u) = 0$. In fact, we do not need to solve this cubic equation because one of the solution is already known: $\mathbf{X}_0$. The other two fixed points are:

$$u_{\pm} = \frac{\alpha \pm \sqrt{\alpha^2 + 4\beta(a - 2\mu/\sigma - bc/d)}}{2\beta}. \tag{3.4}$$

Consequently Eqs. (3.1,3.2) allow either one or three fixed point solutions. In this last case the solutions are: $\mathbf{X}_+ \overset{\text{def}}{=} (u_+, v_+)^{\text{Tr}}$, $\mathbf{X}_0$ and $\mathbf{X}_- \overset{\text{def}}{=} (u_-, v_-)^{\text{Tr}}$

Since we assume β to be positive (see discussion in the previous chapter), Eqs. (3.1,3.2) will have only one fixed point when the following condition is satisfied:

$$a - \frac{2\mu}{\sigma} - \frac{bc}{d} + \frac{\alpha^2}{4\beta} \leq 0, \tag{3.5}$$

otherwise three fixed points exist.

3.2.1 Nullclines of the RDNC model

A convenient way to analyse the fixed points and to get a qualitative picture of the dynamics of a nonlinear ODEs like Eqs. (3.1,3.2), is using the so called nullclines (see *e.g.* [3]). The *nullclines* are the curves in the phase space u vs. v where any of the time derivatives in Eqs. (3.1) and (3.2) is equal to zero. Each of these curves is *implicitly* defined by $g(u, v) = 0$ and $h(u, v) = 0$ respectively. The points where the nullclines intersect are the fixed points of the system.

Some characteristic examples of the nullclines of Eqs. (3.1,3.2) are shown in Fig. 3.1. In Figs. 3.1(a), 3.1(b) and 3.1(c) we increase the value of the model parameter a as all the other parameters are kept constant and the quadratic nonlinearity is zero (*i.e.* $\alpha = 0$). The same is done in Figs. 3.1(d), 3.1(e) and 3.1(f) for a nonzero quadratic nonlinearity (*i.e.* $\alpha \neq 0$). The locations of the fixed points are indicated with full circles if they are stable and open circles if they are unstable. Note that the quadratic nonlinearity breaks the symmetry $(u, v) \to (-u, -v)$ of the system, but it does not change the quantity of fixed points (*cf.* Eq. (3.5)).

In Figs. 3.1(a) and 3.1(b) only one fixed point exists whereas in 3.1(c) three fixed points are present. The unique fixed point is stable in Fig. 3.1(a) and unstable in Fig. 3.1(b). In this last case, a new (stable) time oscillation

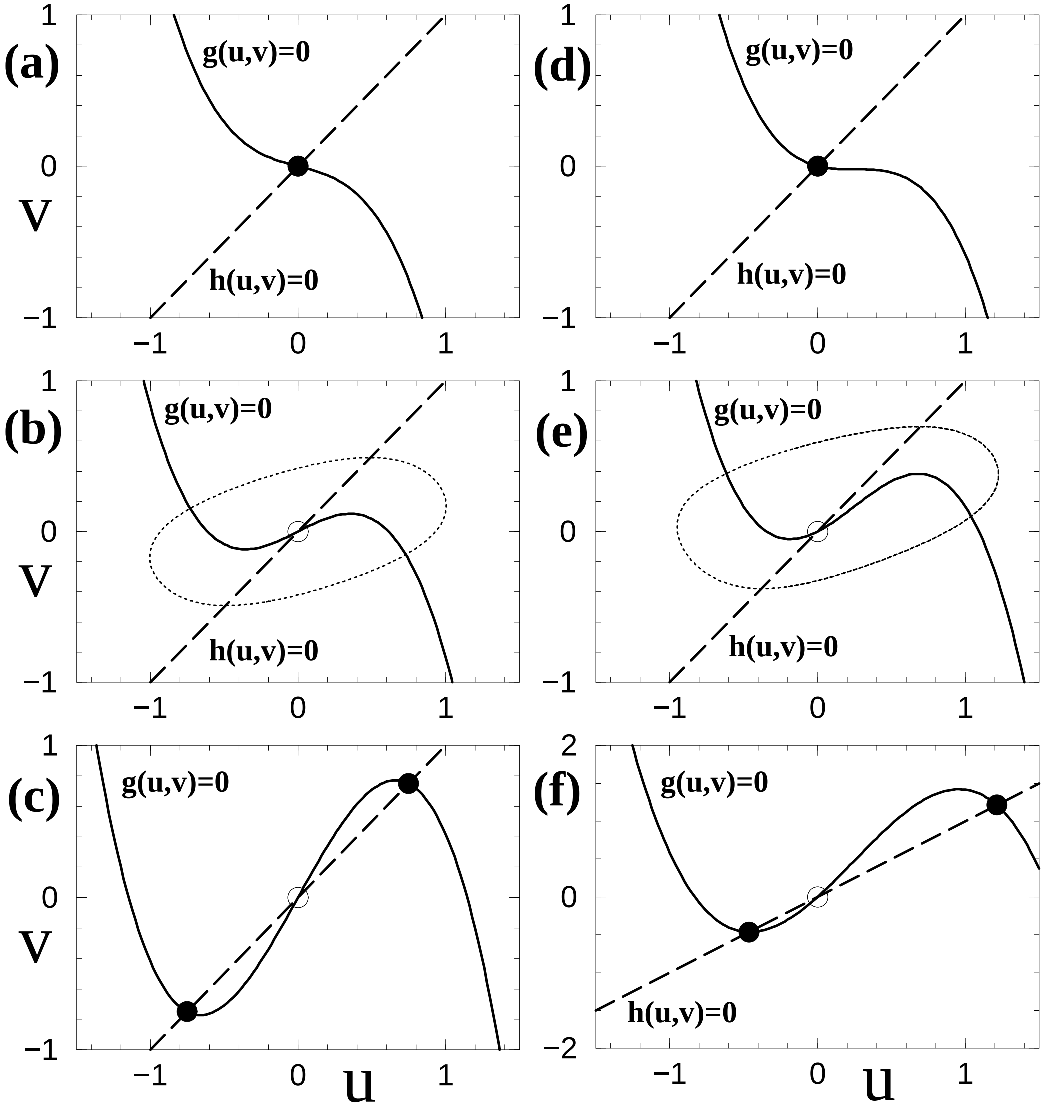

Figure 3.1: Characteristic examples of the nullclines of the Eqs. (3.1,3.2). The full and dashed curves correspond to $g(u, v) = 0$ and $h(u, v) = 0$ respectively. In (a), (b) and (c) we increase the value of the parameter a for $\alpha = 0$ (consequently the symmetry $(u, v) \rightarrow (-u, -v)$ is conserved). The same is done in (d), (e) and (f) for $\alpha = 1$. The full (open) circles show the location of stable (unstable) fixed points. Cases (a) and (d) correspond to monostable situations. In (b) and (e) two oscillatory situations are displayed and the system is bistable in (c) and (f). The dotted curve in (b) and (e) show the location of the stable limit cycle. In (a) and (d) $a = 3$, in (b) and (e) $a = 6$ and in (c) and (f) $a = 11$. The values of the other parameters are $b = 4, c = d = 1, \beta = 4/3, \mu = 2, \sigma = 1$.

occurs. In this case the system is said to be *oscillatory*[2]. The stable *limit cycle* is shown in Fig. 3.1(b) with a dotted curve.

The situation shown in Fig. 3.1(c) correspond to a *bistable* case[3]. A fourth case (not shown in Fig. 3.1) can occur in Eqs. (3.1,3.2) when only one fixed point is present and both, the quadratic nonlinearity and the difference between the time sales of activator and inhibitor, are big. In this case the fixed point is stable, but the dynamics near this fixed point is such that under perturbations exceeding a certain threshold the system undergoes a large excursion in the phase plane before returning again to the fixed point. This type of dynamics is called *excitable* and becomes very interesting when it is coupled to a diffusion mechanism (for some relevant reviews of this topic refer to [2, 3, 36]).

Neither the case of bistability (*cf.* Figs. 3.1(c) and 3.1(f)) nor excitable situation will considered in this thesis. We will restrict ourselves to the study of the stability of the fixed point $\mathbf{X}_0$ in the monostable situation and new solutions arising when the fixed point in unstable. Therefore the concept of linear stability is of crucial importance and we will explain it in more detail in the following sections.

3.3 Bifurcations and Instabilities

One of the organising ideas in the field of dynamical systems is the subject of *bifurcation*. Although this idea is rather old, only in the last decades it has been subject of intensive development both theoretical and practical (*i.e.* in the use of these ideas in many practical situations). For some recent good introductions to this subject we refer to the books [55, 56, 57, 58].

An accurate definition of bifurcations in dynamical systems needs a good deal of mathematical preliminaries, in this section we will give only a very short and crude introduction to it. We will pay special attention to a specific kind of bifurcation; namely the so called linear instability.

3.3.1 Bifurcations and Linear Instabilities

Mathematical models of deterministic physical systems typically consist of dynamical systems. These dynamical systems usually contain parameters. These parameters take explicitly into account the influence of either the

---

[2] The oscillatory situation is frequently found in chemical reactions, population dynamics and many other areas (see *e.g.* [2, 6, 8]).

[3] A lot of effort has been done to study bistable systems when diffusion is added. For an overview of this topic we refer to [2, 3] and references therein.

internal properties of the system or other external features. Often, some subgroup of these parameters can be changed at will by varying some properties of the physical process or by other means. Such parameters are called *control parameters*. Frequently, as these control parameters are varied, the qualitative structure of the solutions of the dynamical system change. These changes are called *bifurcations* and the values of the control parameters for which they happen are called *bifurcation values*.

Although a universal classification of (local) bifurcations of first order ODEs can be done (see for example [55, 56, 57, 58]), here we will concentrate our attention in a particular kind of bifurcations: the *linear instabilities*. In these bifurcations at least one fixed point exists before and after the instability.

More specifically, let us consider a generic system of ODEs like:

$$\partial_t \mathbf{Y}(t) = \mathbf{F}(\chi, \mathbf{Y}(t)), \tag{3.6}$$

where $\mathbf{Y}(t)$ is a vectorial field, χ is the control parameter[4] and $\mathbf{F}$ is a nonlinear vectorial function. Let us suppose that Eq. (3.6) has a *time independent* solution $\mathbf{Y}_0(\chi)$ for any value of the control parameter χ. We will further assume that this solution is stable under small perturbations if $\chi < \chi_c$ and unstable if $\chi > \chi_c$. Thus, at $\chi = \chi_c$ the system of Eq. (3.6) is said to undergo a *linear instability*. This is clearly nothing else than a particular case of bifurcation.

The structure of the phase space of Eq. (3.6) in the vicinity of χ_c is different if χ is bigger or smaller than this value. Hence, a natural question that arises in this case is if the solution $\mathbf{Y}_0$ is the only solution possible or if some new solutions appear. Surprisingly, given some very general conditions, the structure of the solutions near the instability is very restricted. This information is given by a theorem due to Sattinger [5, 59]:

- Suppose that a solution $\mathbf{Y}_0(\chi)$ of the ODE (3.6) *exists* in a neighbourhood of χ_c and that λ_i are the eigenvalues of the Jacobian matrix corresponding to the linearisation of Eqs. (3.6) around $\mathbf{Y}_0(\chi_c)$. If the eigenvalue(s) λ_i with real part(s) equal to zero is(are) a simple root(s) of the characteristic polynomial, then there are *at least one* new branch of solutions that coincides with the solution $\mathbf{Y}_0$ at $\chi = \chi_c$. This(these) new branch(es) either extends to infinity or meets another bifurcation point.

---

[4] For sake of simplicity, in this section, we will assume that only one parameter is varied but similar ideas do apply to the case with multiple control parameters.

3.4 Instabilities in the RDNC model

Let us now address the analysis of possible instabilities of the RDNC model of Eqs. (2.13,2.14). As we saw in Section 3.2, depending on the condition given by Eq.(3.5), the model can have either one or three homogeneous fixed points. Here we will study the stability of $\mathbf{X}_0 = (0,0)^{\mathrm{Tr}}$ when this is the only[5] homogeneous fixed point possible.

- The perturbation ansatz

We will test the stability of $\mathbf{X}_0$ using the following periodic perturbation ansatz:

$$\Delta\mathbf{X}(x) = \mathbf{U}\, e^{ikx+\lambda(k)t} + c.c., \tag{3.7}$$

where the vector $\mathbf{U}$ is arbitrary and can be a complex quantity. This ansatz corresponds to a spatially periodic perturbation with wavenumber k. The time dependence of this ansatz is governed by the function $\lambda(k)$. Note that $\lambda(k)$ can be complex quantity and that the complex conjugate *c.c.* in Eq. (3.7) is used to assure that $\mathbf{X}_0 + \Delta\mathbf{X}$ is real.

The real part of $\lambda(k)$ is the *growth rate* of perturbations with wavenumber k and can be typically calculated as a function of it. If $\mathrm{Re}(\lambda(k))$ is negative for every k, then the solution $\mathbf{X}_0$ is stable. However, under changes of the parameters of the model, it can happen that for a particular $k = k_c$ the growth rate becomes zero. In this case the system is said to be *marginally stable* or *critical* under perturbations with *critical wavenumber* k_c. If we further continue to change the control parameter after such a situation, $\mathbf{X}_0$ will become now unstable against perturbations with wavenumbers k contained in an interval around k_c.

The imaginary part of $\lambda(k)$ is also important because it allows the perturbation to be periodic in time. The case when $Im(\lambda(k_c)) = 0$ is called *Turing instability* and corresponds to the onset of patterns periodic in space and stationary in time. It was first described by Turing fifty years ago [60] and has been subject of a large amount of work [1, 2, 5, 7]. On the other hand, for $Im(\lambda(k_c)) \neq 0$ the instability is of *Hopf* type. This corresponds to an instability leading to a limit cycle oscillation in time.

It is also important to distinguish two cases of the Hopf instability: k_c may be zero nor not. If $k_c = 0$ (and $Im(\lambda(0)) \neq 0$), the *homogeneous Hopf instability* case, the instability leads to (spatially homogeneous) time

---

[5] Note that we can also do the same kind of study for the other fixed points $\mathbf{X}_\pm = (u_\pm, v_\pm)^{\mathrm{Tr}}$ when the condition of Eq. (3.5) is not satisfied. The stability of them can be recast easily in to one for $\mathbf{X}_0$ just doing a spatially homogeneous shift of the variables: $u \to u - u_\pm$ and $v \to v - v_\pm$.

oscillations and has been studied extensively both, in experiments and in theory [1, 2, 5, 6, 7, 8]. In the other hand, if $k_c \neq 0$ (and $Im(\lambda(k_c)) \neq 0$), the **wave instability**, an instability leading to *travelling waves* happens. This last kind of instability has been studied far less than the other two cases [1].

Inserting the ansatz $\mathbf{X}_0 + \Delta\mathbf{X}$ in Eq. (2.17) we get the following set of nonlinear PDEs:

$$\partial_t \Delta\mathbf{X} = \mathbf{\Lambda}[\Delta\mathbf{X}]. \tag{3.8}$$

Linearising these PDEs and considering the form of the ansatz introduced in Eq. (3.7), we get the following eigenvalue problem:

$$\lambda(k)\mathbf{U} = \hat{\mathbf{\Lambda}}(k)\mathbf{U}, \tag{3.9}$$

where the matrix $\hat{\mathbf{\Lambda}}(k)$ is given by:

$$\hat{\mathbf{\Lambda}}(k) \overset{\text{def}}{=} \begin{pmatrix} a - k^2 - \frac{2\mu\sigma}{\sigma^2+k^2} & -b \\ c & -d - \delta k^2 \end{pmatrix}. \tag{3.10}$$

This matrix is nothing else but the Jacobian of the RDNC model around $\mathbf{X}_0$ in Fourier space. The eigenvalues of $\hat{\mathbf{\Lambda}}(k)$ will provide us with the growth rates $\lambda(k)$.

3.4.1 Eigenvalues and Eigenvectors

Since $\hat{\mathbf{\Lambda}}(k) = \hat{\mathbf{\Lambda}}(-k)$ the eigenvalues satisfy the following symmetry:

$$\lambda(k) \equiv \lambda(-k). \tag{3.11}$$

Consequently, if the model is critical for a wavenumber k_c, then it is also critical for $-k_c$.

Since the matrix $\hat{\mathbf{\Lambda}}(k)$ is 2×2 we expect to have generically *two different* eigenvalues $\lambda(k)$ for each wavenumber k. These eigenvalues can be easily calculated using again the fact that the matrix $\hat{\mathbf{\Lambda}}(k)$ is a 2×2. We can write them as:

$$\lambda_{\pm}(k) = \frac{tr\hat{\mathbf{\Lambda}}(k) \pm \sqrt{(tr\hat{\mathbf{\Lambda}}(k))^2 - 4det\hat{\mathbf{\Lambda}}(k)}}{2}. \tag{3.12}$$

If the conditions:

$$det\hat{\mathbf{\Lambda}}(k) > 0 \quad \text{and} \quad tr\hat{\mathbf{\Lambda}}(k) < 0, \tag{3.13}$$

are satisfied for every wavenumber k, then both eigenvalues $\lambda_{\pm}(k)$ have negative real part and consequently the solution $\mathbf{X}_0$ is stable. From Eq. (3.12) it is clear that there are two different ways in which $\mathbf{X}_0$ can become critical under changes of the parameters of the model:

1. There exists a k_c for which: $det\hat{\mathbf{\Lambda}}(k_c) = 0$ and $tr\hat{\mathbf{\Lambda}}(k_c) < 0$ whereas the conditions of Eq. (3.13) are satisfied for all other k.
2. There exists a k_c for which: $tr\hat{\mathbf{\Lambda}}(k_c) = 0$ and $det\hat{\mathbf{\Lambda}}(k_c) > 0$ whereas the conditions of Eq. (3.13) are satisfied for all other k.

In the following we will call these two conditions *instability threshold conditions*. At these threshold conditions the system is critical and there are one or more eigenvalues with zero real part. These are called *critical eigenvalues*.

3.4.1.A Critical Eigenvalues

Let us analyse in more detail the two possible ways in which the RDNC model can become critical.

In Case 1 both eigenvalues are real and: $\lambda_+(k_c) = 0$ and $\lambda_-(k_c) < 0$. Hence there is only one critical eigenvalue. This case corresponds to a Turing instability. In the following we will denote its critical wavenumber k_c with k_T^c.

In Case 2 both eigenvalues are critical and: $\lambda_+(k_c) = +i\omega_c$ and $\lambda_-(k_c) = -i\omega_c$ where:

$$\omega_c \overset{\text{def}}{=} \sqrt{det\hat{\mathbf{\Lambda}}(k_c)}. \tag{3.14}$$

This case corresponds to a Hopf instability with critical wavenumber k_c and *critical frequency* ω_c. If $k_c = 0$ then an homogeneous Hopf instability appears. If, on the other hand, $k_c \neq 0$ then a wave instability arises. In the rest of this thesis we will denote its critical wavenumber k_c with k_W^c.

3.4.1.B Critical Eigenvectors and Solutions

Each critical eigenvalue of the eigenvalue problem of Eq. (3.9) has an associated *critical eigenvector*. Let us now analyse these eigenvectors.

- Turing Case

Using the symmetry of Eq. (3.9) we know that in the Turing case there are *two* critical eigenvalues: $\lambda_+(k_T^c)$ and $\lambda_+(-k_T^c)$ (where $\lambda_+(k_T^c) = \lambda_+(-k_T^c) = 0$). The eigenvalue problem of Eq. (3.9) has the same critical eigenvector $\mathbf{U}_T$ for these two critical eigenvalues. The critical eigenvector $\mathbf{U}_T$ has a very simple form and is calculated in Appendix B. An important property of this critical eigenvector (and the ones for the Hopf case as well) is that its *norm is arbitrary*. Therefore, in the onset of a Turing instability, any linear combination of the vectors:

$$\mathbf{X}_T^c = \mathbf{U}_T e^{ik_T^c x_0} \quad \text{and} \quad \overline{\mathbf{X}_T^c} = \mathbf{U}_T e^{-ik_T^c x_0}, \tag{3.15}$$

is a solution of the RDNC model. In the following we will call $\mathbf{X}_T^c$ and $\overline{\mathbf{X}_T^c}$ the (Turing) *critical solutions* of the RDNC model.

- Homogeneous Hopf Case

In the homogeneous Hopf case we have also two critical eigenvalues: $\lambda_+(0)$ and $\lambda_-(0)$ (where $\lambda_+(0) = \overline{\lambda_-}(0)$). Each of them has an associated eigenvector: $\mathbf{U}_H$ and $\overline{\mathbf{U}_H}$ respectively (see Appendix B for their derivation). Consequently the homogeneous Hopf critical solutions are:

$$\mathbf{X}_H^c = \mathbf{U}_H e^{i\omega_c t_0} \quad \text{and} \quad \overline{\mathbf{X}_H^c} = \overline{\mathbf{U}_H} e^{-i\omega_c t_0}. \tag{3.16}$$

- Wave Case

Finally in the case of a wave instability we have four critical eigenvalues: $\lambda_+(k_W^c)$, $\lambda_-(k_W^c)$, $\lambda_+(-k_W^c)$ and $\lambda_-(-k_W^c)$ (where $\lambda_+(k_W^c) = \lambda_+(-k_W^c) = \overline{\lambda_-}(k_W^c) = \overline{\lambda_-}(-k_W^c)$) and correspondingly four critical solution vectors:

$$\begin{cases} \mathbf{X}_L^c = \mathbf{U}_W e^{i(\omega_c t_0 + k_W^c x_0)} & \text{and} \quad \overline{\mathbf{X}_L^c} = \overline{\mathbf{U}_W} e^{-i(\omega_c t_0 + k_W^c x_0)} \\ \mathbf{X}_R^c = \mathbf{U}_W e^{i(\omega_c t_0 - k_W^c x_0)} & \text{and} \quad \overline{\mathbf{X}_R^c} = \overline{\mathbf{U}_W} e^{-i(\omega_c t_0 - k_W^c x_0)} \end{cases} \tag{3.17}$$

where, as before, the critical eigenvector $\mathbf{U}_W$ is calculated in Appendix B. The first two critical solutions $\mathbf{X}_L^c$ and $\overline{\mathbf{X}_L^c}$ correspond to *left-travelling waves* whereas the last two $\mathbf{X}_R^c$ and $\overline{\mathbf{X}_R^c}$ to *right-travelling waves.*

3.4.2 Threshold conditions for Turing and Hopf instabilities

Now we will proceed to analyse the Turing, homogeneous Hopf and wave instabilities in the RDNC model. Here we will calculate the critical wavevectors and the instability threshold conditions whereas in the next section we will analyse them as function of the parameter space of the model.

- Turing instability

In Section 3.4.1 we saw that the Turing instability appears when $det\hat{\mathbf{\Lambda}}(k)$ becames negative. This will happen first for the k_T^c for which $det\hat{\mathbf{\Lambda}}(k)$ is minimum. Therefore the critical wavenumber k_T^c is given implicitly by the relationship:

$$1 = \frac{bc\delta}{(d + \delta {k_T^c}^2)^2} + \frac{2\mu\sigma}{(\sigma^2 + {k_T^c}^2)^2}. \tag{3.18}$$

Note that it is not convenient to give an closed analytic expression for k_T^c because if we solve (3.18) for k_T^c this leads to a quartic polynomial in ${k_T^c}^2$.

Using Eq. (3.13) and the conditions of Case 1 in Section 3.4.1 we find that if $det\hat{\mathbf{\Lambda}}(k_T^c) \leq 0$, then the RDNC model is unstable against Turing-perturbations. This means that the model will be unstable when:

$$a - {k_T^c}^2 - \frac{2\mu\sigma}{\sigma^2 + {k_T^c}^2} - \frac{bc}{d + \delta {k_T^c}^2} \geq 0. \tag{3.19}$$

The condition that the lhs of this equation is equal to zero defines the *Turing-instability threshold condition*.

- Homogeneous Hopf and Wave instabilities

A similar analysis can be done for the Hopf instability case. To find the critical wavenumber k_W^c we calculate the position of maxima of $tr\hat{\mathbf{\Lambda}}(k)$. This wavenumber is given by:

$${k_W^c}^2 = \sqrt{\frac{2\mu\sigma}{1+\delta}} - \sigma^2. \tag{3.20}$$

Consequently, this wavenumber is different from zero if $\sqrt{2\mu\sigma/1+\delta} - \sigma^2 \geq 0$ (*i.e.* wave instability), otherwise $k_W^c = 0$ (homogeneous Hopf instability).

Finally, the RDNC model will be unstable against Hopf-perturbations if $tr\hat{\mathbf{\Lambda}}(k_W^c) \geq 0$. Or, in terms of the parameters of the model, if:

$$a - d - (1+\delta){k_W^c}^2 - \frac{2\mu\sigma}{\sigma^2 + {k_W^c}^2} \geq 0. \tag{3.21}$$

As before, the lhs equal to zero gives the *Hopf-instability threshold condition.*

In the next Section we will analyse the critical wavenumbers and instability threshold conditions in terms of the parameters of the RDNC model.

3.5 Exploration of the Parameter Space of the RDNC model

The aim of this Section is to analyse the range of possible instability scenarios for different values of the parameters. After a brief discussion of the RDNC model parameters, we will first analyse the critical wavenumbers of the instabilities and then the corresponding threshold conditions. Finally we will discuss some interesting scenarios related to codimension-2 instabilities.

3.5.1 Parameters of the RDNC model

The RDNC model depends on 7 parameters: a, b, c, d, μ, σ and δ. However, an inspection of the parameter dependence of the critical wavenumbers (*cf.* Eqs. (3.18) and (3.20)) and of the instability threshold conditions (*cf.* Eqs (3.19) and (3.21)) shows that not all the parameters are equally relevant. The critical wavenumbers depend on the following parameters:

$$\begin{aligned} k_T^c &= k_T^c(bc, d, \mu, \sigma, \delta) && (3.22) \\ k_W^c &= k_W^c(\mu, \sigma, \delta). && (3.23) \end{aligned}$$

The threshold conditions are defined as implicit functions involving the parameters:

- a, bc, d, μ, σ and δ for Turing.
- a, d, μ, σ and δ for Hopf.

As we can see the wavenumbers and thresholds depend *only* on the product of b and c and *not* on their particular values. Therefore in the following we will fix one of them and vary the other. In particular through this thesis we will fix $c = 1$. Moreover, neither the critical wavenumber k_W^c nor the threshold condition of the Hopf instability depend on bc.

3.5.2 Critical wavenumbers

- Hopf wavenumber

The Hopf critical wavenumber $|k_W^c|$ only depends on the parameters of the nonlocal coupling σ and μ and the diffusion ratio δ. Let us analyse the effect of each of them separately.

In Fig. 3.2(a) we show a schematic drawing of the $|k_W^c|$ as the strength of the nonlocal coupling μ vary. An interesting point to remark is that to have a Hopf instability with a nonzero wavenumber, the nonlocal coupling strength μ should be *bigger* than a critical value given by:

$$\mu_c \overset{\text{def}}{=} \frac{\sigma^3(1+\delta)}{2}. \qquad (3.24)$$

Moreover, the nonlocal coupling should be inhibitory (*i.e.* $\mu > 0$). Therefore, a wave instability will happen only if the the strength of an inhibitory nonlocal coupling is sufficient. In particular, if $\mu = 0$, then Eqs. (2.13,2.14) reduce to a standard two variable reaction-diffusion system of the FHN type. For this type of systems a wave instability is not possible [14]. Therefore *the*

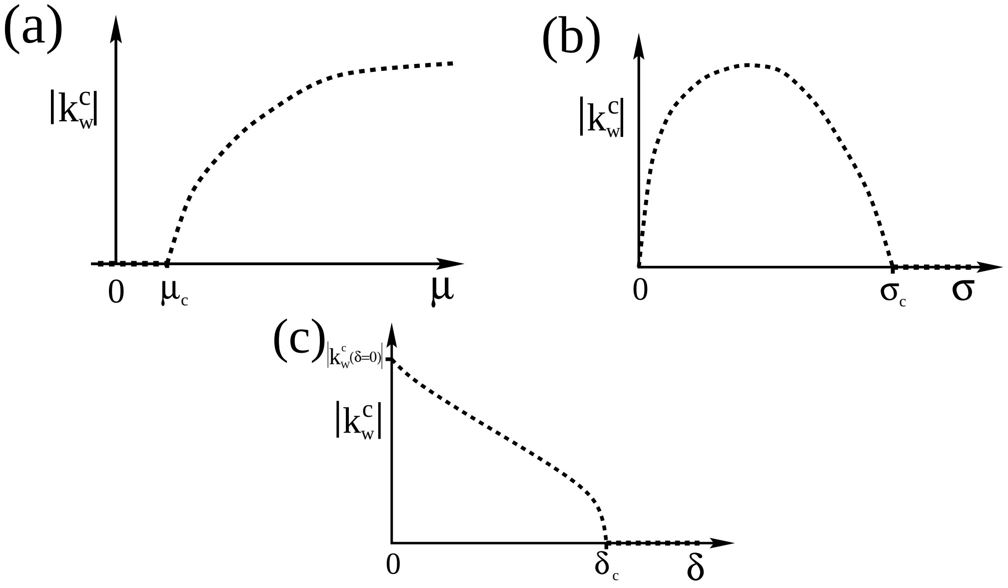

Figure 3.2: Schematic drawings of the critical wavenumber $|k_W^c|$ for the Hopf instability as its parameters μ, σ and δ are varied. Remember that $|k_W^c| > 0$ corresponds to a *wave instability* whereas $|k_W^c| = 0$ indicates a *homogeneous Hopf instability*. In (a) we show the dependence of $|k_W^c|$ on the coupling strength μ. In (b) $|k_W^c|$ is shown as the inverse of the coupling range σ is varied. Finally, in (c) the dependence of $|k_W^c|$ on the diffusion ratio δ is indicated. For the values of μ_c, σ_c, δ_c and $k_W^c(\delta = 0)$ see text.

possibility of a wave instability is induced by the presence of an inhibitory nonlocal coupling[6].

The dependence of $|k_W^c|$ on the coupling range σ^{-1} shows also very interesting features. In Fig. 3.2(b) we can see that if the coupling range is too short (*i.e.* $\sigma > \sigma_c$), then a Hopf instability with a nonzero wavenumber k_W^c is not possible. The critical coupling range is given by:

$$\sigma_c \overset{\text{def}}{=} \left(\frac{1+\delta}{\mu}\right)^{\frac{1}{3}}. \tag{3.25}$$

As we already mentioned in Section 2.3.1, when σ is big we can substitute the nonlocal coupling by a series of spatial derivatives. A second interesting feature is that when coupling range goes to infinity (*i.e.* to global coupling limit $\sigma \rightarrow 0$; see Fig. 3.2(b)) the wavenumber $|k_W^c|$ goes to zero.

The critical wavenumber $|k_W^c|$ also depends on the diffusion ratio δ. As we can see in Fig. 3.2(c), a wave instability can occur only if δ is smaller

---

[6] Or, changing the point of view, by the presence of a second inhibitor in the three variable model of Eqs. (2.4,2.5,2.6).

than a critical value given by:

$$\delta_c \overset{\text{def}}{=} \frac{2\mu}{\sigma^3} - 1. \tag{3.26}$$

This means that *a strongly diffusing inhibitor prevents a wave instability.* For the particular case of a nondiffusing inhibitor the critical wavenumber is:

$$k_W^c(\delta = 0) = \sqrt{\sqrt{2\mu\sigma} - \sigma^2}. \tag{3.27}$$

- Turing wavenumber

For the critical wavenumber of a Turing instability it is not possible to do a similar analysis as for the Hopf instability, because we don't have an explicit expression for the wavenumber. Nevertheless some generic information can be extracted.

For normal values of the coefficients, $|k_T^c|$ *is always bigger or equal than* $|k_W^c|$. To see this we need first to define a new quantity ϵ:

$$\epsilon(k_T^c) \overset{\text{def}}{=} \frac{bc\delta}{(d + \delta {k_T^c}^2)^2}. \tag{3.28}$$

If $bc > 0$ (the case that we are considering in this thesis) then $\epsilon(k_T^c) \geq 0$. If we now rewrite Eq. (3.18) using this new defined quantity, we get:

$${k_T^c}^2 = \sqrt{\frac{2\mu\sigma}{1 - \epsilon(k_T^c)}} - \sigma^2. \tag{3.29}$$

A direct comparison of this equation with Eq. (3.20) tells us that the following relationship is always valid:

$$|k_T^c| \geq |k_W^c| \quad (\text{if} \quad bc > 0). \tag{3.30}$$

Moreover, $|k_T^c| = |k_W^c|$ *only* when the diffusion ratio δ is zero. In this case:

$${k_T^c}^2 = {k_W^c}^2 = \sqrt{2\mu\sigma} - \sigma^2. \tag{3.31}$$

The relationship given in Eq. (3.30) tells us that for the RDNC model, near an instability of $\mathbf{X}_0$, *the period of the Turing structures will be always smaller than the period of the wave structures.*

Apart from $\delta = 0$, another interesting case is $\delta \to \infty$. Here an analytical formula for $|k_T^c|$ can be given. Doing a Taylor expansion of Eq. (3.18) for small δ^{-1}, and keeping only terms $\mathcal{O}(1)$, we obtain:

$${k_T^c}^2 = \sqrt{2\mu\sigma} - \sigma^2. \tag{3.32}$$

Note that $|k_T^c|$ is the same for $\delta = 0$ and $\delta \to \infty$!

3.5.3 Instability threshold conditions

In this subsection we will present a short analysis of the dependence of the instability threshold conditions on the parameters of the RDNC model. A deeper analysis will be done in Appendix C.

- Selection of the bifurcation parameters

As we already explained in Section 3.5.1, the parameter space of the RDNC model is spanned by *six relevant parameters*: a, bc, d, μ, σ and δ. The threshold conditions for the Turing and Hopf instabilities are given by the requirement that the left hand side of Eqs. (3.19) and (3.21) respectively are equal to zero. Note that each of these threshold conditions defines a hypersurface in the parameter space (*i.e.* a space with one dimension less than the parameter space). If the values of the parameters are contained in one of these hypersurfaces, then the RDNC model will be critical. In the field of bifurcation theory, such Turing and Hopf bifurcations are said to be of *codimension-1*.

Since neither k_T^c nor k_W^c depend on the parameter a (*cf.* Section 3.5.2), we will use this parameter to track the instability threshold conditions. Consequently, for $a \geq a_T^c$, where:

$$a_T^c \overset{\text{def}}{=} {k_T^c}^2 + \frac{2\mu\sigma}{\sigma^2 + {k_T^c}^2} + \frac{bc}{d + \delta {k_T^c}^2}, \tag{3.33}$$

the RDNC model is unstable against *Turing perturbations*. On the other hand, for $a \geq a_W^c$, where:

$$a_W^c \overset{\text{def}}{=} d + (1+\delta){k_W^c}^2 + \frac{2\mu\sigma}{\sigma^2 + {k_W^c}^2}, \tag{3.34}$$

the model is unstable to *Hopf perturbations* (recall that the values of k_T^c and k_W^c in Eqs. (3.33) and (3.34) are given by Eqs. (3.18) and (3.20) respectively).

- Control parameters: "driving force" a and diffusion ratio δ

In the Appendix C we present an exhaustive analysis of the possible scenarios for the instability thresholds as *all* the parameters of the model are varied.

In the rest of this chapter and through all this thesis we will span the parameter space using mainly two characteristic *control parameters*: a and δ. All the other parameters of the RDNC model will be considered as *fixed*.

The control parameter a, the "driving force", can be considered as a parameter representing the *kinetics* or *reaction part* of the RDNC model. On the other hand, the diffusion ratio δ describes the *spatial coupling* or *transport mechanism* in the medium. This *qualitative difference* between the parameters a and δ suggests us to use them as primary[7] control parameters of the RDNC model

- Typical instability scenarios

In Fig. 3.3(a)-(c) we plot the threshold conditions a_W^c and a_T^c in the control parameter space a vs. δ for three different values of σ. Each case corresponds to a typical scenario.

In Fig. 3.3(a), where $\sigma = 1$, we see that for $0 \leq \delta \leq 1$ the solution $\mathbf{X}_0$ of the RDNC model has a wave instability if the driving force a is bigger than a_W^c. (*cf.* Eq. (3.34)). On the other hand a Turing instability occurs for $\delta \geq 1$. For big δ (here $\delta \geq 3$) the wave instability turns into a homogeneous Hopf instability, but this happens when the system is already unstable against Turing perturbations. Therefore a homogeneous Hopf instability is not possible in this case.

If we increase the value of σ the transition between wave and homogeneous Hopf appears for lower value of δ. In Fig. 3.3(b), where $\sigma = 1.3$, shows such a behaviour. Now, depending on the value of δ, all three types of instabilities (*i.e.* wave, homogeneous Hopf and Turing) may occur.

If we continue to increase the value of σ, we reach a situation where the nonlocal coupling range is so small that no wave instability can happen. Only a homogeneous Hopf instability is possible for small δ. This situation is shown in Fig. 3.3(c), where $\sigma = 2$.

3.5.4 Codimension-2 instabilities

An interesting feature from our study of the instability thresholds is that threshold corresponding to different instabilities can meet. This will typically happen in a codimension-2 surface in the parameter space. Such instabilities are therefore called *codimension-2 instabilities.*

In the control parameter space spanned by a vs. δ the codimension-2 instabilities occur in isolated points. Such points are marked in Fig. 3.3 with full circles (see also Figs. C.2 and C.3 in the Appendix C). We can distinguish two different types of codimension-2 points:

1. *Codimension-2 homogeneous Hopf-Turing instability* (*e.g.* in Figs. 3.3(b) and 3.3(c)).

---

[7] Note that, beside a, also bc, d, μ and σ characterise the *homogeneous system* of Eqs. (3.1,3.2) and that, beside δ, also μ and σ can be used to characterise the *spatial coupling.* However, the important fact that we want to remark here is that of the spatial coupling parameters μ, σ and δ only δ is not contained in the homogeneous part.

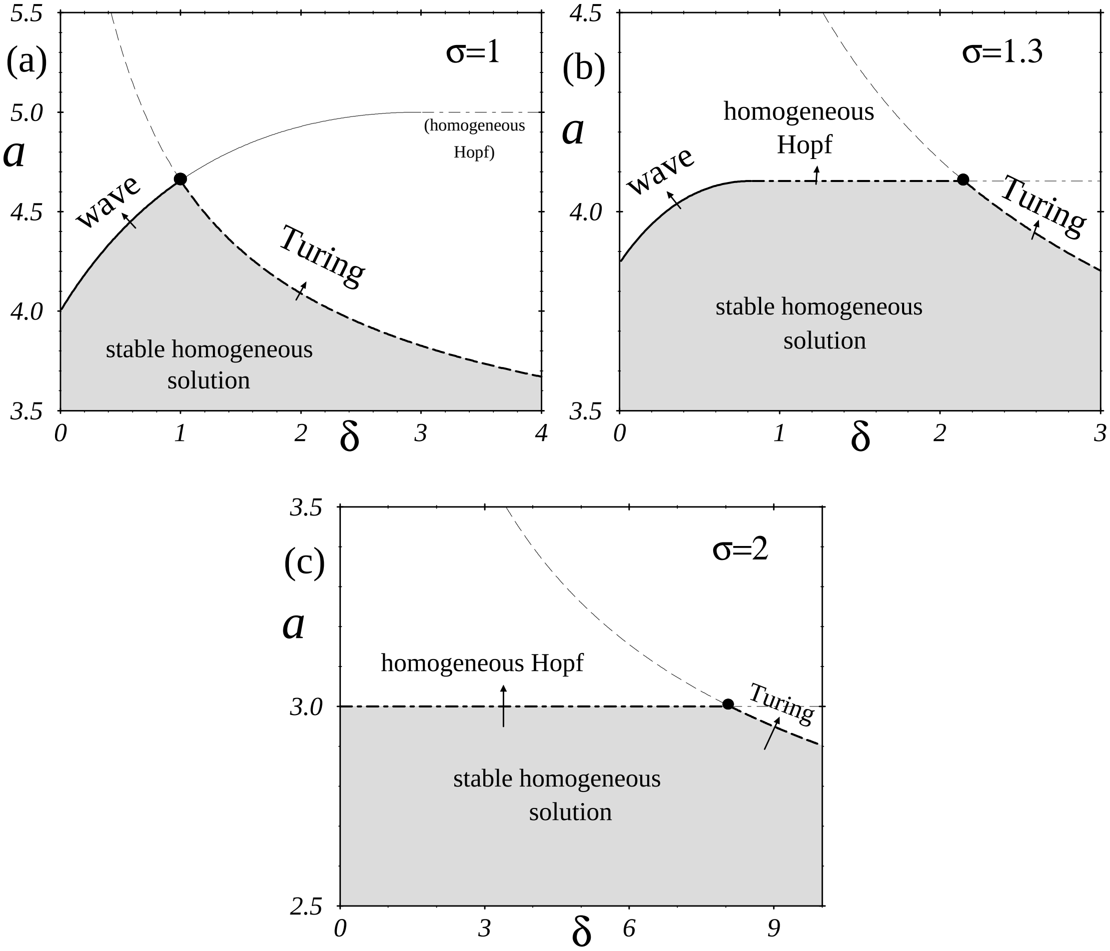

Figure 3.3: In these figures we plot the instability threshold conditions in the control parameter space a vs. δ for three different values of the nonlocal coupling range σ^{-1}. The thresholds of the wave, homogeneous Hopf and Turing instability are indicated with full, dot-dashed and dashed lines respectively. In (a) $\sigma = 1$, in (b) $\sigma = 1.3$ and $\sigma = 2$ in (c). Each of them corresponds to a characteristic scenario. The other parameters of the RDNC model are fixed to: $b = 4$, $c = d = 1$ and $\mu = 2$. The full circles in (a), (b) and (c) show the location of the codimension-2 instability points (see discussion in Section 3.5.4). Note that the value a^c_W of homogeneous Hopf threshold condition does not depend on δ (*cf.* Eq. (C.3) in Appendix C).

2. *Codimension-2 wave-Turing instability* (*e.g.* in Fig. 3.3(a))

The codimension-2 homogeneous Hopf-Turing instability case has been studied in detail previously in a diverse array of systems; both experimentally [61, 62, 63, 64] and theoretically [65, 66, 67, 68, 69, 70, 71, 72]. For a review on this topic see ref. [29]. The second case has been found *e.g.* within some models for binary convection [25, 26, 27], viscoelastic convection [28, 73] and surface reaction [74]. It has been scarcely studied and therefore it will be analysed in detail in this thesis.

- Codimension-2 wave-Turing instability

In this Section we will analyse in more detail the instability thresholds and critical wavenumbers near a codimension-2 wave-Turing instability. Let us select a particular set of the parameter values in which such a codimension-2 instability occurs. In the rest of this thesis we will analyse the case shown in Fig. 3.3(a). Here the parameters of the RDNC model are:

$$b = 4, c = d = 1, \mu = 2 \quad \text{and} \quad \sigma = 1. \tag{3.35}$$

For these parameter vales the codimension-2 instability point in the parameter space a vs. δ is located at $(a^c_{WT}, \delta^c_{WT})$, where:

$$a^c_{WT} = 4\sqrt{2} - 1 \approx 4.657 \quad \text{and} \quad \delta^c_{WT} = 1. \tag{3.36}$$

In Figs. 3.4(a) and 3.4(b) we show the growth rate $Re[\lambda(k)]$ and its corresponding frequency $Im[\lambda(k)]$ as a function of the wavenumber k for the codimension-2 point (*cf.* Eq. (3.36)). We can see that the growth rate is zero (*i.e. marginal*) for two different values of the wavenumber simultaneously: k^c_W and k^c_T. These two critical wavenumbers can be calculated analytically (for the parameter values of Eq. (3.35) and at the codimension-2 point of Eq. (3.36)), they are:

$$k^c_T = \sqrt{2^{3/2} - 1} \approx 1.352 \quad \text{and} \quad k^c_W = \sqrt{2^{1/2} - 1} \approx 0.644 \tag{3.37}$$

In Figs. 3.4(c) and 3.4(d) we show the growth rates for δ smaller and bigger than δ^c_{WT} respectively. In the first case we can see that the solution $\mathbf{X}_0$ has a wave instability. Moreover, there is a *band of wavenumbers* around k^c_W that have positive growth rate. In Fig. 3.4(d) the solution $\mathbf{X}_0$ has a Turing instability (there is also a band of unstable wavenumbers around k^c_T).

In Fig. 3.5 we show the control parameter space and the critical wavenumbers. Note that for $\delta = 0$ both wavenumbers k^c_W and k^c_T are equal (in particular: $k^c_W = k^c_T = 1$) and that for $\delta > 0$ the Turing wavenumber k^c_T is always

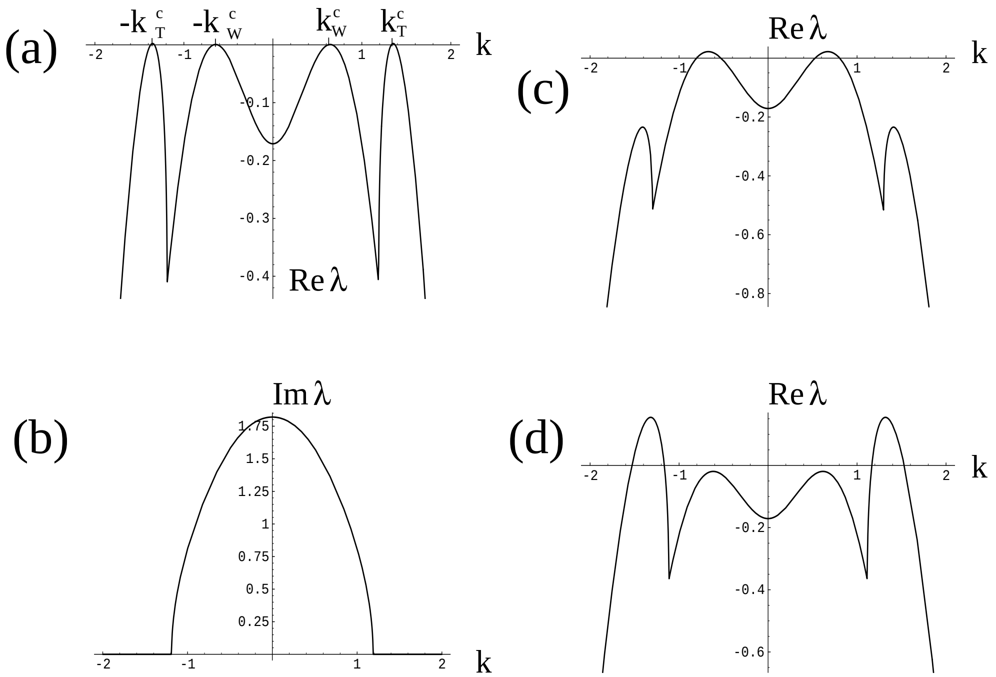

Figure 3.4: Plot of the growth rate $Re[\lambda(k)]$ and critical frequency $Im[\lambda(k)]$ as a function of the wavenumber k at and near the codimension-2 wave-Turing point. In (a) the growth rate and in (b) its corresponding frequency (*cf.* Eq. (3.7)) at the codimension-2 point of the RDNC model are shown. In (c) and (d) the growth rates are shown for two different situations *near* the codimension-2 point. In (c) the control parameters are $a = a^c_{WT}$ and $\delta = 0.9$ (*i.e.* $\delta < \delta^c_{WT}$) In (d) they are $a = a^c_{WT}$ and $\delta = 1.1$ (*i.e.* $\delta > \delta^c_{WT}$).

bigger than k^c_W. This corroborates the properties of the critical wavenumbers discussed in Section 3.5.2.

In Fig. 3.5(a) we can see that the wave instability appears for $1 \geq \delta \geq 0$. In Fig. 3.6 we plot the critical frequency $\omega_c(\delta)$ of the wave instability in this range. This frequency does not vary too much and at the codimension-2 point (*i.e.* $\delta = 1$):

$$\omega_c = \sqrt{2}. \tag{3.38}$$

Other important quantities characterising the waves near the onset of the instability are their phase velocity v_{ph} and group velocity c_g. The *phase velocity*:

$$v_{ph} \overset{\text{def}}{=} \omega_c / k^c_W, \tag{3.39}$$

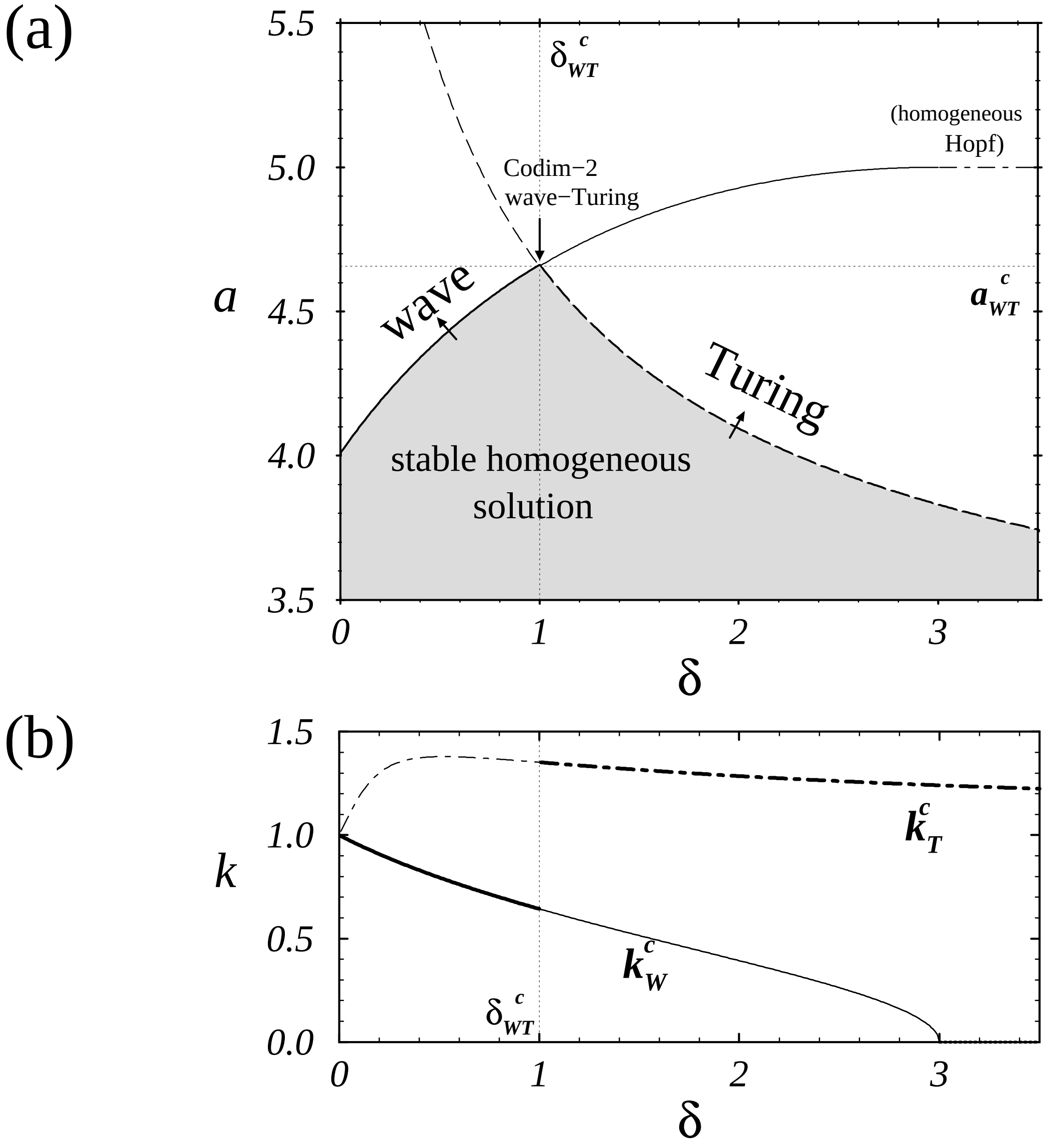

Figure 3.5: In (a) the threshold lines of the wave and Turing bifurcations are plotted in the control parameter space a vs. δ (the values of the other parameters are given in Eq. (3.35)). The Turing and wave threshold lines meet in the codimension-2 wave-Turing point $(a^c_{WT}, \delta^c_{WT})$. The values of a^c_{WT} and δ^c_{WT} are indicated with thin doted lines. In (b) we plot the critical wavenumbers k^c_W and k^c_T of the wave(Hopf) and Turing instabilities for the same parameters values as in (a). Recall that these critical wavenumbers do not depend on a. The thicker lines indicate which critical wavenumber is the selected after the instability. Note that k^c_W is zero (*i.e.* homogeneous Hopf instability) for $\delta \geq 3$ and that $k^c_W = k^c_T$ for $\delta = 0$.

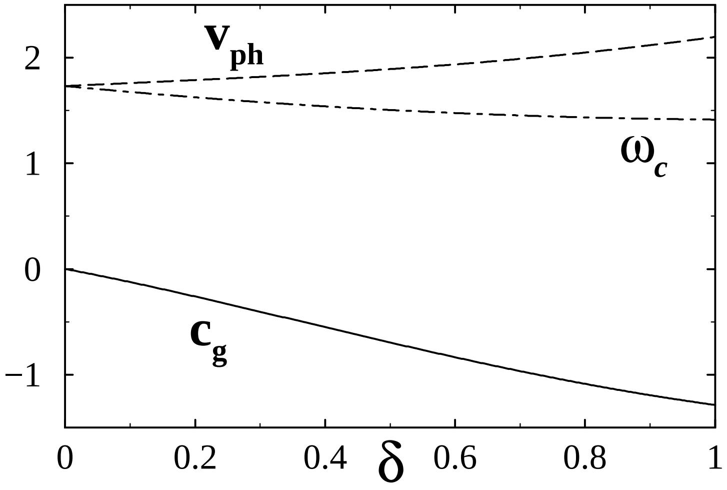

Figure 3.6: In this Figure we show the critical frequency ω_c, the phase velocity v_{ph} and the group velocity c_g of the waves arising in the wave instability as the diffusion ratio δ varies between $0 \leq \delta \leq 1$ ($a = a^c_W$ and the values of the other parameters are given in Eq. (3.35)). Note that ω_c and v_{ph} do not vary too much whereas the group velocity c_g does. Moreover, v_{ph} and c_g have opposite signs and $c_g = 0$ for $\delta = 0$.

Constant Parameters	$b = 4$ $c = d = 1$ $\mu = 2$ $\sigma = 1$
Codimension-2 wave-Turing point	$a^c_{WT} = 4\sqrt{2} - 1 \approx 4.657$ $\delta^c_{WT} = 1$
Critical wavenumbers and frequency	$k^c_T = \sqrt{2^{3/2} - 1} \approx 1.352$ $k^c_W = \sqrt{2^{1/2} - 1} \approx 0.644$ $\omega_c = \sqrt{2} \approx 1.414$
phase and group velocities	$v_{ph} = \sqrt{2}/\sqrt{2^{1/2} - 1} \approx 2.197$ $c_g = -2\sqrt{2^{1/2} - 1} \approx -1.287$

Table 3.1: In this table we summarise the properties of the codimension-2 wave-Turing instability point.

is the velocity with which the waves propagate and the *group velocity*:

$$c_g \overset{\text{def}}{=} \left. \frac{\partial \omega_c}{\partial k} \right|_{k=k_W^c}, \tag{3.40}$$

is the velocity of propagation of a small perturbation. In Fig. 3.6 we can see that the phase velocity v_{ph} is almost constant as δ vary. On the other hand the group velocity c_g decreases[8] from $c_g = 0$ for $\delta = 0$ to a minimum value for $\delta = 1$.

It is also important to remark that the velocities v_{ph} and c_g have *opposite signs*. This last feature means that if a wave propagates to the left, any perturbation on it will travel to the right. As we will see later in this thesis, this property will have a very important impact on the pattern formation near the codimension-2 point.

Finally, let us summarise in Table 3.1 all the attributes of the Codimension-2 wave-Turing instability analysed in this section.

---

[8] The feature that $c_g = 0$ for $\delta = 0$ is not only valid for parameter values of Eq. (3.35) but *also for any other value of the parameters*. This happens because $\partial_k det\hat{\mathbf{\Lambda}}|_{k=k_W^c} \equiv 0$ if $\delta = 0$.

Chapter 4

Derivation of Amplitude Equations

We saw in the previous chapter that the RDNC model has a homogeneous solution that can become unstable when the parameters of the model are changed. These instabilities have been computed and classified using a linear stability analysis. In this chapter we will go beyond this, and perform a *weakly nonlinear analysis* of these instabilities. This approach will provide us with information about the nonlinear behaviour of the system *near* the onset of the instabilities. The approach consists of a perturbative expansion technique which includes multiple scales in time and in space. The final result of this approach will be a set of coupled *amplitude equations*. In the remainder of this thesis we will use these equations to study different pattern forming properties of the RDNC model.

4.1 Introduction

Nonlinear systems often show very complicated behaviour. Typically this behaviour can not be assessed analytically. In some particular cases, however, it is possible to gain some information by restricting the analysis to approximated or asymptotic solutions. One of these cases occurs when a *known* solution of the system is brought to an instability by variation of the parameters of the system. Under these conditions, a perturbative approach can be used to capture the *weakly nonlinear behaviour* of the system near the instability. The final product of this approach is a set of coupled dynamical equations. These equations provide information about the *asymptotic behaviour* of the original system near the onset of the instability. These equations are typically nonlinear and are called *amplitude equations* [1, 5, 6, 7, 75]. They are of enormous importance because their form only depends on the type of instability; *i.e.* they are *universal*. All the particularities of the nonlinear system under study enter *only* in the coefficients of these amplitude equations. We refer to ref. [1] for a comprehensive review on pattern formation with emphasis on amplitude equations and the concept of linear instability. Moreover, since the number of possible instabilities is quite limited, there are few possible types of amplitude equations. For systems of ordinary differential equations, amplitude equations are related to the so called *normal forms* which are the organising idea of *bifurcation theory* [55, 56, 57, 58].

In this chapter we will derive the amplitude equations valid near the instabilities found in the previous chapter. We will also do a preliminary analysis of their behaviour. Further analysis will be preformed in next chapters.

- Organisation of this chapter

This chapter is organised as follows. In the next section we will introduce the method of multiple scales perturbation expansion for a general dynamical system. This introduction will be done in a step-by-step manner. Increasing levels of refinement will be sequentially introduced. In Section 4.3 we will focus on the derivation of amplitude equations for the RDNC model. Only a brief description of the derivation will be done in this section. A detailed derivation will be performed in the Appendix E. Finally, in Section 4.4 we will analyse the coefficients of the amplitude equations previously derived.

4.2 Introduction to the Perturbative Approach near Instabilities

In this section we will explain in detail how amplitude equations can be obtained. Here we will take a constructive approach to the perturbative method. This means that we will start with the simplest perturbative expansion possible and later we will add new features in order to render the method more powerful.

We will consider first the case of a stationary solution becoming unstable in an ODE. Afterward we will consider the dynamics of the emerging solution. Finally, in the end of this section, we will address the kind of extensions that should be done to apply the perturbative method to instabilities in PDEs.

4.2.1 General Setup

Let us consider again the generic ODE (3.6) introduced in section 3.3.1. We will assume that this system has a *time independent* solution $\mathbf{Y}_0(\chi)$ for any value of the control parameter χ. Introducing a new variable $\mathbf{X}(t) \overset{\text{def}}{=} \mathbf{Y}(t) - \mathbf{Y}_0$ (where $\mathbf{X}(t) \in \mathbb{R}^n$) in Eq. (3.6), we get:

$$\partial_t \mathbf{X}(t) = \mathbf{\Lambda}(\chi)\mathbf{X}(t) + \mathbf{h}(\chi, \mathbf{X}(t)), \tag{4.1}$$

where $\mathbf{\Lambda}(\chi)$ is a square matrix and $\mathbf{h}(\chi, \mathbf{X}(t))$ is a vectorial function where all the nonlinearities are included. Very often this nonlinear function does not depend on χ. In the following we will further assume that $\mathbf{h}(\chi, \mathbf{X}(t)) = \mathbf{h}(\mathbf{X}(t))$.

The Eq. (4.1) has a time independent solution at $\mathbf{X}_0 = 0$ for any value of the control parameter χ. Let us further assume that this solution has an instability at $\chi = \chi_c$. Note that $\mathbf{\Lambda}(\chi)$ is nothing else but the Jacobian (*i.e.* the linearisation matrix) around $\mathbf{X}_0 = 0$.

As we saw in the previous chapter, the solution $\mathbf{Y}_0(\chi)$ of Eq. (3.6) is linearly stable as long as the real part of all the eigenvalues of the matrix $\mathbf{\Lambda}(\chi_c)$ is negative. This solution becomes unstable when the real part of, at least, one eigenvalue is equal to zero. Depending on the value of the imaginary part of this eigenvalue λ_i, we can distinguish two different cases:

- $Im(\lambda_i) = 0 \quad \Longrightarrow \quad$ *steady bifurcation*,
- $Im(\lambda_i) \neq 0 \quad \Longrightarrow \quad$ *Hopf bifurcation.*

In the first case a stationary new solution will arise after the instability. In the second case the new solution is oscillatory in time. The *critical frequency* of this oscillation is $\omega_c \overset{\text{def}}{=} \text{Im}(\lambda_i)$. The critical solutions of Eq. (4.1), associated with the critical eigenvalues, are $\mathbf{X}_s^c = \mathbf{U}_s$ for the steady bifurcation and $\mathbf{X}_h^c = \mathbf{U}_h e^{i\omega_c t}$ and $\overline{\mathbf{X}_h^c} = \overline{\mathbf{U}}_h e^{-i\omega_c t}$ for the Hopf bifurcation (see also discussion in section 3.4.1.B). We recall that the norm of the critical eigenvectors $\mathbf{U}_s$ and $\mathbf{U}_h$ is arbitrary and that $\mathbf{U}_s \in \mathbb{R}^n$ and $\mathbf{U}_h \in \mathbb{C}^n$.

4.2.2 Perturbative Expansion

Now Sattinger's theorem can be applied to Eq. (4.1) (see discussion in section 3.3.1, pg. 24). The theorem tells us that near χ_c a new solution of Eq. (4.1) exists and that this solution *coincides* with $\mathbf{X}_0$ at $\chi = \chi_0$. This last feature suggests us to analyse emerging solution using a *perturbative expansion* around the original solution $\mathbf{X}_0$:

$$\mathbf{X}(t) \quad = \quad \mathbf{X}_0 + \varepsilon \mathbf{X}_1(t) + \varepsilon^2 \mathbf{X}_2(t) + \varepsilon^3 \mathbf{X}_3(t) + \mathcal{O}(\varepsilon^4), \tag{4.2}$$

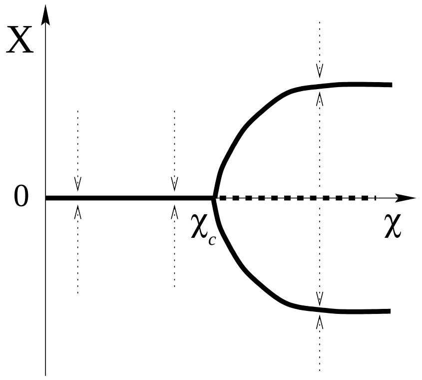

Figure 4.1: This diagram shows the bifurcation diagram of an example of instability where the new branch (stable in this case) grows in a non-analytical way from χ_c. The full lines correspond to branches of stable solutions, dashed to unstable ones and the dotted arrows indicate the different basins of attraction. Here the new branches grow as $\propto \pm(\chi - \chi_c)^{1/2}$. For sake of clarity, in this diagram we consider an one dimensional system (*i.e.* $\mathbf{X} \in \mathbb{R}^1$).

where ε is a small parameter related with the distance of χ to the critical value χ_c (we will discuss this relation in more detail in the next paragraphs), $\mathbf{X}_0$ is the original solution that becomes unstable (recall that $\mathbf{X}_0 \equiv 0$), and the vector fields $\mathbf{X}_l(t)$ with $l = 1, 2, 3, \ldots$ correspond to the perturbations of $\mathbf{X}_0$. These vector fields are *a priori* not known, but they can be calculated. They will provide us information about the location of the emerging branch.

The next step is to insert the ansatz of Eq. (4.2) in Eq. (4.1). Before doing this step we will first discuss in more detail the nature of the small parameter ε used in expansion (4.2).

- Expansion of the control parameter

An important issue arising in the perturbative expansion of Eq. (4.2) is the choice of a suitable small parameter ε. Clearly this parameter should be related with the distance to the threshold $\chi - \chi_c$ and, in particular, $\varepsilon = 0$ if $\chi = \chi_c$. A first approach would be to set ε as proportional to a power of $\chi - \chi_c$. Such a choice will alow for a variation of the amplitude of the field $\mathbf{X}$, with respect to χ, *only* as $(\chi - \chi_c)^n$, where n is a natural number. However, it can happen that this amplitude is $\propto (\chi - \chi_c)^p$, where p is a rational number (for example as a *square root* with $p = 1/2$). The latter kind of growth is called *non-analytical*. A common example of this non-analytic behaviour is found in the pitchfork bifurcation [55, 56, 57, 58], where the new solution branches grow as ∝ $\pm(\chi - \chi_c)^{1/2}$ (see Fig. 4.1 for an illustration of this).

The solution to this kind of problems is to expand *also* $\chi - \chi_c$ in ε:

$$\chi - \chi_c = \varepsilon\gamma_1 + \varepsilon^2\gamma_2 + \mathcal{O}(\varepsilon^3) \tag{4.3}$$

where γ_1, γ_2, … are free parameters to be defined *a posteriori* for sake of consistency of the perturbative analysis. More specifically, as we will see later, the γ-parameters are either zero or they can be directly related with the distance to the onset of the instability $\chi - \chi_c$. In this way any kind of non-analytical behaviour is captured by the perturbative expansion.

- Hierarchy of linear inhomogeneous equations

Since the operator $\mathbf{\Lambda}$ in Eq. (4.1) depends on χ, we should also expand it using Eq. (4.3):

$$\mathbf{\Lambda}(\chi) = \mathbf{\Lambda}_0(\chi_c) + \varepsilon\gamma_1\mathbf{\Lambda}_1(\chi_c) + \varepsilon^2\gamma_2\mathbf{\Lambda}_2(\chi_c) + \mathcal{O}(\varepsilon^3) \tag{4.4}$$

where $\mathbf{\Lambda}_0, \mathbf{\Lambda}_1, \mathbf{\Lambda}_2, \ldots$ are square matrices that do neither depend on χ nor on ε. Their specific form will depend on the original system Eq. (4.1) and can be calculated directly for each case.

The next step is to insert the expansions given by Eqs. (4.2), (4.3), and (4.4) in the original Eq. (4.1). This give us an equation containing terms $\mathcal{O}(\varepsilon), \mathcal{O}(\varepsilon^2), \mathcal{O}(\varepsilon^3), \cdots$. This equation will be *equivalent* to Eq. (4.1) only if it is valid for *every* value of ε or, what amounts to the same, if we require that *each* equation in the following *hierarchy* is satisfied:

$$\begin{array}{lll} \bullet\ \mathcal{O}(\varepsilon): & \mathbf{\Lambda}_0\mathbf{X}_1 - \partial_t\mathbf{X}_1 & = 0 \\ \bullet\ \mathcal{O}(\varepsilon^2): & \mathbf{\Lambda}_0\mathbf{X}_2 - \partial_t\mathbf{X}_2 & = \gamma_1\mathbf{\Lambda}_1\mathbf{X}_1 + \mathbf{\Omega}_2\cdot\mathbf{X}_1\mathbf{X}_1 \\ \bullet\ \mathcal{O}(\varepsilon^3): & \mathbf{\Lambda}_0\mathbf{X}_3 - \partial_t\mathbf{X}_3 & = \gamma_1\mathbf{\Lambda}_1\mathbf{X}_2 + \gamma_2\mathbf{\Lambda}_2\mathbf{X}_1 \\ & & \quad +2\mathbf{\Omega}_2\cdot\mathbf{X}_1\mathbf{X}_2 + \mathbf{\Omega}_3\cdot\mathbf{X}_1\mathbf{X}_1\mathbf{X}_1 \\ \bullet\quad \vdots & & \vdots \end{array} \tag{4.5}$$

where terms of the form $\mathbf{\Omega}_2 \cdot \mathbf{XY}$ and $\mathbf{\Omega}_3 \cdot \mathbf{XYZ}$ are a shorthand notation[1] for the column vector whose i-components are respectively given by:

$$[\mathbf{\Omega}_2\cdot\mathbf{XY}]_i \overset{\text{def}}{=} \Sigma_{j,k}\Omega^i_{2_{j,k}}x_j y_k \quad \text{and} \quad [\mathbf{\Omega}_3\cdot\mathbf{XYZ}]_i \overset{\text{def}}{=} \Sigma_{j,k,l}\Omega^i_{3_{j,k,l}}x_j y_k z_l. \tag{4.6}$$

However, since we want only to gain information about the emerging solutions of Eq. (4.1) *near* the threshold of the bifurcation (*i.e.* $\varepsilon << 1$), we

---

[1] Note that this quadratic and cubic forms are *symmetric* with respect to the order of the vectors $\mathbf{X}, \mathbf{Y}, \ldots$ (*e.g.* $\mathbf{\Omega}_2\cdot\mathbf{XY} \equiv \mathbf{\Omega}_2\cdot\mathbf{YX}$).

will typically need to solve only the initial equations in the hierarchy of Eq. (4.5). Higher orders in ε will give only refinements to the analysis.

One particularity of the system of Eqs. (4.5) is that the equations for each order $\mathcal{O}(\varepsilon^j)$ with $j = 1, 2, ...$ have all the same form:

$$(\mathbf{\Lambda}_0 - \partial_t)\mathbf{X}_j = \mathbf{Y}_j, \tag{4.7}$$

where:

$$\mathbf{Y}_1 \equiv 0 \tag{4.8}$$

$$\mathbf{Y}_j = \mathbf{Y}_j(\mathbf{X}_1, ..., \mathbf{X}_{j-1}) \quad \text{for} \quad j \geq 2. \tag{4.9}$$

Consequently Eq. (4.7) is *linear*. Note that the linear differential operator $\mathbf{\Lambda}_0 - \partial_t$ of this equation does not depend on the order j and that the inhomogeneous terms $\mathbf{Y}_j$ depend *only* on the previous $\mathbf{X}_{j-1}, \ldots, \mathbf{X}_1$ and not on $\mathbf{X}_j$. This last property means that Eqs. (4.7) can be solved *iteratively*, starting with the homogeneous equation for $\mathcal{O}(\varepsilon^1)$, for the successive $\mathbf{X}_j$. In other words: solving the equation $\mathcal{O}(\varepsilon)$ we get $\mathbf{X}_1$, and then inserting this in the equation $\mathcal{O}(\varepsilon^2)$ we can solve for $\mathbf{X}_2$, and so on.

A very important property of the linear operator $\mathbf{\Lambda}_0 - \partial_t$ is that it is *singular*. Consequently, the solution of the homogeneous equation corresponding to $\mathcal{O}(\varepsilon)$ is *different from zero*. Indeed, based in the critical solutions introduced in section 4.2.1, we can propose the following ansatz for equation $\mathcal{O}(\varepsilon)$:

- for the stationary instability: $\mathbf{X}_1 = A_s\mathbf{U}_s$. (4.10)
- for the Hopf instability: $\mathbf{X}_1(t) = \frac{1}{2}(A_h\mathbf{U}_h e^{i\omega_c t} + \overline{A}_h\overline{\mathbf{U}}_h e^{-i\omega_c t})$. (4.11)

Where the vectors $\mathbf{U}_s$ and $\mathbf{U}_h$ were introduced in the end of section 4.2.1 and the free parameters $A_s \in \mathbb{R}^1$ and $A_h \in \mathbb{C}^1$ have been inserted to take into account the fact that the norm of $\mathbf{U}_s$ and $\mathbf{U}_h$ is arbitrary. A_s and A_h can be think as the *amplitudes* of the new solutions arising after the instability. It is important to remark that neither the vectors $\mathbf{U}_s$ and $\mathbf{U}_h$ nor the scalar quantities A_s and A_h depend on time t. Note also that in the Hopf case we are assuming that $\mathbf{X}_1(t) \in \mathbb{R}^n$.

Now we are ready to solve the inhomogeneous equation corresponding to $\mathcal{O}(\varepsilon^2)$. But a problem arises because the linear operator is *noninvertible*. The same problem will also arise for all the equations $\mathcal{O}(\varepsilon^j)$ whit $j \geq 2$. This makes the solution of Eqs. (4.5) a so called *singular perturbation problem*. We will address to this issue in more detail in the next paragraphs.

- Singular Perturbation Theory and Fredholm Alternative Theorem

Let us start with the simplest case that is when the dynamical system of Eq. (4.1) consists of just one variable: $\mathbf{X} \equiv u$. Then the matrix $\mathbf{\Lambda}_0$ is one-dimensional (*i.e.* $\mathbf{\Lambda}_0 = l_0$ where $l_0 \in \mathbb{R}^1$). The new solution arising above the instability can not depend on time. Generically two or more variables are needed for a Hopf bifurcation [55, 56, 57, 58]. Therefore we do not need to consider the time derivatives of Eqs. (4.5). Consequently the singular perturbation problem is trivial because $l_0 u_j = y_j$ has a unique solution *only if* $l_0 \neq 0$. In the case $l_0 = 0$ the problem is undetermined.

For two and more variables the problem becomes more subtle. Let us consider first the case of a stationary instability. Since the new solution (*cf.* Eq. (4.10)) does not depend on time we can neglect the time derivatives in Eqs. (4.5). Now, the *Fredholm Alternative theorem*[2], can be applied. This theorem states that given the linear inhomogeneous problem:

$$\mathbf{\Lambda}_0 \mathbf{X}_j = \mathbf{Y}_j, \tag{4.12}$$

there are two alternative possibilities:

1. The homogeneous problem $\mathbf{\Lambda}_0 \mathbf{X}_j = 0$ has a *trivial kernel* (*i.e.* $\mathbf{X}_j \equiv 0$) and the solution of Eq. (4.12) is unique.

2. The adjoint homogeneous problem $\mathbf{\Lambda}_0^\dagger \mathbf{Z} = 0$ has a nontrivial $\mathbf{Z} \neq 0$ solution, then Eq. (4.12) has a solution if and only if the inhomogeneity in Eq. (4.12) satisfies:

   $$(\mathbf{Z}|\mathbf{Y}_j) = 0, \tag{4.13}$$

   where $(\circ|\circ)$ is the standard scalar product in $\mathbb{R}^n$: *i.e.* $(\mathbf{Z}|\mathbf{Y}_j) \overset{\text{def}}{=} \mathbf{Z} \cdot \mathbf{Y}_j$. This last equation is called the *solvability condition*.

The latter alternative tells us that the inhomogeneous term should be orthogonal to the kernel of the adjoint linear operator.

The treatment of the Hopf instability is more involved because the new solution depends on time. This means that we should include the time derivatives in Eqs. (4.5). The operator $\mathbf{\Lambda}_0 - \partial_{t_0}$ is also singular. Surprisingly, the Fredholm Alternative theorem can be applied again if we take into account that the operator is now $\mathbf{\Lambda}_0 - \partial_{t_0}$ and if a suitable scalar product in this

---

[2] For detailed discussion of this theorem and its implications see for instance [5, 7, 59, 76].

functional space is defined. It is easy to see that the following definition satisfies the properties of a scalar product:

$$(\mathbf{Z}(t)|\mathbf{Y}_j(t)) \overset{\text{def}}{=} \int_0^{2\pi/\omega_c} \overline{\mathbf{Z}}(t) \cdot \mathbf{Y}_j(t)\, dt, \tag{4.14}$$

where the bar stands for complex conjugate and the dot is the standard inner product in $\mathbb{R}^n$. The time integration is done over one oscillation period. Note that the output of this inner product is a constant number and that the two critical solutions X_h^c and $\overline{X_h^c}$, spanning the kernel of the operator $\mathbf{\Lambda}_0 - \partial_{t_0}$, are orthogonal.

Doing an integration by parts we can see that: $(\mathbf{Y}|[\mathbf{\Lambda}_0 - \partial_{t_0}]\mathbf{X}) = ([\mathbf{\Lambda}_0^\dagger + \partial_{t_0}]\mathbf{Y}|\mathbf{X})$. Consequently, the *adjoint linear differential operator* for the Hopf instability case is given by: $\mathbf{\Lambda}_0^\dagger + \partial_{t_0}$. With this we conclude the discussion about the Fredholm alternative theorem.

- Solvability Conditions

Clearly the stationary and Hopf instabilities correspond to the 2^{nd} alternative. In order to perform the singular perturbation treatment, we should make sure that all the inhomogeneous terms in Eqs. (4.5) satisfy the solvability condition of Eq. (4.13). The solvability conditions corresponding to the second (third if the second order is trivial) order equation will give us a nonlinear equation[3] relating the amplitudes A_s and $|A_h|$ to the distance to the criticality $\chi - \chi_c$. Solving this equation we can get the location of the new branch arising near the instability point (see Fig 4.1 for an example). But this equation do not supply any information about *how* the state of the system approaches (or escapes) the new branch. Typically, if the state of the system is near the new branch, the dynamics will became very slow and it will take a long time until the state reaches or escapes the new solution. Using a perturbative expansion including multiple time scales we can get information about the *asymptotic behaviour* of the system near the new branch [76, 77, 78, 79]. We will discuss this method in the next subsection.

4.2.3 Multiple Scales Perturbation Expansion

The *multiple scales perturbation expansion method* (MSPE in the following) consists in supplementing the perturbative expansion of Eqs. (4.2) and (4.3)

---

[3] The step between the solvability conditions and these equations will become more clear in the next section.

with the introduction of a hierarchy of new time scales: $t_0, t_1, t_2, \ldots$. These new variables are related to the original time t by:

$$\partial_t = \partial_{t_0} + \varepsilon \partial_{t_1} + \varepsilon^2 \; \partial_{t_2} + \mathcal{O}(\varepsilon^3). \tag{4.15}$$

The idea behind this approach is that the scale t_0 will contain the fast dynamics (if any) related with the new solution, whereas the remaining scales will describe the slow dynamics near the new branch.

- Ansatz for $\mathbf{X}_1$

If we are dealing with a stationary instability, then t_0 is not necessary. On the other hand, for a Hopf instability the fast time scale t_0 is associated with the limit cycle oscillation. The other time scales $t_1, t_2, \ldots$ are the (slow) variables parametrising the approach to the new solution. In the following we will refer to them as the *stretched* or *slow times*. More specifically, we will consider that the amplitudes A_s, in the ansatz of Eq. (4.10), and A_h, in Eq. (4.11), are functions of the stretched times: $A_s \overset{\text{def}}{=} A_s(t_1, t_2, \ldots)$ and $A_h \overset{\text{def}}{=} A_h(t_1, t_2, \ldots)$. For the Hopf case (*cf.* Eq. (4.11)), the oscillating terms (*i.e.* the imaginary exponentials) vary with t_0 and therefore the new ansatz is:

$$\mathbf{X}_1 = \frac{1}{2}\Big(A_h(t_1, t_2, \ldots)\mathbf{U}_h e^{i\omega_c t_0} + \overline{A}_h(t_1, t_2, \ldots)\overline{\mathbf{U}}_h e^{-i\omega_c t_0}\Big). \tag{4.16}$$

Thus, with this ansatz we are assuming that the characteristic time of variation of the amplitude is *much longer* than the oscillation time around the limit cycle. With this refinement to the perturbative expansion of Section 4.2.2 we expect to capture the slow dynamics near the emerging branches.

- Hierarchy of linear inhomogeneous equations

Inserting Eqs. (4.2,4.3,4.15) in Eq. (4.1), and separating the different orders on ε, we get:

$$\begin{aligned}
&\bullet\ \mathcal{O}(\varepsilon): \ \mathbf{\Lambda}_0\mathbf{X}_1 - \partial_{t_0}\mathbf{X}_1 &&= 0\\
&\bullet\ \mathcal{O}(\varepsilon^2): \mathbf{\Lambda}_0\mathbf{X}_2 - \partial_{t_0}\mathbf{X}_2 &&= \partial_{t_1}\mathbf{X}_1 + \gamma_1\mathbf{\Lambda}_1\mathbf{X}_1 + \mathbf{\Omega}_2\cdot\mathbf{X}_1\mathbf{X}_1\\
&\bullet\ \mathcal{O}(\varepsilon^3): \mathbf{\Lambda}_0\mathbf{X}_3 - \partial_{t_0}\mathbf{X}_3 &&= \partial_{t_1}\mathbf{X}_2 + \partial_{t_2}\mathbf{X}_1 + \gamma_1\mathbf{\Lambda}_1\mathbf{X}_2 + \gamma_2\mathbf{\Lambda}_2\mathbf{X}_1\\
& &&\quad +2\mathbf{\Omega}_2\cdot\mathbf{X}_1\mathbf{X}_2 + \mathbf{\Omega}_3\cdot\mathbf{X}_1\mathbf{X}_1\mathbf{X}_1\\
&\bullet\quad \vdots && \quad\vdots
\end{aligned} \tag{4.17}$$

This is again a hierarchy of linear inhomogeneous equations. Note that the only difference with the expansion of Eq. (4.5) is that now the inhomogeneous part of each linear equations includes time derivatives with respect to the stretched times $t_1, t_2, \ldots$. The operator to invert is given now by $\mathbf{\Lambda}_0 - \partial_{t_0}$. As before, this operator is singular. So we should again use the Fredholm alternative theorem. To do this we need to introduce a suitable scalar product. For a stationary instability the standard euclidian scalar product defined in $\mathbb{R}^n$ is sufficient. In the Hopf case we can define a scalar product as in Eq. (4.14) where now the time integration is done only with respect to t_0.

- Amplitude Equation

The solvability conditions corresponding to each equation $\mathcal{O}(\varepsilon^i)$ with $i > 1$ will provide us with a set *differential equations* for the amplitude. These differential equations have derivatives respect to the stretched times. But, as is clear from Eq. (4.15), the successive $t_1, t_2, \ldots$ correspond to slower and slower time scales. Since we are interested only in an approximation to asymptotic behaviour near the new branch, typically it will be sufficient to consider the solvability conditions corresponding to orders lower than $\mathcal{O}(\varepsilon^4)$. These equations include only derivatives respect to t_2 or t_3. Moreover, some of the t_j's may not be included in the solvability conditions (for example t_2). This means that the amplitude $A(t_1, t_2, \ldots)$ does not depend on it. Consequently, only t_0 and one of the t_j's (with low j) will typically play a rôle in the asymptotic dynamics of the system. In some situations more than one t_j may be necessary[4]. Moreover, since we are interested in the asymptotic behaviour of the emerging solution, is enough to consider A_1 depending just on the low order time scales. The differential equation so obtained is called *amplitude equation*[5] because it describes the asymptotic dynamics of the amplitude of the emerging solution.

4.2.4 Multiple Scales Perturbation Expansion for PDEs

So far we did only analyse ODEs. But, we are interested in analysing instabilities in *PDEs* modelling *spatially extended* pattern forming systems. Moreover, we are interested in models that include, beside spatial derivatives, nonlocal coupling terms. In this subsection we will extend the MSPE technique for PDEs. In Appendix D we will explain how this framework can

---

[4] For an example of such a situation, see the wave instability in the next section (*cf.* Section 4.3.2). There we will see that two different stretched time scales: t_1 and t_2, are necessary!

[5] Note that the amplitude equations are also called, in another context, *normal forms* [55, 56, 58, 59, 80].

be nontrivially extended to consider the more general case of PDEs including nonlocal coupling terms.

The MSPE technique presented in Section 4.2.3 can be applied, with minor modifications, to a PDE. Indeed, depending on the kind of instability, the critical mode may depend on the spatial variable x_0. This dependence should be taken into account in the definitions of the ansatz for $\mathbf{X}_1$ and in the scalar product. This standard MSPE approach will provide us with a ODE describing the slow time evolution of the amplitude. This approach does not consider, however, extended spatial modulations of the amplitude. These modulation can play a important rôle in the asymptotic dynamics of the amplitude. Consequently, a more refined analysis should be implemented in order to obtain information about the dynamics of the *envelope* of the emerging solution. This new approach consists in assuming that the amplitude A of the emerging solution depends not only on a "slow" time (see previous subsection) but also on a "stretched" space variable. This means that the variation of the amplitude (or more precisely envelope) happens on a spatial scale much larger that the intrinsic spatial scale of the original emerging solution (given by the period of the instability: $2\pi/k_c$, where k_c is the critical wavenumber of the instability).

Specifically, this can be done in the framework of the MSPE introducing a new hierarchy of space variables $x_0, x_1, x_2, \ldots$ in the following way:

$$\partial_x = \partial_{x_0} + \varepsilon\ \partial_{x_1} + \varepsilon^2\ \partial_{x_2} + \mathcal{O}(\varepsilon^3). \tag{4.18}$$

The new spatial variable x_0 will account for the original scale of the spatially inhomogeneous emerging solution (if any; when this last solution is homogeneous the variable x_0 will play no rôle and consequently can be neglected), and the variables $x_1, x_2, \ldots$ will give us the *small spatial modulations* the amplitude. This means that $A_1 = A_1(x_1, x_2, \ldots; t_1, t_2, \ldots)$. Normally we will not need to consider all the hierarchy of slow time and stretched spatial scales. It will be enough to consider the low order ones.

We need now to introduce a suitable scalar product. Depending on the kind of instability, this scalar product may eventually include, not only time integration over the t_0 as in Eq. 4.14, but also integration over x_0. We will discuss the necessary definitions for each case in the following section.

Finally, let us remark that the solvability conditions will provide us with a nonlinear equation which includes partial derivatives in the stretched time and space variables. This PDE is called the *amplitude (or envelope) equation.*

4.3 Amplitude Equations for Systems with Nonlocal Coupling

4.3.1 Introduction

In this section we will derive the amplitude equations for the RDNC model. The section is divided in two parts. In the first part we will derive amplitude equations valid near the *codimension-1* Turing and wave instabilities of the RDNC model. In the second part we will consider the derivation of amplitude equations near the *codimension-2* Turing-wave instability.

Before beginning these derivations, want to discuss here two important issues. In Subsection 4.3.1.A we will recall some special features of the RDNC model that will turn to be important in the derivation of amplitude equations. Second, in Subsection 4.3.1.B, we will briefly explain how the MSPE technique can be applied to the nonlocal coupling term of the RDNC model.

4.3.1.A Remarks

For sake of simplicity in the derivation of the amplitude equations we will consider the RDNC model as compactly written in Eq. (2.17). The matrices $\mathbf{\Lambda}_H$, $\mathbf{\Lambda}_D$ and $\mathbf{\Lambda}_{NC}$ will be left expressed in a formal way (*i.e.* not including the original parameters $b, c, d, \sigma, \ldots$ of the RDNC model; *cf.* Eqs. (2.19), (2.20) and (2.21)). Only the dependence of these matrices on the control parameters will be taken into account. In Section 4.4 we will calculate and analyse the coefficients of the amplitude equations as functions of all the parameters of the model.

Let us finally highlight here the most *important features* of the RDNC model that we will take into account in the derivation of the amplitude equations. These features are:

1. The system has two components. In our case one is the activator and the other the inhibitor.

2. As we already mentioned in Section 3.5.3, we will consider the "driving force" a and the diffusion ratio δ as the *control parameters* of the RDNC model. Only the matrices $\mathbf{\Lambda}_H$ and $\mathbf{\Lambda}_D$ of Eq. (2.21) do depend on these bifurcation parameters (moreover, $\mathbf{\Lambda}_H$ depends only on a and $\mathbf{\Lambda}_D$ on δ).

3. Although the nonlocal kernel $\Sigma(|x - x'|)$ of the RDNC model is exponential (*cf.* Eq. (2.22)), the derivation of amplitude equations done in this chapter can be easily applied for other types of kernel.

4. Only the differential equation for the activator field u is nonlinear. This amounts to a particular form of the nonlinear term $\mathbf{h}(\mathbf{X})$ (*cf.* Eq. (2.23)): all the elements, except $\Omega^1_{2_{1,1}} = -\alpha$ and $\Omega^1_{3_{1,1,1}} = \beta$, of the nonlinear terms Ω_2 and Ω_3 in the perturbative expansion of Eq. (4.6) are equal to zero.

4.3.1.B: Multiple Scales Perturbation Expansion for the Nonlocal Coupling

The introduction of a new set of spatial scales (*cf.* Eq. (4.18)) in diffusion operator term of the RDNC model is straightforward. This term becomes:

$$\mathbf{\Lambda}_D \partial_x^2 \mathbf{X} = \mathbf{\Lambda}_D \Big[\partial_{x_0}^2 + \varepsilon \; 2\partial_{x_0}\partial_{x_1} + \varepsilon^2 \; (2\partial_{x_0}\partial_{x_2} + \partial_{x_1}^2) + \mathcal{O}(\varepsilon^3)\Big]\mathbf{X}. \quad (4.19)$$

On the other hand, the introduction of the multiple spatial variables in the nonlocal coupling term is *nontrivial.* A detailed description of how this can be done is given in Appendix D. In the following we will only provide a brief description of this procedure and the final recipe.

The essential idea of the procedure is as follows. First we expand the integrand of the nonlocal coupling term in a Taylor series. The new spatial scales can be now introduced to the elements of this series using the formula given in Eq. (4.18). Reorganising the elements of the resulting series in a different way, it is possible to identify parts of the expansion as elements of other Taylor series. Summating these other Taylor series, we arrive to the following recipe for the introduction of multiple spatial scales in the nonlocal coupling term:

$$\begin{aligned}
\mathbf{\Lambda}_{NC}\int_{-\infty}^{+\infty} \mathbf{\Sigma}(|x-x'|)\mathbf{X}(x';t)dx' &= \mathbf{\Lambda}_{NC}\int_{-\infty}^{+\infty} \mathbf{\Sigma}(|y|)\mathbf{X}(x-y;t)dy \\
&= \mathbf{\Lambda}_{NC}\int_{-\infty}^{+\infty} \mathbf{\Sigma}(|y|)\Big\{\mathbf{X}(x_0-y,x_1,x_2,\cdots;t) \\
&\quad -\varepsilon y\partial_{x_1}\mathbf{X}(x_0-y,x_1,x_2,\cdots;t) \\
&\quad +\varepsilon^2\Big(\frac{y^2}{2}\partial_{x_1}^2\mathbf{X}(x_0-y,x_1,x_2,\cdots;t) \\
&\quad -y\partial_{x_2}\mathbf{X}(x_0-y,x_1,x_2,\cdots;t)\Big) \\
&\quad +\mathcal{O}(\varepsilon^3)\Big\}dy, \qquad (4.20)
\end{aligned}$$

where all the integrations are performed only over x_0 (*i.e.* they do not affect the stretched space variables $x_1, x_2, \cdots$).

4.3.2 Turing and Wave Amplitude Equations

As we mentioned in Section 3.5.3, a convenient parameter to track the codimension-1 instabilities is the "driving force" a. Therefore, in this subsection, we will expand this control parameter as:

$$a - a_c = \gamma_1^a \varepsilon + \gamma_2^a \varepsilon^2 + \mathcal{O}(\varepsilon^3), \tag{4.21}$$

where the instability onset a_c is given in Eq. (3.33) for the Turing and in Eq. (3.34) for the wave instability. In this subsection, all the other parameters of the RDNC model will be kept fixed.

Inserting Eq. (4.21) in the homogeneous operator $\mathbf{\Lambda}_H(a)$ (*cf.* Eq. (2.19)) results in:

$$\mathbf{\Lambda}_H(a) = \mathbf{\Lambda}_{H,0}(a_c) + \varepsilon \gamma_1^a \mathbf{\Lambda}_{H,1}(a_c) + \varepsilon^2 \gamma_2^a \mathbf{\Lambda}_{H,2}(a_c) + \mathcal{O}(\varepsilon^3), \tag{4.22}$$

where:

$$\mathbf{\Lambda}_{H,0}(a_c) = \begin{pmatrix} a_c & -b \\ c & -d \end{pmatrix} \text{ and } \mathbf{\Lambda}_{H,1}(a_c) = \mathbf{\Lambda}_{H,2}(a_c) = \cdots = \begin{pmatrix} 1 & 0 \\ 0 & 0 \end{pmatrix}. \tag{4.23}$$

Inserting the ε-expansions of Eqs. (4.15), (4.2), (4.20) and (4.22) in Eq. (2.17) we can write explicitly all the orders of the multiple scales expansion in a compact form as:

$$\begin{aligned}
\bullet\ \mathcal{O}(\varepsilon):\ & \mathbf{\Lambda}_{H,0}\mathbf{X}_1 + \mathbf{\Lambda}_S^0[\mathbf{X}_1] - \partial_{t_0}\mathbf{X}_1 = 0 \\
\bullet\ \mathcal{O}(\varepsilon^2):\ & \mathbf{\Lambda}_{H,0}\mathbf{X}_2 + \mathbf{\Lambda}_S^0[\mathbf{X}_2] - \partial_{t_0}\mathbf{X}_2 = -\gamma_1^a \mathbf{\Lambda}_{H,1}\mathbf{X}_1 + \partial_{t_1}\mathbf{X}_1 \\
& \qquad -\partial_{x_1}\mathbf{\Lambda}_S^1[\mathbf{X}_1] + \mathbf{\Omega}_2 \cdot \mathbf{X}_1\mathbf{X}_1 \\
\bullet\ \mathcal{O}(\varepsilon^3):\ & \mathbf{\Lambda}_{H,0}\mathbf{X}_3 + \mathbf{\Lambda}_S^0[\mathbf{X}_3] - \partial_{t_0}\mathbf{X}_3 = -\gamma_1^a \mathbf{\Lambda}_{H,1}\mathbf{X}_2 + \partial_{t_1}\mathbf{X}_2 - \partial_{x_1}\mathbf{\Lambda}_S^1[\mathbf{X}_2] \\
& \qquad -\partial_{x_2}\mathbf{\Lambda}_S^1[\mathbf{X}_1] + \partial_{t_2}\mathbf{X}_1 \\
& \qquad -\gamma_2^a \mathbf{\Lambda}_{H,2}\mathbf{X}_1 - \partial_{x_1}^2 \mathbf{\Lambda}_S^2[\mathbf{X}_1] \\
& \qquad +2\mathbf{\Omega}_2 \cdot \mathbf{X}_1\mathbf{X}_2 + \mathbf{\Omega}_3 \cdot \mathbf{X}_1\mathbf{X}_1\mathbf{X}_1 \\
\bullet\ \vdots\ & \qquad \vdots
\end{aligned} \tag{4.24}$$

where, as we mentioned in Section 4.3.1, $\Omega^1_{2_{1,1}} = -\alpha$ and $\Omega^1_{3_{1,1,1}} = \beta$ (all the other elements $\Omega^l_{2_{i,j}}$ and $\Omega^l_{3_{i,j,k}}$ are equal to zero) and where the operators $\mathbf{\Lambda}_S^0[\circ]$, $\mathbf{\Lambda}_S^1[\circ]$ and $\mathbf{\Lambda}_S^2[\circ]$ are given by:

$$\mathbf{\Lambda}_S^0[\circ] \overset{\text{def}}{=} \mathbf{\Lambda}_D \partial_{x_0}^2 \circ + \mathbf{\Lambda}_{NC} \int_{-\infty}^{+\infty} \mathbf{\Sigma}(|x_0 - y|) \circ dy, \tag{4.25}$$

$$\mathbf{\Lambda}_S^1[\circ] \overset{\text{def}}{=} 2\mathbf{\Lambda}_D \partial_{x_0} \circ - \mathbf{\Lambda}_{NC} \int_{-\infty}^{+\infty} \mathbf{\Sigma}(|x_0 - y|)(x_0 - y) \circ dy, \tag{4.26}$$

$$\mathbf{\Lambda}_S^2[\circ] \overset{\text{def}}{=} \mathbf{\Lambda}_D \circ + \mathbf{\Lambda}_{NC} \int_{-\infty}^{+\infty} \mathbf{\Sigma}(|x_0 - y|) \frac{(x_0 - y)^2}{2} \circ dy. \tag{4.27}$$

These new operators include, in a compact form, all the terms coming from the diffusive and nonlocal coupling operators of Eq. (2.17). Note that these operators act *only* over the variable x_0. They leave the stretched space variables $x_1, x_2, \ldots$ and all the time variables $t_0, t_1, \ldots$ unchanged.

In the following we will give just a cursive description of the derivation of the amplitude equations, a detailed analysis is done in Section E.1 of Appendix E.

4.3.2.A Ansatz for the equation $\mathcal{O}(\varepsilon)$

Let us first consider the lowest order in the ε-expansion of Eqs. (4.24) (*i.e.* the equation corresponding to $\mathcal{O}(\varepsilon)$). This equation is nothing else but the RDNC model evaluated at the criticality (*i.e.* $a = a_c$, where $a_c = a_T^c$ or $a_c = a_W^c$ for the Turing or the wave instability case respectively).

In Section 3.4.1 we introduced the critical solutions $\mathbf{X}_T^c$ and $\overline{\mathbf{X}_T^c}$ for the Turing case and $\mathbf{X}_L^c$, $\overline{\mathbf{X}_L^c}$, $\mathbf{X}_R^c$ and $\overline{\mathbf{X}_R^c}$ for the wave case. These critical solutions are complex vectors and are defined up to a indeterminate constant. Since the solution $\mathbf{X}_1$ should be real, a general solution of the equation corresponding to $\mathcal{O}(\varepsilon)$ in the hierarchy of Eq. (4.24) is given by:

1. for Turing: $$\mathbf{X}_1 = \frac{1}{2}(A_T \mathbf{U}_T e^{ik_T^c x_0}) + c.c. \tag{4.28}$$

2. for wave: $$\mathbf{X}_1 = \frac{1}{2}(A_L \mathbf{U}_W e^{i(\omega_c t_0 + k_W^c x_0)} + A_R \mathbf{U}_W e^{i(\omega_c t_0 - k_W^c x_0)}) + c.c. \tag{4.29}$$

where the amplitudes A_T, A_L and A_R are typically complex scalar quantities and the eigenvectors $\mathbf{U}_T$ and $\mathbf{U}_W$ are calculated in Appendix B. As stated in Section 4.2.4, we will assume here that the amplitudes depend only on the smooth and slow variables: $A_T = A_T(x_1, x_2, ...; t_1, t_2, ...)$, $A_L = A_L(x_1, x_2, ...; t_1, t_2, ...)$ and $A_R = A_R(x_1, x_2, ...; t_1, t_2, ...)$.

The second ansatz, for the wave instability case, corresponds to the most general solution possible: *a linear superposition of two counterpropagating waves.* The quantities A_L and A_R correspond to the amplitudes of *waves travelling to the left and right* respectively.

To solve the inhomogeneous equation $\mathcal{O}(\varepsilon^2)$ we need first to perform the solvability conditions over its inhomogeneous term.

4.3.2.B Inner Product definition

The first steep is to define an appropriated inner product. An easy calculation shows that the following operators satisfy the rules of inner product:

1. for Turing: $$(\mathbf{Z}|\mathbf{Y}_j) \overset{\text{def}}{=} \int_0^{2\pi/k_T^c} dx_0 \quad \overline{\mathbf{Z}}^{\mathrm{Tr}} \mathbf{Y}_j, \tag{4.30}$$

2. for wave: $$(\mathbf{Z}|\mathbf{Y}_j) \overset{\text{def}}{=} \int_0^{2\pi/k_W^c} dx_0 \int_0^{2\pi/\omega_c} dt_0 \quad \overline{\mathbf{Z}}^{\text{Tr}}\mathbf{Y}_j. \tag{4.31}$$

4.3.2.C Solvability condition $\mathcal{O}(\varepsilon^2)$

In order to solve the equation $\mathcal{O}(\varepsilon^2)$ in the hierarchy of Eq. (4.24) we should make sure that its inhomogeneous term satisfies the solvability condition of Eq. (4.13). This solvability condition will be evaluated in detail in Appendix E. Here we will only give a short description of the main results.

The main consequence of the solvability condition is that in both cases, Turing and wave instability, we are forced to postulate that (*cf.* Eq. (4.21)):

$$\gamma_1^a \equiv 0. \tag{4.32}$$

Otherwise the perturbative expansion is not consistent.

- Turing instability case

Using Eq. (4.32), the solvability condition $\mathcal{O}(\varepsilon^2)$ implies that:

$$\partial_{t_1} A_T \equiv 0,$$

should be fulfilled by the the amplitude of the Turing pattern (for details refer to Section E.1.B). Or, in other words, that the amplitude A_T *does not depend on the slow time* t_1.

- Wave instability case

On the other hand, for the wave instability case, the solvability condition $\mathcal{O}(\varepsilon^2)$ implies that:

$$\partial_{t_1} A_L - c_g \partial_{x_1} A_L = 0, \tag{4.33}$$

$$\partial_{t_1} A_R + c_g \partial_{x_1} A_R = 0, \tag{4.34}$$

where c_g is the group velocity (*cf.* Eq. (3.40)) of the waves (see Section E.1.D for more details). These last equations indicate that the amplitudes A_L and A_R are constant in the travelling frames $x_1 - c_g t_1$ and $x_1 + c_g t_1$ respectively.

- Solution of the inhomogeneous equation $\mathcal{O}(\varepsilon^2)$

We can now solve the inhomogeneous equation $\mathcal{O}(\varepsilon^2)$. Although this step is conceptually simple, in the RDNC model it is rather lengthly and cumbersome (specially for the wave instability case). Consequently, it will be done in Sections E.1.B and E.1.D of Appendix E for the Turing and wave cases respectively.

The solvability condition of the inhomogeneous equation $\mathcal{O}(\varepsilon^3)$ in the hierarchy of Eq. (4.24) will be discussed separately for the Turing and wave cases.

4.3.2.D Solvability condition $\mathcal{O}(\varepsilon^3)$: Turing Amplitude Equation

In Section E.1.C we discuss in detail the derivation of this solvability condition for the Turing instability. This derivation leads to the following PDE for the amplitude A_T:

$$\partial_{t_2} A_T = \gamma_2^a \kappa_2^{a,T} A_T + d_T \partial_{x_1}^2 A_T - g_{TT} |A_T|^2 A_T, \tag{4.35}$$

where the coefficients $\kappa_2^{a,T}$, d_T and g_{TT} are defined in Eqs. (E.18) and (E.19).

- Amplitude Equation for the Turing instability: Real Ginzburg-Landau Equation

Finally, we rewrite Eq. (4.35) in terms of the original time and space variables t and x (*cf.* Eqs. (4.15) and (4.18) and remember that $A_T = A_T(t_2, \dots; x_1, \dots)$ and therefore *do not depend* on t_0, t_1 or x_0). Additionally, let us reintroduce the control parameter a (*cf.* Eq. (4.21) and recall that $\gamma_1^a \equiv 0$) and use the fact that the amplitude A_T is proportional to ε (*cf.* Eq. (4.2) and Eq. (4.28)) and therefore we can introduce a *normalised amplitude* as: $A_T^\star \overset{\text{def}}{=} \varepsilon A_T$. This rescaling leads to the following *amplitude equation* for the Turing instability:

$$\boxed{\partial_t A_T^\star = \eta_T A_T^\star + d_T \partial_x^2 A_T^\star - g_{TT} |A_T^\star|^2 A_T^\star,} \tag{4.36}$$

where:

$$\eta_T \overset{\text{def}}{=} (a - a_T^c)\kappa_2^{a,T}, \tag{4.37}$$

and where the small parameter ε does not appear.

The PDE (4.36) is usually called in the literature the *real Ginzburg-Landau equation* [1] (RGLE in the following) because its coefficients are real (see discussion in the next paragraph). This equation governs the asymptotic evolution of the amplitude of Turing patterns near an instability. We will analyse basic solutions of this equation and compare them with numerical simulation of the RDNC model in Chapter 5.

Eqs. (E.18) and (E.19) indicate that the coefficients d_T, g_{TT} and $\kappa_2^{a,T}$ (and consequently η_T) are *real quantities*. On the contrary, the amplitude

$A_T^\star \in \mathbb{C}^1$. Its absolute value $|A_T^\star(x,t)|$ gives to the local amplitude of Turing pattern. On the other hand, its phase allows for the emerging patterns to have wavenumbers different from k_W^c (see next chapter for a detailed explanation of this issue).

- Meaning of the coefficients

The coefficient η_T, which is proportional to $a - a_T^c$ (*cf.* Eq. (4.37)), can be interpreted as the *distance to the threshold* of the Turing instability; d_T can be interpreted as a *diffusion* coefficient and g_{TT} is the *nonlinear saturation* coefficient. In Section 4.4 we will analyse these coefficients as functions of the parameters of the RDNC model.

4.3.2.E Solvability condition $\mathcal{O}(\varepsilon^3)$: Wave Amplitude Equations

Let us now address the solvability condition of the inhomogeneous equation $\mathcal{O}(\varepsilon^3)$ for the wave instability case. This derivation will be done in Section E.1.E, here we will just quote the final result. The outcome of solvability condition is the following set of *coupled* PDEs:

$$\begin{aligned}\partial_{t_2} A_L - c_g \partial_{x_2} A_L = {} & \gamma_2^a \kappa_2^{a,W} A_L + \left[d_{L,1} \partial_{x_1}^2 + (d_{L,2} + d_{L,4}) \partial_{x_1} \partial_{t_1} - d_{L,3} \partial_{t_1}^2 \right] A_L \\ & - g_{WW} |A_L|^2 A_L - g_{RL} |A_R|^2 A_L, \qquad (4.38) \\ \partial_{t_2} A_R + c_g \partial_{x_2} A_R = {} & \gamma_2^a \kappa_2^{a,W} A_R + \left[d_{R,1} \partial_{x_1}^2 + (d_{R,2} + d_{R,4}) \partial_{x_1} \partial_{t_1} - d_{R,3} \partial_{t_1}^2 \right] A_R \\ & - g_{WW} |A_R|^2 A_R - g_{RL} |A_L|^2 A_R, \qquad (4.39)\end{aligned}$$

where c_g, as before, is the group velocity (*cf.* Eq. (E.26)) and the coefficients $\kappa_2^{a,W}$, g_{WW} and g_{RL} are defined in Eqs. (E.39), (E.48) and (E.49) respectively. The coefficients $d_{L,j}$ and $d_{R,j}$ are defined in Eqs. (E.40,E.41,E.42,E.43,E.44) and satisfy the following equalities:

$$d_{L,1} = d_{R,1} \quad , \quad d_{L,2} = -d_{R,2} \quad , \quad d_{L,3} = d_{R,3} \quad \text{and} \quad d_{L,4} = -d_{R,4}. \qquad (4.40)$$

- Reduction of the number of variables

Note that Eqs. (4.38,4.39) involve differentiation with respect to *two time variables:* t_1 *and* t_2*, and two space variables:* x_1 *and* x_2. However, using the solvability conditions of the inhomogeneous equation $\mathcal{O}(\varepsilon^2)$ (*cf.* Eqs. (4.33,4.34)), it is possible to *reduce the number of variables to three*: t_1, x_1 and x_2. Specifically, using Eqs. (4.33,4.34) we can write the operators between brackets in Eqs. (4.38,4.39) as a second derivative with respect to the spatial variable x_1. More specifically:

$$\left[d_{L,1}\partial_{x_1}^2 + (d_{L,2}+d_{L,4})\partial_{x_1}\partial_{t_1} - d_{L,3}\partial_{t_1}^2\right]A_L = d_W\partial_{x_1}^2 A_L, \tag{4.41}$$

$$\left[d_{R,1}\partial_{x_1}^2 + (d_{R,2}+d_{R,4})\partial_{x_1}\partial_{t_1} - d_{R,3}\partial_{t_1}^2\right]A_R = d_W\partial_{x_1}^2 A_R, \tag{4.42}$$

where the new coefficient is:

$$d_W \overset{\text{def}}{=} d_{L,1} + c_g(d_{L,2}+d_{L,4}) - c_g^2 d_{L,3} = d_{R,1} - c_g(d_{R,2}+d_{R,4}) - c_g^2 d_{R,3}. \tag{4.43}$$

- Compensation method for the wave amplitude equations

Any analysis of the solvability conditions of Eqs. (4.38,4.39) (with Eqs. (4.41,4.42)) is complicated by the fact that they still involve partial derivatives with respect to *three* variables (namely: t_2, x_1 and x_2). Moreover, extra difficulties arise because this set of equations should be solved *simultaneously* with the solvability conditions of Eqs. (4.33,4.34). Furthermore this last set of equations involve partial derivation with respect to a forth variable t_1! All these features make the weakly nonlinear analysis of the wave instability very complicated[6]. To simplify the description, and in order to get a tractable set of equations, we will use a method proposed by Knobloch[7] in ref. [81]. The method uses *both* sets of solvability conditions (*i.e.* Eqs. (4.33,4.34) *and* (4.38,4.39)) to get just one set of PDEs which depend only on the *original* space and time variables.

The key idea of this method is that each set of solvability conditions is valid in a range depending on the distance ε to the criticality. More precisely; Eqs. (4.33,4.34) are valid $\mathcal{O}(\varepsilon^2)$ whereas Eqs. (4.38,4.39) are $\mathcal{O}(\varepsilon^3)$. This indicates us that if we multiply Eqs. (4.33,4.34) by ε^2 and Eqs. (4.38,4.39) by ε^3 we get two sets of equations valid for the *same* order of ε. Therefore we can *counterbalance* or *compensate* the two solvability conditions by adding these two new sets of equations. Using this *compensation method* we get only one set of coupled PDEs:

$$\begin{aligned}(\varepsilon\partial_{t_1} + \varepsilon^2\partial_{t_2})\varepsilon A_L - c_g(\varepsilon\partial_{x_1} + \varepsilon^2\partial_{x_2})\varepsilon A_L = {} & \varepsilon^2\gamma_2^a\kappa_2^{a,W}\varepsilon A_L + \varepsilon^2 d_W\partial_{x_1}^2\varepsilon A_L \\ & -\varepsilon^3 g_{WW}|A_L|^2A_L - \varepsilon^3 g_{RL}|A_R|^2A_L\end{aligned} \tag{4.44}$$

---

[6] Note that these problems did not arise in the derivation of the Turing amplitude equation (4.36) because there the solvability condition $\mathcal{O}(\varepsilon^2)$ did not depend on x_1 and indicated that the amplitude was independent of t_1.

[7] The method proposed by Knobloch in ref. [81], which he calls *reconstitution method*, is not exactly the same than the one presented here. Nevertheless, the main idea of both methods is the same.

$$(\varepsilon\partial_{t_1}+\varepsilon^2\partial_{t_2})\varepsilon A_R + c_g(\varepsilon\partial_{x_1}+\varepsilon^2\partial_{x_2})\varepsilon A_R = \varepsilon^2\gamma_2^a\kappa_2^{a,W}\varepsilon A_R + \varepsilon^2 d_W\partial_{x_1}^2\varepsilon A_R \qquad (4.45)$$
$$-\varepsilon^3 g_{WW}|A_R|^2A_R - \varepsilon^3 g_{RL}|A_L|^2A_R,$$

where all the terms are valid for the same order of ε.

This last set of equations should be *necessarily* satisfied by the amplitudes. Nevertheless, they are not *sufficient* conditions for the perturbative expansion to be well posed. As we will see in the next chapters, this method does lead to a set of equations that *describe qualitatively and quantitatively* the beauvoir of the RDNC model near the wave instability.

- Amplitude Equations for the wave instability: Coupled Complex Ginzburg-Landau Equations

The Eqs. (4.44,4.45) can be written in a simpler form, independent of ε, if we take into account that the amplitudes $A_L(t_1,t_2,\ldots;x_1,x_2,\ldots)$ and $A_R(t_1,t_2,\ldots;x_1,x_2,\ldots)$ do not depend on t_0 or x_0 (*cf.* Eq. (4.29)) and if we use the ε-expansions for time and space variables (*cf.* Eq. (4.15) and Eq. (4.18) respectively) to restitute the original time and space variables x and t. Furthermore, as in the Turing case, reintroducing the control parameter a (*cf.* Eq. (4.21)) and, finally, defining the *normalised amplitudes* as: $A_L^\star \overset{\text{def}}{=} \varepsilon A_L$ and $A_R^\star \overset{\text{def}}{=} \varepsilon A_R$, we get the following set of two coupled amplitude equations:

$$\boxed{\begin{aligned}
\partial_t A_L^\star - c_g\partial_x A_L^\star &= \eta_W A_L^\star + d_W\partial_x^2 A_L^\star - g_{WW}|A_L^\star|^2A_L^\star - g_{RL}|A_R^\star|^2A_L^\star \qquad (4.46)\\
\partial_t A_R^\star + c_g\partial_x A_R^\star &= \eta_W A_R^\star + d_W\partial_x^2 A_R^\star - g_{WW}|A_R^\star|^2A_R^\star - g_{RL}|A_L^\star|^2A_R^\star \qquad (4.47)
\end{aligned}}$$

where:

$$\eta_W \overset{\text{def}}{=} (a-a_W^c)\kappa_2^{a,W}. \qquad (4.48)$$

If $g_{RL}=0$ then Eqs. (4.46,4.47) decouple and each equation has the form of a *complex Ginzburg-Landau equation* (CGLE in the following). These equations have been studied extensively in the literature [1, 5, 6, 10, 75]. Note that Eq. (4.46) and Eq. (4.47) differ only in the sign of the group velocity term. Typically $g_{RL}\neq 0$ and consequently Eqs. (4.46,4.47) correspond to a set of two *coupled CGLEs*. Some basic solutions of these equations, and their dependence on the coefficient values, will be studied in Chapter 5.

- Meaning of the coefficients

The coefficients $\eta_W, d_W, g_{WW}, g_{RL}$ are complex and c_g is real. In the following we will denote the real part of the complex coefficients with primes and the imaginary with double primes. The coefficient η'_W (which is proportional to $a - a^c_W$) is the *distance to the instability threshold.* η''_W corresponds to a *shift of the oscillation frequency* of the waves respect to the critical frequency ω_c (note that this shift is also proportional to the distance to the instability threshold). c_g is, as we saw before, the *group velocity* of the waves. In the following chapters we will see that this coefficient plays an important rôle in the dynamics of the waves. d'_W is associated the *diffusion* and d''_W with the *dispersion* of the amplitudes. The coefficients g'_{WW}, g''_{WW}, g'_{RL} and g''_{RL} are the nonlinear terms corresponding to: *self-induced nonlinear saturation*, nonlinear *correction of the oscillation frequency*, *cross-induced nonlinear saturation* (or cross-coupling intensity) and nonlinear *correction to the oscillation frequency* induced by the other mode respectively. In Section 4.4 and Chapter 5 we will analyse in detail these coefficients.

4.3.3 Amplitude equation near the codimension-2 wave-Turing instability

Let us now discuss the derivation of amplitude equations near the codimension-2 wave-Turing instability. To some extent the derivation of amplitude equations in this case is a combination of the derivations done previously for Turing and wave instabilities. Consequently here we will put more emphasis on the differences and subtleties arising in this case than in the "standard" features already explained in Section 4.3.2.

Beside the $\varepsilon-$expansion of the control parameter a around its critical value as done in Eq. (4.21), in this case we need also to expand the second control parameter δ as:

$$\delta - \delta_c = \gamma_1^\delta \varepsilon + \gamma_2^\delta \varepsilon^2 + \mathcal{O}(\varepsilon^3), \tag{4.49}$$

where we consider $a_c = a^c_{WT}$ and $\delta_c = \delta^c_{WT}$. Since the diffusion matrix $\mathbf{\Lambda}_D$ (*cf.* Eq. (2.20)) does depend on the diffusion ration δ, we get:

$$\mathbf{\Lambda}_D(\delta) = \begin{pmatrix} 1 & 0 \\ 0 & \delta_c \end{pmatrix} + \varepsilon\gamma_1^\delta \begin{pmatrix} 0 & 0 \\ 0 & 1 \end{pmatrix} + \varepsilon^2\gamma_2^\delta \begin{pmatrix} 0 & 0 \\ 0 & 1 \end{pmatrix} + \mathcal{O}(\varepsilon^3).$$

And consequently the spatial operators $\mathbf{\Lambda}_S^0$, $\mathbf{\Lambda}_S^1$ and $\mathbf{\Lambda}_S^2$ (see Eqs. (4.25), (4.26) and (4.27)) are:

$$\mathbf{\Lambda}_S^0(\delta) = \mathbf{\Lambda}_{S,0}^0(\delta_c) + \varepsilon\gamma_1^\delta \mathbf{\Lambda}_{S,1}^0(\delta_c) + \varepsilon^2\gamma_2^\delta \mathbf{\Lambda}_{S,2}^0(\delta_c) + \mathcal{O}(\varepsilon^3), \tag{4.50}$$

$$\boldsymbol{\Lambda}^1_S(\delta) = \boldsymbol{\Lambda}^1_{S,0}(\delta_c) + \varepsilon\gamma_1^\delta \boldsymbol{\Lambda}^1_{S,1}(\delta_c)\partial^2_{x_1} + \mathcal{O}(\varepsilon^2), \tag{4.51}$$

$$\boldsymbol{\Lambda}^2_S(\delta) = \boldsymbol{\Lambda}^2_{S,0}(\delta_c) + \mathcal{O}(\varepsilon^1), \tag{4.52}$$

where $\boldsymbol{\Lambda}^0_{S,0}(\delta_c)$, $\boldsymbol{\Lambda}^1_{S,0}(\delta_c)$ and $\boldsymbol{\Lambda}^2_{S,0}(\delta_c)$ are respectively given by Eqs. (4.25), (4.26) and (4.27) with $\delta \equiv \delta_c$, and finally:

$$\boldsymbol{\Lambda}^0_{S,1} = \boldsymbol{\Lambda}^0_{S,2} = \begin{pmatrix} 0 & 0 \\ 0 & \partial^2_{x_0} \end{pmatrix} \quad \text{and} \quad \boldsymbol{\Lambda}^1_{S,1} = \begin{pmatrix} 0 & 0 \\ 0 & 2\partial_{x_0} \end{pmatrix}.$$

Finally, inserting ε-expansions of Eqs. (4.2), (4.15), (4.20), (4.22) and (4.50,4.51,4.52) in Eq. (2.17) we get:

$$\begin{array}{lll}
\bullet\ \mathcal{O}(\varepsilon): & \boldsymbol{\Lambda}_{H,0}\mathbf{X}_1 + \boldsymbol{\Lambda}^0_{S,0}[\mathbf{X}_1] - \partial_{t_0}\mathbf{X}_1 = 0 & \\
\bullet\ \mathcal{O}(\varepsilon^2): & \boldsymbol{\Lambda}_{H,0}\mathbf{X}_2 + \boldsymbol{\Lambda}^0_{S,0}[\mathbf{X}_2] - \partial_{t_0}\mathbf{X}_2 = & -\gamma_1^a\boldsymbol{\Lambda}_{H,1}\mathbf{X}_1 - \gamma_1^\delta\boldsymbol{\Lambda}^0_{S,1}[\mathbf{X}_1] + \partial_{t_1}\mathbf{X}_1 \\
 & & -\partial_{x_1}\boldsymbol{\Lambda}^1_{S,0}[\mathbf{X}_1] + \boldsymbol{\Omega}_2\cdot\mathbf{X}_1\mathbf{X}_1 \\
\bullet\ \mathcal{O}(\varepsilon^3): & \boldsymbol{\Lambda}_{H,0}\mathbf{X}_3 + \boldsymbol{\Lambda}^0_{S,0}[\mathbf{X}_3] - \partial_{t_0}\mathbf{X}_3 = & -\gamma_1^a\boldsymbol{\Lambda}_{H,1}\mathbf{X}_2 - \gamma_1^\delta\boldsymbol{\Lambda}^0_{S,1}[\mathbf{X}_2] \\
 & & +\partial_{t_1}\mathbf{X}_2 - \partial_{x_1}\boldsymbol{\Lambda}^1_{S,0}[\mathbf{X}_2] \\
 & & -\partial_{x_2}\boldsymbol{\Lambda}^1_{S,0}[\mathbf{X}_1] + \partial_{t_2}\mathbf{X}_1 \\
 & & -\gamma_2^a\boldsymbol{\Lambda}_{H,2}\mathbf{X}_1 - \gamma_2^\delta\boldsymbol{\Lambda}^0_{S,2}[\mathbf{X}_1] \\
 & & -\partial^2_{x_1}\boldsymbol{\Lambda}^2_{S,0}[\mathbf{X}_1] - \gamma_1^\delta\partial_{x_1}\boldsymbol{\Lambda}^1_{S,1}[\mathbf{X}_1] \\
 & & +2\boldsymbol{\Omega}_2\cdot\mathbf{X}_1\mathbf{X}_2 + \boldsymbol{\Omega}_3\cdot\mathbf{X}_1\mathbf{X}_1\mathbf{X}_1 \\
\bullet\ \vdots & & \vdots
\end{array} \tag{4.53}$$

This hierarchy is very similar to Eq. (4.24), although now we have some extra terms coming from the ε-expansion of δ.

In the following we will present a very short account of the main steps in the derivation of the amplitude equations; a detailed description will be given in Section E.2 of Appendix E.

4.3.3.A Ansatz for the equation $\mathcal{O}(\varepsilon)$

Let us first consider the equation $\mathcal{O}(\varepsilon)$ in the hierarchy (4.53). A general solution of this linear homogeneous equation is given by:

$$\mathbf{X}_1 = \frac{1}{2}\Big(A_T\mathbf{U}_T e^{ik^c_T x_0} + A_L\mathbf{U}_W e^{i(\omega_c t_0 + k^c_W x_0)} + A_R\mathbf{U}_W e^{i(\omega_c t_0 - k^c_W x_0)}\Big) + c.c. \tag{4.54}$$

The interpretation of this ansatz is clear: *it corresponds to a superposition of a Turing pattern, a left-travelling wave and a right-travelling wave* with amplitudes A_T, A_L and A_R respectively.

4.3.3.B Solvability condition $\mathcal{O}(\varepsilon^2)$

A suitable inner product for this case is obtained by adding the inner products defined for the Turing and wave instability cases (*cf.* Eqs (4.30) and (4.31) respectively). This inner product is defined in Eq. (E.50).

In Section E.2.B we give a detailed derivation of the solvability conditions of the inhomogeneous equation $\mathcal{O}(\varepsilon^2)$. The main result of this derivation is that we are forced to assume that:

$$\gamma_1^a \equiv 0 \quad \text{and} \quad \gamma_1^\delta \equiv 0. \tag{4.55}$$

Using this equalities, the solvability conditions $\mathcal{O}(\varepsilon^2)$ become:

$$\begin{aligned} \partial_{t_1} A_T &= 0, & (4.56)\\ \partial_{t_1} A_L - c_g \partial_{x_1} A_L &= 0, & (4.57)\\ \partial_{t_1} A_R + c_g \partial_{x_1} A_R &= 0. & (4.58) \end{aligned}$$

This set of *uncoupled* PDEs is nothing else but the combination of the solvability conditions $\mathcal{O}(\varepsilon^2)$ previously got for Turing and for wave instability cases separately.

The solution of the inhomogeneous equation $\mathcal{O}(\varepsilon^2)$ is given in Eq. (E.64) in Section E.2.B.

4.3.3.C Solvability condition $\mathcal{O}(\varepsilon^3)$: Codimension-2 wave-Turing Amplitude Equation

The solvability condition of the inhomogeneous equation $\mathcal{O}(\varepsilon^3)$ leads to the following set of three coupled partial differential equations (see Section E.2.C for more details):

$$\begin{aligned} \partial_{t_2} A_L - c_g \partial_{x_2} A_L &= (\gamma_2^a \kappa_2^{a,W} + \gamma_2^\delta \kappa_2^{\delta,W}) A_L + d_W \partial_{x_1}^2 A_L \\ &\quad - g_{WW} |A_L|^2 A_L - g_{RL} |A_R|^2 A_L - g_{WT} |A_T|^2 A_L, & (4.59)\\ \partial_{t_2} A_R + c_g \partial_{x_2} A_R &= (\gamma_2^a \kappa_2^{a,W} + \gamma_2^\delta \kappa_2^{\delta,W}) A_R + d_W \partial_{x_1}^2 A_R \\ &\quad - g_{WW} |A_R|^2 A_R - g_{RL} |A_L|^2 A_R - g_{WT} |A_T|^2 A_R, & (4.60)\\ \partial_{t_2} A_T &= (\gamma_2^a \kappa_2^{a,T} + \gamma_2^\delta \kappa_2^{\delta,T}) A_T + d_T \partial_{x_1}^2 A_T \\ &\quad - g_{TT} |A_T|^2 A_T - g_{TW} (|A_L|^2 + |A_R|^2) A_T, & (4.61) \end{aligned}$$

where c_g is, as before, the group velocity of the waves, $\kappa_2^{a,T}$, $\kappa_2^{a,W}$, $\kappa_2^{\delta,T}$ and $\kappa_2^{\delta,W}$ are defined in Eqs. (E.18), (E.39) and (E.69); the coefficients d_W, g_{WW} and g_{RL} are the same than for the codimension-1 wave instability case and are defined in Eqs. (4.43), (E.48) and (E.49); d_T and g_{TT} are equivalent to the definitions for the Turing instability (*cf.* Eqs. (E.18) and (E.19) respectively). Two new coupling coefficients appear in these equations, they are g_{WT} and g_{TW}. They are defined in Eqs. (E.70) and (E.71) respectively.

- Compensation method for the codimension-2 wave-Turing amplitude equations

Eqs. (4.59,4.60,4.61) involve derivatives with respect to *three variables:* t_2, x_1 and x_2. Furthermore, two sets of solvability conditions, given by Eqs. (4.56,4.57,4.58) and Eqs. (4.59,4.60,4.61), should be satisfied simultaneously by the amplitudes A_T, A_L and A_R. The same kind of problems did arise in the derivation of amplitude equations for the wave instability (*cf.* Section 4.3.2.E). Indeed the same compensation method introduced there can be applied here to solve these problems. For details see Section 4.3.2.E.

- Amplitude equations for the codimension-2 wave-Turing instability: coupled real and complex Ginzburg-Landau equations

The final result of of the compensation method is the following set of three coupled amplitude equations valid near the codimension-2 point:

$$\boxed{\begin{aligned}
\partial_t A_L^\star - c_g \partial_x A_L^\star &= \eta_W A_L^\star + d_W \partial_x^2 A_L^\star - g_{WW}|A_L^\star|^2 A_L^\star - g_{RL}|A_R^\star|^2 A_L^\star \\
&\quad - g_{WT}|A_T^\star|^2 A_L^\star \qquad (4.62) \\
\partial_t A_R^\star + c_g \partial_x A_R^\star &= \eta_W A_R^\star + d_W \partial_x^2 A_R^\star - g_{WW}|A_R^\star|^2 A_R^\star - g_{RL}|A_L^\star|^2 A_R^\star \\
&\quad - g_{WT}|A_T^\star|^2 A_R^\star \qquad (4.63) \\
\partial_t A_T^\star &= \eta_T A_T^\star + d_T \partial_x^2 A_T^\star - g_{TT}|A_T^\star|^2 A_T^\star \\
&\quad - g_{TW}(|A_L^\star|^2 + |A_R^\star|^2) A_T^\star \qquad (4.64)
\end{aligned}}$$

where:

$$\eta_W = (a - a_{WT})\kappa_2^{a,W} + (\delta - \delta_{WT})\kappa_2^{\delta,W}, \tag{4.65}$$

$$\eta_T = (a - a_{WT})\kappa_2^{a,T} + (\delta - \delta_{WT})\kappa_2^{\delta,T}, \tag{4.66}$$

and d_T, g_{TT}, c_g, d_W, g_{WW} and g_{RL} where defined in Eqs. (E.18), (E.19), (E.26), (4.43), (E.48) and (E.49) respectively.

A comparison of Eqs. (4.62,4.63,4.64) with the amplitude equations derived previously for the codimension-1 Truing and wave instabilities (*cf.* Eq. (4.36) and Eqs. (4.46,4.47) respectively) shows that Eqs. (4.62,4.63, 4.64) are a set of *coupled real and complex Ginzburg-Landau equations.* We will analyse basic solutions of these equations in Chapter 5.

- Meaning of the coefficients

The meaning of the coefficients $\kappa_2^{a,T}$, d_T, g_{TT}, $\kappa_2^{a,W}$, c_g, d_W, g_{WW} and g_{RL} was discussed in sections 4.3.2.D and 4.3.2.E. There we saw that $\kappa_2^{a,T}$, d_T, g_{TT}

and c_g were real and, $\kappa_2^{a,W}$, d_W, g_{WW} and g_{RL} complex. Here we will analyse the new coefficients appearing in Eqs. (4.62,4.63, 4.64). $\kappa_2^{\delta,T}$ and g_{TW} are real whereas $\kappa_2^{\delta,W}$ and g_{WT} are complex. $\eta'_W = \eta'_W(a,\delta)$ and $\eta_T = \eta_T(a,\delta)$ describe the distances to wave and Turing thresholds respectively. The coefficients g_{TW} and g_{WT} correspond to the *cross-coupling* between Turing and wave patterns. Note that these cross-coupling coefficients are typically different (*i.e.* $g_{TW} \neq g_{WT}$). We will analyse these coefficients in the next section.

4.4 Basic analysis of the coefficients of the amplitude equations

As we saw in the previous section, the amplitude equations depend on many coefficients. The analysis of these coefficients will be started here. Further analysis, including a detailed study of their significance for pattern formation in the RDNC model, will be done in following chapters. In particular, in Chapter 5 we will study basic solutions of the amplitude equations.

An important issue is that not all the coefficients are essential to get a description of the dynamics of the amplitude equations. Doing an appropriated selection of the unit of space and scaling the amplitudes is possible to make various prefactors of the coefficients equal to unity and consequently simplify the study of the amplitude equations. This rescaling of the coefficients will be done in Section 4.4.2.

4.4.1 Coefficients as function of the parameters of the RDNC model

The coefficients of the amplitude equations given in Eqs. (4.36), (4.47,4.46), and (4.63,4.62,4.64) depend on the values of the parameters of the RDNC model. This dependence is typically very complicated. However, some generic information can be extracted without using particular values of the parameters of the RDNC model. In this section we will analyse this and also show some more specific features of the amplitude equation coefficients in the case where the parameters of the RDNC model are as in Eq. (3.35) (*i.e.* the case analysed in detail in Section 3.5.4).

4.4.1.A Turing amplitude equation

- Generic case

Let us start analysing the coefficients of the Turing amplitude equation (4.36).

Using the expression for $\hat{\mathbf{\Lambda}}_{H,2}$ given in Eq. (4.23), then $\kappa_2^{a,T}$, the proportionality constant between η_T and $a - a_T^c$ (*cf.* Eq. (4.37)), becomes: $\kappa_2^{a,T} = [1 + \hat{\Lambda}_{11}(k_T^c)/(\hat{\Lambda}_{21}(k_T^c)\hat{\Lambda}_{12}(k_T^c))]^{-1}$ (*cf.* Eq. (E.18)). One consequence of this is that $\kappa_2^{a,T}$ only depends on the product bc. As we saw in the previous chapter (*cf.* Section 3.5.1), the same happens in the linear stability analysis. Moreover, for the limit $\delta \to \infty$ we get (using Eq. (3.32) and Eq. (C.4)):

$$\kappa_2^{a,T} = 1, \tag{4.67}$$

hence, in this limit, $\kappa_2^{a,T}$ becomes independent of all the other parameters of the RDNC model.

The sign of the nonlinear saturation coefficient g_{TT} will determine if the instability is *supercritical* or *subcritical* (supercritical if $g_{TT} > 0$ and subcritical if $g_{TT} < 0$). The values of the quadratic α and cubic β nonlinearity parameters of the RDNC model are of special importance for the value of g_{TT}. In Eq. (E.19) we can see that g_{TT} does not depend on the sign of α and that a negative β will make the instability subcritical no matter the value of α is. On the other hand, if $\beta > 0$ then there will be a maximal $|\alpha|$ for the instability to be supercritical. In the particular, if $\alpha = 0$ then the nonlinear coefficient is proportional $\kappa_2^{a,T}$:

$$g_{TT} = \frac{3\beta\kappa_2^{a,T}}{4}. \tag{4.68}$$

Consequently, if we discard the spatial dependence of the amplitude A_T, then we find that for $a > a_T^c$ the stationary solution has amplitude: $|A_T^\star|^2 = 4(a - a_T^c)/3\beta$. Hence the amplitude of the emerging Turing pattern after the instability is proportional to the square root of the distance to the threshold and is independent of the other linear parameters of the RDNC model.

- Particular case

Let us now analyse the coefficients $\kappa_2^{a,T}$, d_T and g_{TT} when we vary δ and keep all the other parameters of the model fixed to the values chosen in Section 3.5.4 (*cf.* values of Eq. (3.35)). As was discussed there (see Fig. 3.5), the Turing instability happens if $\delta > 1$ and a is big enough. In Fig. 4.2(a) we plot $\kappa_2^{a,T}$ and in Fig. 4.2(b) d_T for $1 \leq \delta \leq 10$. Note that $\kappa_2^{a,T}$ approximates

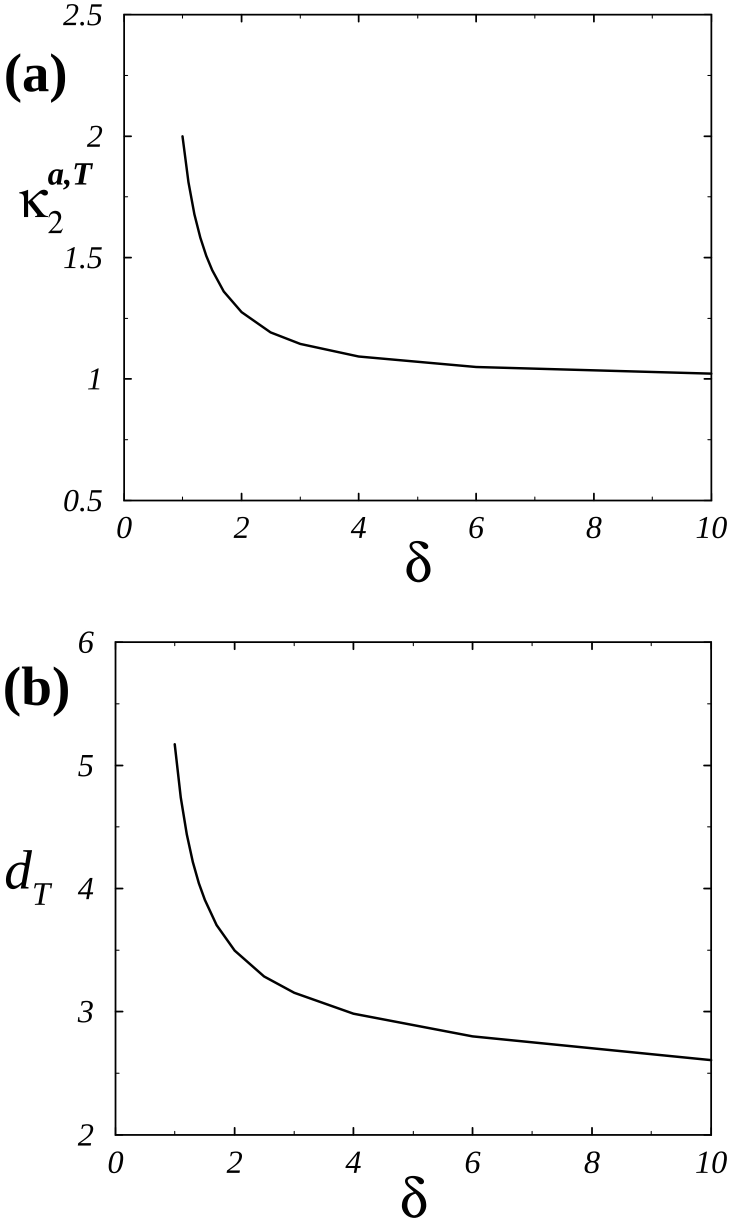

Figure 4.2: The value of the coefficients $\kappa_2^{a,T}$ and d_T are shown as a function of δ in (a) and (b) respectively, where the parameters of the system are as in Eq. (3.35). Note that δ should be bigger than 1 for the Turing instability to happen (see discussion in Section 3.5.4) and that (for $\alpha = 0$) the nonlinear coefficient g_{TT} is proportional to $\kappa_2^{a,T}$ (*cf.* Eq. (4.68)).

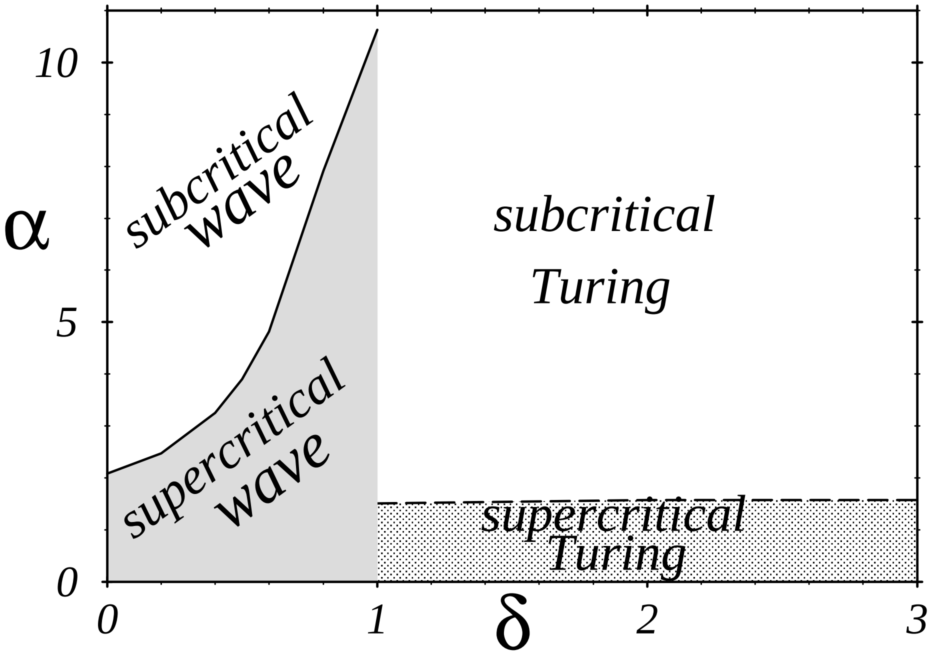

Figure 4.3: The grey regions correspond to supercritical instabilities (i.e. $g_{TT} > 0$ for Turing and $g'_{WW} > 0$ for wave). As the quadratic nonlinearity α is increased a transition from a supercritical to a subcritical instability happens for both, Turing and wave (for $\alpha = 0$ both instabilities are always supercritical). The linear parameters of the model, except the diffusion ratio δ, are fixed to the values given in Eq. (3.35) and the cubic nonlinearity is fixed to $\beta = 4/3$. As was discussed in Section 3.5.4, there is a wave instability for $0 \leq \delta \leq 1$ and a Turing instability for $\delta \geq 1$.

1 for big δ (*cf.* Eq. (4.67)) and that the diffusion coefficient d_T decreases monotonically. In Fig. 4.3 we display the character of the instability (*i.e.* supercritical or subcritical) as a function of δ as the quadratic nonlinearity $|\alpha|$ increases for a constant and positive value of β. Note that the transition from supercritical to subcritical is almost independent from the diffusion ratio δ.

4.4.1.B Wave amplitude equations

- Generic case

We will now analyse the coefficients derived for the wave amplitude equations. As discussed in Section 3.5.4, for $\delta = 0$ the group velocity $c_g \equiv 0$ (see footnote in pg. 40 and Fig. 3.6). Therefore, in this particular case, the solvability conditions of Eqs. (4.33,4.34) indicate that the amplitudes do not depend on t_1. Consequently the compensation method introduced in Section 4.3.2.E is not needed. Thus, the final result of the solvability conditions $\mathcal{O}(\varepsilon^3)$ is a set of two coupled CGLEs as in Eq. (4.46,4.47) with $c_g = 0$. As the diffusion ratio δ increases, c_g departs from zero.

The coefficients $\kappa_2^{a,W}$, d_W, g_{WW} and g_{RL} are very complicated functions of the parameters. The analysis of the dependence of the nonlinear coefficients g_{WW} and g_{RL} on the quadratic α and cubic β nonlinearities is analogous to the one done previously for the Turing case. If $\alpha = 0$, then the nonlinear coefficients assume a simpler form: $g_{WW} = 3\beta\kappa_2^{a,W}/4$ and $g_{RL} = 6\beta\kappa_2^{a,W}/4$ respectively. Consequently, in this limit:

$$g_{RL} \equiv 2 g_{WW}.$$

In the next chapter we will see that his relationship has important consequences for the possible solutions of amplitude equations (4.46,4.47).

- Particular case

For the particular values of the parameters chosen in Eq. (3.35) the wave instability arise if $0 \leq \delta \leq 1$ and a is big enough (for the instability threshold see Fig. 3.5(a)). In Fig. 3.6 we show the value of c_g as δ increases. In Fig. 4.4 we show the values of $\kappa_2^{a,W}$ and d_W as δ vary. Finally, in Fig. 4.3 the transition between supercritical and subcritical wave instability is plotted as a function of the quadratic nonlinearity α for a constant value of β and in the range $0 \leq \delta \leq 1$.

4.4.1.C Codimension-2 wave-Turing amplitude equations

- Generic case

Here we will only address the analysis of the coefficients g_{WT} and g_{TW} corresponding to the coupling between Turing and waves in Eqs. (4.63,4.62,4.64). The other coefficients have been analysed previously. In particular note that both, g_{WT} and g_{TW} (*cf.* Eqs. (E.48) and (E.49) respectively), have an analogous dependence on α and β as g_{TT} or g_{RL}.

- Particular case

For the particular codimension-2 wave-Turing point studied in Section 3.5.4 we have:

$$\eta_W(a,\delta) = \frac{1}{2}\Big[(a-a_c) - {k_W^c}^2(\delta-\delta_c) - i((a-a_c) + {k_W^c}^2(\delta-\delta_c))\Big], \quad (4.69)$$

$$\eta_T(a,\delta) = 2\Big[(a-a_c) + \frac{{k_T^c}^2}{2}(\delta-\delta_c)\Big], \quad (4.70)$$

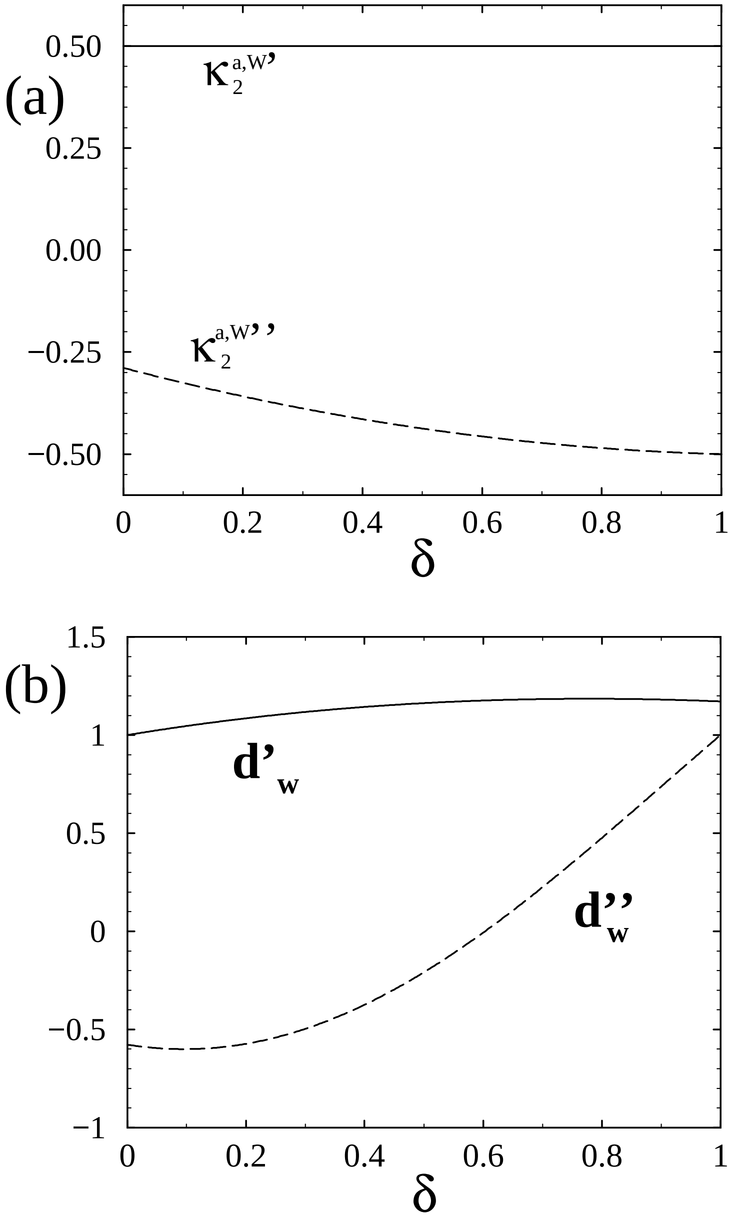

Figure 4.4: The real and imaginary part of $\kappa_2^{a,W}$ (in (a); $\kappa_2^{a,W'}$ and $\kappa_2^{a,W''}$ respectively) and of d_W (in (b); d'_W and d''_W respectively) are shown as function of δ in the span $0 \leq \delta \leq 1$ (*i.e.* the δ-range where the wave instability appears). The other parameters of the RDNC model are as in Eq. (3.35).

$$
\begin{aligned}
\eta_W &= \tfrac{1}{2}[(a-a_c) - {k_W^c}^2(\delta-\delta_c) - i((a-a_c) + {k_W^c}^2(\delta-\delta_c))] \\
\eta_T &= 2[(a-a_c) + \tfrac{{k_T^c}^2}{2}(\delta-\delta_c)] \\
c_g &= -2\sqrt{\sqrt{2}-1} \simeq -1.287119 \\
d_W &= d'_W + i d''_W \simeq 1.17157 + i \\
d_T &= 2(4-\sqrt{(}2)) \simeq 5.17157 \\
g_{WW} &= g'_{WW} + i g''_{WW} = 0.5 - 0.5i \\
g_{RL} &= g'_{RL} + i g''_{RL} = 1 - i \\
g_{WT} &= g'_{WT} + i g''_{WT} = 1 - i \\
g_{TT} &= 2 \\
g_{TW} &= 4
\end{aligned}
$$

Table 4.1: Value of the coefficients of the amplitude equations (4.62,4.63,4.64) at the codimension-2 wave-Turing point given in Table 3.1. The nonlinear parameters of the RDNC model have been fixed to: $\alpha = 0$ and $\beta = 4/3$.

and, for convenience, the values of the coefficients for this the codimension-2 wave-Turing point (*cf.* Table 3.1) are summarised in Table 4.1.

4.4.2 Rescaling of the Coefficients

As we mentioned in the beginning of this section, by doing a suitable selection of the unit of space and rescaling the amplitudes it is possible to make some prefactors of the amplitude equations equal to unity.

- Turing amplitude equation

Let us first analyse the amplitude equation (4.36) for the Turing instability. If we assume that $g_{TT} > 0$ (*i.e.* a supercritical Turing instability) and define a rescaled amplitude as:

$$\widetilde{A}_T \overset{\text{def}}{=} \sqrt{g_{TT}} A_T^{\star}, \tag{4.71}$$

we get:

$$\partial_t \widetilde{A}_T = \eta_T \widetilde{A}_T + d_T \partial_x^2 \widetilde{A}_T - |\widetilde{A}_T|^2 \widetilde{A}_T. \tag{4.72}$$

Moreover, if we change the units of space as: $\widetilde{x} \overset{\text{def}}{=} \frac{x}{\sqrt{d_T}}$, then:

$$\boxed{\partial_t \widetilde{A}_T = \eta_T \widetilde{A}_T + \partial_{\widetilde{x}}^2 \widetilde{A}_T - |\widetilde{A}_T|^2 \widetilde{A}_T \qquad (4.73)}$$

Consequently, if $g_{TT} > 0$, the amplitude equation valid near the Turing instability depends only on *one parameter*.

- Wave amplitude equations

Like in the Turing case, the coefficients of amplitude equations (4.46,4.47) can be simplified using new units for the space:

$$\widetilde{x} \overset{\text{def}}{=} \frac{x}{\sqrt{d'_W}}. \tag{4.74}$$

The amplitude equations are now:

$$\begin{aligned}\partial_t A_L^\star - v_g \partial_{\tilde{x}} A_L^\star &= \eta_W A_L^\star + (1 + ic_1)\partial_{\tilde{x}}^2 A_L^\star \\ &\quad - g_{WW}|A_L^\star|^2 A_L^\star - g_{RL}|A_R^\star|^2 A_L^\star \\ \partial_t A_R^\star + v_g \partial_{\tilde{x}} A_R^\star &= \eta_W A_R^\star + (1 + ic_1)\partial_{\tilde{x}}^2 A_R^\star \\ &\quad - g_{WW}|A_R^\star|^2 A_R^\star - g_{RL}|A_L^\star|^2 A_R^\star\end{aligned}$$

where the new coefficients are:

$$v_g \overset{\text{def}}{=} c_g/\sqrt{d'_W} \quad \text{and} \quad c_1 \overset{\text{def}}{=} d''_W/d'_W. \tag{4.75}$$

Note that now v_g is the rescaled[8] group velocity c_g.

If we assume that $g'_{WW} > 0$ and do a rescaling of the amplitudes $A_L^\star$ and $A_R^\star$ akin to the one done for $A_T^\star$, then we can set g'_{WW} equal to one. Furthermore, if we additionally write the amplitudes in a rotating frame with frequency equal to the correction given by η''_W, then it is possible to eliminate also η''_W from the amplitude equations. Specifically, defining a new set of amplitudes as:

$$\widetilde{A}_L \overset{\text{def}}{=} e^{-i\eta''_W t}\sqrt{g'_{WW}}A_L^\star \quad \text{and} \quad \widetilde{A}_R \overset{\text{def}}{=} e^{-i\eta''_W t}\sqrt{g'_{WW}}A_R^\star, \tag{4.76}$$

we get:

$$\boxed{\begin{aligned}\partial_t \widetilde{A}_L - v_g \partial_{\tilde{x}} \widetilde{A}_L &= \eta'_W \widetilde{A}_L + (1 + ic_1)\partial_{\tilde{x}}^2 \widetilde{A}_L \\ &\quad -(1 - ic_3)|\widetilde{A}_L|^2 \widetilde{A}_L - h_{RL}(1 - ic_2)|\widetilde{A}_R|^2 \widetilde{A}_L, \quad (4.77) \\ \partial_t \widetilde{A}_R + v_g \partial_{\tilde{x}} \widetilde{A}_R &= \eta'_W \widetilde{A}_R + (1 + ic_1)\partial_{\tilde{x}}^2 \widetilde{A}_R \\ &\quad -(1 - ic_3)|\widetilde{A}_R|^2 \widetilde{A}_R - h_{RL}(1 - ic_2)|\widetilde{A}_L|^2 \widetilde{A}_R, \quad (4.78)\end{aligned}}$$

where the new coefficients are:

$$c_2 \overset{\text{def}}{=} -\frac{g''_{RL}}{g'_{RL}} \quad , \quad c_3 \overset{\text{def}}{=} -\frac{g''_{WW}}{g'_{WW}} \quad \text{and} \quad h_{RL} \overset{\text{def}}{=} \frac{g'_{RL}}{g'_{WW}}. \tag{4.79}$$

---

[8] It is important to keep on mind the difference between this two quantities in the remaining of this thesis.

Note that, in contrast to Eq. (4.73) for the Turing instability, the rescaled amplitude equations (4.77,4.78) still depend on many coefficients beside the distance to the instability threshold η'_W. This results in a much richer dynamics. In particular the coefficient h_{RL}, the “intensity” with which right- and left-travelling wave suppress each other, plays a very important rôle. When this coefficient is big, then travelling waves will be selected. On the other hand, for small h_{RL} standing waves are selected. The values of c_1 and c_3 are also important. They can lead to an instability of the waves. In the next chapters we will study these and other properties of Eqs. (4.77,4.78).

- Codimension-2 wave-Turing amplitude equations

Let us finally address the rescaling of the codimension-2 wave-Turing amplitude equations (4.62,4.63,4.64). Clearly, with a change of the unit of space it is not possible to set d_T *and* d'_W simultaneously equal to one. Here we will choose to set d'_W equal to one. To achieve this we will use the rescaling of Eq. (4.74). To simplify the nonlinear coefficients we will use the rescaling of Eq. (4.71) for $A^\star_T$ and Eq. (4.76) for $A^\star_L$ and $A^\star_R$ (and consequently assume that both, Turing and wave, instabilities are supercritical). With this rescaling the amplitude equations (4.62,4.63,4.64) finally become:

$$\boxed{\begin{aligned}
\partial_t \widetilde{A}_L - v_g \partial_{\tilde{x}} \widetilde{A}_L &= \eta'_W \widetilde{A}_L + (1 + ic_1)\partial^2_{\tilde{x}} \widetilde{A}_L - (1 - ic_3)|\widetilde{A}_L|^2 \widetilde{A}_L \\
&\quad - h_{RL}(1 - ic_2)|\widetilde{A}_R|^2 \widetilde{A}_L - h_{WT}(1 - ic_4)|\widetilde{A}_T|^2 \widetilde{A}_L, \qquad (4.80) \\
\partial_t \widetilde{A}_R + v_g \partial_{\tilde{x}} \widetilde{A}_R &= \eta'_W \widetilde{A}_R + (1 + ic_1)\partial^2_{\tilde{x}} \widetilde{A}_R - (1 - ic_3)|\widetilde{A}_R|^2 \widetilde{A}_R \\
&\quad - h_{RL}(1 - ic_2)|\widetilde{A}_L|^2 \widetilde{A}_R - h_{WT}(1 - ic_4)|\widetilde{A}_T|^2 \widetilde{A}_R, \qquad (4.81) \\
\partial_t \widetilde{A}_T &= \eta_T \widetilde{A}_T + d_{TW} \partial^2_{\tilde{x}} \widetilde{A}_T - |\widetilde{A}_T|^2 \widetilde{A}_T \\
&\quad - h_{TW}(|\widetilde{A}_L|^2 + |\widetilde{A}_R|^2)\widetilde{A}_T, \qquad (4.82)
\end{aligned}}$$

where v_g and c_1 are defined in Eq. (4.75), c_2, c_3 and h_{RL} in Eq. (4.79) and the new diffusion coefficient ratio is given by:

$$d_{TW} \stackrel{\text{def}}{=} \frac{d_T}{d'_W}.$$

The new nonlinear coefficients are:

$$h_{WT} \stackrel{\text{def}}{=} \frac{g'_{WT}}{g_{TT}} \quad , \quad c_4 \stackrel{\text{def}}{=} -\frac{g''_{WT}}{g_{TT}} \quad \text{and} \quad h_{TW} \stackrel{\text{def}}{=} \frac{g_{TW}}{g'_{WW}}.$$

$$\begin{aligned}
\eta'_W &= \tfrac{1}{2}[(a-a_c) - {k_W^c}^2(\delta-\delta_c)] \\
\eta_T &= 2[(a-a_c) + \tfrac{{k_T^c}^2}{2}(\delta-\delta_c)] \\
v_g &\simeq -1.18914 \\
c_1 &\simeq 0.85356 \\
d_{TW} &\simeq 4.41422 \\
c_3 &= 1 \\
h_{RL} &= 2 \\
h_{WT} &= 0.5 \\
c_2 &= 1 \\
c_4 &= 0.5 \\
h_{TW} &= 8
\end{aligned}$$

Table 4.2: Value of the coefficients at the codimension-2 wave-Turing point given in Table 3.1 for the rescaled amplitude equations (4.80,4.81, 4.82). The nonlinear parameters are $\alpha = 0$ and $\beta = 4/3$.

For convenience, in Table 4.2 the values of the new coefficients are given for the same codimension-2 wave-Turing point than in Table 4.1.

In the next chapter we will study some simple solutions of the amplitude equations derived here Finally, in the second part of this thesis we will concentrate in more complex solutions of the amplitude equations.

Chapter 5

Basic properties of Turing and wave patterns

In the previous chapter we performed a weakly nonlinear analysis of the RDNC model. As a result of this analysis we derived equations describing the behaviour of the amplitudes of patterns arising near the Turing, wave and codimension-2 wave-Turing instabilities. In this chapter we will use the amplitude equations to study some basic properties of Turing and wave patterns. More specifically, we will analyse the simplest solutions of these equations; namely the ones that correspond to patterns with constant amplitude. The outcome of this analysis will be compared with numerical simulations of the RDNC model. This comparison will show that the weakly nonlinear approach provide a good understanding of the complex nonlinear structures in the RDNC model that arise in the neighbourhood of the instability thresholds.

5.1 Introduction

In the previous chapter we saw that near the Turing, wave and codimension-2 wave-Turing instabilities some "effective" equations can be derived. These equations describe the asymptotic behaviour of the patterns emerging from the instabilities. The main aim of this chapter is to study in detail simple solutions of these equations and compare them with numerical simulations of the RDNC model.

Since the amplitude equations (4.36), (4.46,4.47) and (4.62,4.63,4.64) are nonlinear, they can exhibit a plethora of different solutions. Many of them are complex, but, as we will see latter in this chapter, these equations also allow particularly simple solutions. In these solutions the real and imaginary parts of the amplitudes $A_T^\star(x,t)$, $A_R^\star(x,t)$ and/or $A_L^\star(x,t)$ have the form of *plane waves* and the modulus of their amplitudes is *constant in space and time*[1]. These *constant amplitude solutions* are of special importance because they usually play the rôle of "building blocks" for more complicated solutions. More specifically, as we will see in the next chapter, different constant amplitude solutions, located in different places of the system, can exist simultaneously if the system is big enough. We will see that the dynamics of the spatial regions separating different constant amplitude patterns, the so called interfaces, play a very important rôle in the formation of complex patterns. These interfaces will be analysed in great detail in the second part of this Thesis.

- Organisation of this chapter

This chapter is divided in three sections. In the first section, we will shortly analyse the case of the Turing amplitude equation. In the second section, the amplitude equation for the wave instability will be studied. We will show that they can be used to predict if travelling or standing waves will appear in the RDNC model. Finally, in the last section, we will consider the coupled amplitude equations arising near the codimension-2 wave-Turing instability.

5.2 Turing instability

Let us first analyse briefly the amplitude equation (4.36) (and their rescaled form of Eq. (4.73)) derived in the previous chapter. In Section 4.4.1.A we analysed the coefficients of this equation as the parameters of the model vary. Here we will briefly report its constant amplitude solutions.

It is easy to check that Eq. (4.73) allows the following constant amplitude solution[2]:

$$\bullet \quad \widetilde{A}_T(x,t) = \rho_T e^{i(p_T x)} \tag{5.1}$$

where the constant amplitude is: $\rho_T^2(p_T) = \eta_T - p_T^2$. Note that this solution is not unique; there exist a *family* of constant amplitude solutions. This family

---

[1] Note that the *plane wave* mentioned here are solutions of the *amplitude equations* and should not be confused with the *wave patterns* arising in the RDNC model near the wave or the codimension-2 wave-Turing instabilities.

[2] In order to simplify the notation of the *rescaled amplitude equations* (4.73), (4.77,4.78) and (4.80,4.81,4.82), in this and following chapters, we will not use the tildes in the spatial variables. Consequently, before doing any comparison between their solutions and patterns in the RDNC model, we should first introduce back the diffusion coefficients in the amplitude equations (*cf.* Section 4.4.2).

is parametrised by p_T and corresponds to a spatially periodic pattern in the RDNC model with wavenumber:

$$k_T = k_T^c + \frac{p_T}{\sqrt{d_T}}.$$

In Section 5.4.2 we will compare these solutions with stationary-periodic patterns in numerical simulations of the RDNC model near the Turing instability.

5.3 Wave instability

Let us now address the analysis of amplitude equations (4.77,4.78), valid near the wave instability.

In Section 4.3.2.A we introduced the ansatz of Eq. (4.29) to describe the patterns arising after the wave instability. This ansatz corresponds to a *linear superposition* of two counterpropagating waves. The nonlinearities of the RDNC model will cause these two waves to interact. This interaction gives rise to the main question concerning wave instabilities: do these counterpropagating waves suppress or enhance each other? In the first case travelling waves will be observed in the model whereas in the second standing waves will appear [1]. Since the amplitude equations (4.77,4.78) describe the nonlinear interaction between the amplitudes of two counterpropagating waves, they can be analysed to answer this question.

5.3.1 Constant amplitude solutions: travelling versus standing waves

It is easy to check that the amplitude equations (4.77,4.78) admit *three* different types of constant amplitude solutions; namely:

- $\widetilde{A}_R = \rho_R e^{i(\omega_R t + p_R x)}$ and $\widetilde{A}_L = 0$ (5.2)
- $\widetilde{A}_R = 0$ and $\widetilde{A}_L = \rho_L e^{i(\omega_L t + p_L x)}$ (5.3)
- $\widetilde{A}_R = \rho_{SW} e^{i(\omega_{SW} t + p_{SW} x)}$ and $\widetilde{A}_L = \rho_{SW} e^{i(\omega_{SW} t - p_{SW} x)}$ (5.4)

where the frequencies and amplitudes are given by:

$$\omega_R(p_R) = -v_g p_R - c_1 p_R^2 + c_3 \rho_R^2, \tag{5.5}$$

$$\rho_R^2(p_R) = \eta'_W - p_R^2. \tag{5.6}$$

Similar equations hold for $\omega_L(p_L)$ and $\rho_L^2(p_L)$ (substituting $-v_g$, p_R and ρ_R by $+v_g$, p_L and ρ_L respectively); and finally:

$$\begin{aligned}\omega_{SW}(p_{SW}) &= -v_g p_{SW} - c_1 p_{SW}^2 + (c_3 + h_{RL}c_2)\rho_{SW}^2,\\ \rho_{SW}^2(p_{SW}) &= (\eta'_W - p_{SW}^2)/(1 + h_{RL}).\end{aligned}$$

Eqs. (5.2), (5.3) and (5.4) correspond to three different *one parameter families* of plane wave solutions. These families are parametrised by the wavenumbers p_R, p_L and p_{SW} respectively.

The solutions of Eq. (5.2) and (5.3) correspond respectively to *right-* and *left-travelling waves* in the RDNC model. These travelling waves have wavenumbers:

$$k_R = k_W^c + \frac{p_R}{\sqrt{d'_W}} \quad \text{and} \quad k_L = -k_W^c + \frac{p_L}{\sqrt{d'_W}}, \tag{5.7}$$

and frequencies:

$$\Omega_R = \omega_c + \omega_R \quad \text{and} \quad \Omega_L = \omega_c + \omega_L. \tag{5.8}$$

The solution of Eq. (5.4) correspond to *standing waves* in the RDNC model with wavenumbers $k_{SW} = k_W^c + p_{SW}/\sqrt{d'_W}$ and frequencies $\Omega_{SW} = \omega_c + \omega_{SW}$.

- Stability of constant amplitude solutions: dependence on h_{RL}

Let us now study the stability of the constant amplitude solutions corresponding to travelling and standing waves. In the following we will assume that the wavenumber of these solutions is the critical one, *i.e.* $p_R \equiv p_L \equiv p_{SW} \equiv 0$.

Inserting the ansatz $\widetilde{A}_R = \rho_R + \xi_R(t)$ and $\widetilde{A}_L = \xi_L(t)$ (where $\xi_R(t)$ and $\xi_L(t)$ are small perturbations) in Eqs. (4.77,4.78) and linearising, we get a set of linear ODEs. An easy calculation shows that the solution (5.2) is stable if $h_{RL} > 1$. The same result is obtained for the left-travelling wave solution (5.3).

To analyse the stability of the standing waves defined in Eq. (5.4), we insert the ansatz $\widetilde{A}_R = \rho_{SW} + \xi_R(t)$ and $\widetilde{A}_L = \rho_{SW} + \xi_L(t)$ in Eqs. (4.77,4.78). This solution is stable if $1 > h_{RL} > -1$. Consequently travelling waves are stable and standing waves unstable when $h_{RL} > 1$. The reverse is true when $1 > h_{RL} > -1$. Finally, if $-1 > h_{RL}$, then both solutions are unstable.

Let us analyse the stability of travelling and standing waves as the nonlinear parameters α and β of the RDNC model vary. As was discussed in Section 4.4.1, we can fix the value of the cubic nonlinearity β and vary the absolute value of the quadratic coefficient $|\alpha|$. In the remainder of this thesis

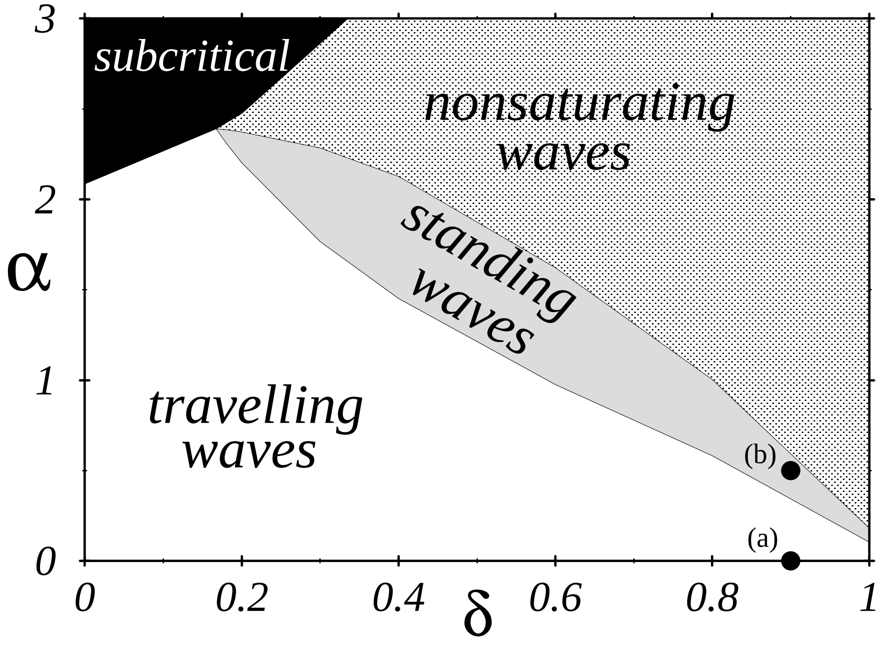

Figure 5.1: Regions in the parameter space δ vs. α (*i.e.* ratio of diffusion vs. quadratic nonlinearity) where travelling waves or standing waves are stable (calculated from the amplitude equations (4.77,4.78) coefficients). The linear parameters of the model are fixed to the values given in Eq. (3.35), the cubic nonlinearity kept fixed to $\beta = 4/3$. Note that the value of the control parameter a (so far $a \geq a_W^c$) does *not change* the predictions of the amplitude equations. For stable travelling waves: $h_{RL} > 1$, standing waves: $1 > h_{RL} > -1$, nonsaturating waves: $-1 > h_{RL}$ and subcritical wave instability: $g_{WW} < 0$. The full dots (a) and (b) correspond to the parameter values of the plots of numerical integrations of the RDNC model shown in Figs. 5.2(a) and 5.2(b) respectively.

we choose $\beta = 4/3$. In Fig. 5.1 we show the selected patterns for different values of the diffusion ration δ as the quadratic nonlinearity α increases. Note that, if α is too big, then the wave instability is subcritical (*i.e.* $g_{WW} < 0$; see discussion in Section 4.4.1.B and Fig. 4.3).

As we saw in Section 4.4.1.B, for $\alpha = 0$ h_{RL} is independent of the value of δ and, since $h_{RL} = 2$, travelling waves are always selected. Note that the region where standing waves are stable is rather small. Examples of numerical simulations showing travelling waves and standing waves are presented in Figs. 5.2(a) and 5.2(b) respectively (the parameters of these simulations correspond to the full dots in Fig. 5.1).

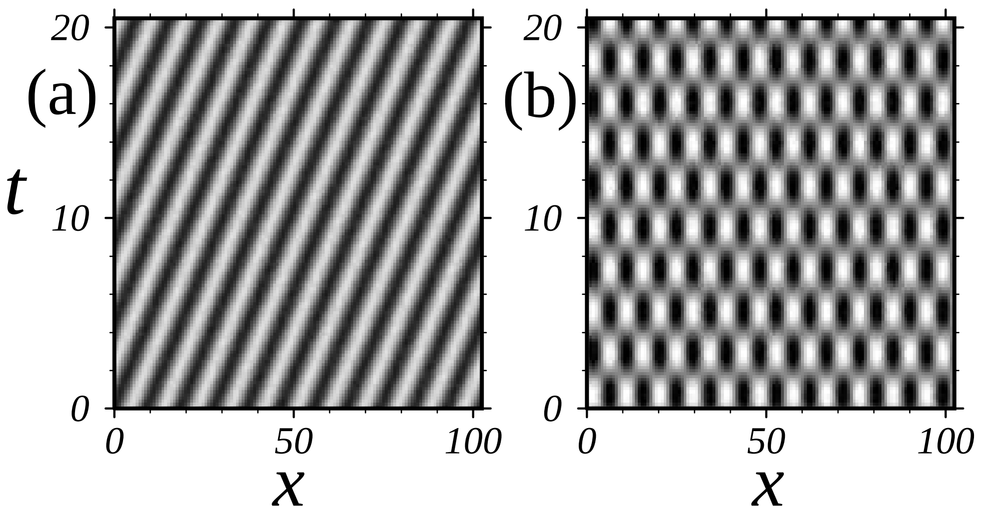

Figure 5.2: Two examples of numerical simulations of the RDNC model showing (right) travelling (in (a)) and standing waves (in (b)). In both simulations random initial conditions were used and only a short interval of the total integration time is shown (the transient until the constant amplitude condition is reached can be very large). The parameters of the RDNC model in (a) and (b) are $\delta = 0.9$, $a = 4.607$, $\beta = 4/3$, and all the other parameters have values as in Eq. (3.35). The quadratic nonlinearity parameter is in (a) $\alpha = 0$ and in (b) $\alpha = 0.5$. In Fig. 5.1 the location in the parameter space δ vs. α of these simulations is shown with full dots.

5.3.2 Comparison with numerical simulations of the RDNC model

In order to gain insight on the range of applicability of the predictions done with of Eqs. (4.77,4.78), let us do a detailed comparison between the constant amplitude solutions of Eqs. (5.2), (5.3) and (5.4) and numerical simulations of the RDNC model. In the following, whenever travelling waves are considered, we will assume that they travel to the right[3]. In this subsection we will further consider only waves with wavenumbers equal to the critical one (*i.e.* $k_R = k_{SW} = k_W^c$ or equivalently $p_R = p_{SW} = 0$).

- Particular case $\alpha = 0$: Only travelling waves

As we said before, for $\alpha = 0$ travelling waves are always selected. In Fig. 5.3 we show, for two different values of δ, a comparison between the predicted and measured values of the amplitude of travelling waves with wavenumber

---

[3] The results should be the same for left-travelling waves, since the RDNC model is symmetric respect to the permutation $x \to -x$.

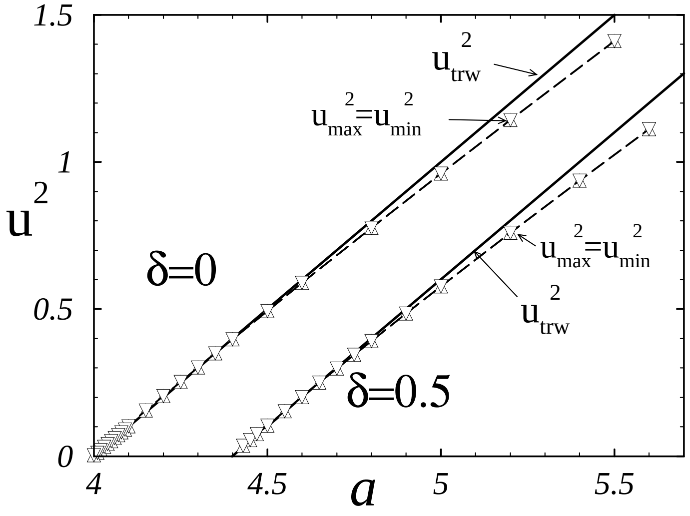

Figure 5.3: Comparison between the maximal value u_{trw} predicted by amplitude equations (4.47,4.46) (full lines) and the measured values of the maxima $|u_{max}|$ and minima $|u_{min}|$ of travelling waves (up and down triangles respectively) observed in numerical simulations of the RDNC model for two different values of δ ($\delta = 0$ and $\delta = 0.5$) and with $\alpha = 0$. The amplitudes are plotted as the parameter a vary. Note that $|u_{max}| = |u_{min}|$. We consider only travelling waves with wavenumbers equal to the critical one (*i.e.* $k_W = k_W^c$). The critical wavenumbers are $k_W^c = 1$ for $\delta = 0$ and $k_W^c \simeq 0.796$ for $\delta = 0.5$. The cubic nonlinearity is $\beta = 4/3$ and the other parameters of the model have values as in Eq. (3.35).

k_W^c. Note that there is a direct relationship between the amplitude of the wave and the maximal and minimal values of the profiles of u and v in the RDNC model. Indeed, using Eq. (5.6) and the ansatz of Eq. (4.29), we can calculate the maximal value u_{trw} of the predicted u-profile predicted by the amplitude equations. This predicted amplitude is proportional to the square root of distance to onset.

In Fig. 5.3 the predicted u_{trw} is compared with the measured maximal (up triangles) and minimal (down triangles) values of the field u of the RDNC model as the parameter a vary (in Fig. 5.5(a) we show the u-profile of a typical example of a right-travelling wave in the RDNC model). Note that near the criticality the amplitude of the wave patterns in the RDNC model is well described by the amplitude equations. Far away from the threshold, however, the amplitude of the patterns observed in the numerical simulations is systematically smaller than the predicted one.

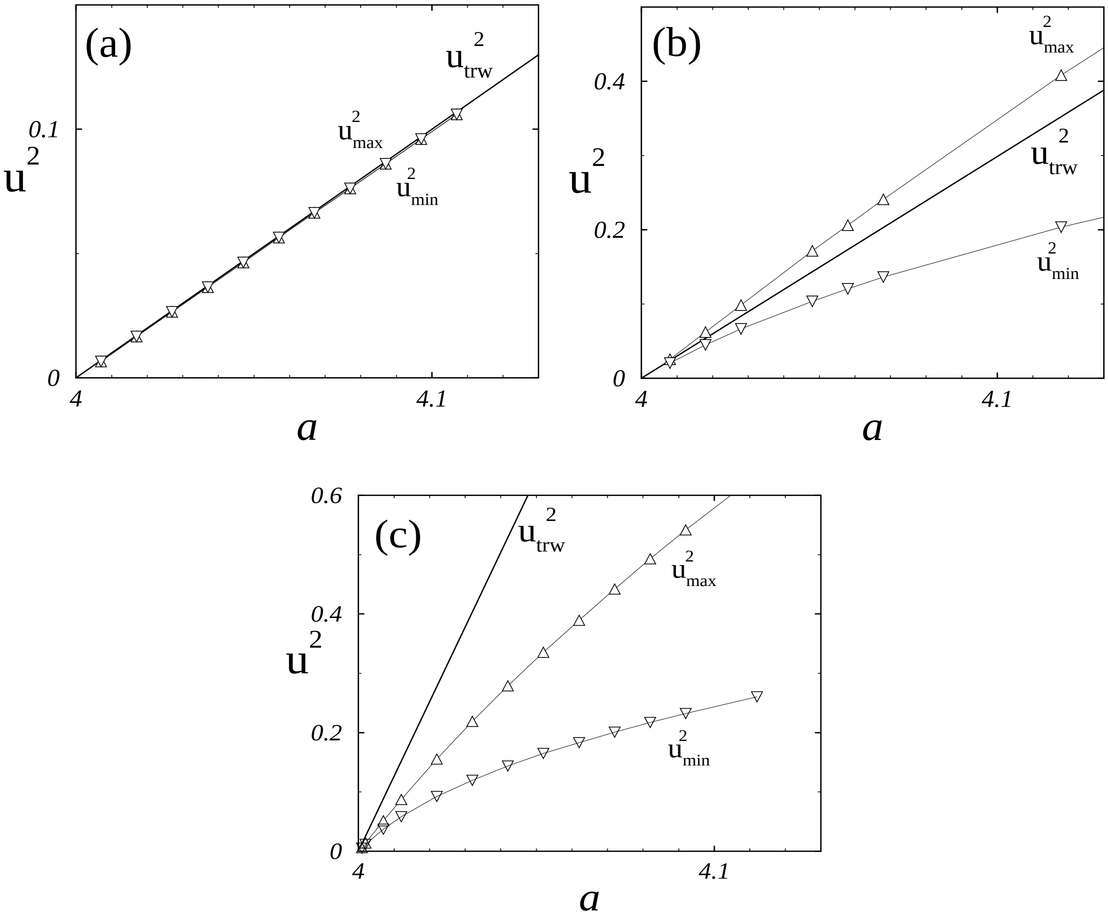

Figure 5.4: Comparison between predicted and measured values of the amplitudes of travelling waves for three different values of the quadratic nonlinearity α and for diffusion ratio $\delta = 0$. See the caption of Fig. 5.3 for a description of the simbols. In (a) $\alpha = 0$, in (b) $\alpha = 1.7$ and in (c) $\alpha = 2$ (recall that the instability turns to subcritical for $\alpha = 2.0844$). The cubic nonlinearity is $\beta = 4/3$ and the other parameters of the model have values in Eq. (3.35). See Fig. 5.5 for two examples of travelling wave profiles in numerical simulations of the RDNC model corresponding to $\alpha = 0$ and $\alpha = 1.7$ (cases shown in (a) and (b) respectively).

- Effect of $\alpha \neq 0$ on travelling waves: Asymmetric waves

Let us now analyse the case $\alpha \neq 0$ (in the parameter region where the amplitude equations (4.77,4.78) predict stable travelling waves; *cf.* Fig. 5.1).

In Fig. 5.4 we show comparisons between the predicted and measured amplitudes of travelling wave patterns for three different values of the quadratic nonlinearity and with $\delta = 0$. We can readily recognise two effects of the quadratic nonlinearity on the travelling wave patterns. The first is that the

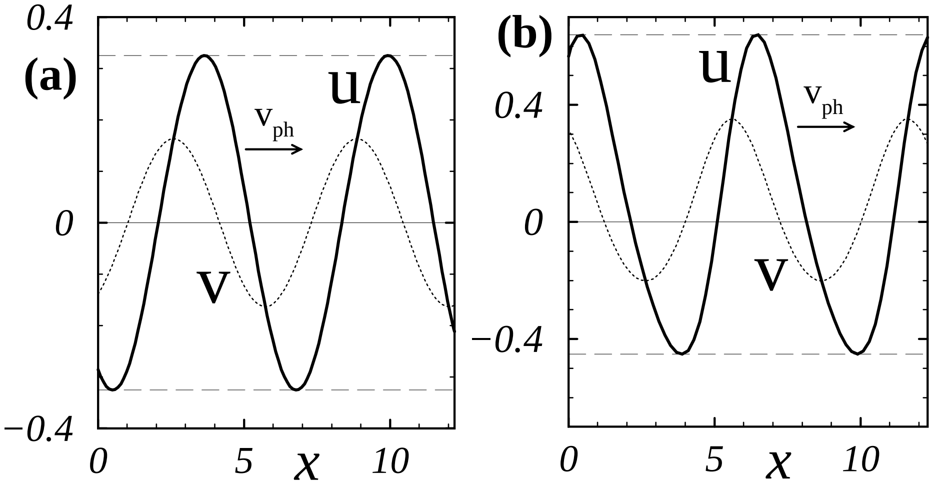

Figure 5.5: Two examples of the $u-$ and $v-$profiles in numerical simulations of the RDNC model, corresponding to travelling waves for $\alpha = 0$ and $\alpha = 1.7$ in (a) and (b) respectively. The thin dashed lines show the location of u_{max} and u_{min}. In both cases $\delta = 0$, $a = 4.10$ and $\beta = 4/2$. The other parameters of the RDNC model have values as given in Eq. (3.35). Note that the profiles of u and v are symmetric in (a) and asymmetric in (b). Consequently $u^2_{max} = u^2_{min}$ in (a) but $u^2_{max} \neq u^2_{min}$ in (b) (*cf.* Fig. 5.4(a) and 5.4(b)).

range of validity of the predictions of the amplitude equations gets very small as α increases from zero. The second is that the absolute value of the minimum and maximum of the u-profile of the travelling wave pattern in the RDNC model become very different as a increases

In Fig. 5.5(a) and (b) the profiles of numerical simulations of the RDNC model are shown for $\alpha = 0$ and $\alpha = 1.7$ respectively. This second effect mentioned previously is easy to understand if we recall that the RDNC model is symmetric respect of $u \to -u$ and $v \to -v$ only if $\alpha = 0$. For a nonzero α this this symmetry is not present any more. In the other hand the ansatz of Eq. (4.29) assumes that this symmetry is always present. Consequently it is natural that this feature is not captured by the amplitude equations description.

The case shown in Fig. 5.4(c), with $\alpha = 2$, is very near the transition to a subcritical wave instability (this happens in this case for $\alpha = 2.0844$; *cf.* Fig. 5.1) and consequently the amplitude equation predictions are valid only in a tiny region near the instability threshold.

- Effect of $\alpha \neq 0$ on standing waves: short range of applicability

Let us now analyse the case of stable standing waves. More specifically, let us consider the parameters corresponding to the full dot (b) in Fig. 5.1. In Fig. 5.2(b) we showed an example of a standing wave in numerical simulation of the RDNC model for these parameter values. In this case the distance to the threshold of the instability was very small. Here we will analyse the dependence of this standing wave pattern as this distance varies.

In Fig. 5.6(a) we compare the measured value amplitude of the waves with the values predicted by the amplitude equations, in the case where these equations predict stability of standing waves. Note that the standing waves are stable in the RDNC model only very near the onset of the instability. Far from there travelling waves become stable. This transition between standing waves and travelling waves is not predicted by the amplitude equations (4.77,4.78) because the stability of the constant amplitude solutions does not depend of the value of η'_W (and consequently $a - a^c_W$). It depends *only* on the coefficient h_{RL}!

Also note that the standing waves are very asymmetric whereas the travelling waves are almost symmetric (*cf.* Figs. 5.6(b) and 5.6(c) respectively). Consequently, it is natural to expect that the range of validity of the predictions done with the amplitude equations is very small for standing waves. This is probably the cause of the standing- to travelling-wave transition seen in the RDNC model.

5.3.3 Sideband Instabilities of Travelling Waves

In the previous subsections we saw that the region in the parameter space where travelling waves are stable is very big. In this subsection we will analyse in detail the effect of the spatial partial derivatives of the amplitude equations (4.77,4.78) when travelling waves with constant amplitude are considered. The travelling waves can travel either to the right or to the left. Here we will assume that the system is initially prepared with a wave travelling *only in one direction*. Under such circumstances Eqs. (4.77,4.78) reduce to the following single CGLE[4]:

$$\partial_t \widetilde{A}_W + s\, v_g \partial_x \widetilde{A}_W = \eta'_W \widetilde{A}_W + (1 + ic_1)\partial_x^2 \widetilde{A}_W - (1 - ic_3)|\widetilde{A}_W|^2 \widetilde{A}_W, \quad (5.9)$$

where, depending if the wave travels to the right or left, the subindex W should be substituted by R or L and s by $s = +1$ or $s = -1$ respectively.

The stability of the constant amplitude solutions of the CGLE has been studied previously by many authors (see *e.g.* [10, 82, 83, 84]). Consequently,

---

[4] Typically CGLE refers to an equation as (5.9) *without* group velocity term.

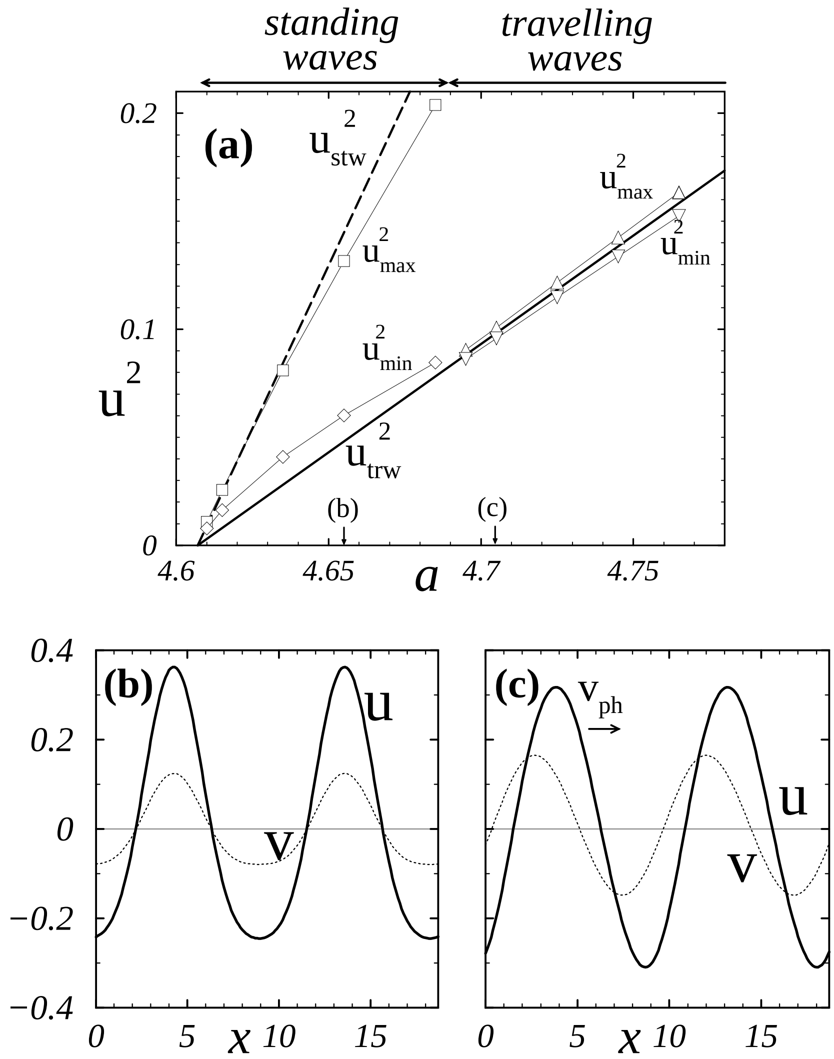

Figure 5.6: In (a) we show a comparison between the amplitude of the observed pattern (squares and diamonds for standing waves and up and down triangles for travelling waves) and the predicted amplitude for standing waves (dashed line) and travelling waves (full line), with wavenumber k_W^c, as the control parameter a vary. The parameters of the model correspond to the full dot (b) in Fig. 5.1 (*i.e.* $\delta = 0.9$, $\alpha = 0.5$, $\beta = 4/3$ and other parameters with values as given in Eq. (3.35)). For these parameter values, the amplitude equations (4.77,4.78) predict that standing waves are stable over travelling waves. This is feature is found in simulations of the RDNC model only if the distance to the onset is small. Indeed, as this distance gets bigger, a transition to stable travelling waves occurs. In (b) and (c) we show examples of the profiles of u and v in numerical simulations of the RDNC model with $a = 4.655$ and $a = 4.705$ respectively. The first case corresponds to a very asymmetric standing wave pattern and the second to almost symmetric travelling wave.

here we will only give a short overview of the main results. From Eqs. (5.2) or (5.3) we deduce that $p_W^2 \leq \eta'_W$. Hence, for a given η'_W, only travelling waves with wavenumbers inside the interval of wavenumbers delimited by $k_W^c \pm p_R^{max}$ (where: $p_W^{max} \overset{\text{def}}{=} \sqrt{\eta'_W}$) can exist (in the following this interval will be called *band of wavenumbers*). Near the sides of this band the constant amplitude solutions of the CGLE may be unstable against spatiotemporal perturbations. This will depend on the values of the coefficients c_1 and c_3 of Eq. (5.9). A straightforward but lengthly stability analysis shows that all the waves with wavenumbers:

$$\eta'_W \geq p_R^2 > \frac{\eta'_W(1 - c_1 c_3)}{2c_3^2 - c_1 c_3 + 3}, \tag{5.10}$$

are unstable. This instability is called *sideband (or Eckhaus) instability* [1, 10].

Note that the condition:

$$1 - c_1 c_3 < 0, \tag{5.11}$$

indicates that all the constant amplitude solution of Eq. (5.9) are unstable. This instability is typically referred as *Benjamin-Feir instability* and Eq. (5.11) as *Benjamin-Feir Condition* [1, 10].

- Benjamin-Feir instability in the RDNC model

In the case of the RDNC model, the value of the coefficient c_1 does not depend on the nonlinear parameters α and β (*cf.* Eq. (4.43)). In Fig. 5.7(a) we plot the coefficeints c_1 and c_3 as a function of the diffusion ratio δ (for the values of the other parameters of the model see Eq. (3.35)). In Fig. 5.7(b) the value of $1 - c_1 c_3$ is plotted for different values of the quadratic nonlinearity α. Note that the Benjamin-Feir condition of Eq. (5.11) is only satisfied in a small interval of δ and for values of α big.

Let us examine the Benjamin-Feir instability in the RDNC model. In particular, if we take $\alpha = 2$ and $\delta = 0$, then the amplitude equation (5.9) predicts that the travelling waves are Benjamin-Feir unstable. As we can see in Fig. 5.8, this prediction only applies to the close vicinity of the instability threshold. At a finite distance from this threshold travelling waves with wavenumber k_W^c are stable in the RDNC model. In the situation presented in Fig. 5.8 this distance is very small. A possible reason for this characteristic is that, as we saw previously, a big value of α considerably reduces the range of applicability of the amplitude equations (the big difference between u_{max}^2, u_{min}^2 and u_{trw}^2 in Fig. 5.8 also points into this direction).

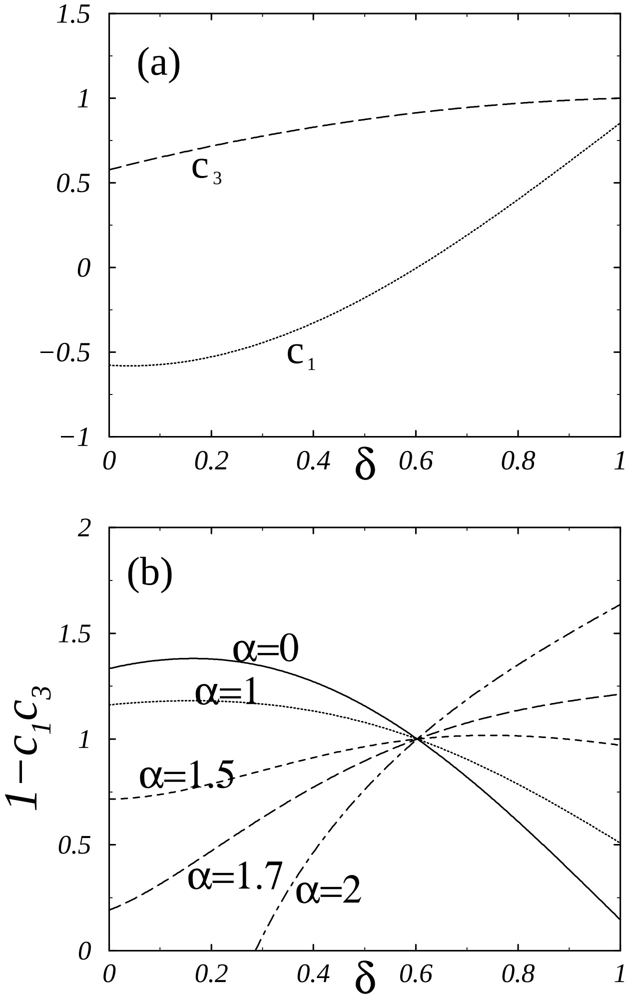

Figure 5.7: Plot of the amplitude equation coefficients c_1 and c_3, in (a), and the Benjamin-Feir condition $1-c_1c_3$, in (b), as the control parameter δ is varied. In (a) the coefficients c_1 and c_3 are plotted for $\alpha = 0$. In (b) the Benjamin-Feir condition $1 - c_1c_3$ is plotted for different values of the quadratic nonlinearity α. Note that the travelling waves are typically stable against sideband instabilities in the hole range: $0 \leq \delta \leq 1$. For $\alpha = 2$, however, there exist an interval $0 \leq \delta \lesssim 0.2861$ where the travelling waves are Benjamin-Feir unstable (because the Benjamin-Feir condition $1-c_1c_3$ is negative). In Fig. 5.8 for a numerical study of travelling waves in the RDNC model in this last case is presented (*i.e.* with $\alpha = 2$ and $\delta = 0$).

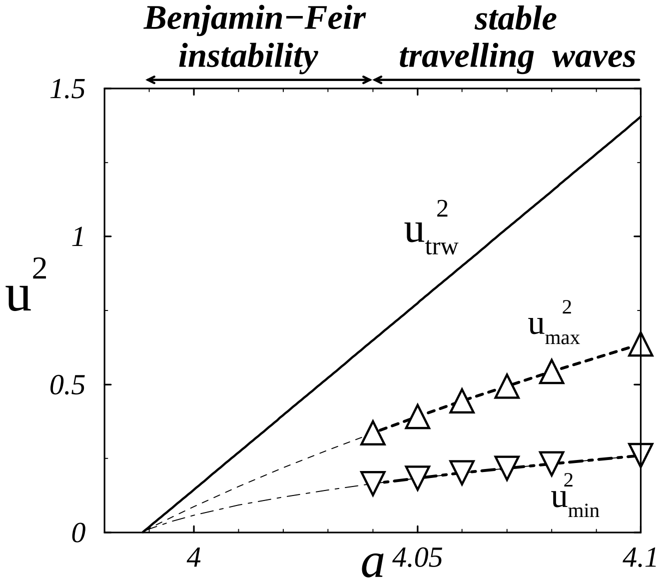

Figure 5.8: Comparison between the amplitude of travelling waves in the amplitude equations and in the RDNC model for $\alpha = 2$ and $\delta = 0$. For these values, the amplitude equations predict that the travelling waves are Benjamin-Feir unstable (*cf.* Fig. 5.7). The other parameters of the model have values as in Eq. (3.35). The full line corresponds to the predicted amplitude of (unstable) travelling wave patterns. The big triangles show the measured maximal and minimal amplitude of the *stable* travelling wave found in the RDNC model (with wavenumber k^c_W) of big length. Note that near the instability threshold travelling waves are not stable. However, if we select a small system length equal to $2\pi/k^c_W$, then a "travelling wave" there is stable! The maximal and minimal amplitude of this pattern is show with a dashed and dot-dashed lines respectively. As expected, the values of the amplitudes measured in a big system (the triangles) coincide with these values, but only far from the onset.

5.4 Codimension-2 wave-Turing instability

In this section we will analyse the codimension-2 wave-Turing instability. This section is divided in two parts. In the first part we will introduce the constant amplitude solutions of the amplitude equations (4.80,4.81,4.82) and in the second we will compare these solutions with numerical simulations of the RDNC model.

5.4.1 Constant amplitude solutions

The amplitude equations (4.81,4.80,4.82) can have many different constant amplitude solutions. These solutions correspond travelling waves, Turing patterns, standing waves, or combinations (superpositions) of them. The coupling parameters h_{RL}, h_{WT} and h_{TW} will determine the stability of each solution.

The solutions presented in Eqs. (5.2), (5.3) and (5.4) supplemented by $\widetilde{A}_T = 0$ correspond to constant amplitude solutions of the amplitude equations (4.80,4.81,4.82). These solutions correspond to right-, left-travelling waves and standing waves respectively. Additionally, a Turing pattern solution is given by:

- $\widetilde{A}_T(x,t) = \rho_T e^{i(p_T x)} \quad , \quad \widetilde{A}_R = 0 \quad \text{and} \quad \widetilde{A}_L = 0 \qquad (5.12)$

with amplitude $\rho_T^2(p_T) = \eta_T - d_{_{TW}} p_T^2$. In the following we will refer to these solutions as *single-TW*, *single-SW* and *single-Tur* respectively.

Let us now present the constant amplitude solutions arising from combinations of the previous solutions. The *mixed travelling wave-Turing pattern solution* (*Mixed-TW-Tur* in the following) is the combination of a right- or left-travelling wave and a Turing pattern. In the first case the is Mixed-TW-Tur given by:

- $\widetilde{A}_R = \rho_R e^{i(\omega_R t + p_R x)} \quad , \quad \widetilde{A}_L = 0 \quad \text{and} \quad \widetilde{A}_T = \rho_T e^{i(p_T x)}. \qquad (5.13)$

where frequence and amplitudes are:

$$\begin{aligned}
\omega_R(p_R) &= -v_g p_R - c_1 p_R^2 + c_3 \rho_R^2 + h_{WT} c_4 \rho_T^2, \\
\rho_R^2(p_R) &= \frac{(\eta'_W - h_{WT}\eta_T) - (p_R^2 - h_{WT} d_{_{TW}} p_T^2)}{1 - h_{WT} h_{TW}}, \\
\rho_T^2(p_T) &= \frac{(\eta_T - h_{TW}\eta'_W) - (d_{_{TW}} p_T^2 - h_{TW} p_R^2)}{1 - h_{WT} h_{TW}}.
\end{aligned}$$

Similar equations correspond to the combination of a left-travelling wave and a Turing pattern.

Finally the *mixed standing wave-Turing pattern solution* (*Mixed-SW-Tur*) is given by:

- $\widetilde{A}_R = \rho_{SW} e^{i(\omega_{SW} t + p_{SW} x)}$, $\widetilde{A}_L = \rho_{SW} e^{i(\omega_{SW} t - p_{SW} x)}$ and $\widetilde{A}_T = \rho_T e^{i(p_T x)}$,

where:

$$\omega_{SW}(p_{SW}) = -v_g p_{SW} - c_1 p_{SW}^2 + (c_3 + h_{RL} c_2)\rho_{SW}^2 + h_{WT} c_4 \rho_T^2,$$

Name	$\lvert\widetilde{A}_R\rvert$	$\lvert\widetilde{A}_L\rvert$	$\lvert\widetilde{A}_T\rvert$
Single-Tur	$=0$	$=0$	$\neq 0$
Single-TW	$\neq 0$ $=0$	$=0$ $\neq 0$	$=0$ $=0$
Single-SW	$\neq 0$	$\neq 0$	$=0$
Mixed-TW-Tur	$\neq 0$ $=0$	$=0$ $\neq 0$	$\neq 0$ $\neq 0$
Mixed-SW-Tur	$\neq 0$	$\neq 0$	$\neq 0$

Table 5.1: Properties of the different constant amplitude solutions of the amplitude equations (4.80,4.81,4.82).

$$\rho^2_{SW}(p_{SW}) = \frac{(\eta'_W - h_{WT}\eta_T) - (p^2_{SW} - h_{WT} d_{TW} p^2_T)}{1 + h_{RL} - 2h_{WT}h_{TW}},$$

$$\rho^2_T(p_T) = \frac{((1 + h_{RL})\eta_T - 2h_{TW}\eta'_W) - ((1 + h_{RL}) d_{TW} p^2_T - 2h_{TW} p^2_R)}{1 + h_{RL} - 2h_{WT}h_{TW}}.$$

In Table 5.1 we summarise the properties of the possible constant amplitude solutions of Eqs. (4.80,4.81,4.82).

- Existence and stability of the constant amplitude solutions: dependence on h_{RL}, h_{WT} and h_{TW}

Let us now analyse the existence and stability of the constant amplitude solutions previously introduced. In the following we will only consider solutions with critical wavenumbers (*i.e.* $p_R = p_L = p_{SW} = p_T \equiv 0$).

The Single-Tur solution exists if $\eta_T > 0$. An straightforward stability analysis shows that this solution is stable if $\eta'_W < h_{WT}\eta_T$. The Single-TW and Single-SW solutions exist if $\eta'_W > 0$. Depending on the value of h_{RL}, either one or the other is stable. If $h_{RL} > 1$, then the Single-TW solution is stable for $\eta'_W > \frac{\eta_T}{h_{TW}}$. On the other hand, for $1 > h_{RL} > -1$ the Single-SW solution is stable if $\eta'_W > \frac{1+h_{RL}}{2h_{TW}}\eta_T$. The existence and stability conditions of the mixed solutions Mixed-TW-Tur and Mixed-SW-Tur are more complicated. All these conditions are summarised in Table 5.2.

Note that, beside the value of h_{RL}, the value of two other quantities play an important rôle in the determination of the existence and stability of the constant amplitude solutions of Eqs (4.80,4.81,4.82). These quantities are the signs of $1 - h_{WT}h_{TW}$ and $1 + h_{RL} - 2h_{WT}h_{TW}$. All these conditions allow us to distinguish *four* different cases. In Fig. 5.9 we show schematic drawings for each case. Note that there is always a region of the control parameter

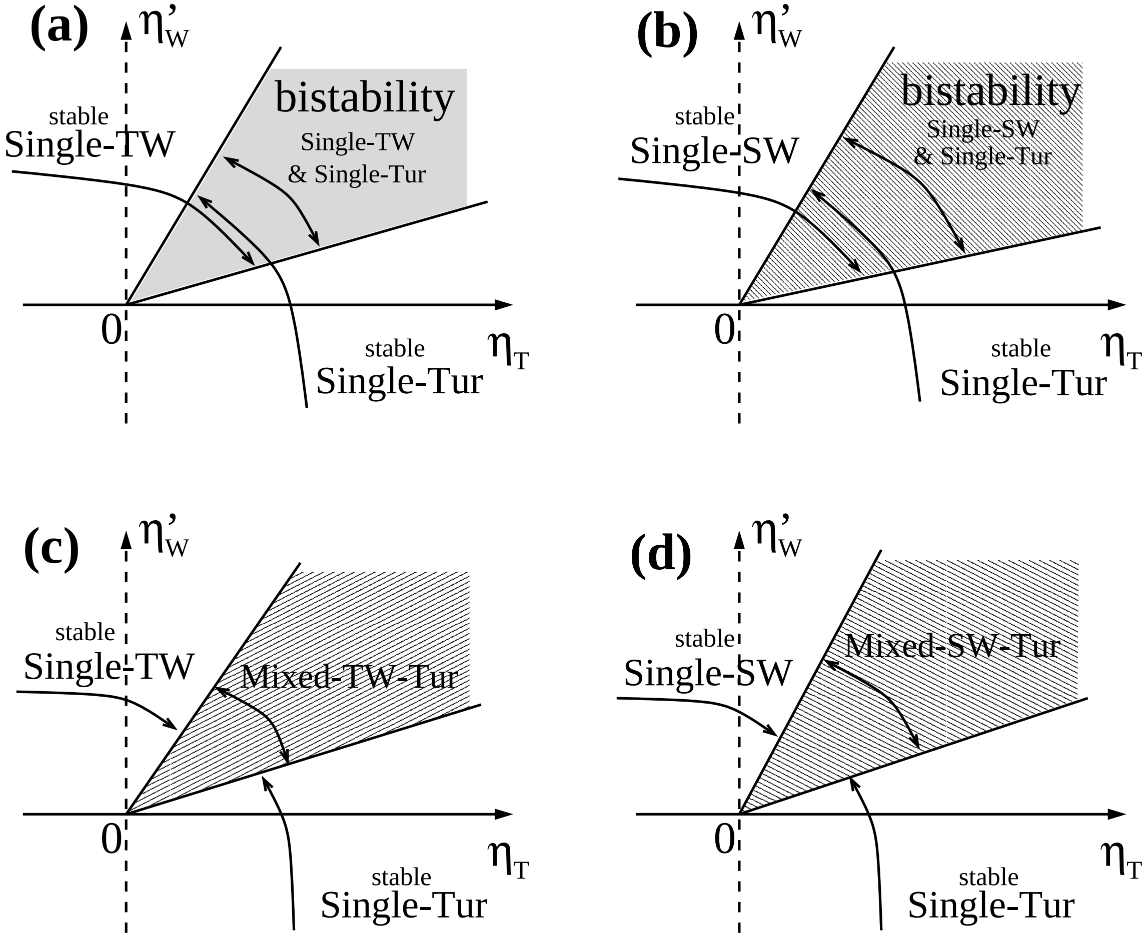

Figure 5.9: Schematic drawings of the regions of the control parameter space η'_W vs. η_T, where each constant amplitude solution is stable. Four different scenarios are shown in (a)-(d). In (a) and (c) $h_{RL} > 1$ whereas in (b) and (c)$1 > h_{RL} > -1$. The diagram (a) corresponds to a situation where $1 - h_{WT}h_{TW} < 0$ whereas in (c) $1 - h_{WT}h_{TW} > 0$. In (b) $1 + h_{RL} - 2h_{WT}h_{TW} < 0$ and, on the contrary, in (d) $1 + h_{RL} - 2h_{WT}h_{TW} > 0$. Note that in situations (a) and (b) there exist a slice of the control parameter space both Turing and wave patterns are stable. On the other hand, in (c) and (d) a solution mixing Turing and wave patterns exists in this central region of the control parameter space.

Name	Existence Conditions	Stability Conditions
Single-Tur	$\eta_T > 0$	$\eta'_W < h_{WT}\eta_T$
Single-TW	$\eta'_W > 0$	$h_{RL} > 1$ and $\eta'_W > \frac{\eta_T}{h_{TW}}$
Single-SW	$\eta'_W > 0$	$1 > h_{RL} > -1$ and $\eta'_W > \frac{1+h_{RL}}{2h_{TW}}\eta_T$
Mixed-TW-Tur	$1 - h_{WT}h_{TW} > 0$, $\eta'_W > h_{WT}\eta_T$ and $\eta'_W < \frac{\eta_T}{h_{TW}}$	$\eta'_W > h_{WT}\eta_T$ and $\eta'_W < \frac{\eta_T}{h_{TW}}$
Mixed-SW-Tur	$1 + h_{RL} - 2h_{WT}h_{TW} > 0$, $\eta'_W > h_{WT}\eta_T$ and $\eta'_W < \frac{(1+h_{RL})\eta_T}{2h_{TW}}$	$\eta'_W > h_{WT}\eta_T$ and $\eta'_W < \frac{(1+h_{RL})\eta_T}{2h_{TW}}$

Table 5.2: Existence and stability conditions for each constant amplitude conditions of the amplitude equations (4.80,4.81,4.82). See Fig. 5.9 for the regions of the control parameter space defined by these conditions.

space η'_W vs. η_T where the single solutions (*i.e.* Single-TW or Single-SW and Single-Tur) are stable (as long as $h_{RL} > -1$!). In cases presented in Figs. 5.9(a) and 5.9(b) these single solutions are stable simultaneously in a central slice of the control parameter space. Consequently, in these regions there are bistability between waves (either travelling or standing) and Turing patterns. On the other hand, in the cases presented in Figs. 5.9(c) and 5.9(d) the central slice corresponds to a region where the mixed solutions (either Mixed-TW-Tur or Mixed-SW-Tur) exist and are stable.

- RDNC model: Bistability between waves and Turing patterns

Let us now analyse the particular case of the codimension-2 point studied in Section 3.5.4. In Table 3.1 we summarised the values of the linear parameter of the RDNC model at this point. As before, we will consider here the cubic parameter β to be fixed (to $\beta = 4/3$) and vary only the quadratic parameter α. In Fig. 5.10 we plot the values of coefficient h_{RL} and the conditions $1-h_{WT}h_{TW}$ and $1+h_{RL}-2h_{WT}h_{TW}$. Note that as α increases from zero, three different regimes appear. In **I**, for zero and small α, the scenario schematised in Fig. 5.9(a) happens; namely a central area of *bistability between travelling waves and turing* patterns exist. For intermediate values of α, in **II**, a the scenario of Fig. 5.9(b) occurs. In this case a central region of *bistability between standing-waves and Turing patterns* exists. Finally, in the regime **III** (for $\alpha > 0.1872$), neither the Single-TW nor the Single-SW solution is stable.

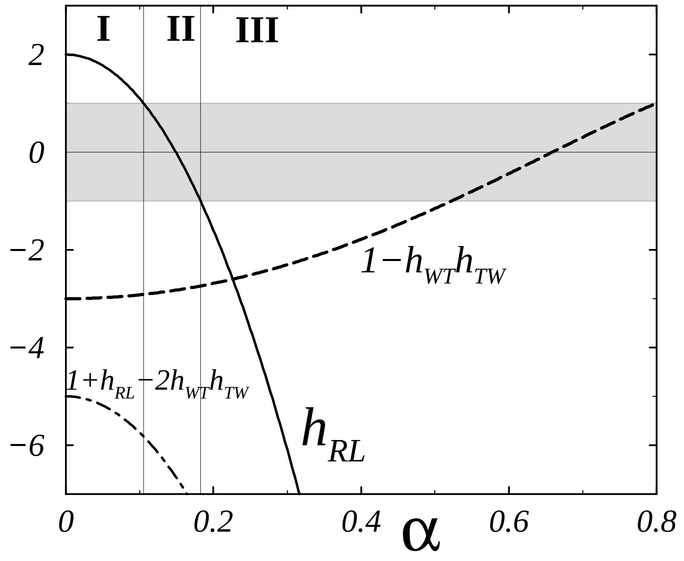

Figure 5.10: Plot of the coefficient h_{RL} (full line) and the quantities $1 - h_{WT}h_{TW}$ (dashed line) and $1 + h_{RL} - 2h_{WT}h_{TW}$ (dot-dashed line) as a function of the quadratic nonlinearity α, in the codimension-2 wave-Turing point given in Table 3.1 (with $\beta = 4/3$; *i.e.* same parameters than in Fig. 5.1). In region **I**, defined by the interval $0 \leq \alpha < 0.1055$, the scenario presented in Fig. 5.9(a) is found. In the region **II**, for $0.1055 < \alpha < 0.1872$, the scenario of Fig. 5.9(b) is predicted. Finally, in region **III**, for $\alpha > 0.1872$, neither the Single-TW nor Single SW solutions are stable. Compare these values of α with the regions shown in Fig. 5.1 for $\delta = 1$.

5.4.2 Comparison with numerical simulations of the RDNC model

Here and in the remaining of this thesis, we will only consider the RDNC model with a pure cubic nonlinearity (*i.e.* $\alpha = 0$). Consequently, a region of *bistability between travelling waves and Turing patterns will exists* near the codimension-2 wave-Turing instability (*i.e.* the case schematised in Fig. 5.9(a)).

To test the theoretical predictions done in the previous subsection we did extensive numerical simulations the RDNC model. We considered travelling waves and Turing patterns with constant amplitudes. Only patterns with critical wavenumbers have been considered (*i.e.* $k_W = k_W^c$ and $k_T = k_T^c$ for wave and Turing patterns respectively). Our main aim here is to test the bistability region predicted by the amplitude equations and compare the amplitude of the predicted and measured constant amplitude solutions.

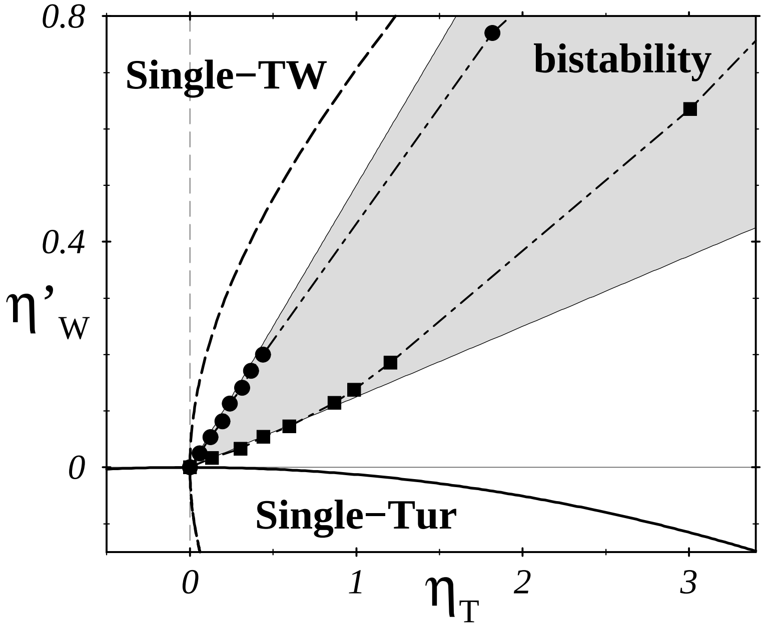

Figure 5.11: Control parameter space η'_W vs. η_T of the amplitude equations near the codimension-2 point (located at $\eta'_W = 0$ and $\eta_T = 0$) studied in Section 3.5.4. The full and dashed lines indicate the wave and Turing instability thresholds respectively. The *thick* and *thin* lines indicate the position of the thresholds in the RDNC model (as calculated with the linear stability analysis) and the in the amplitude equations respectively. The gray region is the bistability area predicted by the amplitude equations. The dots and squares (joined by a dot-dashed line) show the boundary of the bistability region measured in numerical simulations of the RDNC model. Note that the boundary of the bistability region, predicted and measured, coincide near the codimension-2 point, but start to separate as the distance to this point gets bigger.

- Bistability region between travelling waves and Turing patterns

Let us first address the bistability region. In Figs. 5.11 and 5.12 we show this region in the control parameter spaces η'_W vs. η_T and a vs. δ respectively[5]. The codimension-2 point corresponds to the coordinates (0,0) in Fig. 5.11 and to (1,4.657) in Fig. 5.12. The thresholds of the wave and Turing instabilities are marked by full- and dashed-lines respectively. In the amplitude equations these threshold correspond to straight lines (indicated in the fig-

---

[5] Note that these control parameter spaces are directly related by the *linear transformation* given in Eq. (4.69,4.70). This transformation corresponds to a rotation around the codimension-2 point plus a stretching. In this thesis we will use both control parameter spaces interchangeably.

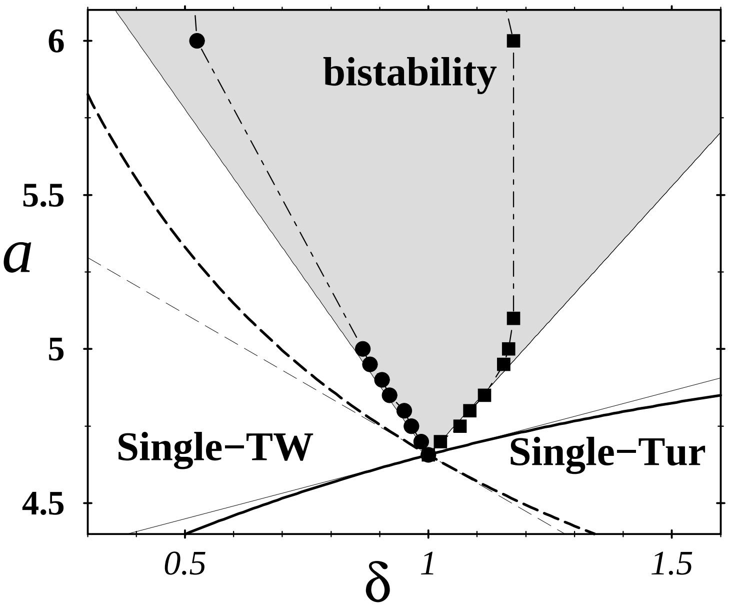

Figure 5.12: Control parameter space a vs. δ of the RDNC model near the codimension-2 point (located at $a = 1$ and $\delta = 4.657$) studied in Section 3.5.4. This parameter space is a transformation (using Eqs. (4.69,4.70)) of the control parameter space η'_W vs. η_T of the amplitude equations shown in Fig. 5.11 (see also comment in Footnote 5). For a description of the lines, dots and squares see caption of Fig. 5.11.

ures by *thin* full and dashed lines) but in the RDNC model they are curves (in the figures they are indicated by *thick* full and dashed curves). The gray regions correspond to the *bistability* area between travelling waves and Turing patterns predicted by the amplitude equations (the stability conditions are given in Table 5.2). The full squares and full dots, joined by dot-dashed lines, display the points in the control parameters space where the travelling waves and Turing patterns respectively become unstable in numerical simulations of the model. Consequently, they correspond to the boundary of the bistability region in the RDNC model. Note that near the codimension-2 point the boundary of this region coincides with the predicted one and that this agreement gets worst as the distance to this point increases.

- Predicted and measured values of the amplitudes

As we did for the wave instability in Section 5.3.2, we can also compare the amplitude of the Single-TW and Single-Tur solutions predicted by the amplitude equations with the maximal value of the u-field measured in numerical

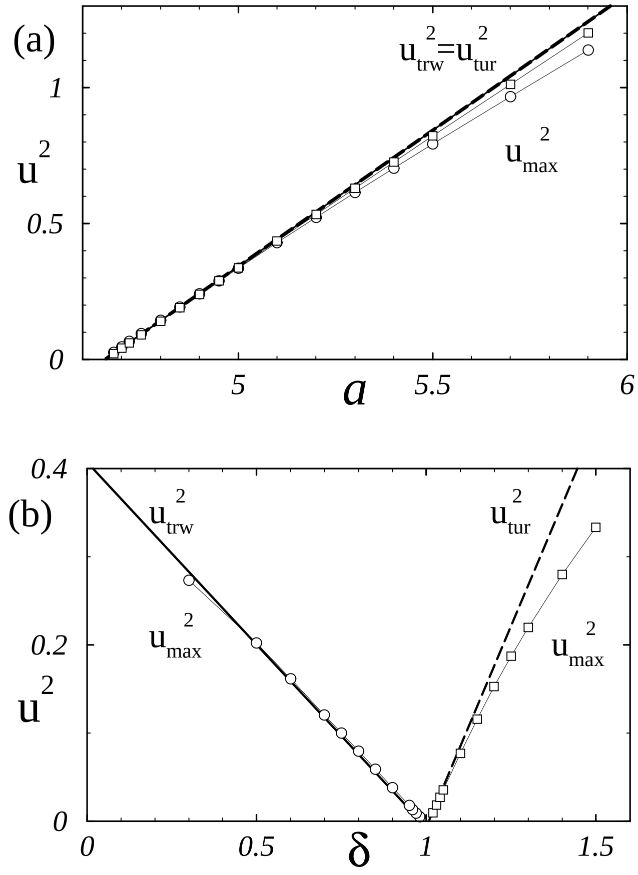

Figure 5.13: Comparison between the maximal values of travelling waves and Turing patters predicted by the amplitude equations and measured in numerical simulation of the RDNC model near the codimension-2 point of Table 3.1. The full and dashed lines show the values predicted by Eqs. (4.63,4.62,4.64) of u_{trw} and u_{tur} respectively. The maximal values of the wave and Turing patterns measured in the RDNC model are indicated with circles and squares respectively. In (a) we keep $\delta = 1$ fixed and vary a, note that theoretically both, wave and Turing patterns, should have the same amplitude. In (b) a is kept fixed to $a = 4.65$.

simulations of the RDNC model. In Fig. 5.13 we show the amplitude of such wave and Turing patterns as we vary the parameter a and keep δ fixed in (a) and as we vary δ keeping a constant in (b). It is interesting to note that the range of applicability of the amplitude equation approach seems to be more extended for the waves than for the Turing patterns (see Fig. 5.13(b)). In Fig. 5.12 we can see that the same remark applies to the right boundary of the bistability region!

Part II

Interfaces

Chapter 6

Classification of interfaces separating periodic patterns with constant amplitude

In the previous chapter we analysed in detail basic solutions of the RDNC model and the amplitude equations. These basic solutions corresponded to constant amplitude patterns in the RDNC model. We saw that different types of basic solutions can exist simultaneously and that they typically suppress each other. In this and following chapters we will study interfaces separating regions of space that contain different basic solutions.

After a short introduction and motivation to the study of interfaces, this chapter is divided in two parts. First, we will establish a classification of interfaces in the RDNC model and state some preliminary remarks. In the second and longer part of this chapter we will introduce the theoretical tools needed to analyse the dynamics of these interfaces. These tools include the coherent structure approach, counting arguments and the leading-edge approach.

6.1 Introduction and motivation

In the preceding chapter we saw that the RDNC model can have different periodic patterns. These patterns arise from different instabilities of a spatially homogeneous solution. They consist of Turing and/or travelling wave patterns. Near the onset of the instabilities the patterns typically have constant amplitude. We also saw that these solutions are stable and that they appear in families. These families are parametrised by their respective wavenumbers. For some values of the parameters of the RDNC model more than one of these families can exist. In that case they suppress each other.

This bistability is seen near the wave instability and near the codimension-2 wave-Turing instability. In the first case the bistability involves two counterpropagating travelling waves. In the second instance, a travelling wave and a Turing pattern can be stable simultaneously.

This bistability between different patterns gives rise to an interesting issue. If the system length is small, then only one pattern is typically observed. Which pattern is selected in this case will depend on the initial conditions. On the other hand, if the system length is big, then different patterns with constant amplitude can exist in different regions of the space. The places in space separating these regions are usually called *interfaces*[1]. Interfaces are an ubiquitous feature of multistable systems.

In Fig. 6.1 we show the outcome of two numerical simulations of the RDNC model starting from a small random perturbation around the unstable fixed point $\mathbf{X}_0$ and using periodic boundary conditions. In Fig. 6.1(a), the parameters are such that the RDNC model is near the wave instability. In Fig. 6.1(b) they are near the codimension-2 wave-Turing instability. In both figures we can see that after a very short transient time, big domains containing constant amplitude patterns develop. In Fig. 6.1(a) these patterns consist of two counterpropagating travelling waves. In Fig. 6.1(b) a left travelling wave and a Turing pattern are seen. In the latter case a right travelling wave is seen with equal probability. We can see that these regions are separated by small transitional zones. These zones are the interfaces.

In Fig. 6.1(a) some of the interfaces initially formed coalesce and only two interfaces survive. These interfaces seem to be either stationary or move very slowly. In Fig. 6.1(b), after a short transient, two interfaces form. They seem to travel with constant velocity. They have different velocities but both travel in opposite direction than the travelling wave (*i.e.* the velocities of the interfaces have opposite sign to the phase velocity v_{ph} of the wave).

Let us now state some questions about these interfaces.

- When do the interfaces move?
- In the cases where they move; do they travel with constant velocity?
- Is this velocity unique?
- Is the size and shape of the interface region stable with time?
- How does the shape of the interfaces change as the distance to the instability vary?

---

[1] Sometimes they are also referred as **fronts** or **domain walls**, depending on the type of patterns that they separate. In the present context the word interface is more appropriated.

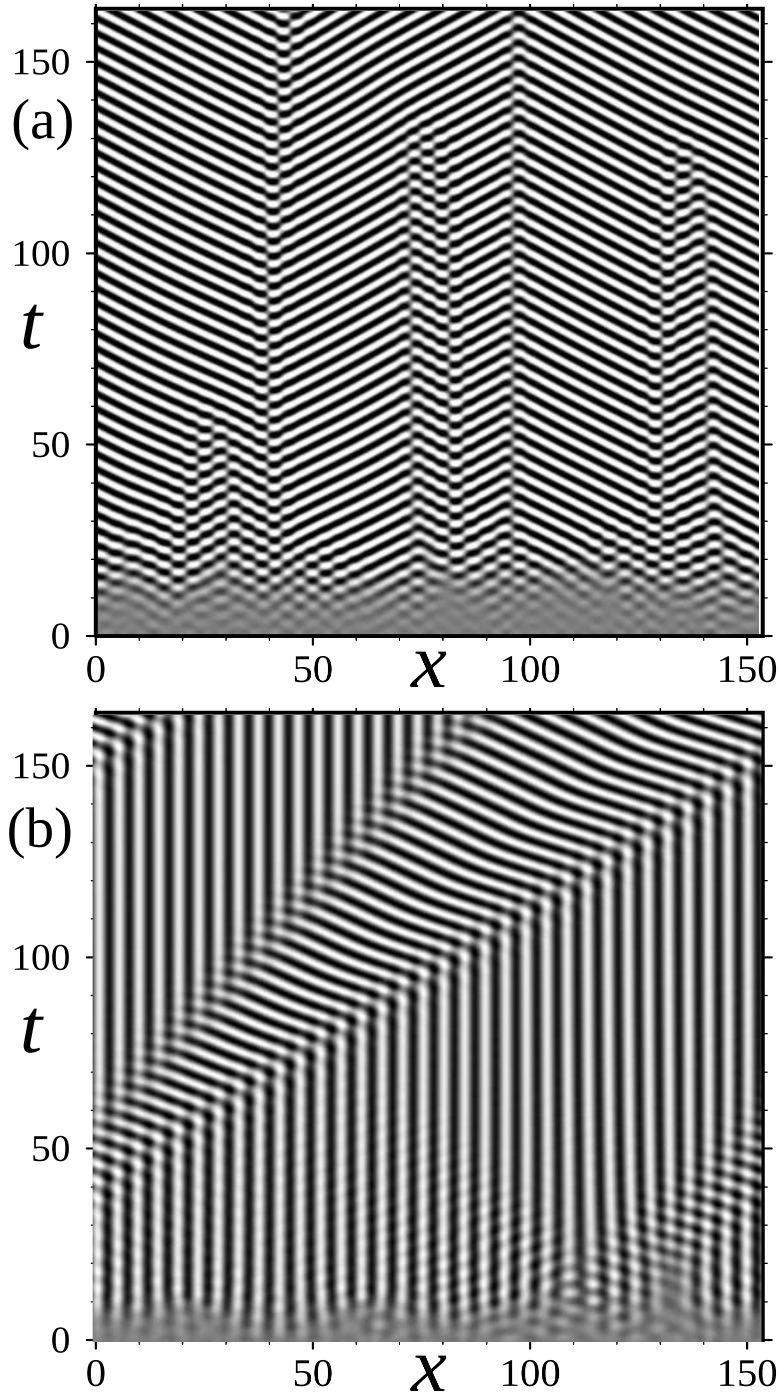

Figure 6.1: Two typical examples of numerical simulations of the RDNC model, starting from random initial conditions, near the wave instability (in (a)) and near the codimension-2 wave-Turing instability (in (b)). In both cases the initial conditions correspond to a small random perturbation around the unstable solution $\mathbf{X}_0$. Periodic boundary conditions were used. In (a) $a = 4.7$ and $\delta = 0.25$ (therefore near a wave instability (*cf.* Fig. 3.5) and in (b) $a = 4.9$ and $\delta = 0.95$ (*i.e.* near a codimension-2 wave-Turing instability).

- Do the qualitative features of interfaces near and far from the instability thresholds differ?

- How do the properties of interfaces change as different kinds of patterns[2] are chosen?

- Do the interfaces *actively select* the two patterns that they separate? Or, are these patterns imposed only by the initial conditions?

- Does the velocity of the interfaces depend on the patterns they separate?

In this and the following chapters we will answer these and other questions regarding interfaces in the RDNC model.

- Organisation of this chapter

In the next section we will examine which kinds of interfaces are possible and classify them. Further analysis of the the interfaces in the RDNC model will be done in following chapters. In the last two section we will give an introduction to the analysis of the interfaces and overview of the theoretical methods to be used in the rest of this thesis.

6.2 Classification of interfaces

A first classification of the possible interfaces can be done if we consider the type of constant amplitude patterns that they separate. In the RDNC model these can be left-, right-travelling waves and Turing patterns.

6.2.A Sinks and sources

Let us first consider interfaces separating counterpropagating waves. We can distinguish two cases: sources and sinks (see Fig. 6.2), depending on the direction of the phase velocity v_{ph} of the waves. In the *sources* the direction of phase velocity of the waves should point away from the interface (see Fig. 6.2(a)). On the contrary, in the *sinks* the phase velocity points towards the interface (see Fig. 6.2(b)). In Fig. 6.1(a) we can see how a travelling source (on the left) and a stationary sink (on the right) emerge in simulations of the RDNC model with random initial condition.

---

[2] Note that, as we mention before, there are typically a family of possible constant amplitude travelling wave and/or Turing pattern solutions.

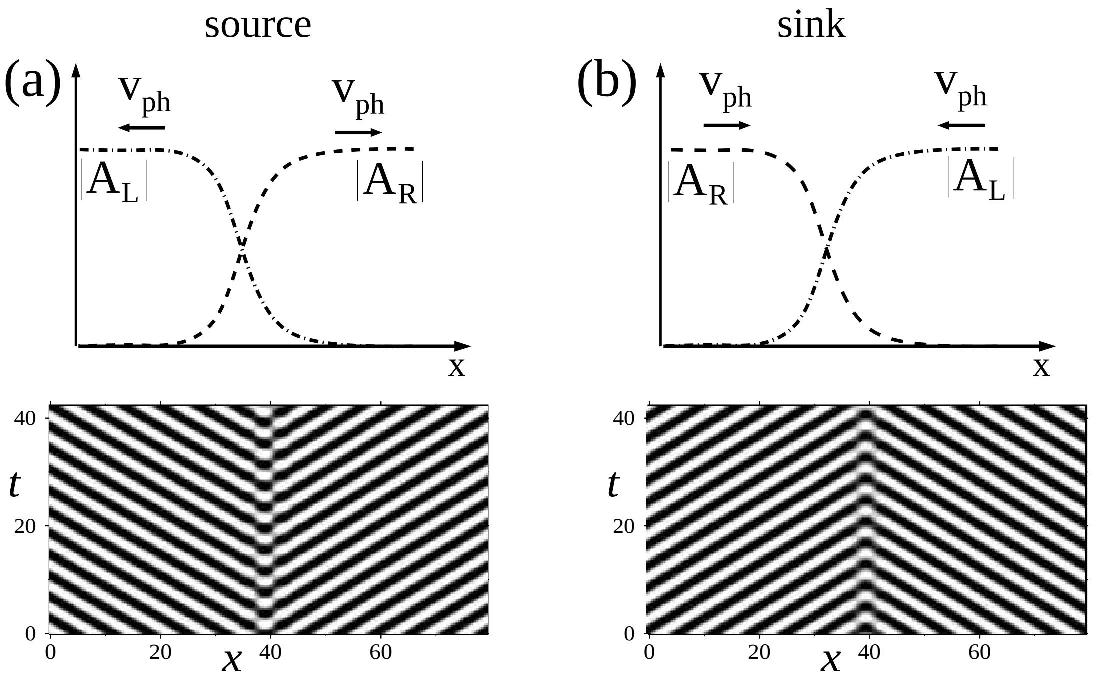

Figure 6.2: Schematic sketch of interfaces separating two counterpropagating travelling waves in the coupled amplitude equations (4.78,4.77) (up) and the corresponding numerical simulations of the RDNC model (down). Depending on the phase velocity v_{ph} of the waves that they separate, the interfaces can be classified as sources, in (a), and sinks, in (b).

6.2.B Inward and Outward wave-Turing Interfaces

In the case when the interface separates a Turing pattern in one side and a travelling wave in the other, we will speak of a wave-Turing interface. We should consider two different sub-cases: inward and outward interfaces. The *inward interfaces* (**INIs** in the following) correspond to the case when the phase velocity on the wave side points in direction to the interface. (see Fig. 6.3(a)). The opposite happens for the *outward interfaces* (**OUIs**). Examples of INIs and OUIs are given in Figs. 6.3(a) and 6.3(b) respectively.

Note that the names *inward and outward do not depend on the direction in which the interface moves.* Neither do they depend on the *respective location*[3] of the Turing and wave domains. This property of the interfaces

---

[3] In Fig. 6.3(a), for example, the inward interface separates a wave on the left and a Turing pattern on the right side. On the other hand, the location of each pattern is reversed for the inward interface shown in Fig. 6.1(b) (the wave domain is now located in on the right side of the interface).

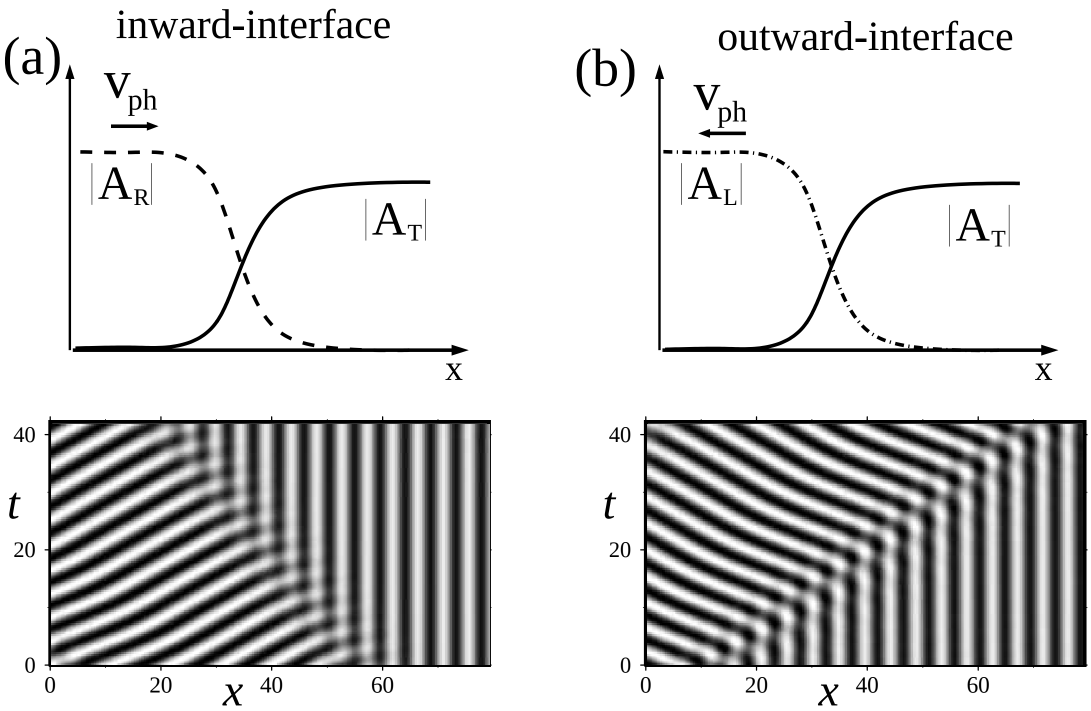

Figure 6.3: Schematic sketch of interfaces separating a wave and Turing domains in the coupled amplitude equations (4.81,4.80,4.82) (up) and the corresponding numerical simulations of the RDNC model. Depending if the phase velocity v_{ph} of the wave side points in the direction of the interface or away from it, they can be classified as inward- or outward-interfaces.

is a consequence of the reflection symmetry of the RDNC model (*i.e.* under the substitution $x \to -x$).

In Fig. 6.1(b) we can see how an OUI (on the left) and an INI (on the right) appear from random initial conditions; the INI travels slower than the OUI. The dynamics of INIs and OUIs will be studied in detail in the following chapters.

6.2.C Other types of interfaces

Let us finally mention that interfaces separating the same type of constant amplitude solutions (for example two right-travelling waves with different wavenumber) are also possible. In such cases it is enough to consider a *single* amplitude equation to describe the interface. Such interfaces in *single* complex Ginzburg-Landau equations have been studied in detail in the literature and are fairly well understood (for a review of this topic see Ref.

[85]). Moreover, as we will see in the following, these interfaces do not play a rôle as important as wave-Turing interfaces in the dynamics of the RDNC model near the codimension-2 instability. Consequently, in this thesis we will concentrate on interfaces involving more than one coupled amplitude equations.

6.3 Introduction to the analysis of interfaces in the RDNC model

In the previous section we saw that, after a short transient time, interfaces either do not move or they approach a constant velocity (this can be readily seen in Fig. 6.1). This important feature will allow us to do a detailed theoretical analysis of the interface dynamics in the *coupled amplitude equations*. Since the coupled amplitude equations are valid only near the instability thresholds, such an analysis will be applicable only in a confined region of the full parameter space of the RDNC model. However, as we will see in the next chapters, this approach will help us to understand the behaviour of interfaces not only in the vicinity of the thresholds! Moreover, since the form of the coupled amplitude equations is independent on the particularities of the instability, this study will provide us with information about the behaviour of similar interfaces either in the RDNC model with other parameter values or in other systems with the same type of instabilities.

Indeed, if we restrict our study to solutions of the coupled amplitude equations (4.47,4.46) (for sinks and sources) and (4.63,4.62,4.64) (for wave-Turing interfaces) that drift with *constant* velocity v_{int} and that have constant shape in a comoving coordinate system, then we can gain a lot of information about their behaviour. These requirements imply that the interfaces move *coherently* and consequently this kind of approximation is usually referred in the literature as *coherent structure approach* [85].

To apply the simple idea sketched in the previous paragraph to wave-Turing interfaces will be a non-trivial enterprise. Moreover, the analysis builds on many features of interfaces in *single* amplitude equations. Consequently, in the rest of this chapter we will introduce in detail these theoretical tools for single amplitude equations. This survey will also illustrate the approach in simpler situations. The actual analysis of the wave-Turing interfaces in the *coupled* amplitude equations will be done in Chapters 7 and 8.

6.4 Theoretical tools for the analysis of interfaces: The case of a single amplitude equation

6.4.1 Introduction

In this section (and in Appendix G) we will give a unified treatment of the topic of interfaces in single amplitude equations. Most of the features to be exposed here are scattered through the literature (see *e.g.* [1, 14, 85, 86]), consequently it will be handy to have them explained here.

This section is divided in main two parts. First, we will analyse the simplest amplitude equation possible: the real Ginzburg-Landau equation (RGLE) with constant phase. Second, we will shortly address the standard RGLE and the complex Ginzburg-Landau equation (CGLE). A more detailed analysis of these two latter cases is to be found in Appendix G.

6.4.2 Simplest case: The real Ginzburg-Landau equation with constant phase

Let us consider first the amplitude equation (4.72) for the Turing instability, derived in chapter 4. The solutions of this RGLE may be complex. Consequently we can write the complex amplitude as $\widetilde{A}_T(x,t) = \rho(x,t)e^{i\Phi_T(x,t)}$ where $\rho(x,t) \geq 0$ and $\Phi_T(x,t)$ are, respectively, the absolute value and phase of the complex amplitude.

Let us now restrict ourselves to the analysis of solutions of Eq. (4.72) *with constant phase* (*i.e.* $\Phi_T(x,t) \equiv$ const.). This leads us to consider the following PDE for the absolute value of the amplitude:

$$\partial_t \rho = \eta_T \rho + d_T \partial_x^2 \rho - \rho^3. \tag{6.1}$$

We recall that η_T, the control parameter, can be either positive or negative.

Eq. (6.1) can be viewed as the simplest possible "amplitude equation"; namely the one that arises when a extended system has a Turing type instability with zero critical wavenumber (*i.e.* $k_T^c \equiv 0$). The homogeneous part of Eq. (6.1) corresponds to the normal form of a *pitchfork* bifurcation [55].

For any value of η_T, Eq. (6.1) admits $\rho = 0$ as a solution. This solution is stable if $\eta_T < 0$ and unstable if $\eta_T > 0$. The other possible spatially homogeneous solution is $\rho = \sqrt{\eta_T}$. It exists only for $\eta_T > 0$ and is always stable. Therefore, for $\eta_T > 0$, Eq. (6.1) is a simple model of a system in which a stable state invades a unstable state.

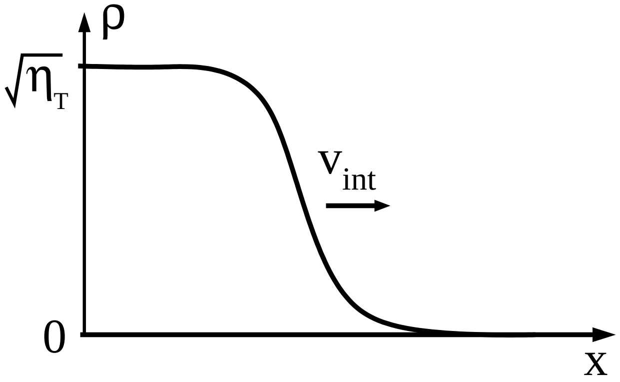

Figure 6.4: Schematic sketch of a front in Eq. (6.1) when $\eta_T > 0$. The stable state $\rho = \sqrt{\eta_T}$ invades the unstable state $\rho = 0$.

6.4.3 Coherent structure approach

Let us now analyse a front separating two domains; one on the left with $\rho = \sqrt{\eta_T}$ and the other on the right with $\rho = 0$ (see Fig. 6.4). Let us also assume that this front stays localised as time evolves and travels with constant speed v_{int}. This amounts to restrict our study to a particular family of solutions; namely front solutions that move with velocity v_{int} and that preserve their shape in a comoving frame. In the literature this is usually called *coherent structure approach*[4]. These assumptions suggest us the use of the following ansatz:

$$\rho(x,t) = a(\xi) \quad \text{with} \quad \xi = x - v_{int}t, \tag{6.2}$$

Note that the velocity v_{int} is a *free parameter*, that can be changed in order to find a coherently translating solution. Inserting ansatz (6.2) in Eq. (6.1), we get the following second order ODE:

$$0 = d_T \partial_\xi^2 a + v_{int} \partial_\xi a + \eta_T a - a^3. \tag{6.3}$$

If we introduce a new variable:

$$\kappa \overset{\text{def}}{=} \partial_\xi a / a, \tag{6.4}$$

corresponding to the *exponential decay rate*[5] to the fixed point $\rho = 0$, into Eq. (6.3), and use the relationship $\partial_\xi \kappa = \partial_\xi^2 a/a - (\partial_\xi a/a)^2$, then we get the

---

[4] Although in this context the term coherent structure is extensively used sometimes other terms, as for example *phase plane method*, are used (see *e.g.* [87, 88]).

[5] The magnitude of κ tells us how "fast" $a(\xi)$ approaches $a = 0$ when $\xi \to +\infty$ or $\xi \to -\infty$.

following system of *first order* ODEs:

$$\partial_\xi a = \kappa a, \tag{6.5}$$

$$\partial_\xi \kappa = \mathcal{K}_S(a, \kappa), \tag{6.6}$$

where:

$$\mathcal{K}_S(a, \kappa) \overset{\text{def}}{=} \frac{1}{d_T}\Big[- v_{int}\kappa - \eta_T + a^2\Big] - \kappa^2. \tag{6.7}$$

- Fixed points

The first step in the analysis of Eqs. (6.5,6.6) is to find its fixed points. From Eq. (6.5) it is clear that they should satisfy that either $a = 0$ or $\kappa = 0$. In the following we will call the first ones *linear fixed points* (and denote them by **L**) and the second ones *nonlinear fixed points* (**N**).

A nonlinear fixed point exists only for $\eta_T \geq 0$ and is unique. It is given by:

$$\mathbf{N}: \quad a_N = \sqrt{\eta_T} \quad \text{and} \quad \kappa_N = 0,$$

and it corresponds to the fixed point $\rho = \sqrt{\eta_T}$ of the amplitude equation (6.1).

The linear fixed points come in pairs: $\mathbf{L}_1$ and $\mathbf{L}_2$. They correspond to two possible decay rates κ to the solution $\rho = 0$ of Eq. (6.1). They are:

$$\mathbf{L}_1: \quad a_{L1} = 0 \quad \text{and} \quad \kappa_{L1} = \frac{1}{2d_T}(-v_{int} - \sqrt{v_{int}^2 - 4\eta_T d_T}), \tag{6.8}$$

$$\mathbf{L}_2: \quad a_{L2} = 0 \quad \text{and} \quad \kappa_{L2} = \frac{1}{2d_T}(-v_{int} + \sqrt{v_{int}^2 - 4\eta_T d_T}).$$

Note that:

$$\kappa_{L1} < \kappa_{L2}. \tag{6.9}$$

For $\eta_T \geq 0$ these fixed points exist only if $|v_{int}| > v^m$, where:

$$v^m \overset{\text{def}}{=} 2\sqrt{\eta_T d_T}. \tag{6.10}$$

If $v_{int} = \pm v^m$ then these two fixed points merge into one. On the other hand for $\eta_T < 0$ they exist for *any* value of v_{int}.

We can further classify the linear fixed points regarding if κ_L is positive or negative. The first case, to be notated by $\mathbf{L}^+$, corresponds to a situation in which $a(\xi)$ grows away from zero as ξ increases (see Fig. 6.5(a)). In the second case ($\mathbf{L}^-$) $a(\xi)$ approaches zero (see Fig. 6.5(b)). The nonlinear fixed point **N** can correspond to any of both cases (see Fig. 6.5).

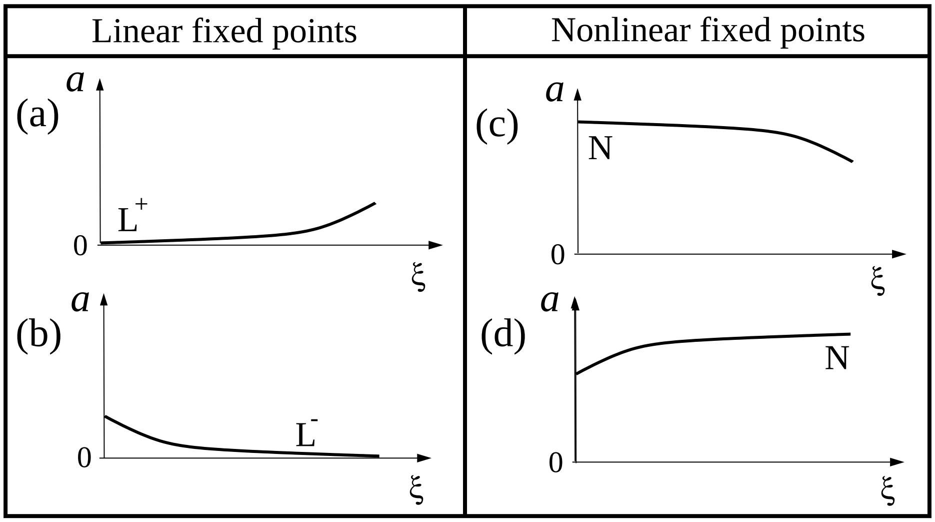

Figure 6.5: Schematic sketch of the trajectories near the fixed points of Eqs. (6.5,6.6).

The front solution of Eq. (6.1) sketched in Fig 6.4 corresponds to an orbit on the phase space of Eqs. (6.5,6.6) going from $\mathbf{N}$ (at $\xi \to -\infty$) to $\mathbf{L}_1$ or $\mathbf{L}_2$ (at $\xi \to \infty$). Such an orbit joining two fixed points is usually called *heteroclinic orbit* (see *e.g.* [55]). The existence of this orbit is a nonlinear phenomena. If such an orbit exist or not will depend on the free parameter v_{int}. For some dynamical systems it is possible to find an analytic expression for the heteroclinic orbit, but in general the only way to investigate this issue is via numerical integration of the system. Despite these limitations, an investigation of the phase space of Eqs. (6.5,6.6) near the fixed points will give us some useful information about the possible heteroclinic orbits.

- Manifold structure of the fixed points

We can readily get the eigenvalues and eigenvectors of the fixed points $\mathbf{L_1}$, $\mathbf{L}_2$ and $\mathbf{N}$. The nonlinear fixed point $\mathbf{N}$ (that exists only for $\eta_T > 0$) has always a positive and a negative eigenvalue. This means that it has one ingoing and one outgoing manifold (see sketch in Fig. 6.6(a)). The linear fixed point $\mathbf{L}_1$ has also a positive and a negative eigenvalue. For $\mathbf{L}_2$ we should distinguish between $\eta_T > 0$ and $\eta_T < 0$. In the first case, both eigenvalues are negative, whereas in the second case, one is positive and the other negative (see Figs. 6.6(a) and 6.6(b) respectively).

We can summarise the manifold structure of the fixed points in the fol-

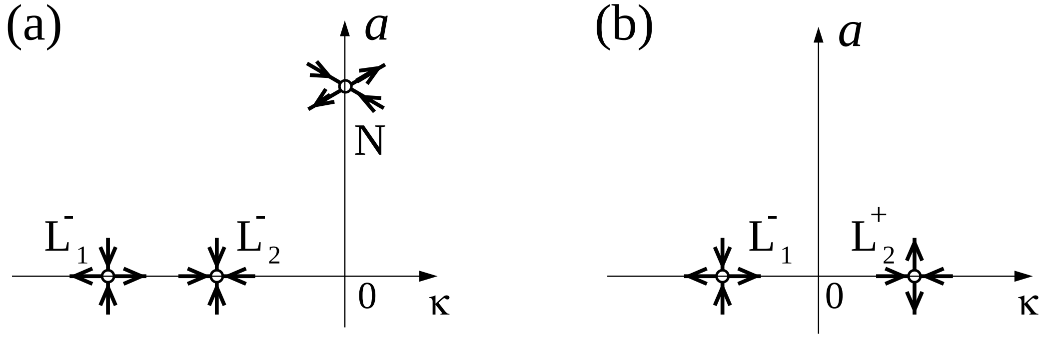

Figure 6.6: Schematic sketch of phase space around the fixed points of Eqs. (6.5,6.6) for $\eta_T > 0$ in (a) and $\eta_T < 0$ in (b). The thick lines show schematically the manifold structure near the fixed points (marked by small circles).

lowing way[6]:

$$\begin{array}{lrcl}
\eta_T < 0 & \text{for all } v_{int} & : & \mathbf{L}_1^-(+,-), \mathbf{L}_2^+(+,-) \\
\eta_T > 0 & \left\{ \begin{array}{r} v_{int} > v^m \\ |v_{int}| < v^m \\ v_{int} < -v^m \end{array} \right. & \begin{array}{c} : \\ : \\ : \end{array} & \begin{array}{l} \mathbf{L}_1^-(+,-), \mathbf{L}_2^-(-,-) \\ \nexists \mathbf{L} \\ \mathbf{L}_1^+(+,+), \mathbf{L}_2^+(+,-) \end{array} \\
\eta_T < 0 & & : & \nexists \mathbf{N} \\
\eta_T > 0 & \text{for all } v_{int} & : & \mathbf{N}(+,-)
\end{array} \qquad (6.11)$$

where v^m was introduced in Eq. (6.10). Finally, note that if $v_{int} = v^m$ (and $\eta_T > 0$), then the *single* linear fixed point has the following manifold structure: $\mathbf{L}^-(0,-)$ (and for $v_{int} = -v^m$: $\mathbf{L}^+(0,+)$).

- Counting arguments for the multiplicity of the heteroclinic orbits

With the manifold structure information at hand, we can now ask if it is possible to gain some knowledge about heteroclinic orbits in Eqs. (6.5,6.6) without having to integrate them. We can make use of the so called *counting arguments* to get an upper limit for the multiplicity[7] of heteroclinic orbits. In the following paragraphs we will give an *ad hoc* explanation of this method for the case of Eqs. (6.5,6.6). For a more general explanation of these arguments please see Appendix F.

As we stated previously, we are interested in orbits joining the fixed points $\mathbf{N}$, at $\xi \to -\infty$, and $\mathbf{L}^-$, at $\xi \to -\infty$, (let us symbolise such an orbit by:

---

[6] Here we use a shorthand notation where, for example, $\mathbf{L}_1^-(+,-)$ means that the fixed point $\mathbf{L}_1$ decays to the right (*i.e.* $\kappa_L < 0$) and has a positive and a negative eigenvalue.

[7] With *multiplicity* we mean the probability to find a nearby heteroclinic orbit *if* one is known to exist for a particular value of the free parameters.

$\mathbf{N} \to \mathbf{L}^-$). Near $\mathbf{N}$, the heteroclinic orbit should flow through its only unstable manifold. We can expect this to happen generically (*i.e.* for any value of the free parameter v_{int}). If we suppose that a heteroclinic orbit exists, then there are two possibilities: either the orbit flows to $\mathbf{L}_1^-$ or to $\mathbf{L}_2^-$. Since $\mathbf{L}_2^-$ has only ingoing manifolds, we expect to find a heteroclinic orbit flowing to this fixed point for *any value* of $v_{int} > v^m$. On the other hand, $\mathbf{L}_1^-$ has one outgoing manifold. The heteroclinic orbit should be perpendicular to this manifold. To achieve this we will have to tune the value of the positive eigenvector by changing the unique free parameter v_{int}. Consequently, we expect to find a heteroclinic orbit $\mathbf{N} \to \mathbf{L}_1^-$ only for *discrete values* of v_{int} (where these values should also satisfy: $v_{int} > v^m$).

We can summarise these results saying that, for $\eta_T > 0$, we expect to find that the heteroclinic orbits belong to the following families:

$$\bullet \quad v_{int} > v^m \begin{cases} \mathbf{N}(+,-) \to \mathbf{L}_2^-(-,-) & \Longrightarrow \quad 1 \text{ PF} \\ \mathbf{N}(+,-) \to \mathbf{L}_1^-(+,-) & \Longrightarrow \quad 0 \text{ PF} \end{cases} \tag{6.12}$$

where 1 PF indicates that the orbits are a one parameter family and 0 PF a discrete family.

- Numerical simulations of Eqs. (6.5,6.6) and Eq. (6.1)

Numerical simulations of ODEs (6.5,6.6) show that the orbit $\mathbf{N} \to \mathbf{L}_1^-$ turns out not to exist and that $\mathbf{N} \to \mathbf{L}_2^-$ exists for any $v_{int} \geq v^m$. In Fig. 6.7 we show some examples of the orbits $\mathbf{N} \to \mathbf{L}_2^-$ for different values of v_{int}.

To test the predictions done with the counting arguments and numerical simulations of ODEs (6.5,6.6), we resort to numerical simulations of fronts in the PDE (6.1). The main result is that (for sufficiently localised initial conditions) the velocity v_{int} of such fronts approaches asymptotically v^m (for a discussion of this topic see [1] and references therein). Consequently, from the continuous family of orbits $\mathbf{N} \to \mathbf{L}_2^-$ typically the one with slowest possible velocity is *selected* in numerical simulations of the PDE (6.1).

6.4.4 Leading-edge approach and marginal stability criterion

The results of the numerical simulations of Eq. (6.1) for a front propagating into an unstable state can be predicted if we use the so called leading-edge approach in combination with the marginal stability criterion. In the following we will give a brief introduction to these topics. For a more extensive discussion and references to the relevant literature, see Chapter 9 of Ref. [14] or [89, 90].

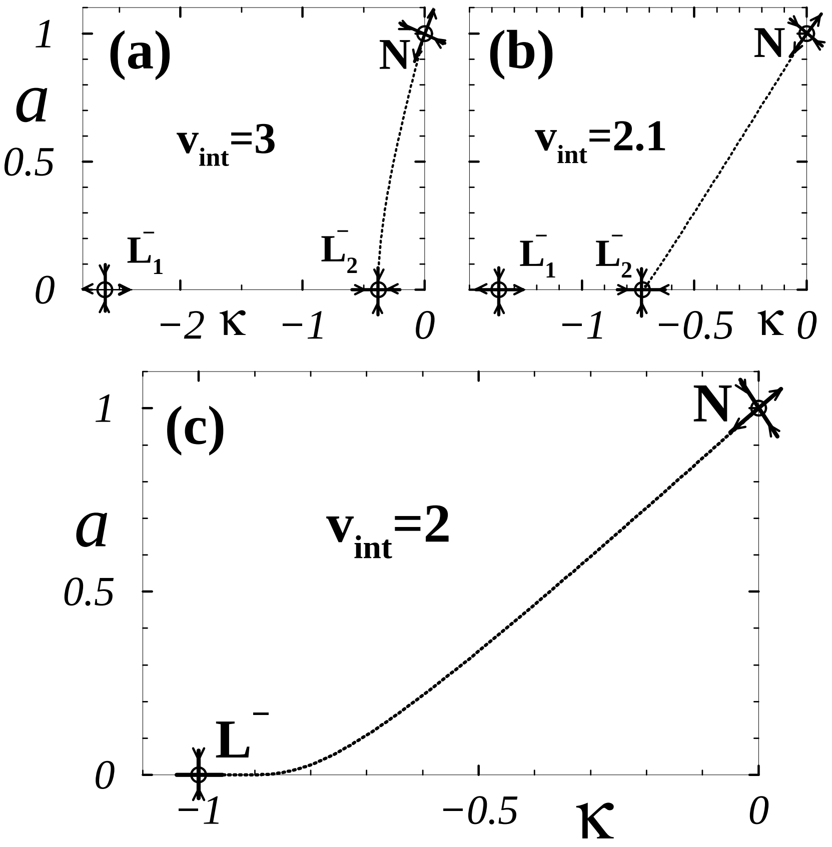

Figure 6.7: Phase space of Eq. (6.5,6.6) with $\eta_T = 1$ and $d_T = 1$ and for various values of v_{int} (note that $v^m = 2$ in this case). In (a) $v_{int} = 3$, in (b) $v_{int} = 2.1$ and in (c) $v_{int} = 2$. The dotted curves shows the heteroclinic orbits going from $\mathbf{N}$ (located at $a_N = 1$ and $\kappa_N = 0$) to $\mathbf{L}_2^-$ for each of these values. These orbits were obtained by numerical simulations of Eq.(6.5,6.6). Note that for $v_{int} = 2$ the linear fixed points $\mathbf{L}_2^-$ and $\mathbf{L}_1^-$ merge into $\mathbf{L}^-$.

The idea behind the *leading edge approach* is that the front dynamics is governed only by the behaviour of the fraction of the front near the unstable state. This part of the front is called the leading edge [92].

Any PDE can be linearised near its unstable fixed points (*e.g.* $\rho = 0$ in Eq. (6.1)). A general solution of the resulting linear PDE can be written as:

$$\rho(x,t) \propto e^{(\Omega(K)t - Kx)},$$

where both $\Omega(K)$ and K are typically complex scalar quantities. From the dispersion relation $\Omega(K)$ we can calculate the velocity of propagation of the general solution as: $v = Re[\Omega]/Re[K]$.

Let us now consider the stability of the leading-edge. After a brief analysis it can be shown [14, 89, 90] that fronts with a velocity smaller than v^* are unstable (in the co-moving frame) to small perturbations. On the other, hand fronts with $v > v^*$ are stable. The velocity v^* is called the *marginal velocity* and is given by the following equations [14]:

$$Re\Big[\frac{d\Omega(K)}{dK}\Big|_{K=K_0}\Big] = v^* \ , \ Im\Big[\frac{d\Omega(K)}{dK}\Big|_{K=K_0}\Big] = 0 \ \text{ and } \ \frac{Re[\Omega(K_0)]}{Re[K_0]} = v^*. \tag{6.13}$$

- Marginal stability criterion: Linear vs. nonlinear propagation

The *marginal stability criterion* states that, for a broad range of models [14, 89, 90, 91], the velocity selected[8] by a front invading an unstable state is the marginal velocity v^*. For the case of Eq. (6.1) this velocity is $v^* \equiv v^m$ which agrees with the results of numerical simulations.

In the following we will refer to the cases where the dynamics of the leading edge (combined with the marginal stability criterion) predict the correct dynamics of the full interface as the *linear propagation* regime [1]. On the other hand, we will apply the term *nonlinear propagation* if a full nonlinear analysis of the interface solution is needed to calculate its velocity.

6.4.5 More complex cases: The real and the complex Ginzburg-Landau equations

Let us now address the case of the RGLE (*cf.* Eq. (4.72)) given by:

$$\partial_t \widetilde{A}_T = \eta_T \widetilde{A}_T + d_T \partial_x^2 \widetilde{A}_T - |\widetilde{A}_T|^2 \widetilde{A}_T, \tag{6.14}$$

and the CGLE:

$$\partial_t \widetilde{A}_H = \eta'_W \widetilde{A}_H + (1 + ic_1)\partial_x^2 \widetilde{A}_H - (1 - ic_3)|\widetilde{A}_H|^2 \widetilde{A}_H. \tag{6.15}$$

Note that this last equation, except for the extra convective term $+sv_g\partial_x\widetilde{A}_H$, is equivalent to Eq. (5.9) studied in Chapter 5.

A short overview of the coherent structure approach and the marginal stability criterion follows. A detailed analysis of these equations and references to the relevant literature are given in Appendix G.

---

[8] The marginal stability criterion is only valid if a compact initial condition has been used to generate the front [93].

- Coherent structure ansatz

The coherent structure ansatz reads: $\widetilde{A}_T(x,t) = e^{i\omega t}\hat{A}(x - v_{int}t)$, for the RGLE and: $\widetilde{A}_H(x,t) = e^{i\omega t}\hat{A}(x - v_{int}t)$, for the CGLE. In both cases $\hat{A}(\xi)$ is a complex quantity. Consequently we can write: $\hat{A}(\xi) = a(\xi)e^{i\phi(\xi)}$. Note that the ansatz have *two* free parameters: ω and v_{int}. Inserting these ansatz in the RGLE and CGLE lead to the following set of coupled ODEs:

$$\partial_\xi a = \kappa a, \tag{6.16}$$

$$\partial_\xi \kappa = \mathcal{K}(a,q,\kappa), \tag{6.17}$$

$$\partial_\xi q = \mathcal{Q}(a,q,\kappa), \tag{6.18}$$

where the new variable $q(\xi) \overset{\text{def}}{=} \partial_\xi \phi$ can be interpreted as a *local wavenumber*. The functions $\mathcal{K}$ and $\mathcal{Q}$ are different for the RGLE and CGLE cases. For the RGLE they are:

$$\mathcal{K}_T(a,q,\kappa) \overset{\text{def}}{=} \frac{1}{d_T}\Big[-v_{int}\kappa - \eta_T + a^2\Big] - \kappa^2 + q^2, \tag{6.19}$$

$$\mathcal{Q}_T(q,\kappa) \overset{\text{def}}{=} \frac{1}{d_T}\Big[-\omega - v_{int}q\Big] - 2\kappa q, \tag{6.20}$$

and for the CGLE:

$$\begin{aligned}\mathcal{K}_H(a,q,\kappa) &\overset{\text{def}}{=} \frac{1}{1+c_1^2}\Big[-v_{int}(\kappa + c_1 q) - \eta'_W - c_1\omega + (1 - c_1c_3)a^2\Big]\\ &\quad -\kappa^2 + q^2, \end{aligned}\tag{6.21}$$

$$\begin{aligned}\mathcal{Q}_H(a,q,\kappa) &\overset{\text{def}}{=} \frac{1}{1+c_1^2}\Big[-\omega - v_{int}(q - c_1\kappa) + c_1\eta'_W - (c_1 + c_3)a^2\Big]\\ &\quad -2\kappa q. \end{aligned}\tag{6.22}$$

- Manifold structure of the fixed points

In Appendix G the fixed points of Eqs. (6.16,6.18,6.18) and their corresponding manifold structure are comprehensively studied. Here we give just a short summary of the manifold structures around the fixed points.

For the RGLE we can summarise the structure with:

$$\begin{array}{lll} \eta_T < 0 & \text{for all } v_{int} & : \ \mathbf{L}_1^-(+,+,-), \mathbf{L}_2^+(+,-,-) \\ \eta_T > 0 & \left\{ \begin{array}{r} v_{int} \geq v^c \\ |v_{int}| < v^c \\ v_{int} \leq -v^c \end{array} \right. & \begin{array}{l} : \ \mathbf{L}_1^-(+,+,-), \mathbf{L}_2^-(-,-,-) \\ : \ \mathbf{L}_1^-(+,+,-), \mathbf{L}_2^+(+,-,-) \\ : \ \mathbf{L}_1^+(+,+,+), \mathbf{L}_2^+(+,-,-) \end{array} \end{array} \tag{6.23}$$

$$\begin{array}{ll}
\eta_T < 0 & : \quad \nexists \mathbf{N} \\
\eta_T > 0 \begin{cases} v_{int} > 0 & : \quad \mathbf{N}^-(+,-,-) \\ v_{int} < 0 & : \quad \mathbf{N}^+(+,+,-) \end{cases} &
\end{array}$$

where v^c is defined in Eq. (G.16). The index + or − in $\mathbf{N}$ denotes the sign of the group velocity of the nonlinear fixed point in the frame moving with velocity v_{int} (see Appendix G for details).

For the CGLE the manifold structure is:

$$\begin{array}{ll}
\eta'_W < 0 \quad \text{for all } v_{int} & : \quad \mathbf{L}_1^-(+,+,-), \mathbf{L}_2^+(+,-,-) \\
\eta'_W > 0 \begin{cases} v_{int} \geq v^c & : \quad \mathbf{L}_1^-(+,+,-), \mathbf{L}_2^-(-,-,-) \\ |v_{int}| < v^c & : \quad \mathbf{L}_1^-(+,+,-), \mathbf{L}_2^+(+,-,-) \\ v_{int} \leq -v^c & : \quad \mathbf{L}_1^+(+,+,+), \mathbf{L}_2^+(+,-,-) \end{cases} & \\
\eta'_W < 0 & : \quad \nexists \mathbf{N} \\
\eta'_W > 0 \begin{cases} v_{int} > v^{cN} & : \quad \mathbf{N}^-(+,-,-), \mathbf{N}^+(-,-,-) \\ |v_{int}| < v^{cN} & : \quad \mathbf{N}^-(+,-,-), \mathbf{N}^+(+,+,-) \\ v_{int} < -v^{cN} & : \quad \mathbf{N}^-(+,+,+), \mathbf{N}^+(+,+,-) \end{cases} &
\end{array} \tag{6.24}$$

where v^c is defined in Eq. (G.27) and v^{cN} is a complicated function of ω (for its definition see [86]).

- Marginal stability criterion

A front invading the unstable state $\widetilde{A}_T = 0$ in the RGLE and $\widetilde{A}_H = 0$ the CGLE, will propagate linearly [1, 85, 89, 90, 91].

For the RGLE the marginal stability criterion predicts that this front selects a velocity:

$$v^* \equiv v^m, \tag{6.25}$$

where v^m is the marginal velocity defined in Eq. (6.10). This front will also select a wavenumber:

$$q_N^* \equiv 0. \tag{6.26}$$

On the other hand for the CGLE the marginal stability criterion predicts the following velocity:

$$v^* = 2\sqrt{\eta'_W(1 + c_1^2)}. \tag{6.27}$$

In this case the wavenumber selected by the front is not equal to zero:

$$q_N^* = \sqrt{\eta'_W}\Big(\frac{\sqrt{1 + c_1^2} - \sqrt{1 + c_3^2}}{c_1 + c_3}\Big). \tag{6.28}$$

For more details, see Appendix G.

Chapter 7

Wave-Turing as Coherent Structures

In this chapter we will initiate the study of the dynamical properties of wave-Turing interfaces near a codimension-2 instability. To achieve this we will apply the coherent structure approach introduced in Chapter 6 to the coupled amplitude equations. The phase space of the resulting set of ordinary differential equations will be analysed. Heteroclinic orbits in this phase space correspond to interfaces in the coupled amplitude equations.

7.1 Introduction

In Section 6.1 we motivated the study of wave-Turing interfaces in the RDNC model with an example of a typical numerical simulation near the codimension-2 instability (*cf.* Fig. 6.1(b)). The examination of interfaces in this numerical simulation prompted us to ask many questions about their behaviour (such as dynamics and scaling properties). The main aim of this chapter is to introduce the approach and the methodology that we will use in the following chapter to answer these questions. Here we will analyse the wave-Turing interfaces in the *coupled* amplitude equations (4.81, 4.80, 4.82) using an *extension* of the coherent structure approach introduced in section 6.4 (and Appendix G) for *single* amplitude equations.

The idea of extending the coherent structure approach to coupled amplitude equations was introduced by van Saarloos and coworkers in Ref. [86] for the case of counterpropagating waves. In the current and following chapters we will expand this idea to the case of codimension-2 instabilities. In the next chapter we will see that this approach provides a clear picture of the dynamics of wave-Turing interfaces.

- Organisation of this chapter

This chapter is organised as follows. In the next section we will motivate and present the reduced set of amplitude equations to be studied in this and following chapters. In Section 7.3 we will apply the coherent structure ansatz to these equations and analyse the phase space of the effective equations. Finally, in Section 7.4 we will shortly analyse the dependence of the scaling properties of wave-Turing interfaces on the control parameters.

7.2 Two coupled amplitude equations

In Chapter 5 we saw that near the codimension-2 point the RDNC model is well described by the *three* coupled amplitude equations (4.63, 4.62, 4.64) derived in Chapter 4. In Fig. 7.1 we show examples of OUIs and INIs in the RDNC model and in the amplitude equations. These numerical simulations are done near the codimension-2 instability. The full line corresponds to the u-profile of the RDNC model and the dotted, dashed and dot-dashed lines show the amplitudes $|A_T^\star|$, $|A_R^\star|$ and $|A_L^\star|$ respectively, obtained in numerical simulations of the amplitude equations.

In Fig. 7.1 we can see that, for both types of interfaces, only the amplitude of one of the two waves is nonzero[1]. This feature is quite natural, since the two counterpropagating waves tend to suppress each other. Consequently, in the rest of this chapter we will assume that in the neighbourhood of the interface one of the travelling waves has zero amplitude. Consequently, the interfaces are well described by the following set of *two* coupled amplitude equations:

$$\boxed{\begin{aligned} \partial_t \widetilde{A}_W + s\, v_g \partial_x \widetilde{A}_W &= \eta'_W \widetilde{A}_W + (1+ic_1)\partial_x^2 \widetilde{A}_W - (1-ic_3)|\widetilde{A}_W|^2 \widetilde{A}_W \\ &\quad - h_{WT}(1-ic_4)|\widetilde{A}_T|^2 \widetilde{A}_W, & (7.1) \\ \partial_t \widetilde{A}_T &= \eta_T \widetilde{A}_T + d_{TW} \partial_x^2 \widetilde{A}_T - |\widetilde{A}_T|^2 \widetilde{A}_T - h_{TW} |\widetilde{A}_W|^2 \widetilde{A}_T, & (7.2) \end{aligned}}$$

where, depending on the travelling direction of the wave, the index s resp. the subscript W should be properly substituted by ±1 resp. R or L. If the wave present in the system travels to the *right* (*left*) we set $s = +1$ ($s = -1$) and substitute W by R (L). The value of the coefficients of these

---

[1] Clearly *any* of the two travelling waves can exist. The initial condition will determine which wave appears.

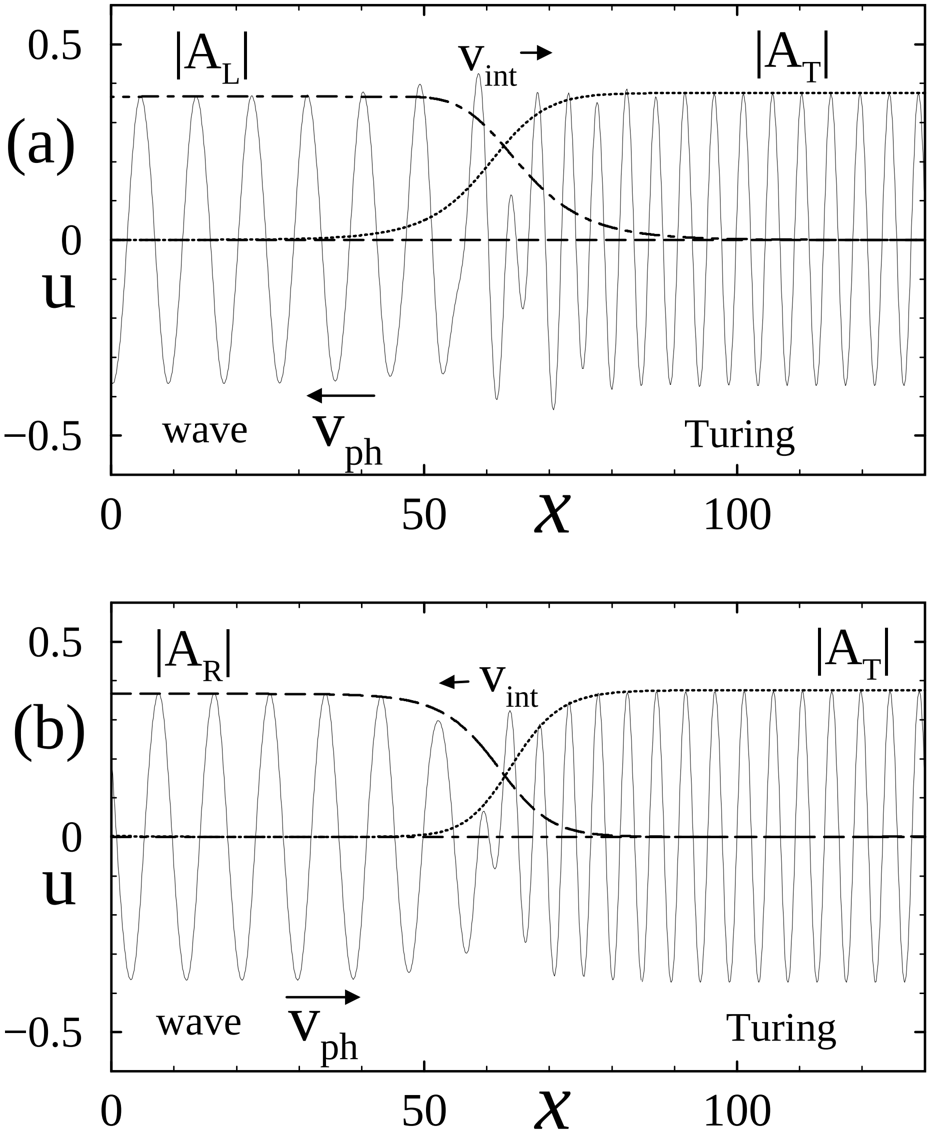

Figure 7.1: Comparison of the u-profile in the RDNC model (full line) and the amplitude of the wave and Turing patterns predicted by the amplitude equations near a OUI in (a), and a INI in (b). We indicate the Turing envelopes $|A_T|$ with a dotted line and the counterpropagating waves $|A_R|$ and $|A_L|$ with dashed and dot-dashed lines respectively. The control parameters of the model are $a = 4.8$ and $\delta = 0.998$. Only a small part of the total length of the system is shown. Note that far from the interface the amplitudes of wave and Turing patterns coincide with the values of the respective envelopes in the amplitude equations and that in both cases the amplitude of one of the waves is zero.

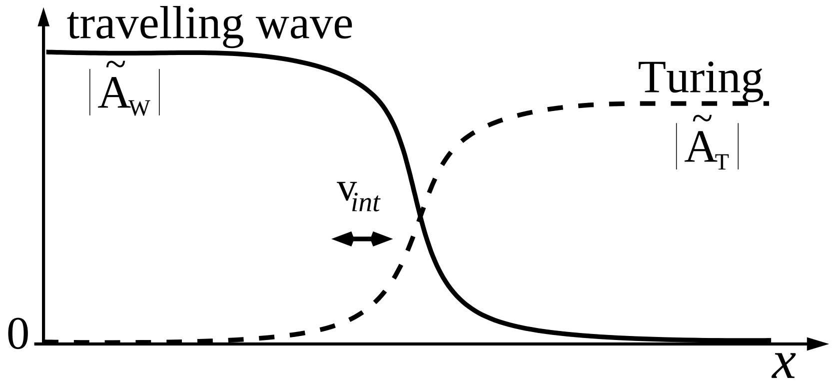

Figure 7.2: Schematic sketch of a wave-Turing interface travelling with velocity v_{int} in the amplitude equations (7.1,7.2). In Table 7.1 we show the substitutions to be done in s and in the subscript W to get a INI or a OUI.

type	name	$s =$	$W \rightarrow$
inward interface	**INI**	$+1$	R
outward interface	**OUI**	-1	L

Table 7.1: Convention for INIs and OUIs in Eqs. (7.1,7.2), when the wave and Turing domains are on the right and left side of the interface respectively (*cf.* Fig. 7.2).

equations are given in Table 4.2 (and, for simplicity, the tildes in the space and time variables have been dropped). As we will see in the next chapter, the results of the analysis of these *two* equations will be in good agreement with numerical simulations of interfaces in the RDNC model.

Without loss of generality, we will further assume that *the travelling wave is located on the left side of the interface, whereas the Turing pattern in on the right* (see sketch in Fig. 7.2). With this convention, an interface with $s = 1$ and $W \rightarrow R$ will be an *inward interface* and the other with $s = -1$ and $W \rightarrow L$ will be then an *outward interface* (*cf.* Section 6.2.B). For convenience we summarise this convention in Table 7.1.

7.3 Interfaces as coherent structures

As we said in Section 7.1, here (and in the next chapters) we will use an extension of the coherent structure ansatz introduced in Section 6.4 (and further expanded in Appendix G), to investigate the interfaces in Eqs. (7.1,7.2).

7.3.1 Ansatz

More specifically we will assume that interface can be written as:

$$\widetilde{A}_W(x,t) = e^{-i\omega_W t}\hat{A}_W(x - v_{int}t), \tag{7.3}$$

$$\widetilde{A}_T(x,t) = e^{-i\omega_T t}\hat{A}_T(x - v_{int}t), \tag{7.4}$$

where ω_W, ω_T and v_{int} are *free parameters*[2] that can be changed in order to get an interface solution. $\hat{A}_W$ and $\hat{A}_T$ are functions of $\xi \overset{\text{def}}{=} x - v_{int}t$.

In principle there could exist interface solutions of Eqs. (7.1,7.2) that are not of the form of the ansatz (7.1,7.2). But, as we will see later, all the interfaces observed in numerical simulations of the amplitude equations are well described by this ansatz. We will address the question about existence of the interfaces in the next chapter.

Substituting the ansatz of Eqs. (7.3,7.4) in the Eqs. (7.1,7.2), introducing: $\hat{A}_W = a_W e^{i\phi_W}$ and $\hat{A}_T = a_T e^{i\phi_T}$, and defining: $q_W \overset{\text{def}}{=} \partial_\xi \phi_W$ and $q_T \overset{\text{def}}{=} \partial_\xi \phi_T$, we get the following set of *six coupled ODEs*:

$$\boxed{\begin{aligned}
\partial_\xi a_W &= \kappa_W a_W && (7.5)\\
\partial_\xi \kappa_W &= \mathcal{K}_{WT} \overset{\text{def}}{=} \frac{1}{1+c_1^2}\Big[-(v_{int} - s\,v_g)(\kappa_W + c_1 q_W) - \eta'_W - c_1\omega_W \\
&\quad + (1 - c_1c_3)a_W^2 + h_{WT}(1 - c_1c_4)a_T^2\Big] - \kappa_W^2 + q_W^2 && (7.6)\\
\partial_\xi q_T &= \mathcal{Q}_{WT} \overset{\text{def}}{=} \frac{1}{1+c_1^2}\Big[-\omega_W - (v_{int} - s\,v_g)(q_W - c_1\kappa_W) + c_1\eta'_W \\
&\quad - (c_1 + c_3)a_W^2 - h_{WT}(c_1 + c_4)a_T^2\Big] - 2\kappa_W q_W && (7.7)\\
\partial_\xi a_T &= \kappa_T a_T && (7.8)\\
\partial_\xi \kappa_T &= \mathcal{K}_{TW} \overset{\text{def}}{=} \frac{1}{d_{TW}}\Big[-v_{int}\kappa_T - \eta_T + a_T^2 + h_{TW}a_W^2\Big] - \kappa_T^2 + q_T^2 && (7.9)\\
\partial_\xi q_T &= \mathcal{Q}_{TW} \overset{\text{def}}{=} \frac{1}{d_{TW}}\Big[-\omega_T - v_{int}q_T\Big] - 2\kappa_T q_T && (7.10)
\end{aligned}}$$

where $\kappa_W \overset{\text{def}}{=} \frac{\partial_\xi a_W}{a_W}$ and $\kappa_T \overset{\text{def}}{=} \frac{\partial_\xi a_T}{a_T}$ are the rates of exponential decay to zero of the wave and Turing amplitudes respectively (for more details see discussion in Section 6.4.3).

---

[2] In Appendix G we motivate the use of the two new free parameters ω_W and ω_T.

If we define the vector $\mathbf{S}(\xi) \overset{\text{def}}{=} (a_W, \kappa_W, q_W, a_T, \kappa_T, q_T)^{\text{Tr}}$ we can write Eqs. (7.5-7.10) in a compact way as:

$$\partial_\xi \mathbf{S}(\xi) = \mathbf{F}(\mathbf{S}(\xi); v_{int}, \omega_W, \omega_T). \tag{7.11}$$

In the remaining of this chapter we will analyse the phase space of Eqs. (7.5-7.10). In the next chapter, in section 8.4, we will perform a detailed study of heteroclinic orbits in Eqs. (7.5-7.10) and compare them with numerical simulations of interfaces in Eqs. (7.1,7.2).

- Remarks

If we compare the set of ODEs (6.16-6.18) obtained in Section 6.4.5 (for a single amplitude equation) with Eqs. (7.5-7.10) we can recognise some similarities between Eqs. (6.16-6.18) and, either the first three equations (7.5-7.7), or the last three equations (7.8-7.10).

Indeed, the functions $\mathcal{K}_{WT}(a_W, q_W, \kappa_W, a_T)$ and $\mathcal{Q}_{WT}(a_W, q_W, \kappa_W, a_T)$ in Eqs. (7.5-7.7) are equivalent to $\mathcal{K}_W(a, q, \kappa)$ and $\mathcal{Q}_W(a, q, \kappa)$ introduced in Eqs. (6.21,6.22) if we substitute η'_W, ω_W and v_{int} by $\eta'_W - h_{WT} a_T^2$, $\omega_W + h_{WT} c_4 a_T^2$ and $v_{int} - s v_g$, respectively. Similarly, $\mathcal{K}_{TW}(a_T, q_T, \kappa_T, a_W)$ and $\mathcal{Q}_{TW}(q_T, \kappa_T)$ in Eqs. (7.8-7.10) are equivalent to $\mathcal{K}_T$ and $\mathcal{Q}_T$ (defined in Eqs. (6.19,6.20) respectively) if we use $\eta_T - h_{TW} a_W^2$ instead of η_T.

Moreover, the fact that Eqs. (7.5-7.7) and (7.8-7.10) are coupled only via $a_W(\xi)$ and $a_T(\xi)$ will simplify the study of these equations.

7.3.2 Fixed points

The first step in the analysis of Eqs. (7.5-7.10) is the study of their fixed points. Eq. (7.5) tells us that the fixed points satisfy that either $a_W = 0$ or $\kappa_W = 0$. Similarly, Eq. (7.8) imposes that either $a_T = 0$ or $\kappa_T = 0$. Since we are interested in interfaces connecting pure travelling waves (for $\xi \to -\infty$) and pure Turing patterns (for $\xi \to +\infty$), the relevant fixed points of Eq. (7.11) are $\mathbf{S}_W$ and $\mathbf{S}_T$, where:

- $\mathbf{S}_W$ have: $a_W \neq 0$, $\kappa_W = 0$ and $a_T = 0$, $\kappa_T \neq 0$,
- $\mathbf{S}_T$ have: $a_W = 0$, $\kappa_W \neq 0$ and $a_T \neq 0$, $\kappa_T = 0$.

The fixed point $\mathbf{S}_W$ corresponds to a pure travelling wave and $\mathbf{S}_T$ to a pure Turing pattern.

The wave-Turing interfaces in Eqs. (7.1,7.2) correspond to heteroclinic orbits in Eqs. (7.5-7.10) joining these two fixed points (in the following we will symbolise this orbits with: $\mathbf{S}_W \to \mathbf{S}_T$). In Fig. 7.3 a sketch of $a_W(\xi)$ and

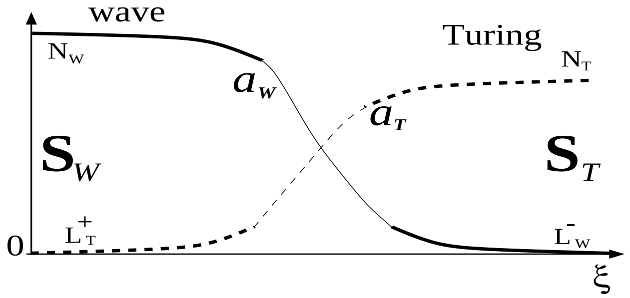

Figure 7.3: Sketch of the components $a_W(\xi)$ and $a_T(\xi)$ of Eqs. (7.5-7.10) near an interface. We show with thick lines the fixed points N_W, L_T^+, N_T and L_W^- that the heteroclinic orbit should join (note that here we use the same names than in Section 6.4.3 and Appendix G to denote the fixed points of Eqs. (7.5-7.7) and (7.8 -7.10)). This heteroclinic orbit should flow from the fixed point $\mathbf{S}_W$ to the fixed point $\mathbf{S}_T$.

$a_T(\xi)$, corresponding to this heteroclinic orbit, is shown. These fixed points have coordinates:

$$\begin{aligned} \mathbf{S}_W &\overset{\text{def}}{=} (a_{W,N}, 0, q_{W,N}, 0, \kappa_{T,L}, q_{T,L}), \\ \mathbf{S}_T &\overset{\text{def}}{=} (0, \kappa_{W,L}, q_{W,L}, a_{T,N}, 0, q_{T,N}). \end{aligned} \tag{7.12}$$

7.3.3 Manifold structure around the fixed points

Let us now analyse the manifold structure of the fixed points defined in Eq. (7.12). Linearising Eq. (7.11) around $\mathbf{S}_W$ and $\mathbf{S}_T$, leads to the equation: $\partial_\xi \mathbf{S}' = \mathcal{T}\mathbf{S}'$, where $\mathbf{S}'$ is the perturbation around either $\mathbf{S}_W$ or $\mathbf{S}_T$ and the matrix $\mathcal{T}$ (the Jacobian) has the following form:

$$\mathcal{T} \overset{\text{def}}{=} \begin{pmatrix} \kappa_W & a_W & 0 & 0 & 0 & 0 \\ t_{2,1}a_W & X & X & t_{2,4}a_T & 0 & 0 \\ t_{3,1}a_W & X & X & t_{3,4}a_T & 0 & 0 \\ 0 & 0 & 0 & \kappa_T & a_T & 0 \\ t_{5,1}a_W & 0 & 0 & t_{5,4}a_T & X & X \\ 0 & 0 & 0 & 0 & X & X \end{pmatrix}, \tag{7.13}$$

where $t_{i,j}$ and X are a set of constants and functions respectively, that we do not need to consider explicitly. a_W, a_T, κ_W and κ_T should be substituted by their respective values at the fixed points $\mathbf{S}_W$ and $\mathbf{S}_T$ (*cf.* Eq. (7.12)).

The most important fact about the Jacobian $\mathcal{T}$ is that, at the fixed point $\mathbf{S}_W$, the upper-right block is zero (since $a_T = 0$) and that the same happens for the lower-left block at $\mathbf{S}_T$ (since now $a_W = 0$). Consequently, the eigenvalues of Eq. (7.13) are the eigenvalues of the upper-left block *plus* the ones of the lower-right block. Thus, the *problem decouples* and the manifold structure is given by the manifold structures of the single RGLE *plus* the single CGLE (*cf.* Eqs. (6.23) and (6.24) respectively in Section 6.4.5), provided that some redefinitions of η'_W, η_T, ω_W and v_{int} are done.

7.3.3.A Manifold structure around $\mathbf{S}_W$

More specifically, the eigenvalues of $\mathbf{S}_W$ will be given by the eigenvalues of the fixed point N_W of a single CGLE (*i.e.* of Eqs. (6.16-6.18) with functions $\mathcal{K}$ and $\mathcal{Q}$ as in Eqs. (6.21,6.22)), where we should use in place of v_{int}:

$$v_{int}^{eff} \overset{\text{def}}{=} v_{int} - s v_g, \tag{7.14}$$

plus the eigenvalues of the fixed point L_T^+ of a single RGLE (*i.e.* of Eqs. (6.16-6.18) with functions $\mathcal{K}$ and $\mathcal{Q}$ as in Eqs. (6.19,6.20)), where we should replace η_T by:

$$\eta_T^{\mathit{eff}} \overset{\text{def}}{=} \eta_T - h_{TW} a_{W,N}^2. \tag{7.15}$$

The manifold structures of N_W and L_T^+ are presented, in the Section 6.4.5, in Eqs. (6.24) and (6.23) respectively.

7.3.3.B Manifold structure around $\mathbf{S}_T$

On the other hand, the eigenvalues of $\mathbf{S}_T$ are given by the eigenvalues of the fixed point N_T (in Eq. (6.23)) plus L_W^- (in Eq. (6.24)), with effectives parameters:

$$\eta_W'^{\mathit{eff}} \overset{\text{def}}{=} \eta'_W - h_{WT} a_{T,N}^2, \tag{7.16}$$

$$\omega_W^{\mathit{eff}} \overset{\text{def}}{=} \omega_W + h_{WT} c_4 a_{T,N}^2, \tag{7.17}$$

$$v_{int}^{eff} \overset{\text{def}}{=} v_{int} - s v_g, \tag{7.18}$$

instead of η'_W, ω_W and v_{int}.

7.3.3.C Counting arguments for the heteroclinic orbit

In the following we will denote the manifold structure of $\mathbf{S}_W$ as N_W, L_T^+ and $\mathbf{S}_T$ as L_W^-, N_T. Summarising, *the counting arguments of the orbit* $\mathbf{S}_W \to \mathbf{S}_T$ *are equivalent to the ones of:*

$$N_W, L_T^+ \to L_W^-, N_T, \tag{7.19}$$

with appropriate redefinitions of η*,* ω *and* v_{int} (see Fig. 7.3).

Region	η'_W	$\eta'_W - h_{WT}\eta_T$	η_T	$\eta_T - h_{TW}\eta'_W$
I	> 0	> 0	< 0	< 0
II	> 0	> 0	> 0	< 0
III	> 0	< 0	> 0	< 0
IV	> 0	< 0	> 0	> 0
V	< 0	< 0	> 0	> 0

Table 7.2: In this table we define the different regions of the parameter space depending on the signs of η'_W, η_T, $\eta'_W - h_{WT}\eta_T$ and $\eta_T - h_{TW}\eta'_W$. See Fig. 8.1(a) for the location of these regions in the control parameter space.

Since the manifold structure around the fixed points of each *single* amplitude equation has many regimes depending in the free parameters v_{int} and ω (*cf.* Eqs. (6.23) and (6.24)), the manifold structure of the *coupled* equations (7.5-7.10) has even more regimes.

7.3.4 Some remarks about the coherent structures

7.3.4.A Regions in parameter space

Beside the different regimes that arise depending on the value of v_{int} and v_{int}^{eff} with respect to the critical velocities v_T^c, v_W^c and v_W^{cN} (defined in the Appendix G, in the Eqs. (G.16) and (G.27)), we can distinguish five different regions of the parameter space depending on the signs of η'_W and η_T. We give the definition of these regions in Table 7.2. In Fig. 7.4 the location of these regions in the control parameter space is given (compare these figures with Figs. 5.11 and 5.12). Note that the boundaries separating these regions are given by the places in parameter space where η'_W, η'^{eff}_W, η_T and η_T^{eff} change signs.

In region **I**, with $\eta'_W > 0$ and $\eta_T < 0$, only travelling waves exist. Equivalently in region **V**, with $\eta_T > 0$ and $\eta'_W < 0$, only Turing patterns exist. In these two regions the amplitude of either the Turing or the wave pattern is zero. Travelling interfaces also exist in these regions; however they consist, in region **I**, of a wave pattern invading a zero state and, in **V**, of a Turing invading zero state.

In regions **II**, **III** and **IV** both patterns can exist. Note that region **III** is the *bistability region* introduced in Chapter 5. An important point is that interfaces can exist, *not only* in region **III**, but also in regions **II** and **IV**. In these regions, one of the patterns is unstable[3], but in practice, where the

---

[3] Note, however, that to obtain this result we assumed that this pattern was infinitely extended.

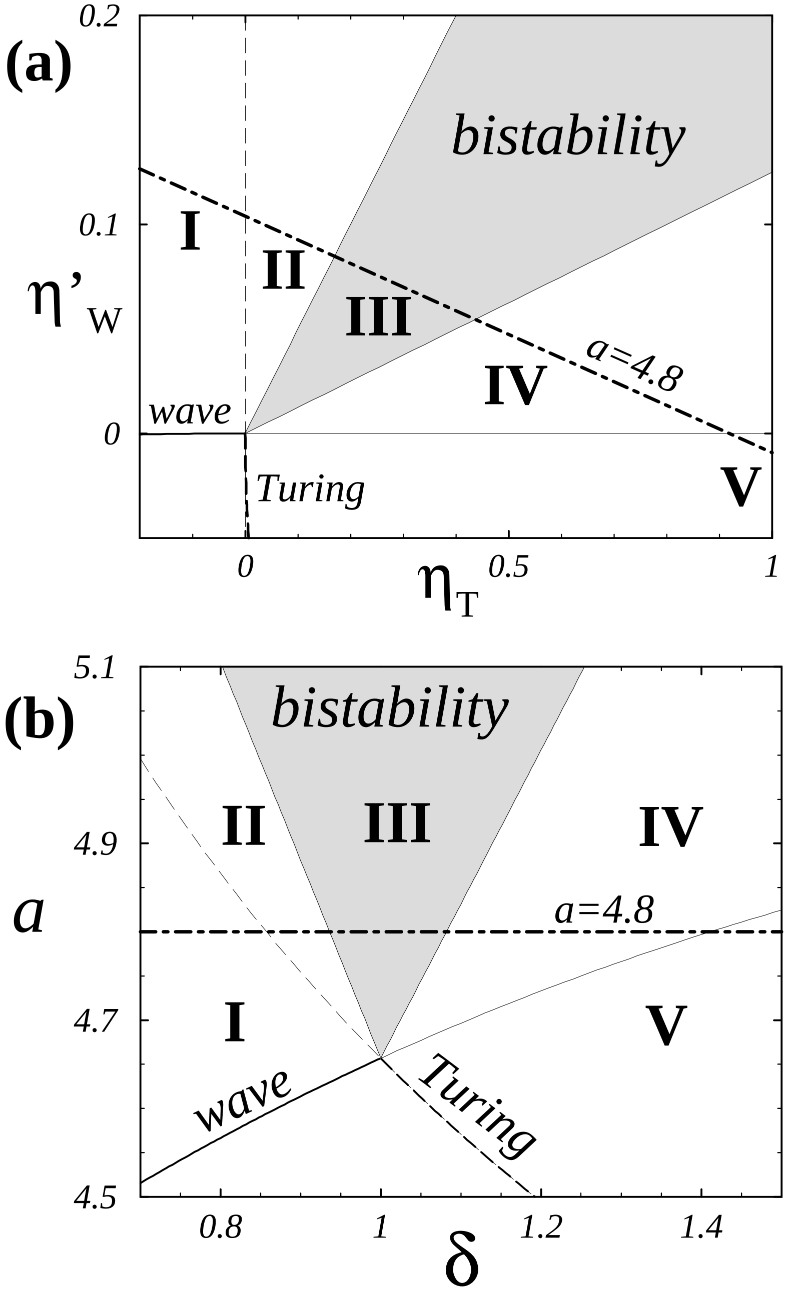

Figure 7.4: The control parameter space near the codimension-2 wave-Turing instability showing the different regions defined in Table 7.2. The dot-dashed lines correspond to a constant value of the control parameter a (in this case: $a = 4.8$). In (a) the space is spanned by the control parameters $\eta'_W(a, \delta)$ and $\eta_T(a, \delta)$ of the amplitude equations (4.81, 4.80, 4.82) and, equivalently, in (b) by the control parameters a and δ appearing in the RDNC model. Compare each of these figures with Figs. 5.11 and 5.12 respectively.

perturbations are very small, this instability can take a long time to switch from one pattern to the other. Meanwhile, a travelling interface separating both patterns is typically observed in numerical simulations of the amplitude equations (and of the RDNC model). In region **V** the amplitudes of the wave and Turing patterns are zero and nonzero respectively. The opposite is true in region **I**.

7.3.4.B Choice of the free parameters of the ansatz

It is possible to use $q_{W,N}$, $q_{T,N}$ and v_{int}, instead of ω_W, ω_T and v_{int}, as the three independent free parameters of the ansatz of Eqs. (7.3,7.4). Since $q_{W,N}$ and $q_{T,N}$ have a direct physical interpretation this alternative is preferable. Indeed, the wavenumber $q_{W,N}$ is equivalent to the parameter p_W (either p_R or p_L) of the constant amplitude travelling wave solutions given in Eq. (5.2) (or Eq. (5.3)), that the interface joins at $\xi \to -\infty$. Equivalently, $q_{T,N}$ is identical to the parameter p_T of the family of constant amplitude Turing solutions given in Eq. (5.12), that the interface joins at $\xi \to +\infty$.

7.3.4.C Relation between free parameters and numerical simulations

In the next chapters we will perform many numerical simulations of Eqs. (7.1,7.2) to investigate the dynamics of interfaces. Let us establish the connection between the free parameters of these simulations and the parameters of the coherent structure ansatz. We will start typically with an *initial condition* corresponding to the left half of the system length with a constant amplitude travelling wave and the right half with constant amplitude Turing structure. In the following we will denote the wavenumbers of these two initial patterns as p_W^{ic} and p_T^{ic}. We can choose freely the value of these two parameters.

With this initial condition a coherently moving interface separating the two patterns will typically develop after a transient time. In this case we should distinguish between three different situations:

1. An interface travelling with velocity v_{int} develops (after a short transient). In this case the interface joins two patterns with wavenumbers p_W^{ic} and p_T^{ic}.
2. The interface that builds joins a pattern with either p_W^{ic} or p_T^{ic} on one side, but selects a particular wavenumber on the other side: p_T^{sel} or p_W^{sel}, which is different from the imposed p_T^{ic} or p_W^{ic} respectively.
3. The interface selects wavenumbers p_W^{sel} and p_T^{sel} in both sides.

Clearly, the wavenumbers p_W^{ic} and p_W^{sel} are directly related to $q_{W,N}$. Equivalently p_T^{ic} and p_T^{sel} are related to $q_{T,N}$. In the next chapter we will alternate between both sets of parameters.

7.4 Scaling of the amplitude equations with the distance to the codimension-2 point

Note that if we perform the following changes of variables: $\partial_{\hat{t}} = \frac{\partial_t}{\eta_T}$ and $\partial^2_{\hat{x}} = \frac{\partial^2_x}{\eta_T}$, and introduce the following scaled amplitudes: $\widehat{A}_W = \frac{\widetilde{A}_W}{\sqrt{\eta_T}}$ and $\widehat{A}_T = \frac{\widetilde{A}_T}{\sqrt{\eta_T}}$, in the coupled amplitude equations (7.1,7.2), then we get:

$$\begin{aligned}
\partial_{\hat{t}}\widehat{A}_W + s\,\frac{v_g}{\sqrt{\eta_T}}\partial_{\hat{x}}\widehat{A}_W &= \frac{\eta'_W}{\eta_T}\widehat{A}_W + (1+ic_1)\partial^2_{\hat{x}}\widehat{A}_W - (1-ic_3)|\widehat{A}_W|^2\widehat{A}_W \\
&\quad -h_{WT}(1-ic_4)|\widehat{A}_T|^2\widehat{A}_W, \\
\partial_{\hat{t}}\widehat{A}_T &= \widehat{A}_T + d_{TW}\partial^2_{\hat{x}}\widehat{A}_T - |\widehat{A}_T|^2\widehat{A}_T - h_{TW}|\widehat{A}_W|^2\widehat{A}_T.
\end{aligned}$$

If $v_g = 0$, then these equations only depend on the ratio η'_W/η_T (and not on η'_W and η_T independently). Consequently, the properties of the interfaces do not change along a "ray" in the control parameter space[4] η'_W vs. η_T of Fig. 7.4(a) or 7.4(b). But, since typically $v_g \neq 0$, the properties of the wave-Turing interfaces will depend on both η'_W/η_T and η_T! In the next chapter we will analyse this issue in more detail.

---

[4] This means that the properties of the interfaces do not vary over a straight line in the control parameter space (with $\eta'_W > 0$ and $\eta_T > 0$) passing through the codimension-2 point.

Chapter 8

Dynamics of interfaces near codimension-2 bifurcations

In this chapter we will study the dynamics and scaling properties of interfaces between competing patterns arising from a codimension-2 instability. Our main objective is to understand the dynamics of wave-Turing interfaces. We will, however, also consider some simpler cases, including Turing-Turing and Hopf-Turing interfaces.

To study the dynamics of interfaces in the coupled amplitude equations we will apply the counting arguments to the coherent structure ansatz introduced in Chapter 7. Further insight will be attained with direct numerical simulations of the amplitude equations. The results of this analysis will be compared with numerical simulations of wave-Turing interfaces in the RDNC model near the codimension-2 instability threshold.

8.1 Introduction

In this chapter we want to understand the dynamical behaviour and scaling properties of wave-Turing interfaces near the codimension-2 instability. To achieve this, we will study the corresponding coupled amplitude equations (7.1,7.2) and compare the results of this investigations with numerical simulations of the RDNC model. In the previous chapter we initiated the analysis of the phase space of the effective ODEs (7.5-7.10). In this chapter we will continue this study.

Before embarking on the study of wave-Turing interfaces we will analyse interfaces in simpler situations. More specifically, we will first study interfaces between two competing Turing patterns. Afterwards, we will discuss the case of interfaces between competing Hopf and Turing domains. Finally, in Section 8.4, we will address the problem of wave-Turing interfaces.

Most of the results of this chapter will not depend on the particular values of the coefficients of the amplitude equations. Consequently, the approach used here will, not only provide us with a good understanding of the dynamics of interfaces near a wave-Turing instability, but it will also elucidate simpler codimension-2 cases (*e.g.* Turing-Turing or Hopf-Turing).

- Organisation of this chapter

In the next section we will give a short description of the strategy that we will use in this chapter. In Section 8.3 we will analyse interfaces in some preliminary cases of coupled amplitude equations. In Section 8.4 we will address the wave-Turing interfaces, first in the amplitude equations and then compare qualitatively and quantitatively their results with numerical simulations of interfaces in the RDNC model.

8.2 Strategy for the study of the interface dynamics

The control parameter space can be spanned either by η'_W and η_T or by a and δ (*cf.* Figs. 7.4(a) and 7.4(b)). Due to the linear mapping introduced in Table 4.2 both alternatives are equivalent. Here we will work mainly with the second choice.

In order to study the interface dynamics we will consider a cut in the parameter space corresponding to constant value of a. In particular we will choose $a = 4.8$ (indicated wit a dot-dashed line in Figs. 7.4). With this cut we will “scan” the different regions of the parameter space.

8.3 Preliminary cases: Turing-Turing and Hopf-Turing interfaces

In order to gain insight into the behaviour of interfaces in Eqs. (7.1,7.2) and their corresponding heteroclinic orbits in Eqs. (7.5-7.10) let us analyse first some special cases. Namely, we will assume that the imaginary part of the coefficients (*i.e.* c_1, c_2 and c_4) and/or the group velocity v_g of Eqs. (7.1,7.2) are zero. We will consider only cases where the cross-coupling coefficients h_{WT} and h_{TW} are such that the patterns suppress each other (i.e. there exist *competition* between the bifurcating patterns). This selection of coefficient values will lead us to analyse in this section interfaces between competing Turing-Turing, Turing-Turing with $v_g \neq 0$ and Hopf-Turing instabilities in Sections 8.3.1, 8.3.2 and 8.3.3 respectively.

- Remarks

Let us remark that, in spite of the new physical interpretation of the patterns involved at the codimension-2 instability, we will keep the subscripts W and T in Eqs. (7.1,7.2) and (7.5-7.10) to indicate the pattern domains on the left and right side of the interface respectively.

Whenever numerical simulation of the partial differential equations (7.1,7.2) are done in this section, the coefficients (except for the aforementioned coefficients set to zero) will be set to the values given in Table 4.2. Consequently the control parameter space of Fig. 7.4(a) (and Fig. 7.4(b)), and the regions plotted on it, are still valid despite the new interpretation of the competing patterns.

- *Caveat Lector*

The description of the interface dynamics in this section will be very involved and consequently not easy to follow. For this reason, in Section 8.3.4 (and Chapter 10) we will give a short summary of the main results of this section.

8.3.1 Turing-Turing interfaces

Let us start by analysing the case where:

$$v_g = c_1 = c_2 = c_4 = 0. \tag{8.1}$$

Such a situation will arise if a pattern forming system is near a codimension-2 instability where *two Turing instabilities*, with different critical wavenumbers, meet. In this subsection we will analyse interfaces separating these two, different, Turing patterns. In the following we will call these Turing-Turing interfaces (**TTIs**).

Note that $v_g = 0$ means that $v_{int}^{eff} \equiv v_{int}$ in Eq. (7.18) and that, as we saw in Section 7.4, the properties of the interfaces depend only on the value of the ratio η'_W/η_T. This peculiarity implies that the behaviour of the interfaces in *any* point of the control parameter space η'_W vs. η_T can be deduced from a unique "cut" that includes regions **I** to **V**. Here we will consider $a = 4.8$.

8.3.1.A Simplest case: Constant phases on *both* sides

In order to get the simplest case where interfaces between competing patterns exist, let us further suppose that both amplitudes, $\widetilde{A}_W$ and $\widetilde{A}_T$ (where $\widetilde{A}_W \equiv \rho_W e^{\Phi_W}$ and $\widetilde{A}_T \equiv \rho_T e^{\Phi_T}$), have *constant phase* (*i.e.* $\Phi_W(x,t) = const.$ and $\Phi_T(x,t) = const.$). Consequently $\omega_W = 0$ and $\omega_T = 0$ in the ansatz of Eqs. (7.3,7.4).

A constant value of both phases implies that the local wavenumbers are:

$$q_W(\xi) \equiv q_T(\xi) \equiv 0.$$

Consequently, the corresponding ODEs are the *four* Eqs. (7.5,7.6,7.8,7.9) (with coefficients as in Eq. (8.1)).

For a Turing instability to be described by a complex amplitude with constant phase, the critical wavenumber of the instability should be $k_T^c \equiv 0$. Therefore, the simplified case that we are analysing here corresponds to a codimension-2 Turing-Turing instability where both instabilities have zero wavenumber[1]. This situation can not happen in a physical model and consequently the analysis to be presented here is just didactic. However, as we will see later, the interfaces that arise in this case will play an important rôle in the analysis of interfaces in the general Turing-Turing, Hopf-Turing and Wave-Turing cases (see Sections 8.3.1.C, 8.3.3 and 8.4 respectively).

- Fixed point $\mathbf{S}_W$

Let us now analyse the fixed point $\mathbf{S}_W$ and its manifold structure. In section 7.3.3.A we saw that the manifold structure of this fixed point can be calculated using the manifold structures around the fixed points N_W and L_T^+ of the single RGLE with constant phase (*cf.* Eq. (6.11)) where η_T should be substituted by η_T^{eff}. Using Eq. (7.6) we get: $a_{W,N}^2 = \eta'_W$, and consequently:

$$\eta_T^{\mathit{eff}} = \begin{cases} \eta_T - h_{TW}\eta'_W & \text{if } \eta'_W \geq 0 \quad (i.e. \text{ in regions } \mathbf{I\text{-}IV}) \\ \eta_T & \text{if } \eta'_W < 0 \quad (i.e. \text{ in region } \mathbf{V}) \end{cases} . \tag{8.2}$$

In Fig. 8.1(a) we illustrate the values of $\eta_W'^{\mathit{eff}}$, η'_W, η_T^{eff} and η_T for the case of constant value of the control parameter a. Note how the points where each value changes signs define the boundaries between regions **I-V**.

We can now compute the manifold structure of $\mathbf{S}_W$. Using Eq. (6.11) we deduce that, if $\eta'_W > 0$ (*i.e.* in regions **I-IV**), the manifold structure of this

---

[1] Alternatively; it can be said that this case corresponds to a codimension-2 Pitchfork-Pitchfork bifurcation in an extended system.

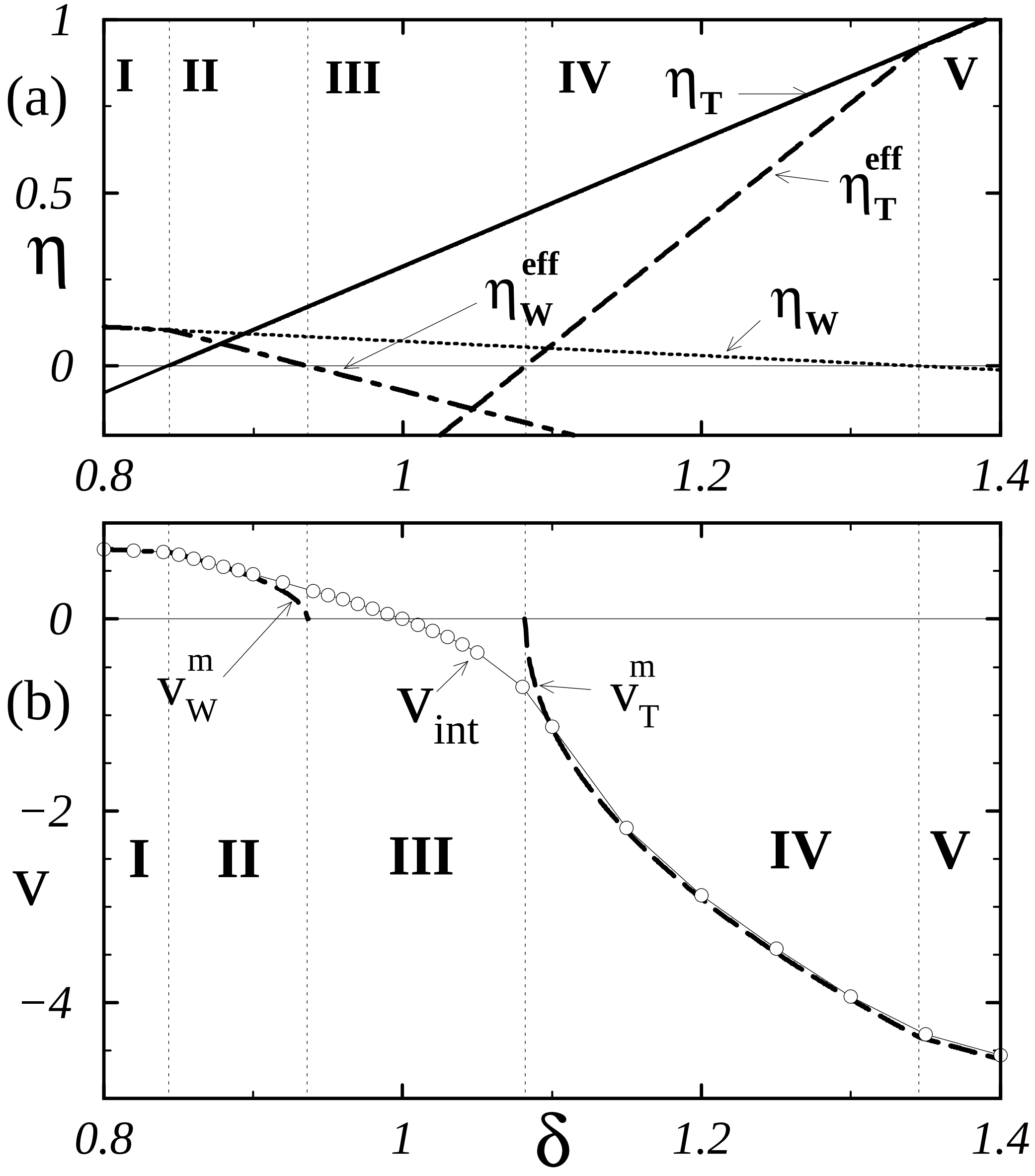

Figure 8.1: Plot of the values of the different η (in (a)) and of the velocity v_{int} of TTIs (with constant phase) as as the control parameter δ varies and a is kept constant ($a = 4.80$). Note, in (a), that the values of δ for which the etas change signs are the boundaries of regions **I** to **V**. In (b) the circles and the thin line joining them show the velocity of the interface v_{int} measured from numerical simulations of Eqs. (7.1,7.2) with coefficient values as in Eq. (8.1). The dot-dashed and dashed thick lines correspond to the interface velocities v_W^m and v_T^m introduced in Eqs. (8.7) and (8.4) respectively. See Figs. 8.3(a) and 8.3(b) for a detailed plot of the interface velocity.

fixed point has many different cases, depending on the values of η_T^{eff} and v_{int}. They can be summarised in the following way:

$$\begin{cases} \text{if} \quad \eta_T^{\mathit{eff}} < 0 \ (\textit{i.e.} \text{ in reg. } \textbf{I-III}) \text{ and } \quad \forall v_{int} : & N_W(+,-), L_{T,2}^{+}(+,-) \\ \text{if} \quad \eta_T^{\mathit{eff}} > 0 \ (\textit{i.e.} \text{ in reg. } \textbf{IV}) \text{ and } \begin{cases} v_{int} > v_T^m : & \nexists L_T^{+} \\ v_{int} < v_T^m : & \begin{cases} N_W(+,-), L_{T,1}^{+}(+,+) \\ N_W(+,-), L_{T,2}^{+}(+,-) \end{cases} \end{cases} \end{cases} \tag{8.3}$$

where the critical velocity is given by:

$$v_T^m = -2\sqrt{\eta_T^{\mathit{eff}} d_{TW}}. \tag{8.4}$$

Consequently, depending on the sign of η_T^{eff} and the value of v_{int}, there exist two, one or no fixed point $\mathbf{S}_W$. Note that in the case where two fixed points exist (*i.e.* in region **IV** and for $v_{int} > v_T^m$) they have manifold structures: $\mathbf{S}_{W1}(+,-,+,+)$ and $\mathbf{S}_{W2}(+,-,+,-)$ (where $\mathbf{S}_{W,1} \equiv N_W, L_{T,1}^{+}$ and $\mathbf{S}_{W,2} \equiv N_W, L_{T,2}^{+}$ if we use the notation introduced in section 7.3.3.C), and satisfy: $\kappa_{T,L1} < \kappa_{T,L2}$ (*cf.* Eq. (6.9)).

On the other hand, for $\eta'_W < 0$ (*i.e.* in region **V**) the fixed point N_W does not exist. This last case will be discussed later in this section.

- Fixed point $\mathbf{S}_T$

Similarly, in the case of the fixed point $\mathbf{S}_T$ the relevant parameters to calculate the manifold structure are η_T and $\eta_W'^{\mathit{eff}}$ (see discussion in Section 7.3.3.B) where:

$$\eta_W'^{\mathit{eff}} = \begin{cases} \eta'_W - h_{WT}\eta_T & \text{for } \eta_T > 0 \quad (\textit{i.e.} \text{ in regions } \textbf{II-V}) \\ \eta'_W & \text{for} \quad \eta_T \le 0 \quad (\textit{i.e.} \text{ in region } \textbf{I}) \end{cases} . \tag{8.5}$$

In Fig. 8.1(a) the values of these quantities are plotted as a function of δ, for a constant value of a.

If $\eta_T > 0$ (*i.e.* in regions **II-V**), then the manifold structure around $\mathbf{S}_T$ can be summarised by:

$$\begin{cases} \text{if} \quad \eta_W'^{\mathit{eff}} < 0 \ (\textit{i.e.} \text{ in reg. } \textbf{III-V}) \text{ and } \quad \forall v_{int} : & N_T(+,-), L_{W,1}^{-}(+,-) \\ \text{if} \quad \eta_W'^{\mathit{eff}} > 0 \ (\textit{i.e.} \text{ in reg. } \textbf{II}) \text{ and } \begin{cases} v_{int} > v_W^m : & \begin{cases} N_T(+,-), L_{W,1}^{-}(+,-) \\ N_T(+,-), L_{W,2}^{-}(-,-) \end{cases} \\ v_{int} < v_W^m : & \nexists L_W^{-} \end{cases} \end{cases} \tag{8.6}$$

where:

$$v_W^m = 2\sqrt{\eta_W'^{\mathit{eff}}}. \tag{8.7}$$

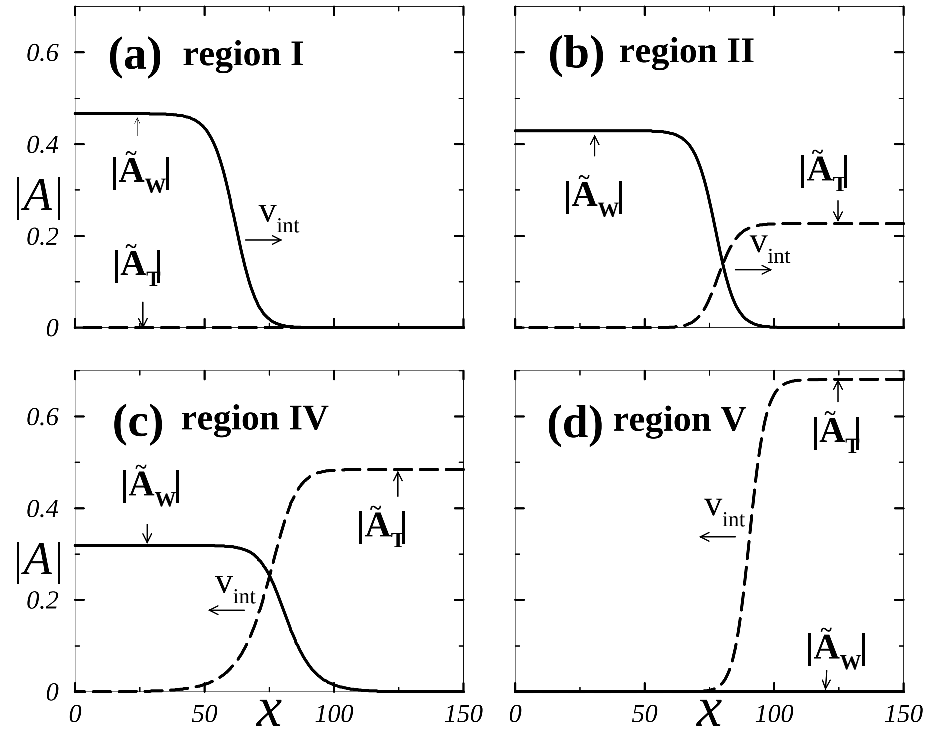

Figure 8.2: Plots of the amplitudes near a TTI (with constant phase) in *numerical simulations* of the coupled amplitude equations (7.1,7.2) (with coefficients as in Eq. (8.1)). The amplitudes $|\widetilde{A}_W|$ and $|\widetilde{A}_T|$ are plotted with full and dashed lines respectively. The simulations were done with four different values of δ and constant value of a. Only a small part of the system, near the interface, is shown in each case. The arrows indicate the direction of movement of the interface. In all the figures $a = 4.80$ and in (a) $\delta = 0.82$ (*i.e.* region **I**), (b) $\delta = 0.90$ (*i.e.* region **II**), (c) $\delta = 1.10$ (*i.e.* region **IV**) and (d) $\delta = 1.35$ (*i.e.* region **V**).

Note again that in region **II**, where two fixed points $\mathbf{S}_{T,1} \equiv N_T, L^-_{W,1}$ and $\mathbf{S}_{T,2} \equiv N_T, L^-_{W,2}$ exist, they satisfy (*cf.* Eq. (6.9)):

$$\kappa_{W,L1} < \kappa_{W,L2}. \tag{8.8}$$

In region **I**, where $\eta'_W < 0$, the fixed point N_T does not exist. This case will be discussed later.

- Interface velocity: numerical simulations of the amplitude equations

The circles joined by a thin line in Fig. 8.1(b) show the velocity v_{int} of TTIs, measured in numerical simulations of the PDEs (7.1,7.2), with coefficients as in Eq. (8.1) (and using $p_W^{ic} \equiv p_T^{ic} \equiv 0$ as initial conditions). As an illustration of the shape of these interfaces, in Fig. 8.2 we show four different examples of the profiles of the amplitudes $|\widetilde{A}_W|$ and $|\widetilde{A}_T|$. Note that in regions **I** and **II** the velocity v_{int} is positive whereas in **IV** and **V** is negative; the direction of movement of the interface changes in region **III**.

In the rest of this subsection we will analyse these data using counting arguments and the leading edge approach. This analysis will explain the features seen in Fig. 8.1(b) and give further generic insight on the dynamics of TTIs

- Interface velocity: theoretical predictions

Let us now analyse in detail the dynamics of TTIs with constant phase. Here we will study theoretically the interface velocity in each region.

- Regions I and V

The properties of interfaces in regions **I** and **V** are equivalent. Let us first analyse region **I**. Here the nonlinear fixed point N_T does not exist. This can be seen in Fig. 8.2(a) where the profiles of $|\widetilde{A}_W|$ and $|\widetilde{A}_T|$ near the interface are shown. Note that the amplitude $|\widetilde{A}_T|$ of the Turing pattern is always zero. Consequently, the interface consists in nothing else but a front separating $|\widetilde{A}_T| = a_{W,N}$ and $|\widetilde{A}_T| \equiv 0$. The counting arguments for such a front^2 have been done already in Section 6.4.3 (*cf.* Eq. (6.12)).

We saw in Section 6.4.4 that the dynamics of such fronts is in accord with the linear propagation regime (**LP** in the following). This is; the behaviour of the front is well captured by the dynamics of the leading edge combined with the marginal stability criterion. We recall that this approach predicts that the front will propagate with velocity equal to the marginal velocity $v_W^m(\eta_W'^{eff})$ introduced in Eq. (8.7) (note that in this region $\eta_W'^{eff} \equiv \eta_W'$).

In Fig. 8.3(a) (see also Fig. 8.1(b)) we show the *measured* interface velocity v_{int} and the *theoretical* marginal velocity v_W^m. Note that, as expected, both coincide in region **I**.

Let us now analyse the behaviour in region **V**. In Fig. 8.2(d) the profiles of $|\widetilde{A}_W|$ and $|\widetilde{A}_T|$ are shown in this region. In this case $|\widetilde{A}_W| \equiv 0$. Consequently the analysis of the interfaces in this region is equivalent to region **I**. The marginal velocity of the leading edge is given now by $v_T^m(\eta_T^{eff})$ (*cf.* Eq. (8.4)).

---

[2] Note that if we allow the value of $|\widetilde{A}_T|$ to be different from zero in the interface neighbourhood, then the the counting arguments of the interfaces are given by $N_W, L_T^+ \to L_T^- L_W^-$. But the results of these counting arguments give the same values than for the the orbit $N_W \to L_W^-$ (*i.e.* either a 0 or 1 PF; see Eq. (6.12)).

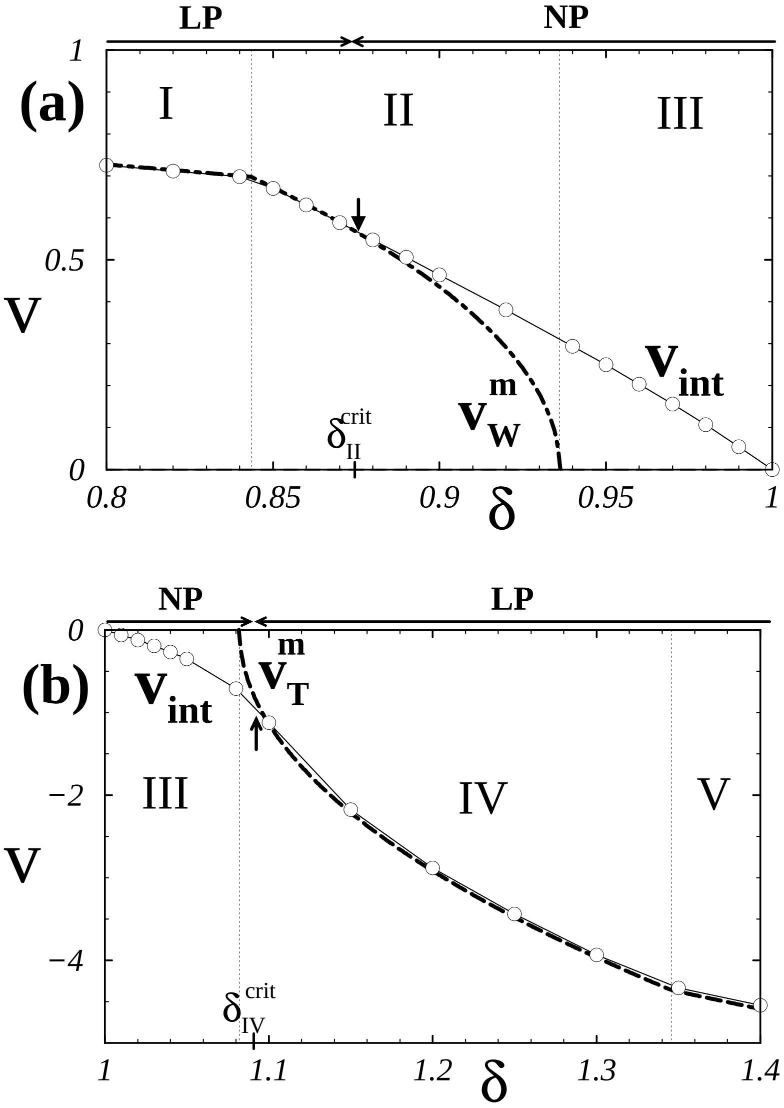

Figure 8.3: The circles show the velocity v_{int} of TTIs measured from numerical simulations of Eqs. (7.1,7.2) (with coefficients as in Eq. (8.1)) as a function of δ and for a fixed a ($a = 4.8$). These figures are close-ups of Fig. 8.1(b). In (a) values of $\delta < 1$ are shown; the dot-dashed line corresponds to the marginal velocity v_W^m (*cf.* Eq. (8.7)). In (b) $\delta > 1$ and the dashed line is the marginal velocity v_T^m (*cf.* Eq. (8.4)). Note the good agreement between the theoretical marginal velocities: v_W^m and v_T^m, and the measured v_{int} in regions **I** and **V** and in part of regions **II** and **IV**. The places where v_{int} becomes different from the marginal values in regions **II** and **IV** are indicated with a thick arrows and the corresponding values of δ with δ_{II}^{crit} and δ_{IV}^{crit}. The regimes where linear and nonlinear propagation of the TTI are valid are denoted by **LP** and **NP** respectively.

Notice the good agreement in region **V** between the measured v_{int} and v_T^m in Fig. 8.3(b) (see also Fig. 8.1(b)).

Furthermore, in Figs. 8.3(a) and 8.3(b) it can be seen that the leading edge dynamics does also predict the interface velocity in part of regions **II** and **IV**. This will be analysed in more detail in the following paragraphs.

- Regions II and IV

The behaviour of the interface is very similar in regions **II** and **IV**. Let us first discuss the case of region **II**. The possible heterogenous orbits and their respective counting arguments can be summarised as (*cf.* Appendix F):

$$\begin{cases} v_{int} > v_W^m \begin{cases} N_W(+,-), L^+_{T,2}(+,-) \to N_T(+,-), L^-_{W1}(+,-) & \Rightarrow 0 \text{ PF} \\ N_W(+,-), L^+_{T,2}(+,-) \to N_T(+,-), L^-_{W2}(-,-) & \Rightarrow 1 \text{ PF} \end{cases} \\ v_{int} < v_W^m \qquad\qquad\qquad\qquad\qquad \nexists L^-_W \end{cases} \tag{8.9}$$

Note that heteroclinic orbits are possible only if $v_{int} \geq v_W^m$. In particular, for $v_{int} > v_W^m$ two possible orbits exist. These orbits have different values of κ_W; namely (*cf.* Eqs. (6.8,6.9)):

$$\kappa_{W,L1} = \frac{-v_{int} - \sqrt{v_{int}^2 - 4\eta'^{eff}_W}}{2} \quad \text{and} \quad \kappa_{W,L2} = \frac{-v_{int} + \sqrt{v_{int}^2 - 4\eta'^{eff}_W}}{2}. \tag{8.10}$$

In the special case where $v_{int} \equiv v_W^m$ there is only *one orbit possible* since $L^-_{W1} \equiv L^-_{W2}$. Note that the counting arguments are not valid in this case because there is a eigenvalue of $\mathbf{S}_T$ (*i.e.* $\mathbf{S}_T(+,-,0,-)$) *equal to zero.* This orbit has the following decaying rate:

$$\kappa_W^m \overset{\text{def}}{=} -v_W^m/2. \tag{8.11}$$

In Fig. 8.3(a) we plot v_{int} (circles) and v_W^m (dot-dashed line) in region **II**. Note that in part of this region these velocities are equal. This occurs for $\delta < \delta_{II}^{crit}$ and corresponds to the **LP** regime. For $\delta > \delta_{II}^{crit}$ the velocity v_{int} is bigger than v_W^m. This corresponds to the nonlinear propagation (**NP**) regime.

Let us now examine in detail the differences between the **LP** and **NP** regimes. In Fig. 8.4 we plot the value of the decaying rate κ_W *measured*[3] directly from the numerical simulations of the PDEs (big circles joined by a

---

[3] To calculate this value we perform the ratio between $\partial_x |A_W(x,t)|$ and $|A_W(x,t)|$. This ratio goes to a constant value on the right side of the interface. This constant value is the measured κ_W.

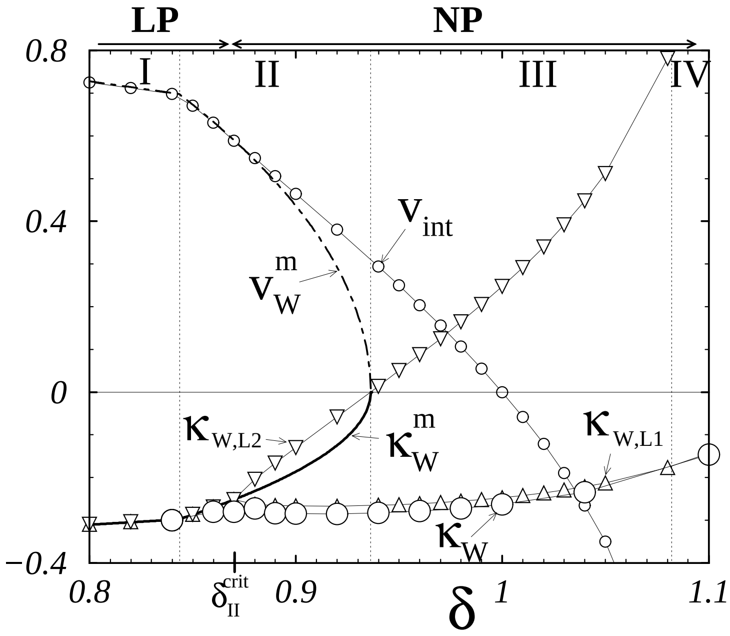

Figure 8.4: Plot of the decaying rates of the TTIs. The big circles correspond to the values of the *measured* κ_W from the numerical simulations of the amplitude equations (see caption in Fig. 8.1 for details). The down and up triangles correspond to $\kappa_{W,L1}$ and $\kappa_{W,L2}$ respectively, as *calculated* using Eqs. (8.10) (where for v_{int} we use the values measured in the numerical simulations; the small circles). The thick full line corresponds to the *theoretical* value κ_W^m corresponding to interfaces with velocity equal to the marginal v_W^m (the equation for κ_W^m is given in Eq. (8.11)). Note that the measured κ_W coincides with κ_W^m for $\delta < \delta_{II}^{crit}$. In this region the TTI are in the **LP** regime. For $\delta > \delta_{II}^{crit}$ the decaying rate κ_W coincides with $\kappa_{W,L1}$. In this region the TTI are in the **NP** regime and the counting arguments (*cf.* Eq. (8.9)) predict a 0 parameter family of heteroclinic orbits.

thin line) and the value of the *theoretical* κ_W^m (*cf.* Eq. (8.11)) with a thick full line. We also plot in this figure the values of $\kappa_{W,L1}$ and $\kappa_{W,L2}$ (up and down triangles respectively). These last values are calculated inserting the measured values of v_{int} and $\eta_W'^{eff}$ in Eq. (8.10). Note that, as far as $\delta < \delta_{II}^{crit}$, the measured κ_W coincides with the marginal κ_W^m (and here: $\kappa_{W,L1} = \kappa_{W,L2} = \kappa_W^m$). On the other hand, for $\delta > \delta_{II}^{crit}$, the measured values of κ_W coincide with $\kappa_{W,L1}$ (calculated using Eq. (8.10)). This means that the TTI corresponds[4] to the orbit: $N_W, L_T^+ \to N_T, L_{W1}^-$, which is a 0 PF; *i.e.* a *discrete set* (recall the counting arguments of Eq. (8.9)). This is in full agreement with the behaviour of the TTIs in numerical simulations of the

---

[4] Note that the counting arguments of Eq. (8.9) predict the existence of two different types of heteroclinic orbits: a 0 PF and a 1 PF. We *conjecture* that the interfaces in the coupled amplitude equations correspond always the the orbit with smaller multiplicity.

amplitude equations.

Consequently, for $\delta < \delta_{II}^{crit}$ the interface velocity is given by the leading edge approach; whereas for $\delta > \delta_{II}^{crit}$ the counting arguments predict a discrete set. Note that it is not obvious that the leading edge approach will work for $\delta < \delta_{II}^{crit}$ (in region **II**); there the interfaces join two patterns with *nonzero* amplitude! Also note that the value of δ_{II}^{crit} corresponds to the point where the $\kappa_{W,L1}$ determined by the discrete family becomes equal to κ_W^m. But since the value of $\kappa_{W,L1}$ can not be calculated analytically, the δ_{II}^{crit}, signalling the transition between the **LP** and **NP** regimes, can only be obtained numerically. The value of δ_{II}^{crit} will typically depend on the values of the coefficients of the coupled amplitude equations.

Note that in the **LP** regime the counting arguments are *inconclusive* since one of the eigenvalues around the fixed points is zero and consequently is not *hyperbolic*[5].

The discussion of the interface behaviour in region **IV** is equivalent to the previous discussion for region **II**. In Fig.8.3(b) the values of v_{int} and v_T^m are plotted (see also Fig. 8.1(b)). They coincide if $\delta > \delta_{IV}^{crit}$. Note that the range of validity of the **LP** regime is very big (*i.e.* δ_{IV}^{crit} is near the border between regions **III** and **IV**). For $\delta < \delta_{IV}^{crit}$ the TTI corresponds to the **NP** regime.

Note that the values of δ_{II}^{crit} and δ_{IV}^{crit} depend on the control parameter a. But, as we saw in Section 7.4, they are part of a straight line in the control parameter space passing through the codimension-2 point.

- Region III (bistability)

The **NP** regime extends to region **III**. Here only one orbit is possible and the counting arguments give:

$$N_W(+,-), L_{T,2}^{+}(+,-) \rightarrow N_T(+,-), L_{W,1}^{-}(+,-) \quad \Rightarrow 0 \text{ PF}. \qquad (8.12)$$

The velocity v_{int} of this discrete[6] orbit can only be calculated numerically. Nevertheless, some generic information about this velocity can extracted just analysing the velocities in regions **III** and **IV**. Indeed; v_{int} should be *positive* in the border between regions **II** and **III** and *negative* between regions **III** and **IV**. Consequently, v_{int} should be zero somewhere in region **III**. Therefore, the velocity of the TTI reverses. In Fig. 8.1(b) the value of this velocity is plotted for a constant value of the parameter a.

---

[5] In Appendix F we explain in detail why the fixed points should be hyperbolic for the counting arguments to be valid.

[6] Note that, although a discrete set theoretically allows for more than one velocity value, in practice a *unique* velocity is typically found!

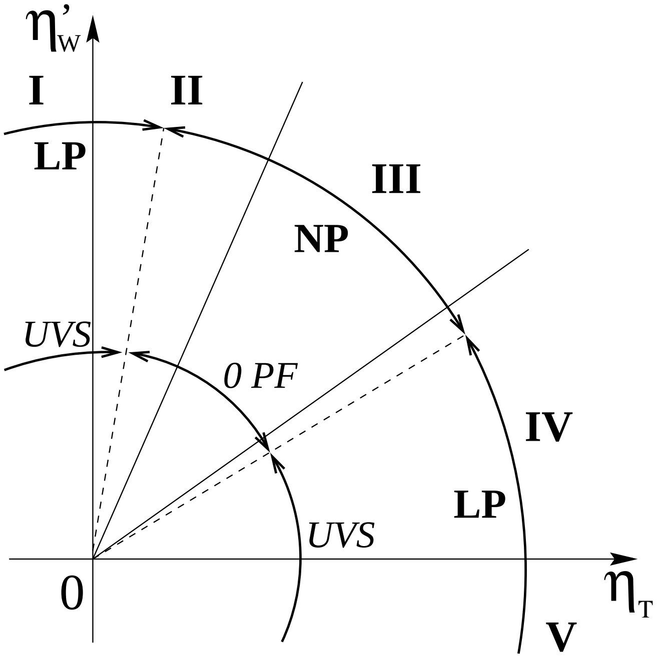

Figure 8.5: Schematic summary of the results for *Turing-Turing interfaces with constant phase in both sides*. The different regions **I** to **V** are indicated in the control parameter space η'_W vs. η_T. In the outer semicircle indicates the range of validity of the **LP** and **NP** regimes. In the inner one we indicate the kind of parameter family corresponding to the interface. In the **NP** regime this is a *discrete set*. This is symbolised by *0 PF*. In the **LP** regime a unique velocity is selected (this is indicated with *UVS*). Consequently, for any value of the control parameters, only one interface is typically realized in numerical simulations of the coupled amplitude equations.

- Summary of results for Turing-Turing interfaces with constant phase in both sides

Let us now summarise the results for interfaces separating two Turing patterns with constant phase.

The dynamics of the interfaces is given by either the **LP** or **NP** regime. The change between these regimes occurs in two straight lines in the control parameter space (see sketch in Fig. 8.5). This lines are located in regions **II** and **IV** respectively. Their exact location depends on the coefficients of the amplitude equations and can only be calculated numerically.

The **NP** regime is found in a central region of the control parameter space (in region **III** and part of regions **II** and **IV**). In this regime the counting arguments predict a discrete family of heteroclinic orbits (*i.e.* 0 PF). The velocity of this interface should reverse signs in region **III** and can only be calculated numerically.

In the rest of the control parameter space the interfaces correspond to the **LP** regime. This regime predicts a *unique velocity selected* (*UVS*). The selected velocity can be calculated analytically.

Finally, let us mention that the interface solution described previously will play an important rôle in the more general cases to be described in the following subsections.

8.3.1.B Wavenumber selection: Constant phase *only* in one side

Let us consider now interfaces separating two Turing patterns where only one of them has constant phase. Physically this case will arise whenever the critical wavenumbers of the Turing patterns are equal zero for one pattern and nonzero for the other. In the following we will assume that $k_W^c \neq 0$ and $k_T^c = 0$ (the opposite case: $k_W^c = 0$ and $k_T^c \neq 0$, will give equivalent results). The constant phase assumption implies that:

$$q_T(\xi) \equiv 0,$$

and that there are two free parameters: v_{int} and ω_W (or, equivalently, v_{int} and the wavenumber $q_{W,N}$ in the left side). Note that $q_{W,N}$ is related to the wavenumber p_W^{ic} imposed initially (on the left side) in numerical simulations of interfaces in the PDEs of Eqs. (7.1,7.2) and to the selected p_W^{sel}. For more details see Section 7.3.4.C.

- Remark: Interface solutions with constant phase

The corresponding ODEs are the *five* Eqs. (7.5,7.6,7.7,7.8,7.9) (with coefficients as given in Eq. (8.1)). Note that the heteroclinic orbit found in Section 8.3.1.A should still be present in these ODEs. Indeed, the phase space of the ODEs studied in the previous subsection are a restricted portion of the present phase space. In the following we will see that this interface solution exists always and plays an important rôle.

- Interface velocity: numerical simulations of the amplitude equations

In order to get insight into the dynamics of interfaces, let us first examine some numerical simulations of the amplitude equations. In Figs. 8.6 and 8.7 we plot the interface velocity v_{int} measured in numerical simulations of the PDEs (7.1,7.2) (with coefficients as in Eq. (8.1) for three different values of

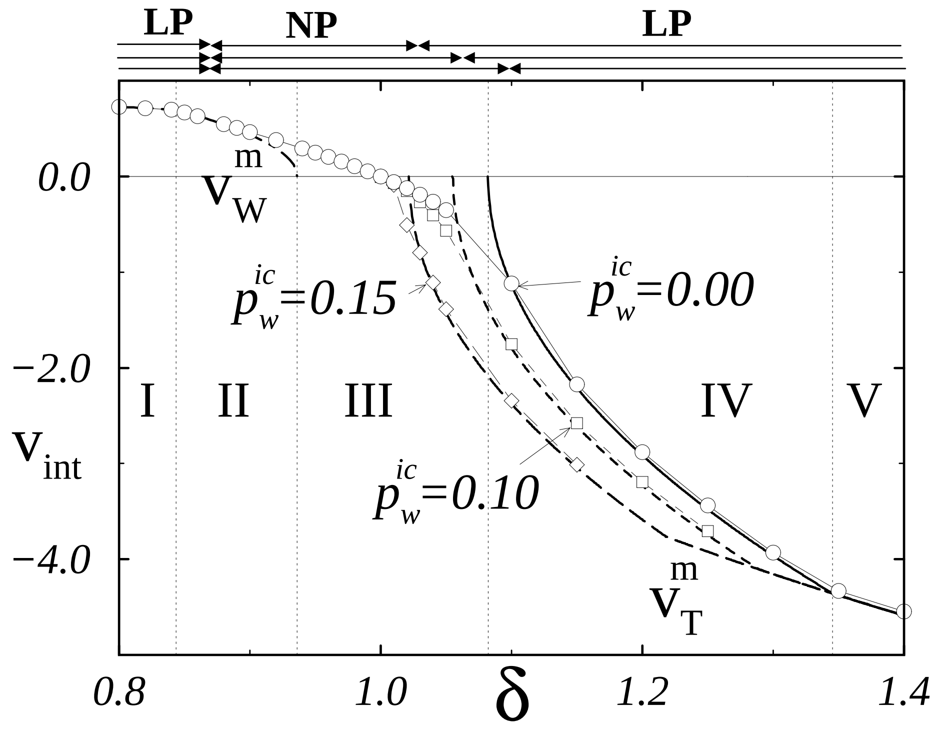

Figure 8.6: Interface velocity v_{int} measured in simulations of Eqs. (7.1,7.2) (with coefficients as in Eq. (8.1)) for three different values of the initial wavenumber p^{ic}_W (circles of $p^{ic}_W = 0$, squares for $p^{ic}_W = 0.10$ and rhombs for $p^{ic}_W = 0.10$) and $p^{ic}_T = 0$. The theoretical velocities v^m_T and v^m_W are also plotted (note that v^m_T depends on p^{ic}_W). In Fig. 8.7 a magnification of this figure, showing region **III**, is given. The **LP** and **NP** regimes are indicated in the upper part of this figure. Note that for big δ the boundary between these regimes depends on p^{ic}_W. For positive velocities only one interface exists. On the contrary, for negative velocities, there is a continuous family of interfaces parametrised by p^{ic}_W.

initial wavenumber p^{ic}_W (and $p^{ic}_T \equiv 0$). As expected, for $p^{ic}_W \equiv 0$ the interface dynamics is equivalent to the case analysed in the previous subsection. For $p^{ic}_W \neq 0$ there are two different scenarios, depending if v_{int} is positive or negative. For $v_{int} > 0$ a particular wavenumber is selected: $p^{sel}_W \equiv 0$. On the other hand for $v_{int} < 0$ a family of interfaces exist (except in region **V**), this family is parametrised by p^{ic}_W. We will now perform a theoretical analysis in order to understand these features.

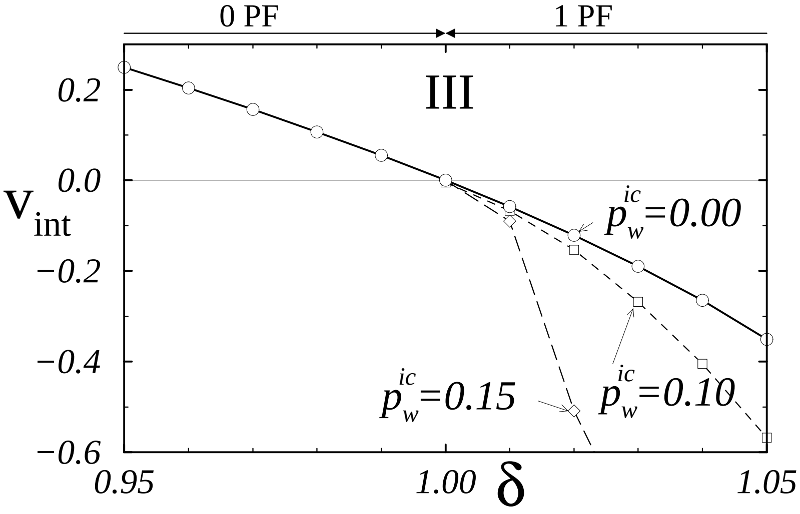

Figure 8.7: Magnification of Fig. 8.6 showing the behaviour of the TTIs in region **III** (see caption of Fig. 8.6 for details). From Eq. (8.13) we know that as far as $v_{int} > 0$ there exist a unique interface (*i.e.* 0 PF); for $v_{int} < 0$ the interface is a continuous family (*i.e.* 1 PF). This family is parametrised by $q_{W,N}$ (or, equivalently, by p_W^{ic}).

- Interface velocity: theoretical predictions

The counting arguments for this case are very similar to what we did in the previous subsection. Consequently, here we will only mention the differences and state directly the most important results.

First note that since: $a_{W,N}^2 = \eta'_W - q_{W,N}^2$, then: $\eta_T^{eff} = \eta_T - h_{TW}\eta'_W + h_{TW}q_{W,N}^2$ (compare with Eq. (8.2)). Consequently, the sign of η_T^{eff} does not necessarily change at the border between regions **III** and **IV** (this depends on the parameter $q_{W,N}$). On the other hand η_T^{eff} is still given by Eq. (8.5).

In region **I**, as discussed in Section 8.3.1.A, the interfaces consist of a front of $|A_W| \neq 0$ invading a unstable and equal to zero state. This invading state can have a nonzero wavenumber $q_{W,N}$. We saw in Section 6.4.5 that the dynamics of such fronts agree with the **LP** regime. This regime predicts that the selected velocity will be v_W^m, given in Eq. (8.7), and that the front selects a wavenumber equal to zero (*cf.* Eq. (6.26)). The **LP** regime extends to part of region **II** as well.

To calculate the manifold structure around $\mathbf{S}_W$ and $\mathbf{S}_W$ we need the structure of the nonlinear fixed points: N_T and N_W, and of the linear ones: L_T^+ and L_W^-. For N_T and L_T^+, they are given in Eq. (6.11). The fixed points

N_W and L_W^- have each *three eigenvalues.* Their manifold structures are given in Eq. (6.23).

In region **II** the counting arguments and the selection mechanism of the interfaces are equivalent to the discussion of the previous Section 8.3.1.A. The change between the **LP** and **NP** regime occurs for the same value of δ_{II}^{crit}.

In the central part of region **III**, where $\eta_W' > 0$, $\eta_W'^{eff} < 0$, $\eta_T > 0$ and $\eta_T^{eff} < 0$, there is *only one type* of interface and it has the following multiplicity depending on the sign of the velocity:

$$\begin{cases} \text{if } v_{int} > 0\text{:} & N_W^-(+,-,-), L_{T,2}^+(+,-) \rightarrow N_T(+,-), L_{W,1}^-(+,+,-) \Rightarrow 0 \text{ PF} \\ \text{if } v_{int} < 0\text{:} & N_W^+(+,+,-), L_{T,2}^+(+,-) \rightarrow N_T(+,-), L_{W,1}^-(+,+,-) \Rightarrow 1 \text{ PF} \end{cases} \tag{8.13}$$

Compare this with Eq. (8.12) in Section 8.3.1.A.

Consequently, in region **III**, as far as v_{int} is positive, there is only one interface. On the other hand, if $v_{int} < 0$, then there is a family of interfaces (see Fig. 8.7). Note that, as far as $v_{int} > 0$, the interface solution is the *same* than the one obtained in the previous subsection.

In the rest of region **III** and in region **IV** the counting arguments predict that both, a 1 PF and a 2 PF, may exist. As before, here only the heteroclinic orbit with lower multiplicity (*i.e.* the 1 PF) is observed in numerical simulations of the amplitude equations. Important to remark is that the transition between the **NP** and **LP** regimes does not necessarily happen for the δ_{IV}^{crit} found in the previous subsection. Indeed; this will happen only for $q_{W,N} \equiv 0$. If $q_{W,N} \neq 0$ this transition occurs at a value of δ smaller than δ_{IV}^{crit} (see Fig. 8.6). In the **LP** regime the dynamics of the interfaces is exactly the same than in the case analysed in Section 8.3.1.A. But, since η_T^{eff} is a function of $q_{W,N}$, the marginal velocity v_T^m given in Eq. (8.4) depends on this wavenumber (*i.e.* $v_T^m \equiv v_T^m(q_{W,N})$). Consequently, depending on $q_{W,N}$, different interface velocities are selected (in the following we will symbolise this *multiple velocities selection* mechanism with MVS). In Fig. 8.6 we plot the value of this marginal velocities.

- Summary of results for Turing-Turing interfaces with constant phase on the right side

We can now summarise the results for interfaces separating two Turing patterns, where one of them (on the right side of the interface in our convention) has constant phase. In Fig. 8.8 these results are schematised. Note that this figure is very similar to Fig. 8.5, but there is a sector of the control parameter space, corresponding to negative velocities, where a one parameter

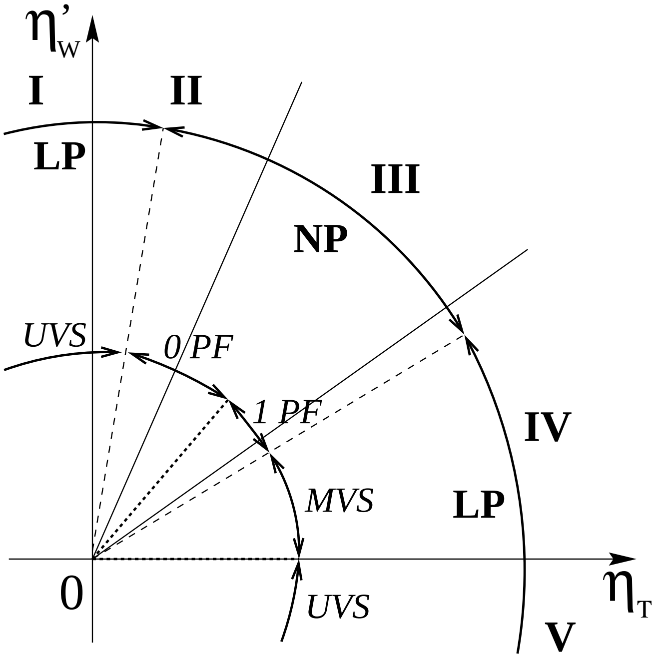

Figure 8.8: Schematic summary of the results for *Turing-Turing interfaces with constant phase on the right side.* The outer semicircle indicates the range of validity of the **LP** and **NP** regimes. The inner semicircle displays the multiplicity of the interfaces. By *1 PF* or *0 PF* in the **NP** regime we denote that the interfaces are a one parameter family or a discrete set respectively. In the **LP** regime only one or multiple interfaces are selected (symbolised by *UVS* and *MVS* respectively). In this last case the interfaces are parametrised by p_W^{ic}. Compare this scheme with Fig. 8.5. The only difference is that now there is a range of the the control parameters for which the interface appears as a one parameter family.

family of fronts is possible. This family is parametrised by the wavenumber p_W^{ic} imposed initially. In Fig. 8.9 we indicate the behaviour of the TTIs as a function of the initial wavenumber p_W^{ic}. Finally let us stress the fact that the Turing domain on the left side will select a particular wavenumber (equal to zero) if it is invading the other domain. Conversely, if this Turing domain is being invaded by the other pattern, a hole family of wavenumbers are possible. As we will see later, this behaviour carries over to other cases where a Turing domain is involved.

Finally let us remark that the case where the pattern in the left side of the interface has constant phase (*i.e.* with: $q_W(\xi) = 0$ and $q_T(\xi) \neq 0$) gives equivalent results.

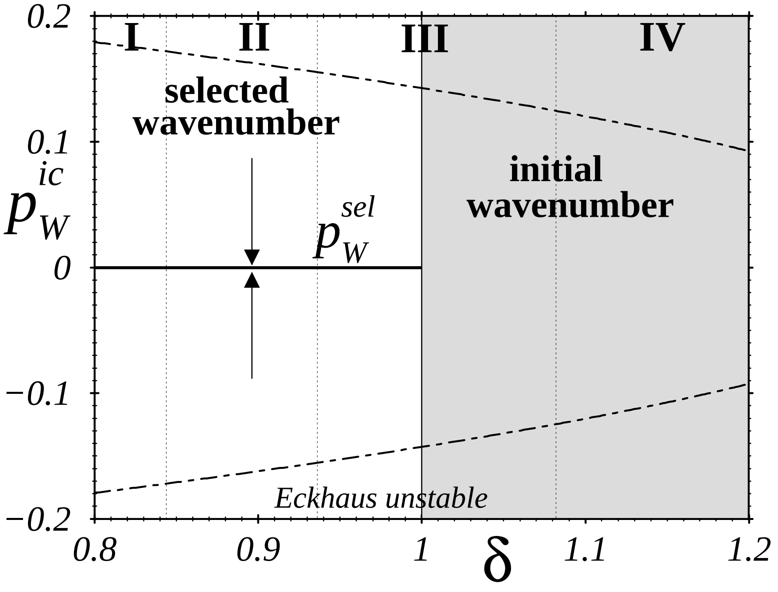

Figure 8.9: In this figure we indicate the behaviour of TTIs for different initial values of p_W^{ic}, as a function of δ and for a constant a ($a = 4.8$ in this case). In the gray area there exist an interface for any initial value of p_W^{ic} (*i.e.* there is a 1 PF of interfaces). Conversely, in the white area only interfaces with wavenumber $q_{W,N} = 0$ exist (*i.e.* a discrete set). Consequently, if a $p_W^{ic} \neq 0$ is imposed initially, then, after a transient time, an interface with $q_W^{sel} = 0$ will be selected. This is suggested by the arrows pointing to $q_{W,N} = 0$. The change between these two behaviours is produced when the interface velocity changes signs (*cf.* Fig. 8.7). Therefore, *if a Turing pattern is invading, then the interface will select a zero wavenumber* for this Turing pattern. Conversely; *if the Turing pattern is being invaded, then any wavenumber is possible.* This last wavenumber being determined only by the initial conditions. The dot-dashed lines shows the maximal and minimal wavenumber that do not have sideband (Eckhaus) instability.

8.3.1.C General Turing-Turing case

Let us now address the general case of interfaces separating two, distinct, Turing domains. The corresponding ODEs are the *six* Eqs. (7.5,7.6,7.7,7.8, 7.9,7.10) (with coefficients as given in Eq. (8.1)). The phase space of the four and five ODEs analysed in Sections 8.3.1.A and 8.3.1.B respectively, are contained in the phase space of these six ODEs. Consequently, the heteroclinic solutions found there also exist here.

The counting arguments of this case are similar, although more involved, than the analysis done in Sections 8.3.1.A and 8.3.1.B. In the following we will

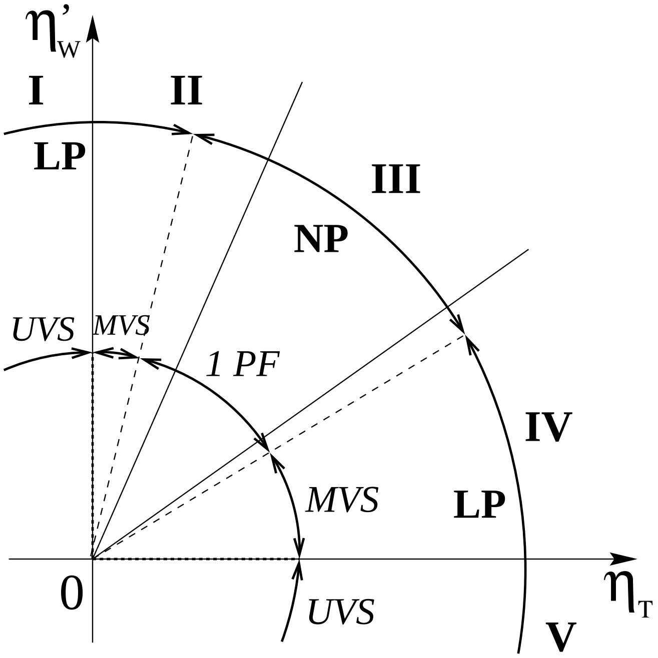

Figure 8.10: Schematic summary of the results for *Turing-Turing interfaces*. As in Figs. 8.5 and 8.8, the outer semicircle displays the range of validity of the **LP** and **NP** regimes. The inner semicircle shows the selection mechanism valid. With *1 PF* we indicate that a one parameter family of interfaces is predicted by the counting arguments. In the **LP** regime either a unique interface is selected (*UVS*) or many interfaces are possible (*MVS*). Which one is selected will depend on, either $|q_{W,N}|$, or $|q_{T,N}|$. Compare this scheme with Figs. 8.5 and 8.8.

only mention the most important facts and results arising from the counting arguments.

The effective η_T^{eff} and $\eta_W'^{eff}$ are functions of $q_{W,N}$ and $q_{T,N}$ respectively. The most important fact is that in a central region of the control parameter space, where $\eta_T^{eff} < 0$ and $\eta_W'^{eff} < 0$, these counting arguments predict a 1 PF of heteroclinic orbits. In Fig. 8.10 we summarise the results of the counting arguments.

The TTI solution with $q_{W,N} = q_{T,N} = 0$ found in section 8.3.1.A is also present here. The prediction of a 1 PF of heteroclinic orbits in a central region means that this solution is now a member of a family of interfaces. In section 8.3.1.B we saw that for $v_{int} < 0$ there is a 1 PF of TTIs with $q_{T,N} \equiv 0$ and parametrised with $q_{W,N}$. For $v_{int} > 0$ also a 1 PF of interfaces exists and they have $q_{W,N} \equiv 0$ and are parametrised by $q_{T,N}$. These two types of solutions combined give the 1 PF of TTIs predicted by the counting

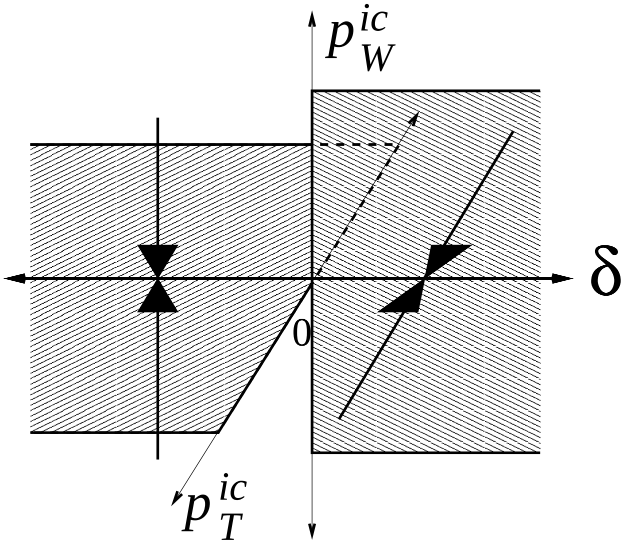

Figure 8.11: In this figure we schematise the behaviour of the interface with respect to p_W^{ic} and p_T^{ic}, as a function of δ and for constant a in the Turing-Turing codimension-2 instability case. The vertical plane (*i.e.* $p_T^{ic} \equiv 0$) is equivalent to the scheme presented in Fig. 8.9. The gray surfaces indicate the combinations of p_W^{ic} and p_T^{ic} for which an interface exists. TTIs with parameters out from these surfaces are not stable. After a transient time, they will select either wavenumbers $q_{W,N} = 0$ and $q_{T,N} = p_T^{ic}$ for $v_{int} > 0$ (for small δ) or $q_{T,N} = 0$ and $q_{W,N} = p_W^{ic}$ for $v_{int} < 0$ (for big δ). These behaviour is indicated with thick arrows.

arguments for positive and negative values of v_{int}. In Fig. 8.11 we schematise the behaviour of the 1 PF interfaces respect to their parameters.

- Summary of results for Turing-Turing interfaces

Let us finally summarise the most important result for TTIs. The invading Turing pattern will select a particular wavenumber. This wavenumber is *equal to zero.* In the invaded Turing domain can have any wavenumber. This wavenumber is typically the one imposed by the initial conditions. The velocity of the interface is a function of the wavenumber of the invaded domain.

8.3.2 Turing-Turing interfaces with $v_g \neq 0$

In the previous Section 8.3.1, we studied the dynamics of TTIs. The natural next step is to study interfaces separating Hopf and Turing domains. Here, however, we will briefly study the effect of the group velocity on the TTIs.

Physically this case is not relevant; nevertheless it will help us to understand some features of the dynamics of wave-Turing interfaces to be investigated in Section 8.4.

We will study interfaces in Eqs. (7.1,7.2) and their corresponding orbits in Eqs. (7.5-7.10) if we consider:

$$c_1 = c_2 = c_4 = 0. \tag{8.14}$$

Moreover, to make the analysis simpler, we will consider that the amplitudes in both sides are constant (as in Section 8.3.1.A).

Since $v_g \neq 0$, there are two types of interfaces: INI and OUI (see Table 7.1). Here, however, we prefer not to use this names which we will reserve for the wave-Turing interfaces. Consequently, we will differentiate them by the sign of s (*cf.* Eq. (7.1,7.2)). In Table 7.1 the connection between the sign of s and INI or OUI is given.

The interface dynamics in general, and the counting arguments in particular, is very similar to the case discussed in Section 8.3.1.A. Therefore, here we will discuss only the differences.

The fact that $v_{int}^{eff} \neq v_{int}$ (*cf.* Eq. (7.18)) should be taken into account for the analysis of the manifold structure of the single fixed points L_W^- and N_W. This effective velocity *does change* the marginal velocity v_W^m of Eq. (8.7) but does not influence v_T^m (*cf.* Eq. (8.4)). Indeed; the new marginal velocity in regions **I** and **II** is given by:

$$v_W^m(s) = 2\sqrt{\eta_W'^{eff}} + s v_g, \tag{8.15}$$

and consequently depends on the sign of s. In Fig. 8.12 we show the value of these new marginal velocities and velocity v_{int} of the interfaces measured in numerical simulations of the corresponding coupled amplitude equations. We show also in this figure the velocity corresponding to a standard Turing-Turing interfaces (*i.e.* $v_g = 0$ or, equivalently, $s = 0$) discussed in Section 8.3.1.A (*i.e.* TTIs with constant phase on both sides of the interface).

In Fig. 8.12 we can see that, as in the case discussed in Section 8.3.1.A, in a central region of the control parameter space the **NP** regime applies. Here the counting arguments predict a 0 PF of orbits. In the rest of the parameter space the dynamics of the interface is described by the **LP** regime. The transitions between the **LP** and **NP** regimes are influenced by the value of v_g. Moreover, these transitions do not occur any more in a straight line in the parameter space as we saw in Section 8.3.1 (for more details see discussion in Section 7.4).

Note also the radical influence of the group velocity in their propagation velocity for small δ. Indeed, the interfaces with $s = 1$ do not change the

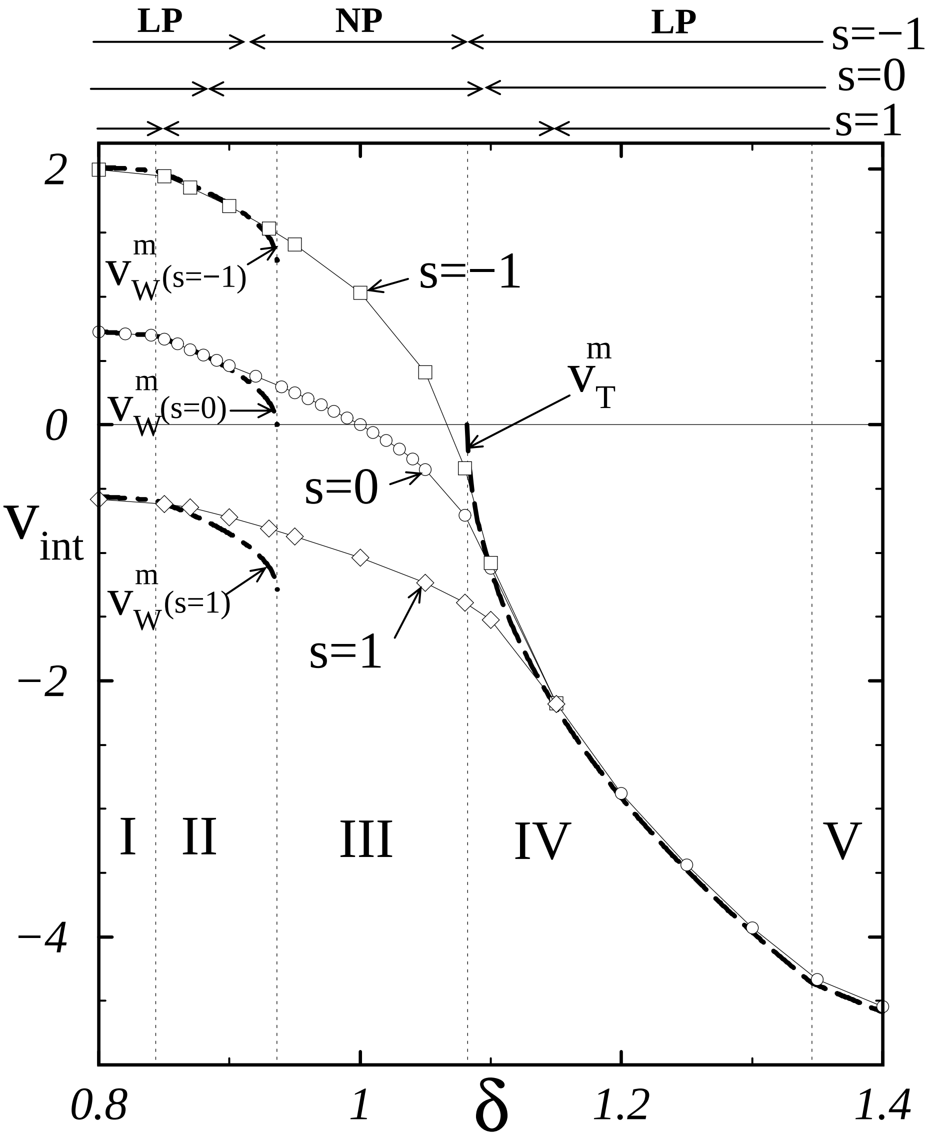

Figure 8.12: Plot of the velocity v_{int} of interfaces in Eqs. (7.1,7.2) with coefficients as in Eq. (8.14) and $v_g \neq 0$ (the values of the other coefficients are as in Table 4.2) for a constant value of a (in this case $a = 4.8$). The squares and rhombs correspond to the velocity of interfaces with $s = -1$ and $s = 1$ respectively. The velocity v_{int} of TTIs (*i.e.* $v_g = 0$ or $s = 0$; *cf.* Fig. 8.1(b)) is also shown (with circles). The theoretical marginal velocities $v_W^m(s)$ (*cf.* Eq. (8.15)) and v_T^m are indicated with dot-dashed and dashed lines. Note that the transition between the **LP** and **NP** regimes depends on s (this is shown in the upper part of the figure). Note that the velocity of the interfaces is independent of the group velocity v_g for big δ (in the **LP** regime) and that the interfaces with $s = 1$ always propagate in the same direction (for the constant value of a used here; see text for more details).

direction of propagation. This is: one of the domains does *always*[7] invade the other.

8.3.3 Hopf-Turing interfaces

Let us now study the dynamics of Hopf-Turing interfaces (HTI in the following). In this case:

$$v_g = 0.$$

- Turing amplitude with constant phase

As a first approach, let us consider that the Turing amplitude has constant phase: $q_T(\xi) = 0$. Note, on the other hand, that we *should* alow $q_W(\xi) \neq 0$.

The corresponding ODEs to study are the *five* Eqs. (7.5-7.9). The counting arguments in this case are similar to the analysis done for the TTI with constant phase in one side in Section 8.3.1.B. Consequently, we will here only discuss the main differences between these two cases.

In region **I** the dynamics of the interface (front in this case) is given, as we mentioned in Section 6.4.5, by the marginal stability criterion. The marginal velocity is (*cf.* Eq. (6.27)):

$$v_W^* = 2\sqrt{\eta_W'^{eff}(1+c_1^2)}, \tag{8.16}$$

compare this formula with Eq. (8.7). In Fig. 8.13 we plot this marginal velocity and the interface velocity v_{int} measured in numerical simulations of the coupled amplitude simulations. Note that the **LP** regime, as in the previous cases, extends into part of region **II**. An important feature to remark is that the interface selected in the **LP** regime (in regions **I** and **II**) has *nonzero* wavenumber given by (*cf.* Section 6.4.5):

$$q_{W,N}^* = \sqrt{\eta_W'^{eff}}\Big(\frac{\sqrt{1+c_1^2} - \sqrt{1+c_3^2}}{c_1 + c_3}\Big). \tag{8.17}$$

In Fig. 8.14 we plot the value of $q_{W,N}^*(\eta_W'^{eff})$ and the measured wavenumber p_W^{sel} in numerical simulations of the amplitude equations. Note that in both regimes, **LP** and **NP**, the selected wavenumber is always *different from zero.*

---

[7] Note that this is true only near the codimension-2 point. Indeed, for this to be valid: $v_W^m(s=1) < 0$. But, as we can see in Eq. (8.15), if we increase η_W' it is always possible to make $v_W^m(s=1)$ positive.

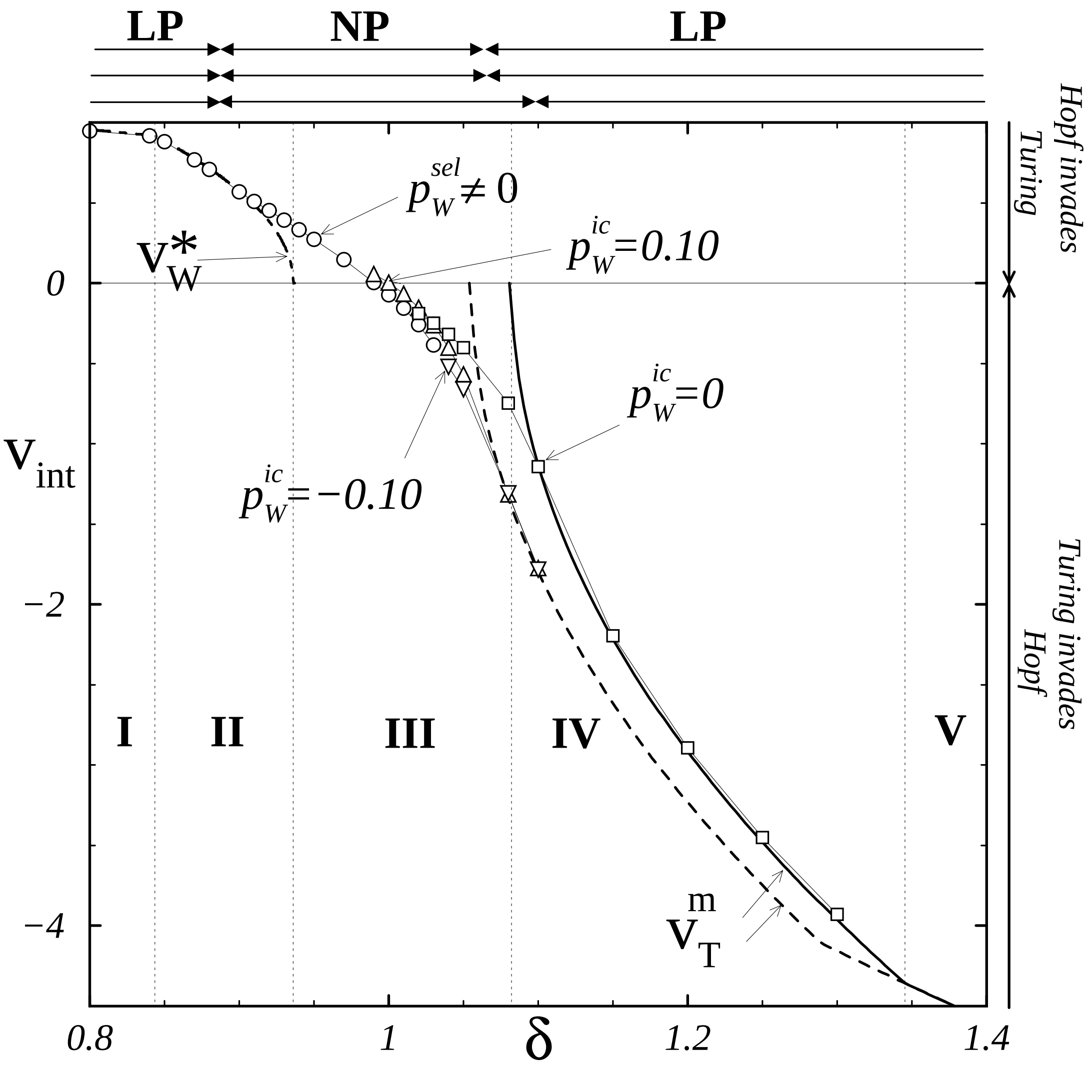

Figure 8.13: Velocity v_{int} of the *Hopf-Turing interfaces* measured in numerical simulations of Eqs. (7.1,7.2) with $v_g = 0$ (the values of the other coefficients are as in Table 4.2) for a constant value of a (here: $a = 4.8$). Three different values of the initial wavenumber p_W^{ic} have been used. Note that for big δ this initial wavenumber stays, whereas for smaller δ a unique wavenumber p_W^{sel} is selected (in Figs. 8.14 we plot the value of p_W^{sel}). The place where the behaviour of the interfaces changes depend on p_W^{ic}. In Fig. 8.17 we show a magnification of the region where this happen (see also Fig. 8.15). The values of the marginal velocities v_W^* (*cf.* Eq. (8.16)) and v_T^m (*cf.* Eq. (8.4)) are also shown. The range of validity of the **LP** and **NP** regimes is shown in the upper part for each value of p_W^{ic}.

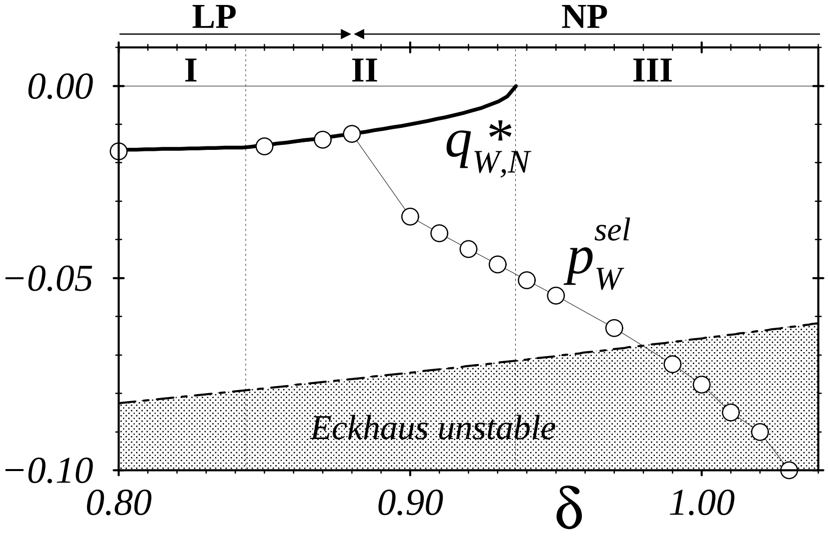

Figure 8.14: Plot of p^{sel}_W as a function of δ and for a fixed value of a ($a = 4.8$). Also shown is the wavenumber $q^*_{W,N}$ predicted by the marginal stability criterion (*cf.* Eq. (8.17)). The **LP** and **NP** regimes are indicated in the upper part of the figure. An important point to remark is that the selected wavenumber p^{sel}_W becomes Eckhaus unstable for big vales of δ. In Fig. 8.16 we show an example of the dynamics of the interface in this regime.

An interesting feature is that the absolute value of the selected wavenumber p^{sel}_W increases[8] with δ in the **NP** regime. Simultaneously, the band of wavenumbers stable against sideband instabilities shrinks (see Fig. 8.14). Consequently, for δ big enough, the selected wavenumber is unstable (see Figs. 8.14 and 8.15). In this case the interface will generate phase slips which will destabilise the interface itself. In Fig. 8.16 we present an example of this phenomena. Note that the defects are generated periodically and that the movement of the interface is unsteady.

Another interesting difference with the behaviour of TTIs is that the transition between a discrete and a continuous family of interfaces is more involved. Indeed, if we compare the manifold structure of the nonlinear fixed points in the *single* RGLE and *single* CGLE in Eqs. (6.23) and (6.24) respectively, then we can see that the CGLE case has more freedom. Indeed, for a given value of v_{int}, the RGLE has only one nonlinear fixed point, whereas the CGLE has two. In a central region of the control parameter space, where

---

[8] This will strongly depend on the values of the coefficients of the amplitude equations and consequently is not generic.

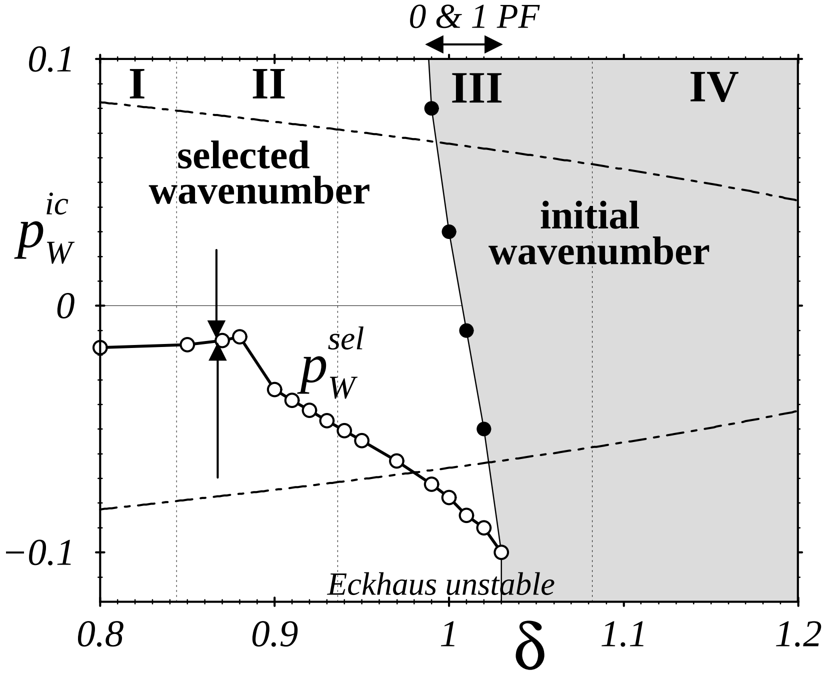

Figure 8.15: Behaviour of the HTIs as a function of p_W^{ic} and the control parameter δ when a is kept constant ($a = 4.8$). Compare with Fig. 8.9 for TTIs. Note that the selected wavenumber p_W^{sel} is always *different from zero* (see also Fig. 8.14) and that the boundary between the unique interface solution and the family of solutions is a function of p_W^{ic}. Consequently for the same value of δ (where $\delta \approx 1$ in this case) *both* types of interfaces may be accessed! In the upper part of the figure the region where this happens is indicated. In Fig. 8.17 we show this boundary for three different values of p_W^{ic}.

$\eta'_W > 0$, $\eta'^{eff}_W < 0$, $\eta_T > 0$ and $\eta^{eff}_T < 0$, and if the velocity v_{int} there is small enough then each fixed point contributes to a family of interfaces (see Fig. 8.15). The counting arguments tell us that one of the families is 0 PF and the other is 1 PF. In Fig. 8.17 we plot the velocity v_{int} in this region for three different values of p_W^{ic}. Note that there is *bistability* between the interface solution that selects a particular wavenumber and the family of interfaces parametrised by p_W^{ic}. In Fig. 8.15 we indicate the behaviour of the HTIs for different initial values of p_W^{ic}. Here we can again see the bistability between the two possible types of HTIs.

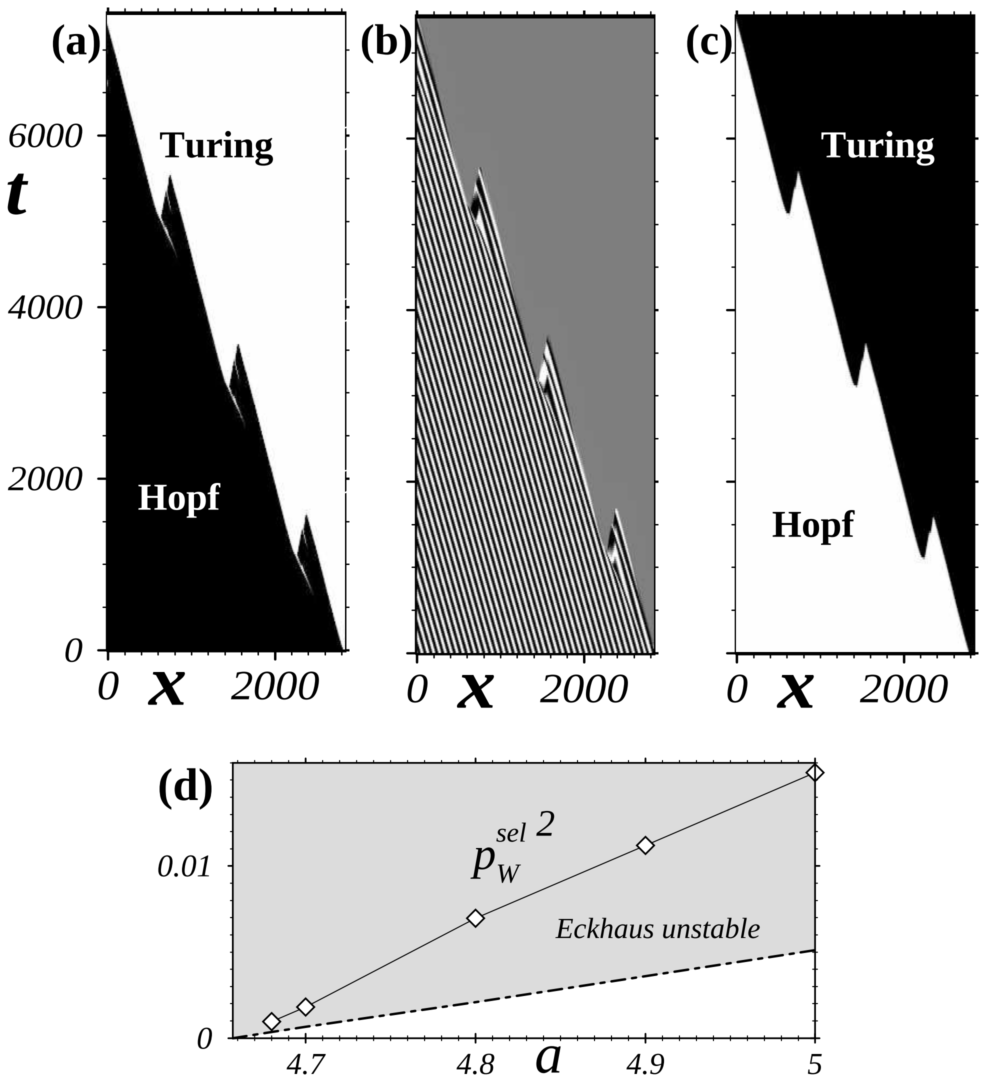

Figure 8.16: In (a), (b) and (c) we display space-time plots showing the values of $|\widetilde{A}_W|$, $Re(\widetilde{A}_W)$ and, respectively, $|\widetilde{A}_T|$ near a HTI in numerical simulations of the amplitude equations with $a = 4.80$ and $\delta = 1.02$. Black and white correspond to high and, respectively, low values of the fields plotted (the homogeneous gray in (b) corresponds to $Re(\widetilde{A}_W) = 0$). In this case the HTI selects a wavenumber p_W^{sel} which is Eckhaus unstable (*cf.* Eq. (5.10) and see Fig. 8.15). Note that the interface does move unsteadily. This happens because spatio-temporal defects (*i.e.* palaces where $|\widetilde{A}_W| = 0$) are periodically generated. These defects turn the interface unstable. In Fig. 8.14 we can see that $p_W^{sel} \simeq -0.09$ is Eckhaus unstable. In (d) we plot the wavenumber p_W^{sel} selected by the HTI as a function of a and for a constant value of δ (here $\delta = 1$). Also plotted is the maximal wavenumber q_W^{EH} allowed by the Eckhaus instability (dot-dashed line). Note that the selected wavenumber is always bigger than this maximal value. Even very near the codimension-2 point!

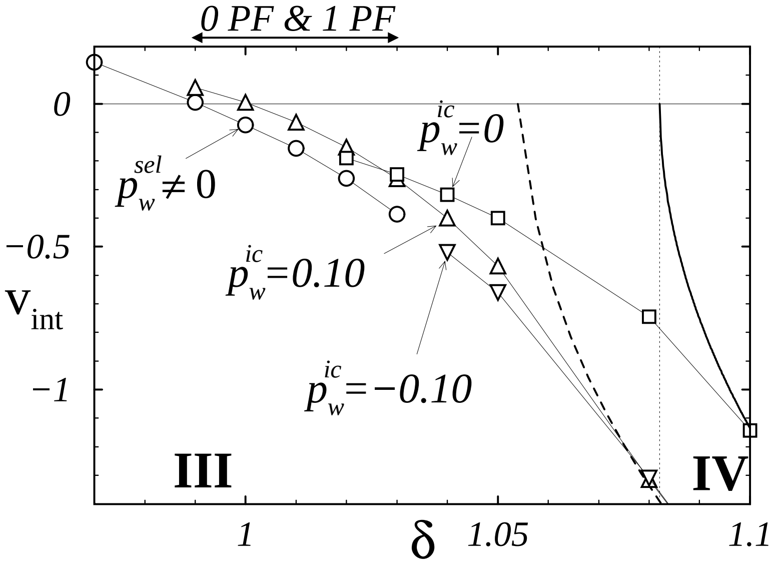

Figure 8.17: Interface velocity v_{int} in the Hopf-Turing case (for details see the caption of Fig. 8.13). Three different p_W^{ic} are used. Note that for small δ a particular velocity is selected for the HTIs. This interface has a nonzero wavenumber p_W^{sel} in the Hopf side. In Fig. 8.14 we plot the value of this wavenumber. On the other hand, for big δ, a family of HTIs exists. The transition between these two behaviours depends on p_W^{ic}. In Fig. 8.15 we show the values of δ and p_W^{ic} of this transition.

- Summary of results for HTI where the Turing has constant phase

Let us now summarise the results for HTIs with constant phase in the Turing domain.

In Fig. 8.18 we schematise the behaviour of the HTIs. In regions **I**, **II** and part of **III**, typically when the Hopf pattern invades the Turing pattern, the HTIs select a wavenumber on the Hopf side. This wavenumber is different from zero. Consequently, sideband instabilities of the Hopf domain may happen. In regions **V**, **IV** and part of **III**, typically when the Turing pattern invades the Hopf, there exist a one parameter family of interfaces. The transition between these two different families of interfaces is complicated and may exhibit bistability.

- General case

Let us now briefly discuss the general case of HTIs where $q_T(\xi) \neq 0$.

Equivalently to the discussion of TTI interfaces, the interface solution

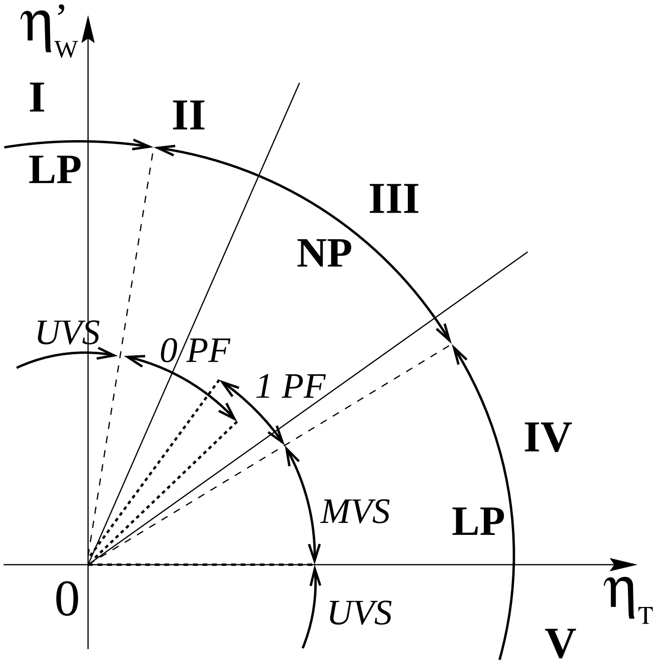

Figure 8.18: Schematic summary of the results for *Hopf-Turing interfaces with constant phase on the Turing domain.* The outer semicircle displays the range of validity of the **LP** and **NP** regimes. Compare this scheme with Fig. 8.5 for the TTIs. The selection mechanism in the **LP** regime is equivalent to the TTI case. The inner semicircle displays the multiplicity of the interfaces. By *1 PF* or *0 PF* we denote that the interfaces are a one parameter family or a discrete set respectively. The main difference with Fig. 8.5 is that now there exist a region of the control parameter space where two families of interfaces exist simultaneously (see Figs. 8.15 and 8.17).

found in the previous paragraphs still exists if we allow $q_T(\xi) \neq 0$. In general a interface solution with $q_{T,N} \neq 0$ will exist if the velocity $v_{int} > 0$. Namely; if the Hopf pattern invades the Turing pattern. Otherwise: $q_{T,N} = 0$, and consequently $p_T^{sel} = 0$.

8.3.4 Summary of this section

Since Section 8.3 is long and involved, we will give here a short summary of the main results for the Turing-Turing, Hopf-Turing and Turing-Turing with $v_g \neq 0$ interfaces.

The dynamics of interfaces can be divided in two different regimes: **LP** and **NP**.

- Linear Propagation Regime

In the **LP** regime the interface dynamics is governed by the the dynamics of the leading edge of the invading pattern. The marginal stability criterion (see Section 6.4.4) allows us to calculate analytically the values of the selected velocity and wavenumbers. These selected values are typically such that the counting arguments are not applicable (since they correspond to singular cases). The wavenumber selected for the invading pattern depends on the type of pattern (*i.e.* either Turing or Hopf). If the Turing pattern is invading, then the interface selects a wavenumber equal *zero* for it. On the other hand, if the invading domain of the Hopf type, then the interface selects a *nonzero* wavenumber for it.

The **LP** regime is if found in areas of the control parameter space where either η'_W or η_T is small. These areas are illustrated in Figs. 8.10 and 8.18 for the Turing-Turing and Hopf-Turing interfaces respectively. In part of these areas one of the patterns has zero amplitude. There, the interfaces consist of fronts of a stable state invading an unstable one. We saw in Section 6.4.4 that the dynamics of these fronts is governed by the leading edge. However, the **LP** regime nontrivially applies to other areas of the parameter space where both patterns have nonzero amplitudes.

- Nonlinear Propagation Regime

In the **NP** regime the dynamics of the interface depends on the nonlinear properties of the coupled amplitude equations. The multiplicity of the interfaces is in agreement with the predictions of the counting arguments.

The **NP** regime appears in a central region of the control parameter space, typically including the bistability region (see Figs. 8.10 and 8.18 for the Turing-Turing and Hopf-Turing interfaces respectively). Near the transition between the **LP** and **NP** regimes the dynamics of the interfaces is the same in both regimes.

The Turing-Turing interfaces appear always as a one parameter family (see Fig. 8.10). This family is parametrised by the wavenumber of the invaded Turing domain. The wavenumber of the invading Turing is unique and equal to zero.

The case of the Hopf-Turing interfaces is more complex. If the Turing domain invades the Hopf, then the wavenumber of Turing is unique and equal to zero. The selection mechanism of the wavenumber in the Hopf domain is complex. Indeed, in a central region of the parameter space (see Figs. 8.18 and 8.15), depending on the initial conditions, this wavenumber can be selected or not.

- Effect of the group velocity

Let us now describe the effect of a group velocity term in the Turing-Turing interfaces.

The counting arguments for this case are almost equivalent to the case without group velocity. On the other hand, the group velocity v_g has a big effect on the interface velocity. If $v_g = 0$ then typically the interfaces reverse their propagation direction inside the central region of the control parameter space (see Fig. 8.1(b) for the Turing-Turing case). In Fig. 8.12 we show the interface velocity if $v_g \neq 0$. We can see that for big values of δ the interface velocity is independent of v_g. On the other hand, for small values of δ the interface velocity differs greatly on the sign of v_g. Near the codimension-2 point one of the interfaces never reverses its propagation direction!

In the next section we will see that the wave-Turing interfaces share many of the properties appearing in Hopf-Turing and Turing-Turing with $v_g \neq 0$ interfaces.

8.4 Wave-Turing interfaces

Let us finally address the study of the dynamics of INI and OUI near a codimension-2 wave-Turing instability.

Since $v_g \neq 0$, as we saw in Section 7.4, the dynamics of the wave-Turing interfaces in the control parameter space η'_W vs. η_T can not be deduced from a single "cut" as done in the previous section for the TTIs and HTIs. Consequently the study will be done in two steps. In the first step, in Section 8.4.1, we will study the dynamics of the interfaces for a constant value of control parameter a. In the second step, in Section 8.4.2, we will analyse the change of the shape and other properties of the interfaces with the distance to the codimension-2 bifurcation.

Finally, in Section 8.4.3 we will perform a quantitative comparison between the dynamics of INI and OUI in the coupled amplitude equations and in the RDNC model.

8.4.1 Interface dynamics

This case is a combination of the the HTIs discussed in section 8.3.3 and the TTIs with $v_g \neq 0$ discussed in section 8.3.2. Let us discuss the case where the Turing domain has constant phase.

As in the previous section, the dynamics of the interfaces can be divided in two different regimes: linear and nonlinear propagation.

- Linear Propagation Regime

This regime is valid in regions **I**, **V** and part of regions **II** and **IV**. The marginal velocity in regions **I** and **II** is given by:

$$v_W^*(s) = 2\sqrt{\eta_W'^{eff}(1+c_1^2)} + sv_g. \tag{8.18}$$

Note that this velocity is the marginal velocity v_W^* of HTIs (*cf.* Eq. (8.16)) shifted by $\pm v_g$. These interfaces select a nonzero wavenumber for the wave domain. This wavenumber is the same for OUI and INI, and is given by Eq. (8.17). On the other hand, in regions **IV** and **V** the marginal velocity is given by the value v_T^m define in Eq. (8.4) and is not affected by v_g.

In Fig. 8.19 we plot the marginal velocities $v_W^*(s)$ and v_T^m and the interface velocities v_{int} of INI and OUI measured in simulations of the coupled amplitude equations with initial wavenumber $p_W^{ic} = 0$. Note that the range of applicability of the **LP** regime is bigger for OUIs than for INIs.

- Nonlinear Propagation Regime

The counting arguments for this case are equivalent to the arguments for Hopf-Turing interfaces. The only modification is to take into account $v_{int}^{eff} \neq v_{int}$ (*cf.* Eq. (7.18)). This implies that the transition between a 0 and 1 PF described in Section 8.3.3 (see also summary in Section 8.3.4) happens for OUIs and INIs in different places of the control parameter space. We recall that this transition was induced by a change in the manifold structure of the nonlinear fixed point $\mathbf{N}_W$ (*cf.* Eq. (6.24)). The manifold structure of this fixed point determined by v_{int}^{eff} and consequently depends on the the sign of s (*cf.* Eq (7.18)). In Fig. 8.20 we show the velocities v_{int} of INI and OUI in region **III** (with $p_W^{ic} = 0$). In Fig. 8.21 we display the behaviour of the OUI and INI as a function of the initial wavenumber p_W^{ic} in the wave domain. Note that the location of the transition between the discrete and continuous parameter families is different for OUIs and INIs. This happens because this transition occurs for small values of $v_{int} - sv_g$ (*cf.* Fig. 8.20). Near this transition both, a discrete and a continuous parameter family of interfaces, are possible. Consequently, depending on the value of p_W^{ic} there is two "basins of attraction" (*cf.* Fig. 8.21). The same type of "bistability" between families of interfaces was found in the Hopf-Turing case (*cf.* Section 8.3.3).

Finally let us mention that the selected wavenumber p_W^{sel} of the wave domain can be Eckhaus unstable. In Fig 8.22 we plot these wavenumbers for INI and OUI (we also plot additionally the wavenumber selected by HTIs). The

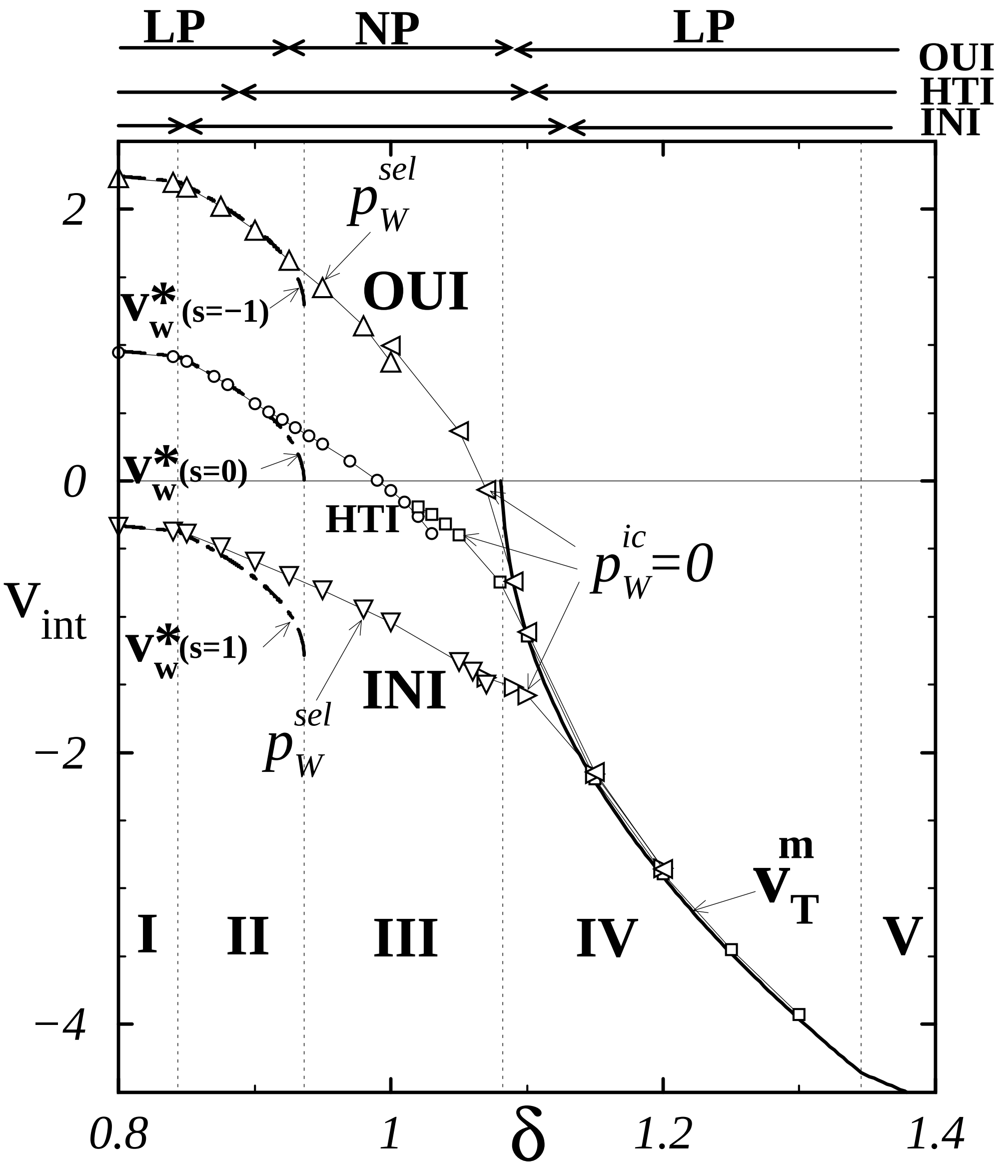

Figure 8.19: Interface velocity v_{int} of wave-Turing interfaces measured in numerical simulations of amplitude equations. Compare this figure with Figs. 8.12 and 8.13. The triangles show the values of v_{int} OUI and INI obtained doing simulations of Eqs. (7.1,7.2) with coefficients as in Table 4.2 and $a = 4.80$. Here we plot only simulations with initial wavenumber $p_W^{ic} = 0$. Additionally we show (with circles and squares) the values of v_{int} for Hopf-Turing interfaces (for more details see Figs. 8.13 and 8.17). The range of validity of the **LP** and **NP** regimes are indicated in the upper part of the figure for each type of interface. In Fig. 8.20 a magnification of the interface behaviour in region **III** is shown. The thick full and dot-dashed lines show the values of the marginal velocities v_T^m and $v_W^*(s)$ respectively.

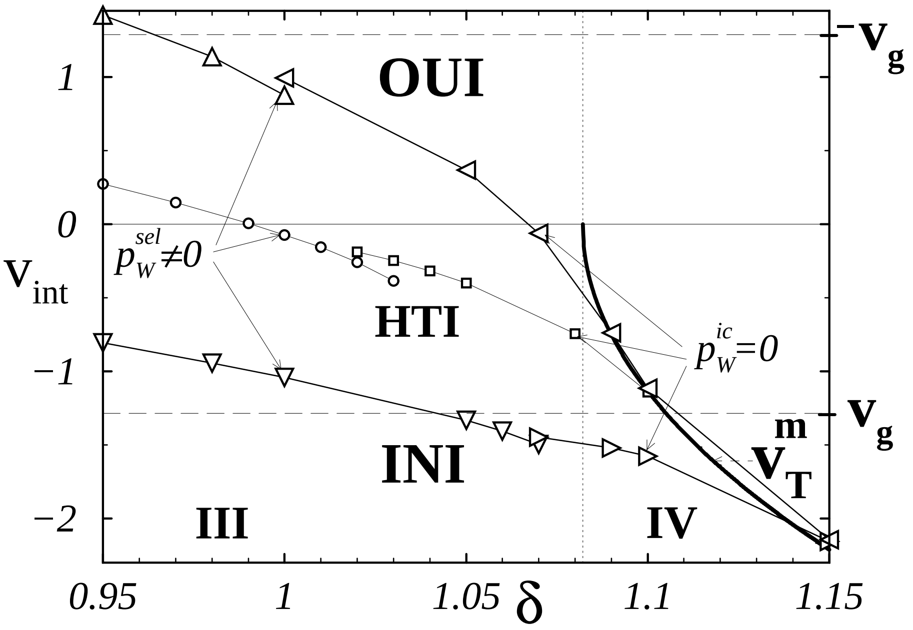

Figure 8.20: Magnification of the interface velocity v_{int} shown in Fig. 8.19. Here we show the interface dynamics near the central area of the control parameter space (for details see caption of Fig. 8.19). We plot here only interfaces with initial wavenumber $p_W^{ic} = 0$. Note that the transition between a unique interface (for small δ) and a one parameter family (parametrised by p_W^{ic}) happens is shifted with v_g. In Fig. 8.21 the location of this transition is shown for different values of p_W^{ic}. In Fig. 8.22 we plot the value of the wavenumber p_W^{sel} selected (for small *delta*) in by the discrete family of interfaces. The long-dashed lines show the values of $\pm v_g$.

dynamics of the interfaces with Eckhaus unstable wavenumbers is equivalent to the description given in Section 8.3.3 for the Hopf-Turing interfaces.

8.4.2 Scaling properties

In this subsection we will study the shape and size of wave-Turing interfaces near the codimension-2 instability in the coupled amplitude equations (7.1,7.2). To study these scaling properties we will again make use the leading edge approach and the marginal stability criterion.

In Fig. 8.23 we show some examples of OUIs and INIs near the codimension-2 point. The amplitudes $|\widetilde{A}_W|$ and $|\widetilde{A}_T|$ are plotted for different values of the control parameter a. This parameter approaches the codimension-2

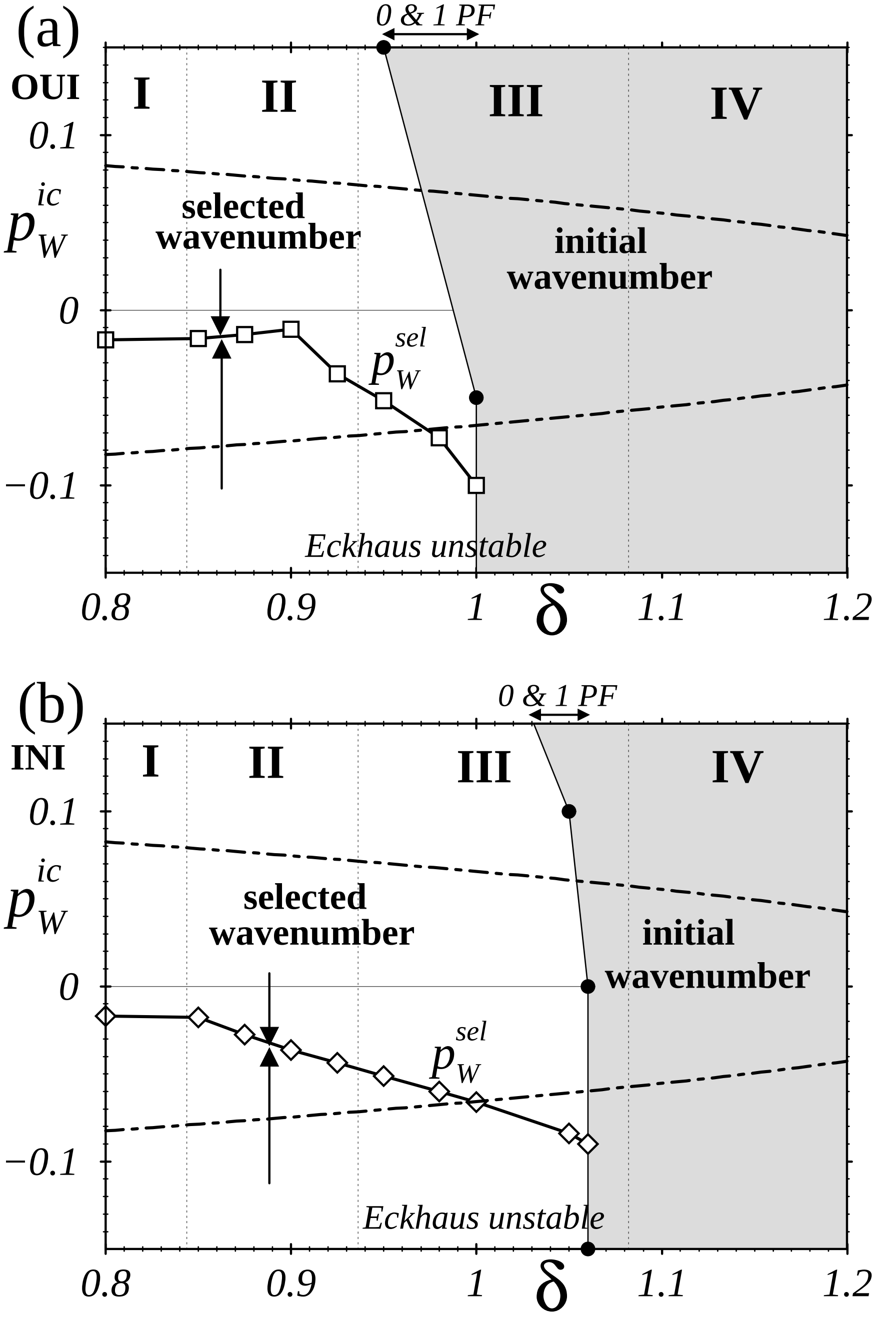

Figure 8.21: In (a) and (b) we display the behaviour of the OUI and INI respectively, for different values of p_W^{ic} and for $a = 4.8$. Compare with Figs. 8.9 and 8.15 for TTIs and HTIs respectively. Note that both kinds of interfaces have the same characteristics; namely a discrete (continuous) family of interfaces for small (big) δ. The most important difference between (a) and (b) is that the transition between the two families is is shifted, such that for the OUI it happens for lower values of δ than for the INI.

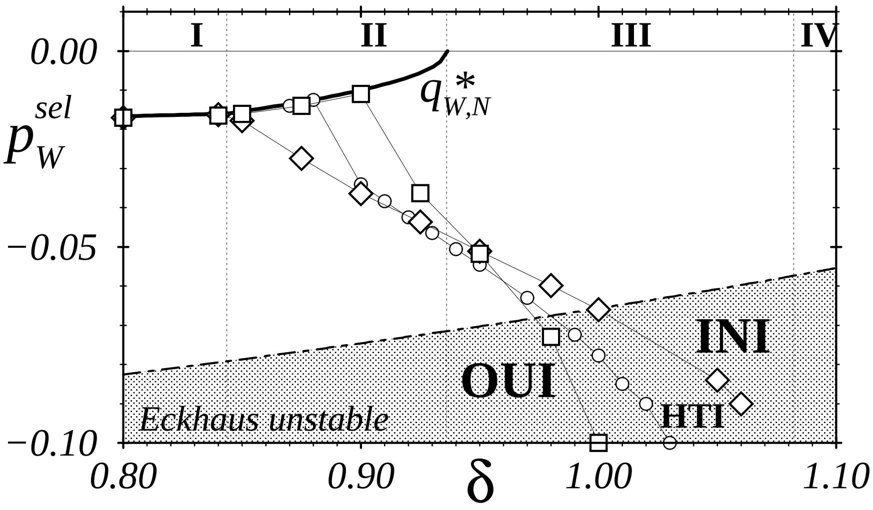

Figure 8.22: Plot of the wavenumbers p_W^{sel} selected by the OUI (squares) and INI (rhombs) for $a = 4.80$. Additionally, we show (with small circles) the p_W^{sel} selected by the HTI (for details see Fig. 8.14). We also plot the wavenumber $q^*_{W,N}$ predicted in the **LP** regime (for details see the caption of Fig. 8.14). Note that the selected wavenumbers become Eckhaus unstable for big δ.

point and δ is kept constant ($\delta = 1$). The asymptotical values reached by the amplitudes decrease as the codimension-2 point is approached. The shape of the OUI does not change significantly. On the other hand, the INIs display a wide region where both amplitudes $|\widetilde{A}_W|$ and $|\widetilde{A}_T|$ are almost zero.

8.4.2.A Scaling of Inward Interfaces

Let us now discuss in detail the scaling properties of the INIs. The region of where both amplitudes are small will be called the *core*. In Fig. 8.23 we can see that this core gets bigger as we approach the codimension-2 point.

The existence of the core allows us to define a width for the INI near the codimension-2 point. Between many possibilities, we choose here to define this *width* as the spatial distance between the amplitudes $|\widetilde{A}_W|$ and $|\widetilde{A}_T|$, when both are half of the value approached asymptotically by $|\widetilde{A}_W|$ as $x \to -\infty$. In Figure 8.23(b) this definition of the width is illustrated for some examples of the INI.

In Figure 8.24 the width of the core of INIs is plotted against the control parameter a for a constant value of δ (here $\delta = 1$). The width becomes very large near the codimension-2 point. Moreover, the width *diverges* for a value

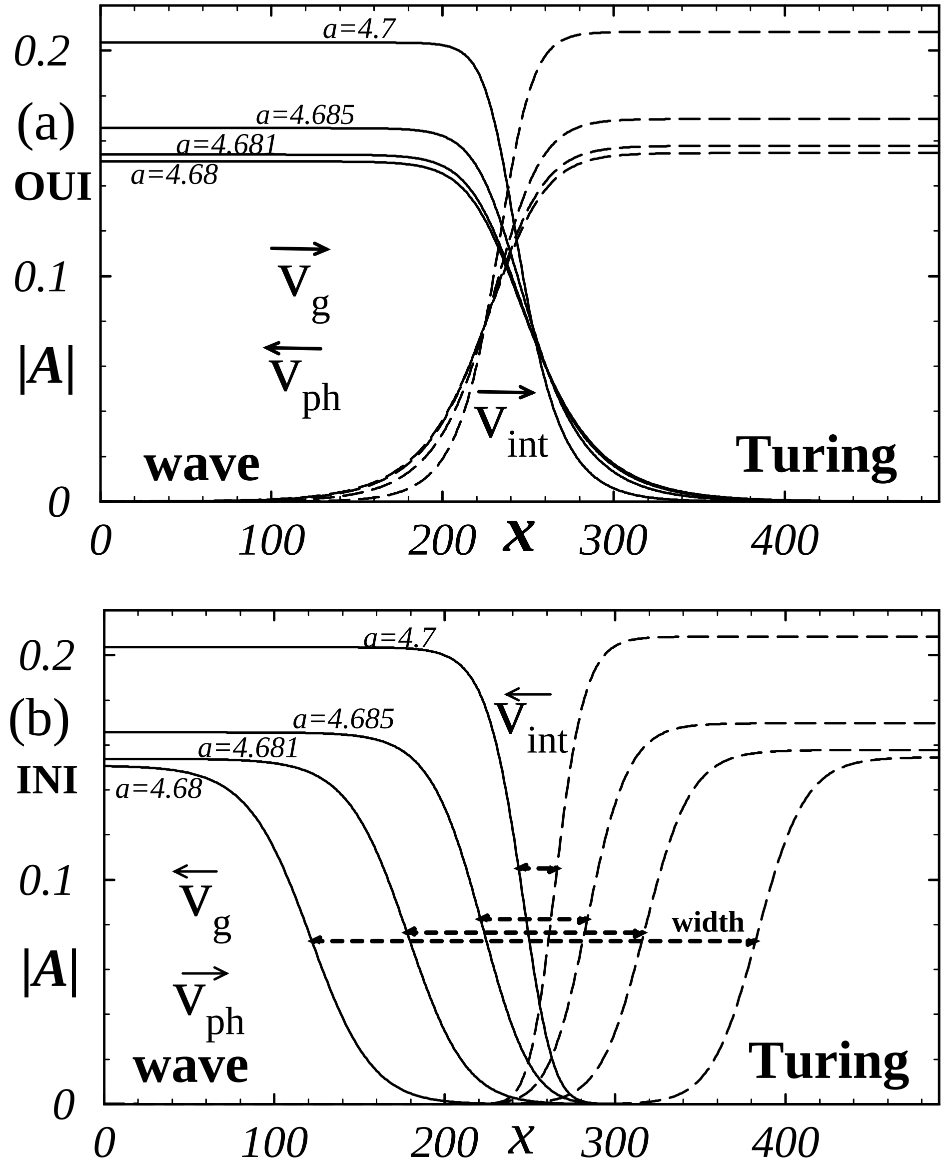

Figure 8.23: Plots of the amplitudes $|A_W|$ (full line) and $|A_T|$ (dashed line) for different values of the control parameter a near a OUI in (a) and a INI in (b) obtained from numerical simulations of the amplitude equations (7.1,7.2) with coefficients as in Table 4.2. The values of the control parameter a are indicated in the figure and $\delta = 1$. Only a small region around the interfaces is shown in each case. Note that the width of the INI, shown in (b) with short-dashed lines, *diverges* as the instability threshold is approached (recall that $a^c_{WT} = 4.657$). In Fig. 8.24 we plot the width of the INIs as a function of the control parameter a.

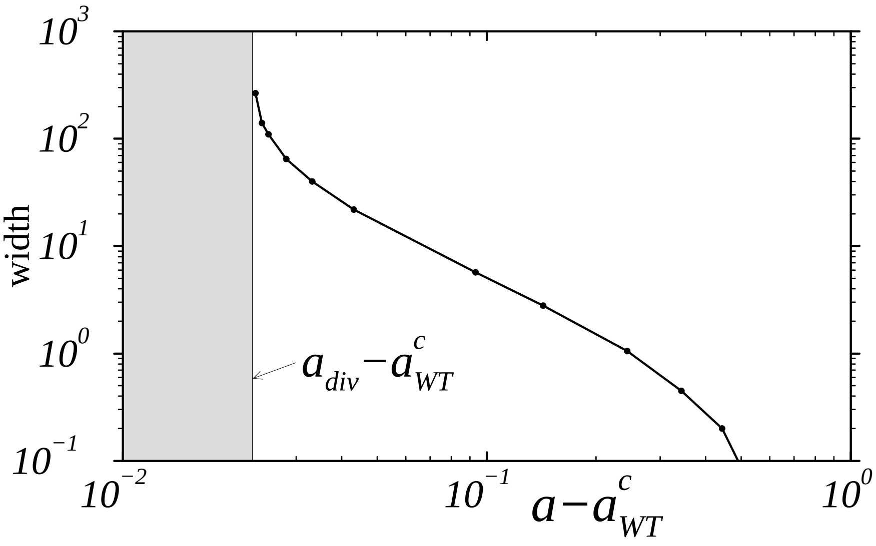

Figure 8.24: Width of the INI (*cf.* Fig. 8.23(b)) measured in numerical simulations of the coupled amplitude equation (7.1,7.2) as the instability threshold is approached (see the caption of Fig. 8.23 for details of the simulations). Here we keep δ fixed ($\delta = 1$) and vary the control parameter a. Four examples of this width are shown in Fig. 8.23(b). Note that the width diverges as the control parameter a approaches a critical value a_{div} (where $a_{div} > a^c_{WT}$). Consequently, in the gray area no stable INI can exist! The value of a_{div} can be calculated analytically.

of the control parameter a_{div} which is *bigger* than a^c_{WT}. Consequently in the range $a^c_{WT} \leq a < a_{div}$ *stable INIs can not exist*!

- Computation of a_{div} and η'^{div}_W

The critical value a_{div} is a function of δ and consequently defines a curve in the control parameter space. Given the linear mapping between the parameters a vs. δ and η'_W vs. η_T, a critical line in this last parameter space can be defined. This line is given by the function $\eta'^{div}_W(\eta_T)$. The values of $a_{div}(\delta)$ and $\eta'^{div}_W(\eta_T)$ can be computed analytically.

In Fig. 8.25 we show an example of INI with a large core. Note that in the core region both: $|\widetilde{A}_W|$ and $|\widetilde{A}_T|$, are almost zero. This suggests that we can consider the INI as two weakly interacting fronts. Consequently, for very large cores, we can neglect the coupling terms $-h_{WT}(1-ic_4)|\widetilde{A}_T|^2\widetilde{A}_W$ and $-h_{TW}|\widetilde{A}_W|^2\widetilde{A}_T$ in the amplitude equations (7.1,7.2). This leads[9] to a

---

[9] A similar method has been used by van Hecke *et al.* in ref. [86] to calculate the onset of divergence of sources of counterpropagating waves.

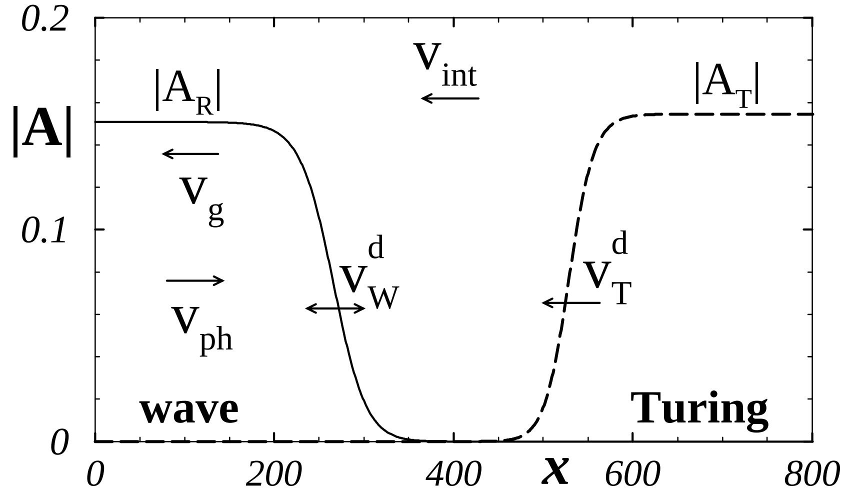

Figure 8.25: Plot of the amplitudes $|\widetilde{A}_W|$ (full line) and $|\widetilde{A}_T|$ (dashed line) of an INI with a large core. The values of the control parameter values are $a = 4.68$ and $\delta = 1$ (for other details of the numerical simulations see the caption of Fig. 8.23). Note that the core is so big that we can assume that the INI is built by two *noninteracting* fronts. One of the fronts corresponds to a Turing pattern invading an unstable zero state. This front has velocity v_T^d (*cf.* (8.19)) and is always negative. The other front corresponds to a wave pattern invading the zero state with velocity v_W^d. Depending on the value of η'_W this velocity can be positive or negative (*cf.* Eq. (8.20)).

set of two *uncoupled* amplitude equations equations: a RGLE and a CGLE with group velocity term. The properties of fronts in these equations was discussed in Section 6.4.5. The Turing front in the RGLE will propagate with velocity (*cf.* Eq. (6.25)):

$$v_T^d \overset{\text{def}}{=} -2\sqrt{\eta_T d_{TW}}. \tag{8.19}$$

Note that this velocity is always negative (see *e.g.* Fig. 8.25). This front will select the wavenumber equal to zero for the Turing domain (*cf.* Eq. (6.26)). The wave front in the CGLE will propagate with velocity (*cf.* Eq. (6.27)):

$$v_W^d \overset{\text{def}}{=} 2\sqrt{\eta'_W(1 + c_1^2)} + v_g. \tag{8.20}$$

If η'_W is small (big) this velocity is negative (positive) (recall that $v_g < 0$; see Table 4.2). This front selects a nonzero wavenumber for the wave domain (*cf.* Eq. (6.28)).

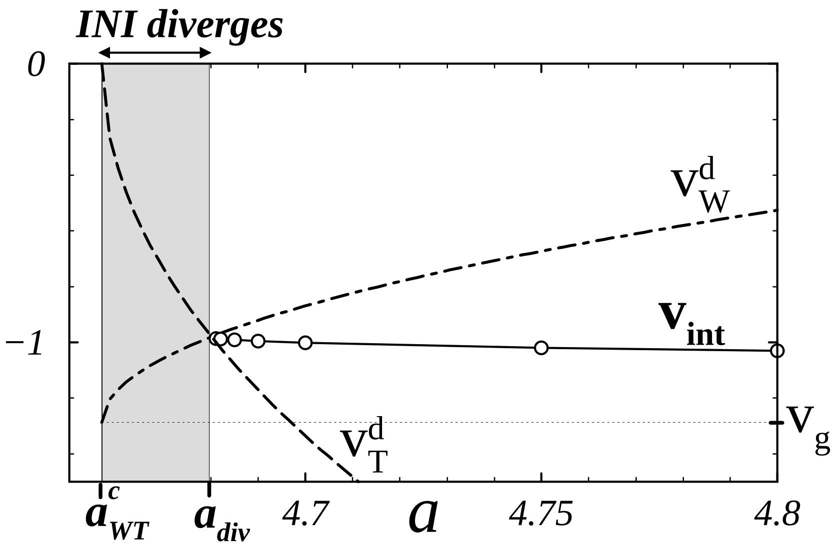

Figure 8.26: Plot of the front velocities v_T^d (dashed) and v_W^d (dot-dashed) as a function of the control parameter a for a constant value of δ ($\delta = 1$). If $a_{WT}^c \leq a < a_{div}$ then $v_T^d - v_W^d > 0$ and consequently the core width expands. In the gray area only OUIs can exist. For $a > a_{div}$ the two fronts overlap. Consequently a normal INI builds. The circles show the velocity v_{int} of the INI measured in numerical simulations of Eqs. (7.1,7.2). Note that, as expected, at $a = a_{div}$ the velocity v_{int} coincides with $v_T^d = v_W^d$.

In Fig. 8.26 we plot the marginal velocities v_T^d and v_W^d as a function of a for a fixed value of δ. If $a \approx a_{WT}^c$ (but $a \geq a_{WT}^c$) then the Turing front is almost stationary (since $v_T^d \approx 0$) and the wave front has negative velocity (*i.e.* $v_T^d \approx v_g$). Consequently the core region will *expand* unbounded. The same happens for $a_{WT}^c \leq a < a_{div}$ since $v_T^d - v_W^d > 0$ (see grey area in Fig. 8.26). On the other hand, $a > a_{div}$ the core region *shrinks* and consequently, after a some time, the fronts will start to overlap again. The coupling terms will provide a saturation to this shrinking. Finally a core of, stable, finite size is achieved (see Fig. 8.24).

The previous description implies that the divergence of the INI will happen for $a = a_{div}$, when both fronts travel with the same velocity. The condition $v_T^d = v_W^d$ provides us with an analytical way to compute $a_{div}(\delta)$ and $\eta_W^{\prime div}(\eta_T)$. The critical $\eta_W^{\prime div}$ is given by:

$$\eta_W^{\prime div}(\eta_T) = \frac{1}{1+c_1^2}(\sqrt{\eta_T d_{TW}} - \frac{v_g}{2})^2. \tag{8.21}$$

In Figure 8.27 we plot this quadratic equation on $\sqrt{\eta_T}$. In the region below

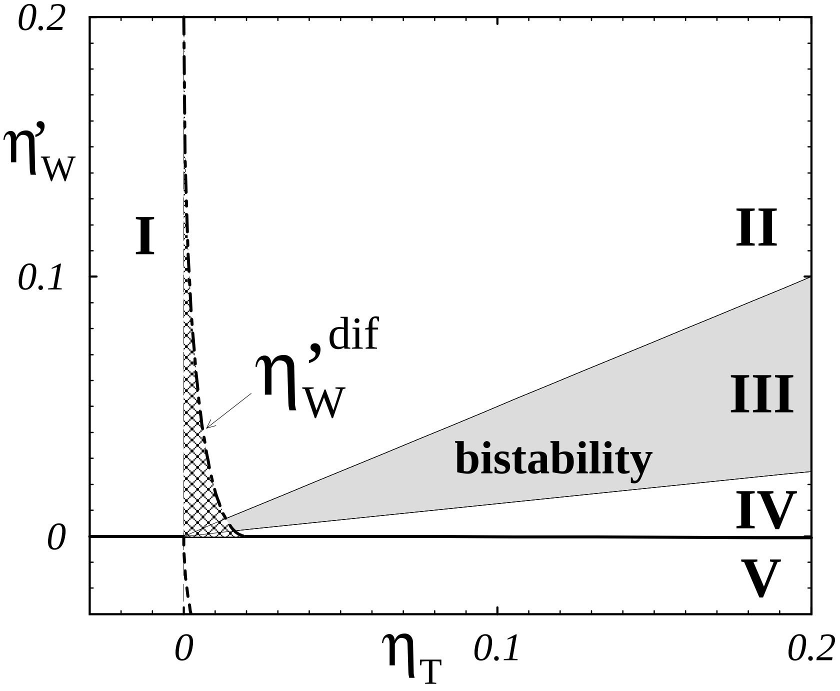

Figure 8.27: The hatched area corresponds to the region of the parameter space η'_W vs. η_T where stable INIs *can not exist*. The dot-dashed line shows the value of $\eta'^{div}_W(\eta_T)$ introduced in Eq. (8.21). In Fig. 8.28 the same information is shown in the control parameter space a vs. δ.

this line stable INIs can not exist (see hatched area in Fig. 8.27). Using the relationship between η'_W and η_T and the control parameter a and δ, we can directly calculate from Eq. (8.21) the critical $a_{div}(\delta)$. In Fig. 8.28 we plot this threshold line in the control parameter space a vs. δ.

An interesting to point to remark is that at $a = a_{div}(\delta)$ the interface velocity v_{int} can be computed analytically since $v_{int} = v^d_T = v^d_W$. Eq. (8.19) implies that this velocity is always negative. Consequently, the Turing domain invades the wave side for any value of δ. Moreover, the wavenumbers selected by this interface can be calculated analytically. The invading Turing domain has a zero wavenumber, whereas the wavenumber on the invaded wave side is different from zero.

8.4.2.B Scaling of Outward Interfaces

As we mentioned before, the OUI exist in all the control parameter space. However, its dynamics has some important features near the codimension-2

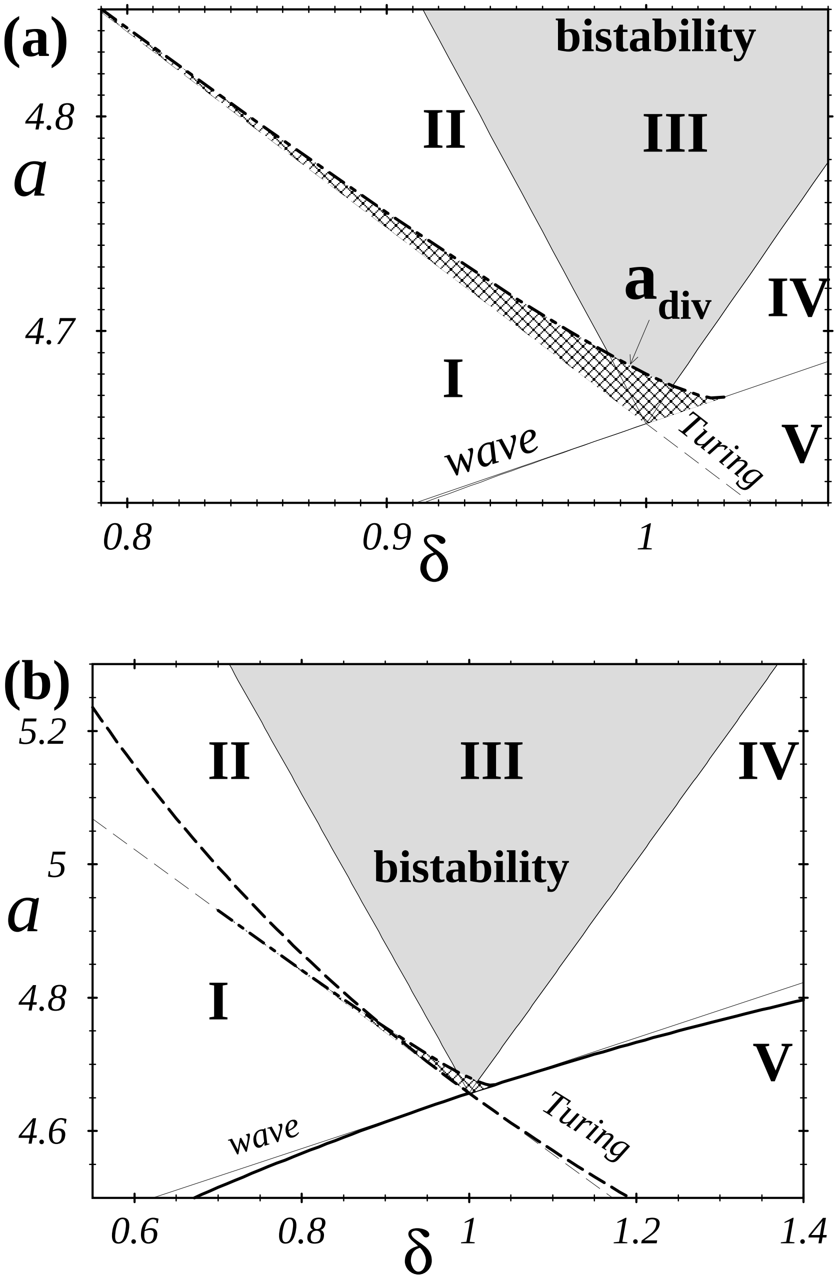

Figure 8.28: The hatched area corresponds to the region of the parameter space a vs. δ where a stable INI can not exist. The dot-dashed line corresponds to the threshold a_{div}. A small region of the parameter space is shown in (a). The thick full and dashed curves in (b) are the thresholds of Turing and wave instabilities respectively, as calculated from the linear stability analysis (for more details see discussion in the caption of Fig. 5.12).

point.

In the **LP** regime the interface velocity should be $v_{int} \approx -v_g$ in region **I** and part of region **III** and $v_{int} \approx 0$ in region **V** and part of region **IV**. Consequently, in between (*i.e.* in region **II** and part of regions **II** and **IV**) the interface velocity will "jump" between these two values!

8.4.3 Comparison with the RDNC model near the wave-Turing instability

In this last subsection we will compare quantitatively the dynamics of interfaces in the amplitude equations and in the RDNC model near the wave-Turing instability.

In Fig. 7.1 we presented a comparison between the u-profile of the RDNC model and a solution of the corresponding amplitude equations (7.1,7.2). We can see in this figure that the asymptotic values of the wave and Turing amplitudes: $|\widetilde{A}_W|$ and $|\widetilde{A}_T|$, coincide with the maximal values of the respective patterns. Here we will devote our attention to compare *quantitatively* the interface velocity.

In Fig. 8.29 we show a comparison between the velocity v_{int} of the INI and OUI in the amplitude equations (7.1,7.2) and in the RDNC model in a "cut" through the control parameter space (in this cut a is kept constant). In the simulations of the amplitude equations we took as initial conditions: $p_W^{ic} = 0$ and $p_T^{ic} = 0$. The wave and Turing domains in the RDNC model had initial wavenumbers equal to k_W^c and k_T^c respectively. Note that the interfaces in the amplitude equations and in the RDNC model exhibit the same qualitative behaviour. For small values of δ the interfaces select for the wave domain a total wavenumber k_W^{sel} different from k_W^c (*i.e.* $p_W^{sel} \neq 0$). On the other hand, for big δ the initial wavenumbers stay. For both types of interfaces, INIs and OUIs, the velocities measured in numerical simulations of the RDNC model are in good agreement with the amplitude equation predictions. Note that this agreement is better in the central region of the control parameter space.

In Fig. 8.30 we do an equivalent comparison in a particular point of the control parameter space, but now the value of the initial wavenumber on the wave side varies. Here we put as initial condition for the numerical simulation of the RDNC model a wave domain with wavenumber $k_W = k_W^c + p_W^{ic}$ and a Turing domain with $k_T \equiv k_T^c$. Note that also here the interface velocities agree.

With these comparisons we finish this chapter, in the following chapter we will investigate some new features of the interfaces arising far from the

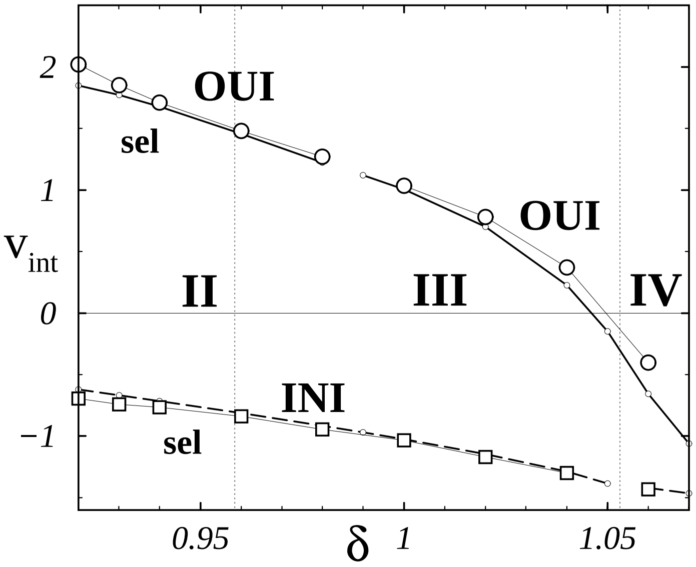

Figure 8.29: Here we compare the value of v_{int} measured in the amplitude equations (7.1,7.2) and in the RDNC model for different values of the control parameter δ and as a is kept constant: $a = 4.75$ (see Table 3.1 for the values of the other parameters). The thick full and dashed lines correspond to the values of v_{int} measured in numerical simulations of the amplitude equations for OUI and INI respectively. The values of v_{int} measured in simulations of the RDNC model for OUIs and INIs are indicated with big circles and big squares respectively. The range of δ in which the OUIs and INIs select a wavenumber $p_W^{sel} \neq 0$ is indicated with **sel**.

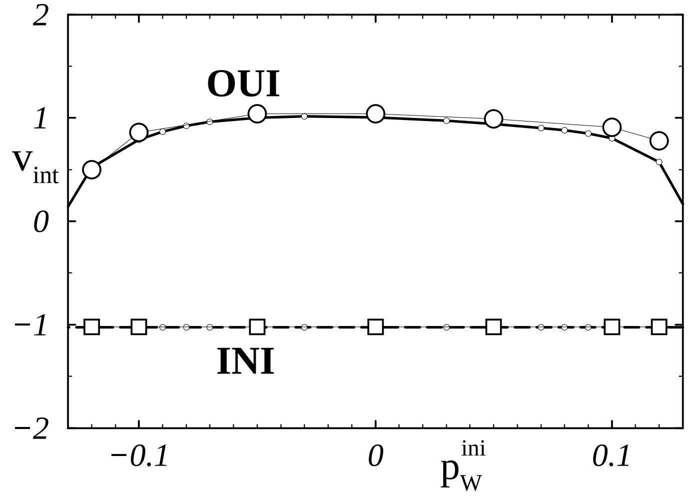

Figure 8.30: Here we compare v_{int} in the amplitude equations and in the RDNC model when the control parameters δ and a are kept constant and the initial wavenumber p_W^{ic} in the wave side is changed. The values of the control parameters are $a = 4.75$ and $\delta = 1$. See Fig. 8.29 for the details about the values of the other parameters and for an explanation of the different symbols used in this figure.

codimension-2 instability.

Chapter 9

Nonadiabatic effects in wave-Turing interfaces

In previous chapters we studied in detail the behaviour of interfaces near the codimension-2 wave-Turing instability. We saw that the coupled amplitude equations provide a convenient framework for a theoretical analysis of interfaces in the RDNC model near the instability threshold.

In this chapter we will address interfaces separating wave and Turing patterns at a substantial distance from the codimension-2 instability. We will see that new effects, not predicted by the coupled amplitude equations, will appear in numerical simulations of interfaces in the RDNC model. The interfaces may exhibit a locking of their velocities to values which are fixed by the wavenumbers and frequencies of the wave and Turing domains that they separate. Finally we will see that this velocity locking effect provides a mechanism for the formation of stable patches of one pattern embedded into the other. These drifting pattern domains are stable in a big region of the control parameter space.

9.1 Introduction

In Section 8.4 we studied general properties of wave-Turing interfaces *near* the codimension-2 point. More specifically, in Sections 8.4.1 and 8.4.2 the dynamics and scaling of the interfaces close to the codimension-2 point was analysed in the coupled amplitude equations (7.1,7.2). Finally, in Section 8.4.3 we compared of the dynamics of interfaces in the RDNC model with the predictions of the amplitude equations. We saw that the amplitude equations provide a convenient way to analyse the interface dynamics near the codimension-2 point.

The amplitude equations provide an effective description which is strictly valid *only near* the codimension-2 point. In Chapter 5 we saw that, as the distance to the instability threshold increases, effects not present in the amplitude equations may appear in simulations of the RDNC model. These new effects are typically called *nonadiabatic* [1]. In this chapter we will explore the nonadiabatic effects that may arise in the dynamics of wave-Turing interfaces.

- Organisation of this chapter

This chapter is organised as follows. In Section 9.2 we will study the nonadiabatic effects arising in single interfaces. We will first address the case of OUIs and later the INIs. In Section 9.3 we will consider the possibility of formation of stable drifting patterns domains.

9.2 Interface Velocity Locking

Simulations of interfaces in the RDNC model far away from the codimension-2 point show *qualitatively* similar behaviour to interfaces in the amplitude equations. Some details, nevertheless, differ. In this section we will investigate in detail these differences.

9.2.1 Locking of Outward Interfaces

Let us start by considering the case of OUIs. In Fig. 9.1 we show a comparison between the velocity v_{int} of OUIs in the amplitude equations (7.1,7.2) and the RDNC model, for a constant value of the control parameter $a = 5.2$. An equivalent comparison was shown in Fig. 8.29 for $a = 4.75$. In Fig. 9.1 the distance to the codimension-2 instability is *substantial* (recall that the codimension-2 point is located at $a^c_{WT} = 4.657$ and $\delta^c_{WT} = 1$).

Let us now examine side by side Figs. 9.1 and 8.29 in detail. The selection mechanism for the wavenumbers is the same in both figures. For small δ the OUI selects a unique wavenumber k_W different from k^c_W. On the other hand, for big δ the initial wavenumber is conserved (in both figures the simulations had initial conditions with $k^{ic}_W = k^c_W$).

The velocity of the OUI in the RDNC model, although similar with the velocity in the amplitude equations in both figures, has a particular feature in Fig. 9.1. It exists a range of δ for which the velocity is almost constant in the RDNC model. In order to understand the interface behaviour in this "plateau", in Fig 9.2 we show four examples of OUIs in the RDNC model.

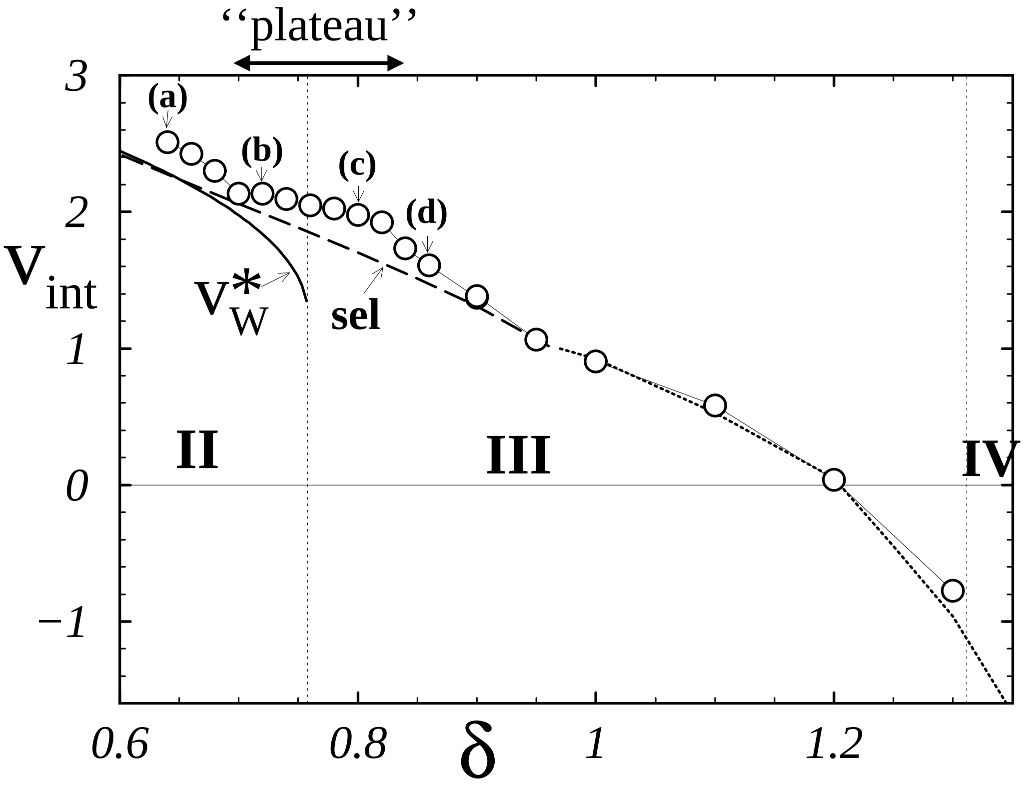

Figure 9.1: Comparison between the velocity v_{int} of an OUI in numerical simulations of the RDNC model (big circles) and the amplitude equations (7.1,7.2) (dashed and doted lines) for a constant value of a. This control parameter is $a = 5.2$ and consequently the simulations are far from the wave-Turing instability (recall that $a^c_{WT} = 4.657$ and compare this figure with Fig. 8.29 where $a = 4.7$). All the other coefficients and parameters of the amplitude equations and the RDNC model have the same values than in Fig. 8.29. The simulations of the amplitude equations where done with $p^{ic}_T = 0$ and $p^{ic}_W = 0$. The dashed line indicates that a different wavenumber $p^{sel}_W \neq 0$ is selected by the interface and the dotted line that $p^{ic}_W = 0$ stays. The marginal velocity $v^*_W(s = -1)$ (*cf.* Eq. (8.18)) is also plotted. The numerical simulations of the RDNC model where done with $k^{ic}_W = k^c_W$. For $\delta \lessapprox 0.90$ a wavenumber $k^{sel}_W \neq k^c_W$ is selected. This is in agreement with the predictions of the amplitude equations. The range for which the velocity of the interfaces in the model has a "plateau" is indicated in the upper part of the figure. The symbols (a), (b), (c) and (d) show the location and velocity of the four examples of OUIs presented in Fig. 9.2. Note that simulations inside the "plateau" (*i.e.* examples (b) and (c)) do not have spatio-temporal defects. For all other values of δ the OUIs exhibit defects as the interface travels.

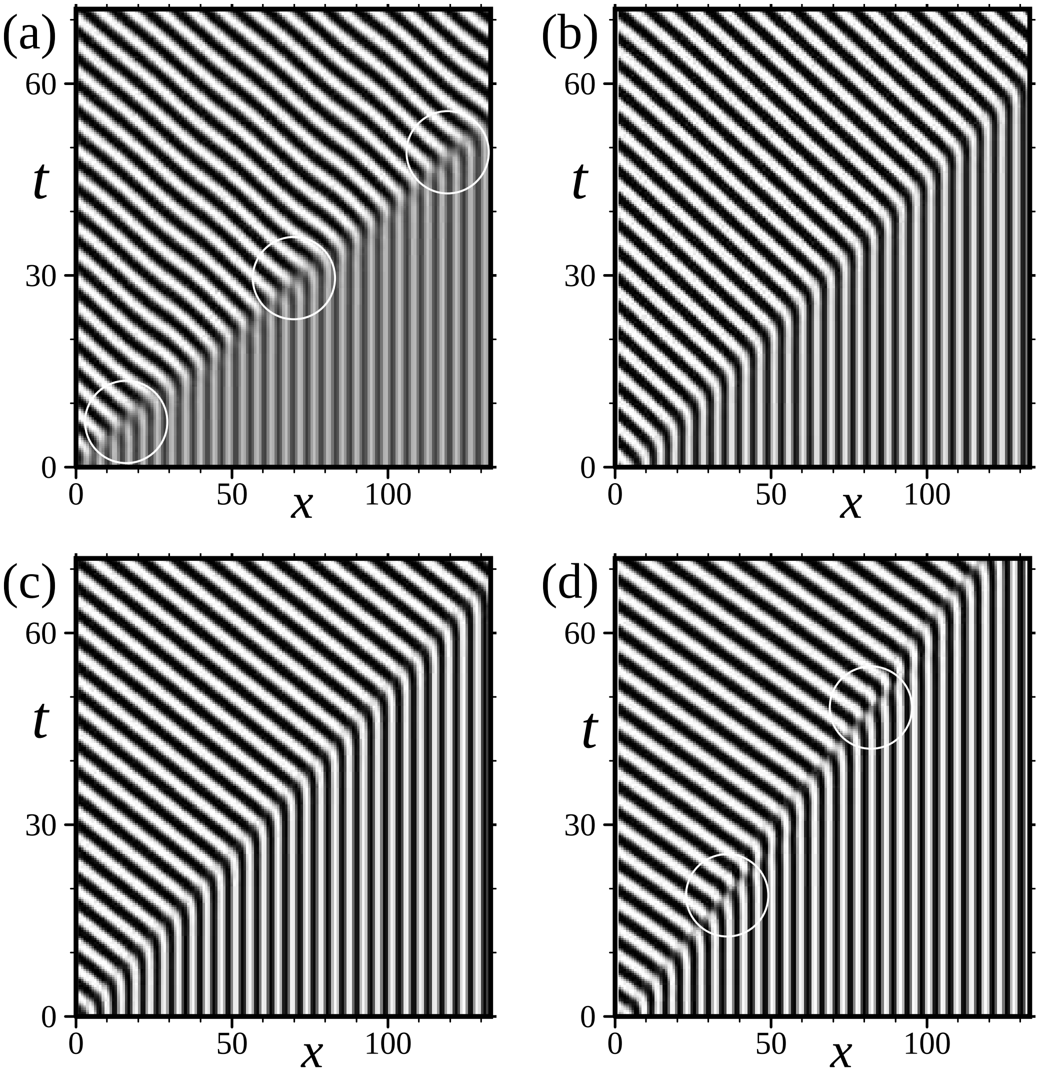

Figure 9.2: Four examples of OUIs in numerical simulations of the RDNC model with $a = 5.2$. The value of the control parameter δ is: $\delta = 0.64$ in (a), $\delta = 0.72$ in (b), $\delta = 0.80$ in (c) and $\delta = 0.86$ in (d). All these figures show space-time plots of field u of the RDNC model. The colours black and withe correspond to maximal and minimal values of u respectively. In all cases only a small region near the OUI is shown. The velocities of these interfaces are indicated in Fig. 9.1. Note that the OUI in examples (a) and (d) generate spatio-temporal defects as it travels. The locations of these defects are indicated with a circle. The OUIs in examples (b) and (c) do not produce defects as they travel. Their velocities are contained in the “plateau” of Fig. 9.1. The location of these examples in the control parameter space is indicated in Fig. 9.5.

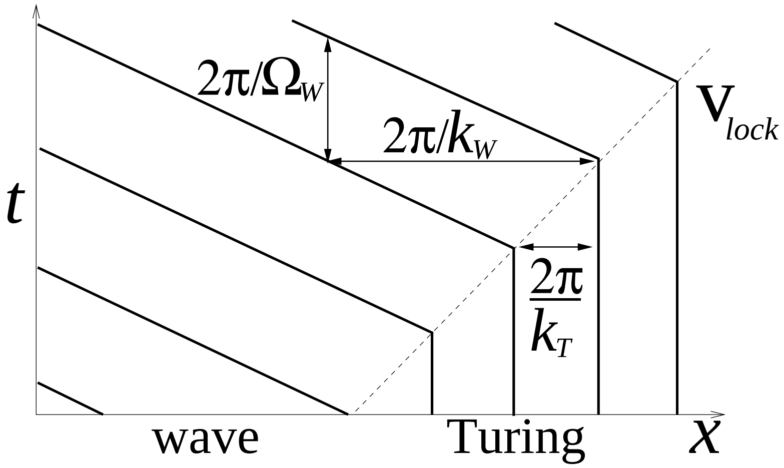

Figure 9.3: Geometrical construction for the velocity v_{lock} of an defect-free OUI. The thick lines show, schematically, the position of either the maxima or the minima of the pattern near the interface. These maxima and minima are conserved across the interface zone. This condition implies that the interface can only travel with velocity equal to v_{lock}. The dashed line corresponds to the trajectory this interface. An simple geometrical analysis shows that this constrain implies that $v_{lock} = \Omega_W/(k_T - k_W)$. Note that if we invert the direction of the time t, then the same geometrical construction implies that a defect-free INI should have velocity: $v_{lock} = -\Omega_W/(k_T - k_W)$.

The numerical simulations displayed in Figs. 9.2(b) and 9.2(c) are *inside* the plateau whereas in Figs. 9.2(a) and 9.2(d) are *outside* it. Note that the simulations outside the plateau display spatio-temporal defects whereas inside they don't. Let us now explore this feature of the interfaces in more detail.

- Interfaces without spatio-temporal defects

Note that for an interface to be defect-free, its velocity should satisfy a special *constraint*. Indeed, since the maxima and minima of the patterns are conserved across the interface, a *geometrical construction* dictates the velocity. This construction is shown in Fig. 9.3. Note that the total wavenumber k_W and frequency Ω_W of the wave and the wavenumber k_T of the Turing pattern impose a unique value v_{lock} for the velocity. This value is given by:

$$v_{lock} = \frac{\Omega_W}{k_T - k_W}. \tag{9.1}$$

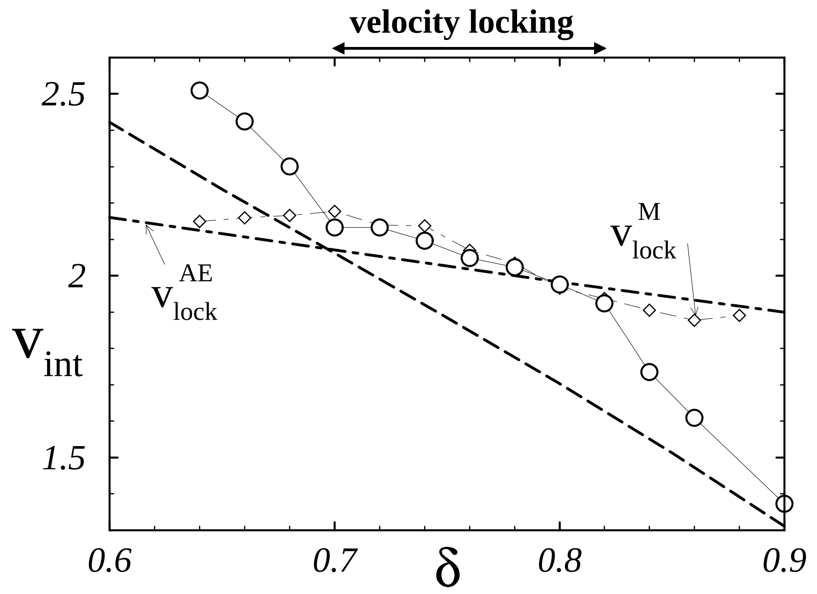

Figure 9.4: In this figure we plot the vales of the OUI velocity v_{int} (dashed line) and v_{lock}^{AE} (dot-dashed line) calculated using Eq. (9.1) in the amplitude equations (7.1,7.2) for $a = 5.2$. These two curves coincide only for a single value of δ. The big circles display the measured values of v_{int} in the RDNC model (in Fig. 9.1 we show the values of v_{int} over a bigger range of δ). The rhombs correspond to the values of v_{lock}^{M} calculated using the v_{int}, k_W and Ω_W measured in numerical simulations of the RDNC model. Note that the velocity of the OUIs in the RDNC model concord with the values of v_{lock}^{M} over an interval of δ. This locking velocity interval is displayed in the upper part of this figure and is equivalent with the "plateau" of Fig. 9.1.

- Interfaces with v_{lock} in the amplitude equations

In the framework of the amplitude equations, the total wavenumbers are $k_T = k_T^c + p_T$ and $k_W = k_W^c + p_W$ for Turing and wave patterns respectively and the total frequency of the waves is $\Omega_W = \omega_c + \omega_W(p_W)$ (where the function $\omega_W(p_W)$ was given in Eq. (5.5)). Inserting these values in Eq. (9.1) we can calculate v_{lock}^{AE}. In Fig. 9.4 we plot the values of v_{int} measured in the amplitude equations (dashed line) and the calculated values of v_{lock}^{AE} (dot-dashed line). Note that these velocities coincide only for a particular value of δ (for $a = 5.2$ this value is $\delta \approx 0.697$). The same happens for other values of the control parameter a (although the value of δ for which $v_{int} = v_{lock}^{AE}$ vary with a). Consequently, the amplitude equations predict the existence of defect-free OUIs only along a curve[1] in the control parameter space a vs.

---

[1] Note that this result is plausible since the rapidly varying space and time scales, which contain information about the critical wavenumbers k_W^c and k_T^c and frequency ω_W, have

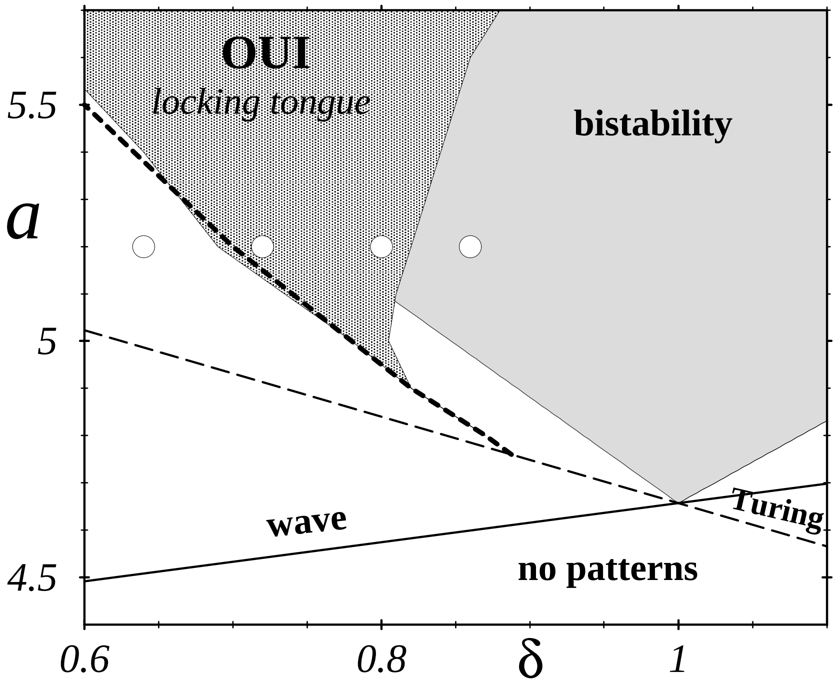

Figure 9.5: Parameter space of the RDNC model in the neighbourhood of the codimension-2 point showing the locking tongue for the OUI (gray region). The thick short-dashed curve shows the values of a and δ where the velocity of the OUI in the amplitude equations coincide with v_{lock}^{AE} (*cf.* Fig. 9.4). Note that near the codimension-2 point the tongue coincides with the predictions of the amplitude equations. As a increases the range of the parameter space where the OUI exhibit locking also increases. The four open circles display the locations of the examples shown in Fig. 9.2.

δ. This curve is shown in Fig. 9.5 with a thick short-dashed line.

- Interfaces with v_{lock} in the RDNC model

The values of Ω_W, k_W and k_T measured in numerical simulations of OUI in the RDNC model can be inserted in Eq. (9.1) to calculate v_{lock}^{M}. In Fig. 9.4 we display this velocity for different values of δ and with $a = 5.2$. Note that the values of v_{lock}^{M} and v_{int} agree in the plateau region. Consequently, we can say that the velocity of the interfaces in this plateau is *locked* to v_{lock}^{M}. This locking phenomena is characterised by the *absence of defects at the interface.*

Let us now study the velocity locking range as the control parameter a

---

been factored out in the amplitude equations.

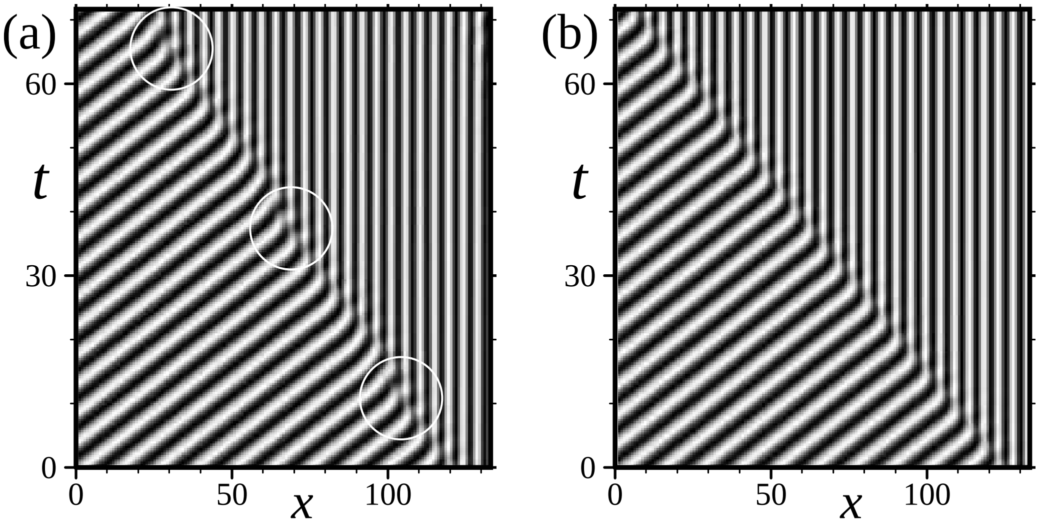

Figure 9.6: Two examples of space-time plots showing INIs in the RDNC model with and without defects (in (a) and (b) respectively). The location of each spatio-temporal defect in (a) is indicated with a white circle. Both examples have $a = 5.4$ and the value of the diffusion ratio is $\delta = 0.95$ in (a) and $\delta = 1.02$ in (b). See the caption of Fig. 9.2 for further details of the values of the model parameters. See Fig. 9.7 for the location of examples (a) and (b) in the control parameter space.

vary. In Fig. 9.5 we show the area in the control parameter space where the velocity locking occurs in the RDNC model. This area shrinks to the line predicted by the amplitude equations as the codimension-2 point is approached. On the other hand, as $a - a^c_{WT}$ increases, the range of δ where the velocity is locked enlarges. In the following we will refer to the area in the control parameter space, where the velocity of the interfaces is locked, as the *locking tongue*[2] (*cf.* Fig. 9.5). Note that the locking tongue covers a big part of the control parameter space when the distance to the codimension-2 point is substantial.

9.2.2 Locking of Inward Interfaces

An equivalent velocity locking effect may occur for the INIs.

In Fig. 9.6 we show two examples of INIs in numerical simulations of the RDNC model at a substantial distance to the codimension-2 point. We can again find an area of the control parameter space where the INIs exhibit

---

[2] Although other forms of locking are plausible, as for example that two periods of wave coincide with one of Turing or vice-versa, we did not find evidence of their existence in the RDNC model.

velocity locking. A geometrical construction, equivalent to the one presented for the OUIs, dictates again the locking velocity for INIs (see caption of Fig. 9.3). This velocity is given by: $v_{lock} = -\Omega_W/(k_T - k_W)$. In Fig. 9.7 we display the location in the control parameter space of the locking tongue for the INIs.

Note that the locking tongues for the OUIs and INIs appear for small and big values of δ respectively. The locking of the INIs appears in a region of the control parameter space where there exist a one parameter family of interfaces (*cf.* Section 8.4.1). This family is parametrised by the wavenumber k_W. The locking tongue displayed in Fig. 9.7 corresponds to INIs with $k_W = k_W^c$. INIs with $k_W \approx k_W^c$ can also exhibit locking of their velocities. The location in the control parameter space of these locking tongues depends only weakly on the parameter k_W. In the following we will consider only INIs with $k_W = k_W^c$.

9.3 Drifting Pattern Domains

9.3.1 Introduction

In the previous section we saw that the velocities of OUIs *and* INIs may exhibit a locking effect. Moreover, we saw in Fig. 9.7 that the locking tongues for OUIs and INIs begin to overlap for $a \gtrsim 5.7$. What does happen in this overlapping region?

This section we will be devoted to the exploration of this overlapping region and its consequences.

- Motivation

To motivate the our study, let us consider a typical numerical simulation of the RDNC model with control parameters inside the region of overlapping between the OUI and INI locking tongues. In Fig. 9.8 we show such a space-time plot. The numerical simulation was started with random initial conditions. We can see that, after a short transient time, two domains of travelling waves, embedded in a background of Turing patterns, arise. The wave patterns inside these domains travel in opposite directions. Both domains drift in opposite direction to the waves that they contain and are composed of locked interfaces[3]. After some time both domains collide. A unique domain arises as a result of this collision[4]. The resulting domain is

---

[3] Note that the locked interfaces, constituting the domain, travel with slightly different velocities. This happens because the wavenumber of the Turing background is not uniform.

[4] In general, the outcome of collisions between domains in the RDNC model depends on the relative size of each domain. If both domains are of similar size, then they may

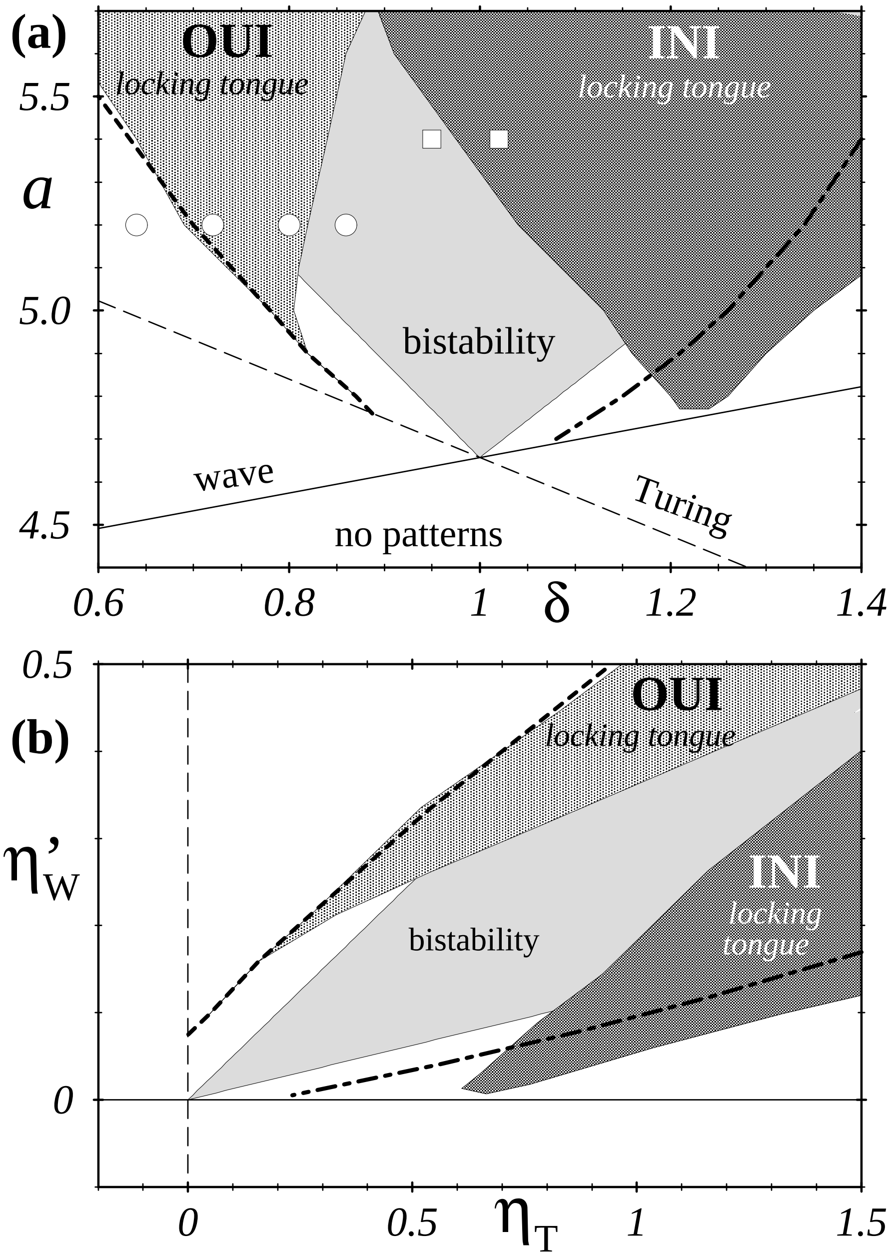

Figure 9.7: Control parameter space a vs. δ, in (a), and η'_W vs. η_T, in (b), in the neighbourhood of the codimension-2 point showing the locking tongues for OUI and INI (grey and dark grey regions respectively). See Fig. 9.5 for a more detailed representation of the locking tongue of OUIs. The curves where the velocity of OUI and INI in the amplitude equations coincide with v_{lock}^{AE} are shown with thick dashed and dot-dashed lines respectively. The big circles and squares in (a) indicate the values of the control parameters in the examples shown in Fig. 9.2 and Fig. 9.6 respectively. Note that for $a \gtrsim 5.7$ both tongues start to overlap.

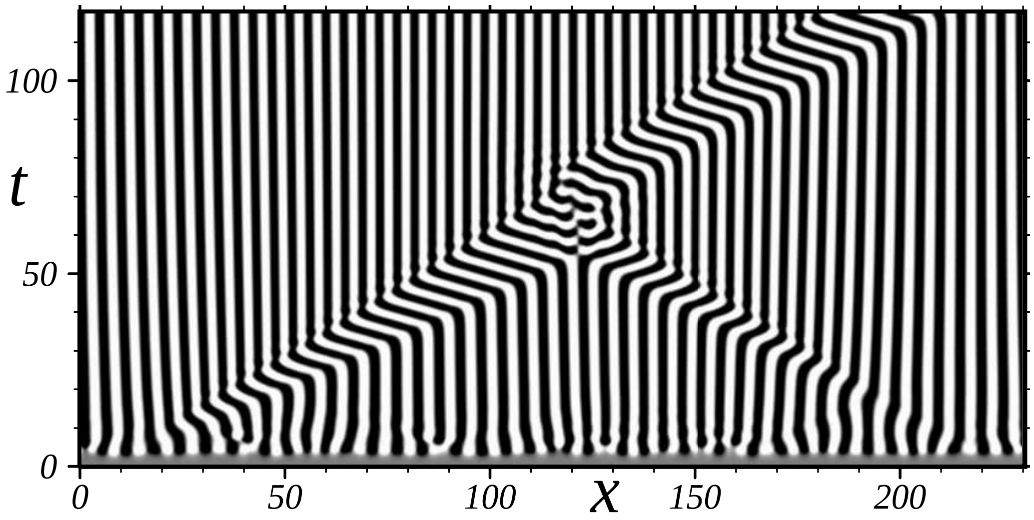

Figure 9.8: Typical example of a space-time plot of the RDNC model with control parameters inside the overlapping region between the OUI and INI locking tongues (*cf.* Fig. 9.7). In this numerical simulations we used random initial conditions. These initial conditions consisted in a small random perturbation around the unstable solution $\mathbf{X}_0$. The colour black (white) corresponds to big (small) values of the field u. Periodic boundary conditions were used and the values of the control parameters are $a = 6$ and $\delta = 0.84$ (in Fig. 9.10 we indicate with an open circle this location in the control parameter space). See the caption of Fig. 8.29 for an account of the values of the other parameters of the RDNC model.

also composed by locked interfaces and has constant size. In the following we will call this domain as *drifting pattern domain* (or, shortly, **DPD**).

For slightly different values of the control parameters (but still inside the overlapping region), the opposite scenario, consisting of a domain filled with a Turing pattern drifting in a background of travelling waves, may also be observed. In the following we will also call these domains DPDs.

- Large DPDs as two noninteracting interfaces

In Fig. 9.9 we display a typical example of a DPD of large width. Note that this DPD can be considered as composed of two *noninteracting* interfaces. One of these interfaces is a OUI and the other a INI (they are located in the the left and right side of Fig. 9.9 respectively). If both interfaces exhibit no defects and are locked, their velocities should have equal magnitude $|v_{lock}|$ but opposite signs. This ensures constant width and allows the construction

---

annihilate, resulting in a perfect Turing pattern.

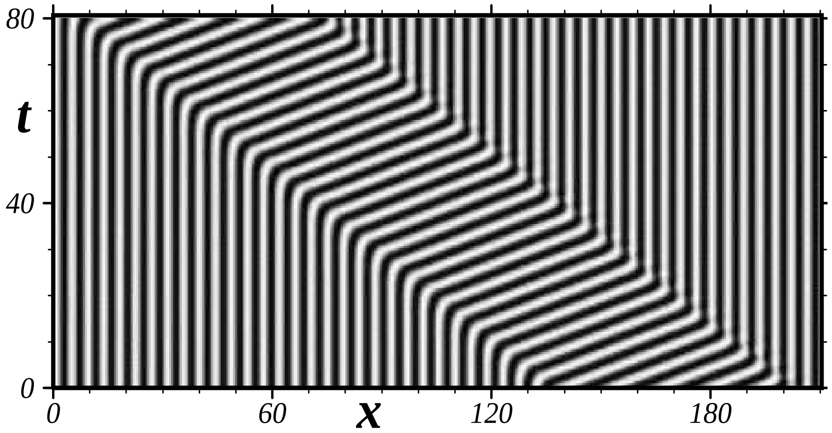

Figure 9.9: In this space-time plot we display a DPD of significant size found in numerical simulations of the RDNC model. The control parameters have values $a = 6.0$ and $\delta = 0.84$ (same values than in Fig. 9.8) and only a small part of the system of length $L = 409.6$ is shown. For the values of the other parameters of the model see Fig. 8.29. In Fig. 9.10 we display, with an open circle, the location of this simulation in the control parameter space.

of DPDs of arbitrary size.

9.3.2 Phase Diagram

The region of existence of large DPDs starts to open where the locking tongues for both interface types begin to overlap (see Fig. 9.7). This is the case for $a \gtrsim 5.7$. Above that value, DPDs spontaneously form from a variety of initial conditions. We have determined the parameter region, where they propagate with constant width and drift speed, from extensive simulations in systems with sizes $L > 400$ and periodic boundary conditions. The hatched area in Fig. 9.10 displays the parameter region where DPDs are found.

- Subregions

We can distinguish three different subregions in the phase diagram of Fig. 9.10:

- In region **B**, DPDs of any size, with two locked interfaces travelling at the same speed, are found. In Fig. 9.9 we show an example of this DPDs.

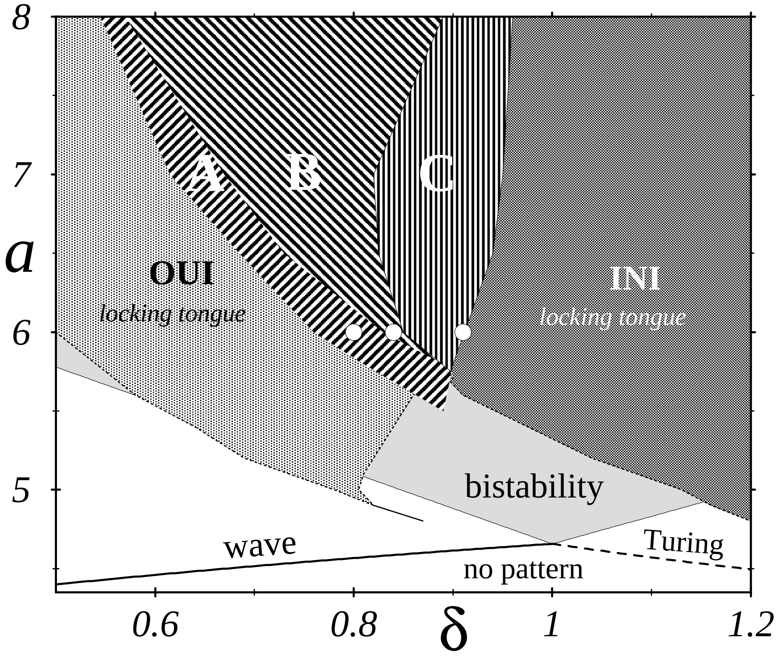

Figure 9.10: The hatched area display the region of existence of DPDs obtained in simulations of the RDNC model. The light-grey area corresponds to the bistable region between travelling waves and Turing patterns, as calculated from the amplitude equations. The OUI and INI locking tongues are shown with gray and dark-gray areas respectively. In region **B** DPDs of any size exist; the size being determined only by the initial condition (*cf.* Fig. 9.9). In region **C** small domains of wave patches travelling in a Turing background are found (*cf.* Fig. 9.11(b)). In region **A** only DPDs containing a single Turing cell are stable (*cf.* Fig. 9.11(a)). The three circles correspond to the location of simulations shown in Figs. 9.9, 9.11(a) and 9.11(b).

- In region **A**, the inward-interface is no longer locked and its speed is smaller than $|v_{lock}|$. Therefore large domains of Turing (wave) patterns contract (expand) in size until only a stable DPDs containing a single Turing cell is left. In Fig. 9.11(a) we show an example of this kind of DPDs.

- In region **C**, the outward-interface selects a k_W^{sel} which would be unstable against Turing patterns in an infinite domain. Therefore, the wave domain forming the DPD is mostly replaced by a Turing pattern. However, small DPDs with a few wavelength of wave pattern are still encountered. At the outer boundary of region **C**, only DPDs with a single wave cell are found to be stable. In Fig. 9.11(b) we show an example of this type of DPDs.

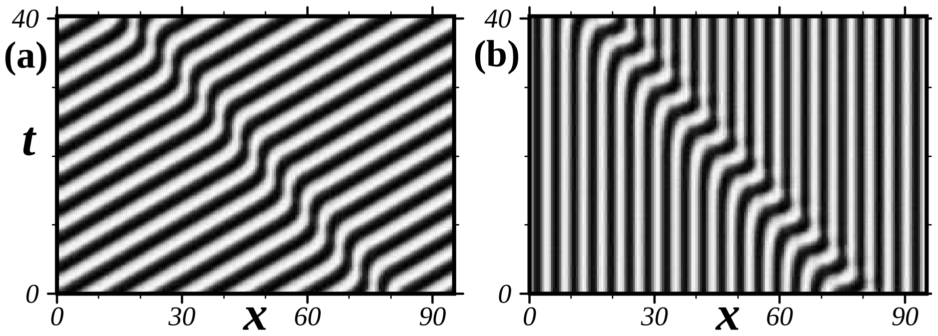

Figure 9.11: Space-time plots of the field u showing two examples of DPDs consisting of a single cell of Turing and wave respectively found in numerical simulations of the RDNC model. In both cases $a = 6.0$, and in (a) $\delta = 0.80$ whereas in (b) $\delta = 0.91$. For the values of the other parameters of the RDNC model see Fig. 8.29. In Fig. 9.10 we display, with two open circles, the location in the control parameter space of the simulations (a) and (b).

Note that the lower part of region **A** exists in part of the control parameter space where neither OUIs nor INIs are locked. This is in apparent contradiction with the picture of the DPDs as composed by two locked interfaces. Nevertheless this picture can not be applied to the DPDs in **A** because they contain a single Turing cell and consequently they can not be analysed as two noninteracting wave-Turing interfaces. This picture applies only to the DPDs found in region **B**.

- Robustness of the DPDs

The DPDs are a *very robust phenomena* inside the hatched region of Fig. 9.10. In this region, almost any initial condition leads to the formation of DPDs. Moreover, far away from the codimension-2 point, this region covers a considerable area of the control parameter space.

All the numerical simulations of the RDNC model presented in this chapter had a pure cubic nonlinearity (*i.e.* $\alpha = 0$). All results concerning DPDs have been checked for $\alpha \neq 0$ and do not change qualitatively as long as α is not too large (*cf.* Section 5.4.1 and Fig. 5.10).

- DPDs in other contexts

To conclude this chapter we would like to mention that patterns similar to DPDs have been reported in a variety of hydrodynamical experimental systems, see *e.g.* [94, 95]. These patterns have been related to secondary instabilities (parity breaking [1, 96]) of stationary patterns [94, 97, 98, 99].

Chapter 10

Conclusions

In the following we will give a short summary of the main results of this thesis. We will also provide a brief overview of the principal open issues that arise from the work done in this thesis.

10.1 Summary of Results

Let us begin this last chapter giving a restatement of the main results of this thesis.

10.1.1 Instabilities in the RDNC model

A linear stability analysis of the stationary solution of the RDNC model has been performed. The main results of this analysis are:

- Beside the standard homogeneous Hopf and Turing instabilities that can typically happen in reaction-diffusion models of activator-inhibitor type, a third kind of instability may occur in the RDNC model. This new instability is the wave bifurcation. The possibility of a wave instability is induced by the presence of an inhibitory nonlocal coupling.

- For the parameter values selected in this thesis, the model exhibits a wave instability for slow inhibitor diffusion, while, for fast inhibitor diffusion, a Turing instability is found. For moderate values of the inhibitor diffusion these two instabilities occur simultaneously at a codimension-2 wave-Turing bifurcation.

10.1.2 Amplitude Equations

We performed a weakly nonlinear analysis of the RDNC model near the Turing, wave and codimension-2 wave-Turing instabilities. This analysis provided us a set of amplitude equations describing the behaviour of the amplitudes of patterns arising near the instabilities. These equations consist of, either a single or, a set of coupled PDEs of the Ginzburg-Landau type.

- Amplitude Equations Predictions: Basic Solutions

The main results of the analysis of these amplitude equations are:

- The strength of the quadratic nonlinearity α of the RDNC model plays a very important rôle in the stability of different simple solutions of the amplitude equations.
- The Turing, wave and codimension-2 wave-Turing bifurcations are supercritical if α is small.
- For small values of α, travelling waves are preferred over standing waves. Upon increase of the strength α, standing waves get stabilised and the waves may even become Benjamin-Fair unstable.
- Depending on the value of α, a variety of bifurcation scenarios are possible near the codimension-2 wave-Turing instability. For $\alpha = 0$ or small, a region of bistability between travelling waves and Turing patterns is found. In this region both patterns compete.

- Comparison with numerical simulations of the RDNC model

The outcome of the analysis of the amplitude equations has been compared quantitatively with numerical simulations of the RDNC model. This comparison shows that for $\alpha = 0$ or small, the range of applicability of the amplitude equations is large. For significant values of α, this range becomes very small (*i.e.* nonadiabatic effects play a important rôle). One of these nonadiabatic effects is the stabilisation of travelling waves in the RDNC model, at a substantial distance from the instability threshold, in the case where the amplitude equations predict stable standing waves.

10.1.3 Interfaces

In the second part of this thesis we presented a detailed study of interfaces separating wave and Turing patterns arising from a codimension-2 wave-Turing bifurcation. Two different types of wave-Turing interfaces have been recognised, inward and outward, depending on the relationship between their phase and group velocities. They have different properties.

Near the codimension-2 instability the dynamics of such interfaces was analysed in the framework of the set of coupled Ginzburg-Landau equations. These results have been compared with numerical simulations of the RDNC model near and far away from the codimension-2 instability.

- Interfaces near the instability threshold

In order to analyse the dynamics and scaling properties of interfaces in the coupled amplitude equations we used a coherent structure ansatz. This ansatz leads to a set of ODEs. The interfaces in the amplitude equations correspond to heteroclinic orbits in the phase space of these ODEs. This phase space has been studied theoretically using counting arguments. Further insight on the interface dynamics has been obtained with direct numerical simulations of the amplitude equations.

Although, our main objective was the analysis of wave-Turing interface dynamics, we did also consider the dynamics of some simpler types of interfaces; namely Turing-Turing and Hopf-Turing interfaces. The main results of these analysis were:

- The concept of invading and invaded pattern plays a very important rôle in the analysis of interface dynamics.
- The interface dynamics can be complex. In our analysis, however, we found some general properties. One of these properties is that the interface dynamics can be divided in two different regimes: linear and nonlinear propagation.
    - In the linear propagation regime the interface dynamics is governed by the behaviour of the leading edge of the invading pattern. In this regime, interface velocity can be calculated analytically.
    - In the nonlinear propagation regime the multiplicity of the interfaces is in accord with the predictions of the counting arguments. Typically, the interface velocity can only be numerically calculated.
- Interfaces may propagate unsteadily if they select a wavenumber which is Eckhaus unstable. In this case, spatio-temporal defects are periodically generated as the interface travels. These defects may destabilise the interface itself.

- The scaling properties of inward and outward interfaces are different. In particular, we saw that inward interfaces can not exist in the proximity of the codimension-2 bifurcation because their width diverges at a finite distance from the threshold.

All the properties mentioned here have been tested quantitatively in numerical simulations of wave-Turing interfaces in the RDNC model near the instability threshold. We conclude that the coupled amplitude equations provide a convenient framework for a theoretical analysis of interfaces in the RDNC model near the instability threshold. Or equivalently, that the dynamics of interfaces separating small amplitude patterns is well described by the result of the coupled Ginzburg-Landau equations.

- Interfaces far away from the instability threshold

We did also compare the theoretical predictions of the amplitude equations with numerical simulations of the model at a substantial distance from the codimension-2 instability.

We saw that a new effect, not predicted by the coupled amplitude equations, may appear in interfaces separating large amplitude patterns. This nonadiabatic effect consists in a locking of the interface velocity. This locking mechanism is imposed by the absence of defects near the interfaces and happens for inward- and outward-interfaces. The value of this locking velocity is fixed by the wavenumbers and frequencies of the wave and Turing domains that the interface separate.

Another interesting issue found in the model is that the regions of control parameter space where the locking mechanism happens for inward and outward interfaces (*i.e.* the locking tongues) overlap at a substantial distance from the codimension-2. In this overlapping region stable drifting pattern domains (DPDs) can be formed. These domains of travelling waves embedded in a Turing pattern background and vice versa are robust. The region where DPDs exist covers, far away from the codimension-2 point, a considerable area of the control parameter space.

10.2 Open Issues

Let us finally address some important open issues that arise from the work done in this thesis.

- Interfaces between standing waves and Turing patterns

During the second part of this thesis we studied extensively interfaces separating *travelling* waves and Turing patterns. But, as we saw in Section 5.4.1, near a wave-Turing instability a region of bistability between *standing* waves and Turing patterns may exist (this situation does indeed appear in the RDNC model for big values of α; *cf.* Fig. 5.10). Are interfaces separating these patterns possible? Which is the dynamics of such interfaces?

- Generality of Interface velocity locking and DPDs

Although our study of interfaces at a substantial distance from the wave-Turing instability has been reported exclusively in the RDNC model, we think that the results of these studies (*i.e.* interface locking and DPDs) are not limited to this model and should carry over to other physical systems with similar pattern forming instabilities. We have done some preliminary work with such a system. This system consisted of a Swift-Hohenberg model supplemented with a diffusing inhibitor[1]. We did also find DPDs in the vicinity of the codimension-2 wave-Turing instability of this model.

Altogether, we think that the existence of interface-locking tongues is more fundamental than the existence of DPDs. For the latter phenomenon one needs both OUIs and INIs to display locking tongues *and* superposition of these tongues.

- Principle governing defect-free interfaces

A nonadiabatic effect consisting in defect-free interfaces separating counter-propagating waves (*i.e.* sinks and sources; *cf.* Section 6.2.A) has been found in experiments near a wave instability [100]. This experiments consisted in a convecting fluid locally heated along wires [101, 102, 103]. Consequently, one may inquire if there exist some general mechanism leading to defect-free interfaces.

- 2D Issues

All over this thesis we did consider that the model had only one spatial dimension. Naturally, some questions regarding the pattern formation features of the RDNC model in two dimensions arise. Which kind of patterns are stable near the Turing and wave instabilities? What happens in this case with

---

[1] More precisely the model had two variables u and v, with the dynamics: $\partial_t u = au - bv - (1+\partial_x^2)^2 u - u^3$ and $\partial_t v = cu - dv + \delta \partial_x^2 v$ (please compare this model with the RDNC model in Eqs. (2.13,2.14).

the interfaces separating these stable patterns? Do wave-Turing interface exist?

Appendix A

Derivation of the Nonlocal Coupling

In this Appendix we will solve the following equation:

$$eu(x,t) = fw(x,t) - \gamma \partial_x^2 w(x,t), \tag{A.1}$$

using the *Green's Function Method.* Equation (A.1) does not include time derivatives and corresponds to a PDE for $w(x,t)$ which depends on the externally given function $u(x,t)$. Since this PDE is linear, this equation can be analytically solved as a functional of $u(x,t)$.

If we represent both w and u in its Fourier representations: $w(x;t) = \frac{1}{2\pi}\int_{-\infty}^{+\infty} \hat{w}(k;t)e^{ikx}dk$ and $u(x;t) = \frac{1}{2\pi}\int_{-\infty}^{+\infty} \hat{u}(k;t)e^{ikx}dk$ then Eq. (A.1) can be written as:

$$\int_{-\infty}^{+\infty} \{e\hat{u}\}e^{ikx}dk = \int_{-\infty}^{+\infty} \{\hat{w}(f+\gamma k^2)\}e^{ikx}dk. \tag{A.2}$$

The terms inside the brackets should be equal in both sides. Consequently each Fourier coefficient should satisfy:

$$\hat{w}(k) = \hat{u}(k)\frac{e}{f+\gamma k^2} = \frac{e}{2\sqrt{\gamma f}}\hat{u}(k)\frac{2\sqrt{f/\gamma}}{f/\gamma\, + k^2}. \tag{A.3}$$

Multiplying both sides of this equation by $\frac{1}{2\pi}\int_{-\infty}^{+\infty} dke^{ikx}$ and recalling the identity: $\int_{-\infty}^{+\infty} e^{-\sigma|x'|}e^{-ikx'}dx' = \frac{2\sigma}{\sigma^2+k^2}$, we get:

$$\begin{aligned} \frac{1}{2\pi}\int_{-\infty}^{+\infty} dke^{ikx}\hat{w}(k) &= \frac{1}{2\pi}\int_{-\infty}^{+\infty} dk\left[e^{ikx}\frac{e}{2\sqrt{\gamma f}}\hat{u}(k)\int_{-\infty}^{+\infty} e^{-\sigma|x'|}e^{-ikx'}dx'\right] = \\ &= \frac{e}{2\sqrt{\gamma f}}\int_{-\infty}^{+\infty} dx'\left[e^{-\sigma|x'|}\frac{1}{2\pi}\int_{-\infty}^{+\infty} dke^{ik(x-x')}\hat{u}(k)\right], \end{aligned} \tag{A.4}$$

where $\sigma = \sqrt{f/\gamma}$. Finally, we obtain $w(x,t)$ as a *functional* of $u(x,t)$ (i.e. $w(x,t) = F[u(x,t)]$):

$$w(x;t) = \frac{\mu}{g} \int_{-\infty}^{+\infty} e^{-\sigma|x'|} u(x-x';t)\,dx', \tag{A.5}$$

where $\mu = g\sqrt{e^2/4\gamma f}$.

Appendix B

Eigenvectors for the Turing and Hopf instabilities

In this Appendix we will calculate the critical eigenvectors $\mathbf{U}_T$, $\mathbf{U}_H$ and $\mathbf{U}_W$ of the RDNC Model. These eigenvectors have been introduced in Section 3.4.1.B. and correspond to the Turing, homogeneous Hopf and wave instability respectively.

Critical eigenvectors for 2×2 matrices

Let us mention that the calculation of the critical eigenvectors $\mathbf{U}_T$, $\mathbf{U}_H$ and $\mathbf{U}_W$ can be done in a very simple way if we take into account that the RDNC model only has *two* variables.

We recall that the critical eigenvector of a 2×2 matrix like:

$$\mathbf{M} = \begin{pmatrix} M_{11} & M_{12} \\ M_{21} & M_{22} \end{pmatrix}, \tag{B.1}$$

with a unique real[1] critical eigenvalue (i.e. with $det[\mathbf{M}] = 0$ and $tr[\mathbf{M}] \neq 0$, *cf.* Eq. (3.12)) can be computed as:

$$\mathbf{U} = \begin{pmatrix} 1 \\ -\frac{M_{11}}{M_{12}} \end{pmatrix}. \tag{B.2}$$

Note that the norm of this critical eigenvector is *arbitrary*!.

Depending on the type of the instability the matrix $\mathbf{M}$ will assume a different form. Before calculating the eigenvectors for each particular case, let us mention that if the matrix M has one critical eigenvalue, then its adjoint

---

[1] Note that the coefficients M_{ij} can be complex.

$\mathbf{M}^{\dagger}$ (remember that $\mathbf{M}^{\dagger} = \overline{\mathbf{M}}^{\mathrm{Tr}}$) has also one critical eigenvalue. The adjoint critical eigenvector $\mathbf{U}^{\dagger}$ satisfy the condition: $\mathbf{M}^{\dagger}\mathbf{U}^{\dagger} = 0$. Consequently the adjoint critical eigenvector is given by:

$$\mathbf{U}^{\dagger} = \begin{pmatrix} 1 \\ -\frac{\overline{M}_{11}}{\overline{M}_{21}} \end{pmatrix}. \tag{B.3}$$

Eigenvalues of the RDNC model

Let us now calculate the critical eigenvalues of the RDNC model for the different instabilities.

- Turing instability

As we saw in Section 3.4.1, the eigenvalue problem defined by Eq. (3.9) has only one critical eigenvector. The imaginary part of this eigenvalue is equal to zero. Consequently the matrix $\hat{\mathbf{\Lambda}}(k_T^c)$ (*cf.* Eq. (3.10)) satisfies the requirements done previously for M (*i.e.* $\mathbf{M} = \hat{\mathbf{\Lambda}}(k_T^c)$). Hence, the critical eigenvector is given by:

$$\mathbf{U}_T = \begin{pmatrix} 1 \\ -\frac{\hat{\Lambda}_{11}(k_T^c)}{\hat{\Lambda}_{12}(k_T^c)} \end{pmatrix}. \tag{B.4}$$

The adjoint of $\hat{\mathbf{\Lambda}}(k_T^c)$ will have the following adjoint critical eigenvector:

$$\mathbf{U}_T^{\dagger^{\mathrm{Tr}}} = (1, -\frac{\hat{\Lambda}_{11}(k_T^c)}{\hat{\Lambda}_{21}(k_T^c)}). \tag{B.5}$$

- Homogeneous Hopf and wave instabilities

Let us treat the homogeneous Hopf and wave cases simultaneously. In this case the imaginary part of the critical eigenvalues of Eq. (3.9) is different from zero. These critical eigenvalues are $\lambda_+(k_W^c) = i\omega_c$ and $\lambda_-(k_W^c) = -i\omega_c$. Consequently, if we define $\mathbf{M} = \hat{\mathbf{\Lambda}}(k_W^c) - i\omega_c$ for the eigenvalue $\lambda_+(k_W^c)$ and $\mathbf{M} = \hat{\mathbf{\Lambda}}(k_W^c) + i\omega_c$ for $\lambda_-(k_W^c)$, then the matrices $\mathbf{M}$ satisfy the requirements done in the beginning of this appendix (*cf.* Eq. (B.1)). Hence the critical eigenvector corresponding to $\lambda_+(k_W^c)$ is given by:

$$\mathbf{U}_W = \begin{pmatrix} 1 \\ -\frac{\hat{\Lambda}_{11}(k_W^c) - i\omega_c}{\hat{\Lambda}_{12}(k_W^c)} \end{pmatrix}, \tag{B.6}$$

and for $\lambda_-(k_W^c)$ is $\overline{\mathbf{U}_W}$.

Note that in the homogeneous Hopf case (*i.e.* $k_W^c = 0$):

$$\mathbf{U}_H = \begin{pmatrix} 1 \\ -\frac{\hat{\Lambda}_{11}(0) - i\omega_c}{\hat{\Lambda}_{12}(0)} \end{pmatrix}, \tag{B.7}$$

and $\overline{\mathbf{U}_H}$ are the critical eigenvectors.

Finally, the adjoint critical eigenvector for $\lambda_+(k_W^c)$ is given by:

$$\overline{\mathbf{U}_W^{\dagger}}^{\mathrm{Tr}} = (1, -\frac{\hat{\Lambda}_{11}(k_W^c) - i\omega_c}{\hat{\Lambda}_{21}(k_W^c)}). \tag{B.8}$$

An equivalent formula is valid for the adjoint critical eigenvector corresponding to the eigenvalue $\lambda_+(k_W^c)$.

Appendix C

Effect of the parameters in the instability threshold conditions

In this Appendix we will do an exhaustive analysis the possible scenarios for the Turing, homogeneous Hopf and wave instability thresholds as the parameters δ, σ, μ, d and bc are varied.

Effect of the diffusion ratio δ

Here we want to analyse the effect of the diffusion ratio δ on the instability threshold conditions defined by Eqs. (3.33) and (3.34).

- Limit $\delta = 0$

Let us start with the particular limit $\delta = 0$. As we saw in Section 3.5.2, the wavenumbers of the Turing and wave instability are equal (*i.e.* $|k_T^c| = |k_W^c|$). Therefore the corresponding threshold conditions are given by:

$$a_T^c = 2\sqrt{2\mu\sigma} - \sigma^2 + \frac{bc}{d} \tag{C.1}$$

$$a_W^c = 2\sqrt{2\mu\sigma} - \sigma^2 + d. \tag{C.2}$$

This means that when increasing the parameter a there will be a wave instability first if $d < \sqrt{bc}$. We will discuss this in more detail later in this appendix.

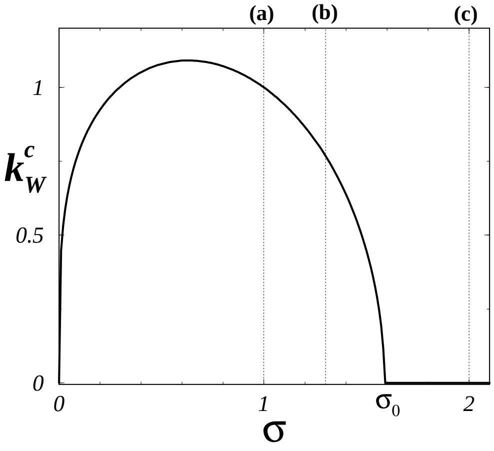

Figure C.1: In this figure we plot, for $\delta = 0$, the value of k_W^c as a function of σ (*cf.* Eq. (3.20) and compare with Fig. 3.2). The thin doted lines in show the location of the three different values of σ used in Figs. 3.3(a), 3.3(b) and 3.3(c).

- δ big

On the other hand, if δ is big then $k_W^c = 0$ (see Fig. 3.3(d) and Section 3.5.2). Consequently the threshold condition is given by:

$$a_W^c = \frac{2\mu}{\sigma} + d. \tag{C.3}$$

In Section 3.5.2 we saw that in this limit k_T^c can be calculated analytically. Therefore using Eq. (3.32) we get:

$$a_T^c = 2\sqrt{2\mu\sigma} - \sigma^2. \tag{C.4}$$

This means that, for big δ, the wave instability will happen first only if $d < 2\sqrt{2\mu\sigma} - \sigma^2 - 2\mu/\sigma$. But if $\mu, \sigma \geq 0$ then $2\sqrt{2\mu\sigma} - \sigma^2 - 2\mu/\sigma \leq 0$. Since in this thesis we assume that $d > 0$ *the RDNC model has always a Turing instability for big* δ.

Effect of the nonlocal coupling range $1/\sigma$

In section 3.5.3 we mentioned that the cases shown in Figs. 3.3(a), 3.3(b) and 3.3(c) correspond to *three qualitatively different scenarios.* We can ask now if for other values of σ new scenarios appear. The answer is not.

To see this we can use Eq. (3.20) for the critical wavenumber $|k_W^c|$ as function of σ. In Fig. C.1 plot the value of k_W^c for $\delta = 0$. The values of σ in each Fig. 3.3(a), 3.3(b) and 3.3(c) are indicated by thin doted lines.

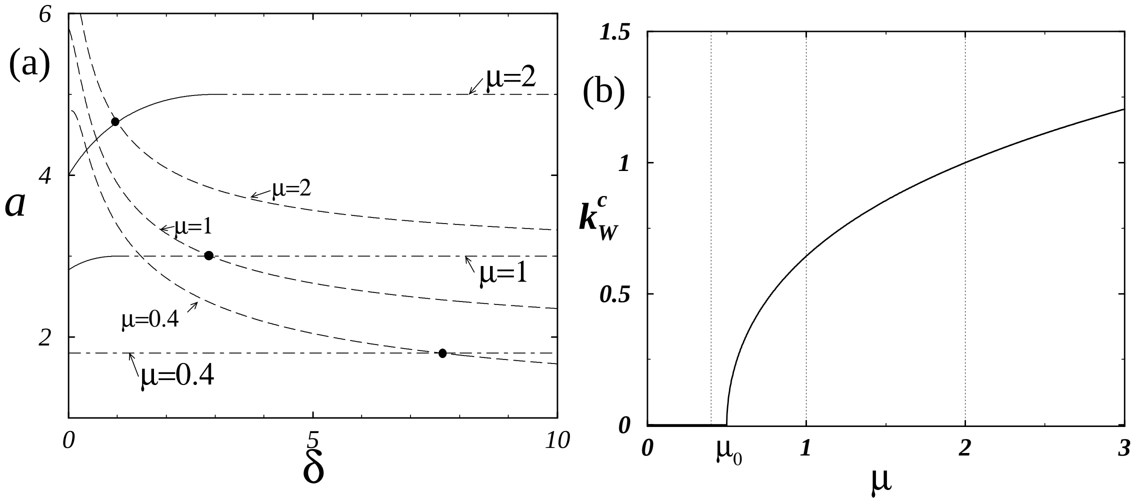

Figure C.2: In (a) we show the instability threshold lines for Turing (dashed), wave (full) and homogeneous Hopf (dot-dashed) in the parameter space a vs. δ for three different values of the nonlocal coupling strength μ. Note that as μ increases the Turing, homogeneous Hopf and wave lines move up. Note also that the qualitative effect of increasing μ is the same than increasing σ (compare with Figs. 3.3(a)-(c)). Consequently there are *three different scenarios* possible (see text). The black circles show the position of the codimension-2 instability points (see discussion in Section 3.5.4). In (b) the value of $|k_W^c|$ corresponding to $\delta = 0$ is show as a function of μ. The thin doted lines in (b) indicate the values of μ used in (a). All the other parameters of the RDNC model are fixed to: $b = 4, c = 1, d = 1$ and $\sigma = 1$.

The scenario presented in Fig. 3.3(a) will happen so far $0 < \sigma \leq \sigma_T$. The critical value $\sigma_T = \sigma_T(bc, d, \mu)$ corresponds to the value of σ for which the δ defined by the condition $a_W^c = a_T^c$ coincides with the δ where the transition between wave and homogeneous Hopf occurs. The value of σ_T can be get only numerically (for the parameter values of Figs. 3.3(a)-(c) $\sigma_T \approx 1.18$).

On the other hand, the scenario shown in Fig. 3.3(b) will happen when $\sigma_T < \sigma \leq \sigma_0$. The critical value $\sigma_0 \overset{\text{def}}{=} (2\mu)^{1/3}$ corresponds to the first value of σ for which $|k_W^c|$ with $\delta = 0$ is zero (see Fig. C.1). For the parameter values of Fig. 3.3(a)-(c) $\sigma_0 \approx 1.59$.

Finally, for $\sigma > \sigma_0$ the scenario of Fig. 3.3(c) occurs.

Effect of the nonlocal coupling strength μ

Now we want to analyse the effect of μ on the threshold conditions.

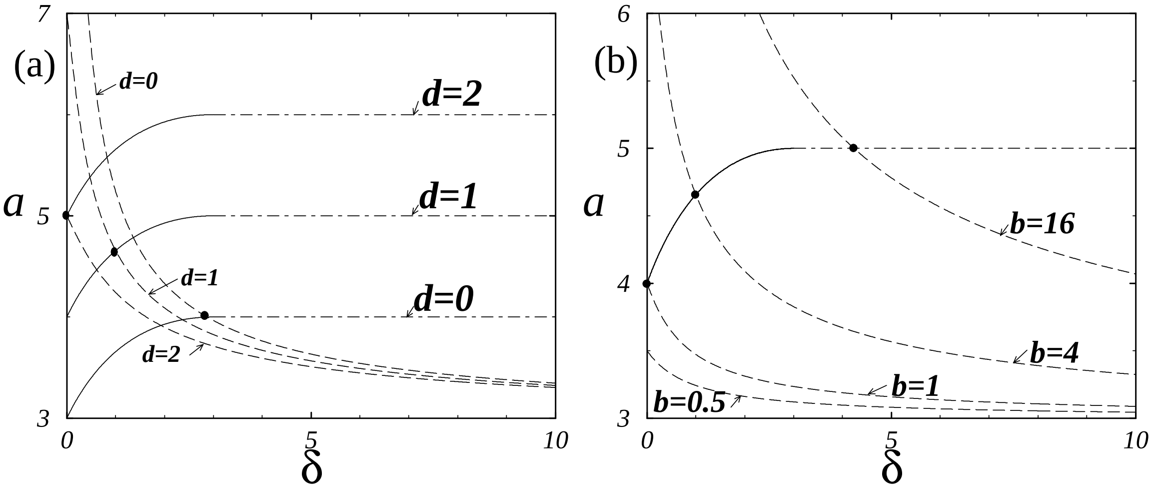

Figure C.3: In (a) we show the effect of the parameter d in the bifurcation lines in the parameter space a vs. δ. In (b) the same is done for the parameter b. The threshold of the Turing, homogeneous Hopf and wave instability are indicated with full, dot-dashed and dashed lines respectively. The black dots show the position of the codimension-2 instability points. The remaining parameter of the RDNC model are fixed to $b = 4, c = 1, \sigma = 1$ and $\mu = 2$ in (a) and to $c = 1, d = 1, \sigma = 1$ and $\mu = 2$ in (b).

In Fig. C.2(a) we take the situation shown in Fig. 3.3(a) (for the values of the parameters see caption of this figure) and vary μ. We see that as we *decrease the value of* μ from $\mu = 2$ to $\mu = 0.4$ the three qualitatively different scenarios discussed in Section 3.5 are again found. Namely, for $\mu = 2$ the same than scenario on Fig. 3.3(a) occurs. The situation of $\mu = 1$ is equivalent to Fig. 3.3(b) and for $\mu = 0.4$ is equivalent to Fig. 3.3(c).

In Fig. C.2(b) we plot the wavenumber $|k_W^c|$ as a function of μ for $\delta = 0$. The doted lines indicate the values of μ used in Fig. C.2(a). We can now classify the scenarios seen in Fig. C.2(a). An equivalent scenario to $\mu = 2$ will occur if $\mu_T \leq \mu$ where μ_T is defined in the same way than σ_T (for the values of the parameters of Fig. C.2 $\mu_T \approx 1.354$). For $\mu_0 \leq \mu < \mu_T$ where $\mu_0 \overset{\text{def}}{=} \sigma^3/2$ an equivalent scenario than for $\mu = 1$ happens (for Fig. C.2 $\mu_0 = 0.5$). Finally, for $\mu < \mu_0$ the same situation than for $\mu = 0.4$ happens.

Effect of the parameters of the reaction part d and b

Let us now explore the two remaining parameters d and b. As before, let us start with the situation plotted in Fig. 3.3(a) (*i.e.* $d = 1$ and $b = 4$).

- Parameter d

In Fig. C.3(a) we vary the value of d. For big δ all the Turing threshold lines converge to the same value. This value is given in Eq. (C.4). The more relevant feature of Fig. C.3(a) is that for $d > bc$ (see discussion for $\delta = 0$ in the beginning of this appendix) a Hopf instability is not possible (for Fig. 3.3(a) $bc = 4$).

- Parameter b

In Fig. 3.3(b) we vary the value of the parameter b. As we saw previously, neither the homogeneous Hopf nor the wave threshold lines do depend on this parameter.

Classification of possible instability scenarios in the control parameter space a vs. δ

To conclude this appendix we want to summarise the results found here and in section 3.5.3.

There exist only four different scenarios of instabilities possible in the control parameter space a vs. δ. These scenarios are:

1. Only a Turing instability occurs for any δ (*e.g.* for $d = 2$ in Fig. C.3(a) and for $b = 1$ and $b = 0.5$ in Fig. C.3(b)).
2. A homogeneous Hopf instability appears for small δ and a Turing instability for big δ (*e.g.* in Fig. 3.3(c) and for $\mu = 0.5$ in Fig. C.2(a)).
3. A wave instability occurs for small δ and a Turing instability for big δ (*e.g.* in Fig. 3.3(a) and for $d = 0$ in Fig. C.3(a)).
4. As δ increases there exist first a wave, then an homogeneous Hopf and finally a Turing instability (*e.g.* in Fig. 3.3(b), for $\mu = 1$ in Fig. C.2(a) and for $b = 16$ in Fig. C.3(b)).

Appendix D

Treatment of the nonlocal coupling

In this appendix we will explain in detail how the *multiple-scale perturbation expansion* [77, 78, 79], described in section 4.2.4, can be implemented in a nonlocal coupling term. The implementation is non trivial and is composed of the following steps:

- Change of Coordinates

The first step is to introduce the change of coordinated: $y \overset{\text{def}}{=} x - x'$, in the nonlocal coupling term of Eq. (2.17). This yields:

$$\Lambda_{NC} \int_{-\infty}^{+\infty} \mathbf{\Sigma}(|x - x'|)\mathbf{X}(x'; t)dx' = \Lambda_{NC} \int_{-\infty}^{+\infty} \mathbf{\Sigma}(|y|)\mathbf{X}(x - y; t)dy.$$

- Taylor Expansion around $\mathbf{X}(x; t)$

The next step is to expand in a Taylor series the function $\mathbf{X}(x - y; t)$ around $\mathbf{X}(x; t)$:

$$\int_{-\infty}^{+\infty} \mathbf{\Sigma}(|y|)\mathbf{X}(x - y; t)dy = \int_{-\infty}^{+\infty} \mathbf{\Sigma}(|y|)\Big\{1 - y\partial_x + \frac{y^2}{2}\partial_x^2 - \frac{y^3}{6}\partial_x^3 + \cdots + (-1)^n \frac{y^n}{n!}\partial_x^n + \cdots \Big\}\mathbf{X}(x; t)dy. \quad \text{(D.1)}$$

- Introduction of the Multiple Scales

In order to implement the multiple scales (*cf.* Eq. (4.18)) in the nonlocal coupling, we substitute each partial derivative in the terms inside the brackets of Eq. (D.1) with the following operators:

- $\partial_x \;\rightarrow \partial_{x_0} + \varepsilon\ \partial_{x_1} + \varepsilon^2\ \partial_{x_2} + \mathcal{O}(\varepsilon^3)$
- $\partial_x^2 \;\rightarrow \partial_{x_0}^2 + \varepsilon\ 2\partial_{x_0}\partial_{x_1} + \varepsilon^2\ (2\partial_{x_0}\partial_{x_2} + \partial_{x_1}^2) + \mathcal{O}(\varepsilon^3)$
- $\partial_x^3 \;\rightarrow \partial_{x_0}^3 + \varepsilon\ 3\partial_{x_0}^2\partial_{x_1} + \varepsilon^2\ (3\partial_{x_0}^2\partial_{x_2} + 3\partial_{x_0}\partial_{x_1}^2) + \mathcal{O}(\varepsilon^3)$

  $\vdots$
- $\partial_x^n \;\rightarrow \partial_{x_0}^n + \varepsilon\ n\partial_{x_0}^{n-1}\partial_{x_1} + \varepsilon^2\ (n\partial_{x_0}^{n-1}\partial_{x_2} + \frac{n!}{2!(n-2)!}\partial_{x_0}^{n-2}\partial_{x_1}^2) + \mathcal{O}(\varepsilon^3)$

  $\vdots$

These substitutions in Eq. (D.1) lead to:

$$\begin{aligned}
\int_{-\infty}^{+\infty}\mathbf{\Sigma}(|y|)\mathbf{X}(x-y;t)dy = \int_{-\infty}^{+\infty} & \mathbf{\Sigma}(|y|)\Big\{1 - y\Big(\partial_{x_0} + \varepsilon\ \partial_{x_1} + \varepsilon^2\ \partial_{x_2} + \mathcal{O}(\varepsilon^3)\Big) \\
& + \frac{y^2}{2}\Big(\partial_{x_0}^2 + \varepsilon\ 2\partial_{x_0}\partial_{x_1} + \varepsilon^2\ (2\partial_{x_0}\partial_{x_2} + \partial_{x_1}^2) + \mathcal{O}(\varepsilon^3)\Big) \\
& - \frac{y^3}{6}\Big(\partial_{x_0}^3 + \varepsilon\ 3\partial_{x_0}^2\partial_{x_1} + \varepsilon^2\ (3\partial_{x_0}^2\partial_{x_2} + 3\partial_{x_0}\partial_{x_1}^2) + \mathcal{O}(\varepsilon^3)\Big) \\
& + \cdots \\
& + (-1)^n\frac{y^n}{n!}\Big(\partial_{x_0}^n + \varepsilon\ n\partial_{x_0}^{n-1}\partial_{x_1} \\
& \qquad + \varepsilon^2\ (n\partial_{x_0}^{n-1}\partial_{x_2} + \frac{n!}{2!(n-2)!}\partial_{x_0}^{n-2}\partial_{x_1}^2) + \mathcal{O}(\varepsilon^3)\Big) \\
& + \cdots\Big\}\mathbf{X}(x_0, x_1, x_2, \cdots; t)dy.
\end{aligned}$$

- Reorganisation of the Elements of the Series

Let us now group the terms inside the brackets of the previous series in orders of ε. These groupings are:

- $\mathcal{O}(1)\ :\quad \Big\{1 - y\partial_{x_0} + \frac{y^2}{2}\partial_{x_0}^2 + \frac{y^3}{6}\partial_{x_0}^3 + \cdots + (-1)^n\frac{y^n}{n!}\partial_{x_0}^n + \cdots\Big\}\mathbf{X}$
- $\mathcal{O}(\varepsilon)\ :\quad -y\partial_{x_1}\Big\{1 - y\partial_{x_0} + \frac{y^2}{2}\partial_{x_0}^2 + \cdots + (-1)^{n-1}\frac{y^{n-1}}{(n-1)!}\partial_{x_0}^{n-1} + \cdots\Big\}\mathbf{X}$
- $\mathcal{O}(\varepsilon^2) :\quad \frac{y^2}{2}\partial_{x_1}^2\Big\{1 - y\partial_{x_0} + \cdots + (-1)^{n-2}\frac{y^{n-2}}{(n-2)!}\partial_{x_0}^{n-2} + \cdots\Big\}$

  $\quad -y\partial_{x_2}\Big\{1 - y\partial_{x_0} + \frac{y^2}{2}\partial_{x_0}^2 + \cdots + (-1)^{n-1}\frac{y^{n-1}}{n-1!}\partial_{x_0}^{n-1} + \cdots\Big\}\mathbf{X}$
- $\vdots$

- Resumation of the Series

Note that all the series inside the brackets in the previous expressions are all equal. Moreover, these series (applied to $\mathbf{X}(x_0, x_1, x_2, \cdots; t)$) are nothing else than the Taylor expansions of $\mathbf{X}(x_0 - y, x_1, x_2, \cdots; t)$ around $\mathbf{X}(x_0, x_1, x_2, \cdots; t)$.

Taking these two properties into account, we can summate these series to get the following expression for the nonlocal coupling term:

$$\boxed{\begin{aligned}\mathbf{\Lambda}_{NC}\int_{-\infty}^{+\infty}\mathbf{\Sigma}(|x-x'|)\mathbf{X}(x';t)dx' = \mathbf{\Lambda}_{NC}\int_{-\infty}^{+\infty}\mathbf{\Sigma}(|y|)\Big\{&\mathbf{X}(x_0-y,x_1,x_2,\cdots;t)\\ &-\varepsilon y\partial_{x_1}\mathbf{X}(x_0-y,x_1,x_2,\cdots;t)\\ &+\varepsilon^2\Big(\frac{y^2}{2}\partial_{x_1}^2\mathbf{X}(x_0-y,x_1,x_2,\cdots;t)\\ &-y\partial_{x_2}\mathbf{X}(x_0-y,x_1,x_2,\cdots;t)\Big)\\ &+\mathcal{O}(\varepsilon^3)\Big\}dy,\end{aligned}}$$

This last equation gives us a way to introduce the multiple scales in the nonlocal coupling operator.

- Remarks

It should be remarked that the procedure explained in this appendix is not an approximation. No expansion has been truncated. It is a rigorous expansion in powers of ε.

The method does not depend on the form of the kernel $\mathbf{\Sigma}(|x-x'|)$. The only restriction is that all the terms in the Taylor expansion[1] of Eq. (D.1) should remain finite (*i.e.* they should not *diverge*). This restriction will be satisfied by every "well behaved" kernel (i.e. infinitely differentiable). The most notorious example in which this restriction fails is the case of of a constant kernel (*i.e.* for called *global coupling*: $\mathbf{\Sigma}\int_{-\infty}^{+\infty}\mathbf{X}(x-y;t)dy$, see section 2.3.1).

---

[1] Mathematically, when the kernel $\Sigma(|y|)$ have this property is said that the kernel is *compact*.

Appendix E

Derivation of Amplitude Equations in the RDNC model

In this appendix we will derive the amplitude equations in the RDNC model corresponding to the codimension-1 Turing and wave instabilities (in Section E.1) and to the codimension-2 wave-Turing instability (in Section E.2).

E.1 Turing and Wave Amplitude Equations

Let us first address the derivation of the amplitude equations corresponding to the codimension-1 Turing and wave instabilities.

In Eq. (4.24) we presented the hierarchy of linear inhomogeneous equations resulting from inserting the ε-expansions of Eqs. (4.15), (4.2), (4.20) and (4.22) in the RDNC model. In this hierarchy a series of new operators: $\mathbf{\Lambda}_S^0[\circ]$, $\mathbf{\Lambda}_S^1[\circ]$ and $\mathbf{\Lambda}_S^2[\circ]$, appeared (*cf.* Eqs. (4.25), (4.26) and (4.27)). Taking into account that, as we will see later, the solutions $\mathbf{X}_1, \mathbf{X}_2, \mathbf{X}_3, \ldots$ of the hierarchy (4.24) consist of a sum of terms $\propto e^{ikx_0}$ (for some k), it is useful to consider the action of these operators over a generic vector of the form: $\mathbf{V}(k) = \mathbf{U}e^{ikx_0}$ where $\mathbf{U}$ is an arbitrary column vector; the result is:

$$\mathbf{\Lambda}_S^0\mathbf{V}(k) = \hat{\mathbf{\Lambda}}_S^0(k)\mathbf{U}e^{ikx_0} \quad \text{where} \quad \hat{\mathbf{\Lambda}}_S^0(k) \overset{\text{def}}{=} \begin{pmatrix} -k^2 - \frac{2\mu\sigma}{\sigma^2+k^2} & 0 \\ 0 & -\delta k^2 \end{pmatrix}, \tag{E.1}$$

$$\mathbf{\Lambda}_S^1\mathbf{V}(k) = \hat{\mathbf{\Lambda}}_S^1(k)\mathbf{U}e^{ikx_0} \quad \text{where} \quad \hat{\mathbf{\Lambda}}_S^1(k) \overset{\text{def}}{=} \begin{pmatrix} i2k - \frac{i4\mu\sigma k}{(\sigma^2+k^2)^2} & 0 \\ 0 & i2\delta k \end{pmatrix}, \tag{E.2}$$

$$\mathbf{\Lambda}_S^2\mathbf{V}(k) = \hat{\mathbf{\Lambda}}_S^2(k)\mathbf{U}e^{ikx_0} \quad \text{where} \quad \hat{\mathbf{\Lambda}}_S^2(k) \overset{\text{def}}{=} \begin{pmatrix} 1 - \frac{2\mu\sigma(\sigma^2+k^2)-8\mu\sigma k^2}{(\sigma^2+k^2)^3} & 0 \\ 0 & \delta \end{pmatrix}, \tag{E.3}$$

where the matrices $\hat{\mathbf{\Lambda}}_S^0(k)$, $\hat{\mathbf{\Lambda}}_S^1(k)$ and $\hat{\mathbf{\Lambda}}_S^2(k)$ are functions of the wavenumber

k. Note also that: $\mathbf{\Lambda}_{H,0} + \hat{\mathbf{\Lambda}}_S^0(k) \equiv \hat{\mathbf{\Lambda}}(k)|_{a=a_c}$ (where the matrix $\hat{\mathbf{\Lambda}}(k)$ was introduced in Eq. (3.10)) and that the matrices $\hat{\mathbf{\Lambda}}_S^1(k)$ and $\hat{\mathbf{\Lambda}}_S^2(k)$ can be expressed in term of $\hat{\mathbf{\Lambda}}(k)|_{a=a_c}$ in the following way: $\hat{\mathbf{\Lambda}}_S^1(k) = -i\partial_k \hat{\mathbf{\Lambda}}(k)|_{a=a_c}$ and $\hat{\mathbf{\Lambda}}_S^2(k) = -\frac{1}{2}\partial_k^2 \hat{\mathbf{\Lambda}}(k)|_{a=a_c}$.

E.1.A Equation $\mathcal{O}(\varepsilon)$; Turing and wave cases

The solutions of the homogeneous equation $\mathcal{O}(\varepsilon)$ were presented and discussed in Section 4.3.2.A. (*cf.* Eqs. (4.28) and (4.29) for the Turing and wave instabilities).

To solve the inhomogeneous linear equation corresponding to $\mathcal{O}(\varepsilon^2)$ in Eq. (4.24) we should first make sure that its inhomogeneous part satisfies the solvability condition given in Eq. (4.13). This solvability condition provides us information about the amplitudes A_T, A_L and A_R. We will do this separately for the Turing and wave cases.

E.1.B Equation $\mathcal{O}(\varepsilon^2)$; Turing case

It is easy to check that the following definition satisfies the inner product rules:

$$(\mathbf{Z}|\mathbf{Y}_j) \overset{\text{def}}{=} \int_0^{2\pi/k_T^c} \overline{\mathbf{Z}}^{\text{Tr}} \mathbf{Y}_j \, dx_0. \tag{E.4}$$

With the inner product so defined we can perform the solvability condition:

$$\left({\mathbf{X}_T^c}^\dagger \middle| [-\gamma_1^a \mathbf{\Lambda}_{H,1} + \partial_{t_1} - \partial_{x_1} \mathbf{\Lambda}_S^1 + \mathbf{\Omega}_2 \cdot \mathbf{X}_1] \mathbf{X}_1 \right) = 0, \tag{E.5}$$

where the solution $\mathbf{X}_1$ was given in Eq. (4.28) and ${\mathbf{X}_T^c}^\dagger \overset{\text{def}}{=} \mathbf{U}_T^\dagger e^{ik_T^c x_0}$ is the adjoint of the critical solution $\mathbf{X}_T^c$ (for the definition of the corresponding adjoint operator see discussion in Section 4.2.2). The adjoint eigenvector $\mathbf{U}_T^\dagger$ is calculated in Appendix B. After performing the integration over space, we end up with the following condition:

$$\overline{\mathbf{U}_T^\dagger}^{\text{Tr}} [-\gamma_1^a A_T \mathbf{\Lambda}_{H,1} + \partial_{t_1} A_T - \partial_{x_1} A_T \hat{\mathbf{\Lambda}}_S^1(k_T^c)] \frac{\mathbf{U}_T}{2} = 0. \tag{E.6}$$

After some algebra, it can be shown that:

$$\overline{\mathbf{U}_T^\dagger}^{\text{Tr}} \hat{\mathbf{\Lambda}}_S^1(k_T^c) \mathbf{U}_T \equiv i \frac{\partial_k det(\hat{\mathbf{\Lambda}}(k))}{\hat{\mathbf{\Lambda}}_{22}(k)} \bigg|_{k=k_T^c, a=a_T^c}, \tag{E.7}$$

where $\hat{\mathbf{\Lambda}}(k)$ was introduced in Eq. (3.10). On the other hand, as we saw in Section 3.4.2, in the Turing instability case: $\partial_k det(\hat{\mathbf{\Lambda}}(k))\Big|_{k=k_T^c, a=a_T^c} = 0$. Hence, the solvability condition reduces to the following differential equation for A_T:

$$\partial_{t_1} A_T = \gamma_1^a \kappa_1^{a,T} A_T, \tag{E.8}$$

where:

$$\kappa_1^{a,T} \stackrel{\text{def}}{=} \frac{\overline{\mathbf{U}_T^\dagger}^{\text{Tr}} \mathbf{\Lambda}_{H,1} \mathbf{U}_T}{\overline{\mathbf{U}_T^\dagger}^{\text{Tr}} \mathbf{U}_T}. \tag{E.9}$$

This quantity is typically nonzero. The value of γ_1^a is *a priori* not known, but if $\gamma_1^a \neq 0$ then Eq. (E.8) tells us that the amplitude of the Turing mode will either grow unbounded or become zero. None of these results is consistent with the perturbative analysis (*cf.* Eq. (4.2)) since we are assuming that the amplitude of the new solution is small (but different from zero) when the distance to the instability is also small. Consequently, the only physical possibility is to set:

$$\gamma_1^a \equiv 0, \tag{E.10}$$

and consequently $\partial_{t_1} A_T \equiv 0$.

Now we can proceed to solve the inhomogeneous equation corresponding to the $\mathcal{O}(\varepsilon^2)$ equation:

$$\mathbf{\Lambda}_{H,0}\mathbf{X}_2 + \mathbf{\Lambda}_S^0[\mathbf{X}_2] - \partial_{t_0}\mathbf{X}_2 = -\partial_{x_1}\mathbf{\Lambda}_S^1[\mathbf{X}_1] + \mathbf{\Omega}_2 \cdot \mathbf{X}_1\mathbf{X}_1. \tag{E.11}$$

A general solution of this inhomogeneous equation is obtained by adding a particular solution of this inhomogeneous problem to the solutions of the homogeneous equation. This general solution is:

$$\mathbf{X}_2 = \Gamma \mathbf{X}_1 + \mathbf{X}_{2,T}^{Inh}, \tag{E.12}$$

where Γ is an arbitrary constant and the inhomogeneous solution $\mathbf{X}_{2,T}^{Inh}$ is given by:

$$\begin{aligned}\mathbf{X}_{2,T}^{Inh} = \frac{1}{2}\Big[&-\partial_{x_1} A_T \mathbf{V}_1^{Inh} e^{ik_T^c x_0} - \frac{\alpha}{2}\Big(A_T^2 \mathbf{V}_2^{Inh} e^{i2k_T^c x_0} + |A_T|^2 \mathbf{V}_0^{Inh} e^0\Big)\Big] \\ &+c.c.,\end{aligned} \tag{E.13}$$

where:

$$\mathbf{V}_1^{Inh} \overset{\text{def}}{=} \begin{pmatrix} \frac{\hat{\Lambda}^1_{S_{11}}(k_T^c)}{\hat{\Lambda}_{11}(k_T^c)} \\ 0 \end{pmatrix} \quad , \quad \mathbf{V}_2^{Inh} \overset{\text{def}}{=} \frac{1}{det\hat{\Lambda}(2k_T^c)} \begin{pmatrix} \hat{\Lambda}_{22}(2k_T^c) \\ -\hat{\Lambda}_{21}(2k_T^c) \end{pmatrix},$$

$$\mathbf{V}_0^{Inh} \overset{\text{def}}{=} \frac{1}{det\hat{\Lambda}(0)} \begin{pmatrix} \hat{\Lambda}_{22}(0) \\ -\hat{\Lambda}_{21}(0) \end{pmatrix}. \tag{E.14}$$

Note that in the computation of $\mathbf{X}_{2,T}^{Inh}$ we have used the specific form of the nonlinearity in the RDNC model (*i.e.* the specific values of the tensor Ω).

E.1.C Equation $\mathcal{O}(\varepsilon^3)$; Turing case

For the inhomogeneity in the equation corresponding to $\mathcal{O}(\varepsilon^3)$ we get the following solvability condition:

$$\begin{aligned}&\left(\mathbf{X}_T^{c\,\dagger}\middle|[-\partial_{x_2}\mathbf{\Lambda}_S^1 + \partial_{t_2} - \gamma_2^a\mathbf{\Lambda}_{H,2} - \partial_{x_1}^2\mathbf{\Lambda}_S^2 + \mathbf{\Omega}_3\cdot\mathbf{X}_1\mathbf{X}_1]\mathbf{X}_1\right)\\ &\qquad + \left(\mathbf{X}_T^{c\,\dagger}\middle|[-\partial_{x_1}\mathbf{\Lambda}_S^1 + 2\mathbf{\Omega}_2\cdot\mathbf{X}_1]\mathbf{X}_2\right) = 0.\end{aligned} \tag{E.15}$$

Introducing $\mathbf{X}_2$ (*cf.* Eq. (E.12)) in this equation, we get:

$$\begin{aligned}&\left(\mathbf{X}_T^{c\,\dagger}\middle|[-\partial_{x_2}\mathbf{\Lambda}_S^1 + \partial_{t_2} - \gamma_2^a\mathbf{\Lambda}_{H,2} - \partial_{x_1}^2\mathbf{\Lambda}_S^2 + \mathbf{\Omega}_3\cdot\mathbf{X}_1\mathbf{X}_1]\mathbf{X}_1\right)\\ &\qquad + \Gamma\left(\mathbf{X}_T^{c\,\dagger}\middle|[-\partial_{x_1}\mathbf{\Lambda}_S^1 + 2\mathbf{\Omega}_2\cdot\mathbf{X}_1]\mathbf{X}_1\right)\\ &\qquad + \left(\mathbf{X}_T^{c\,\dagger}\middle|[-\partial_{x_1}\mathbf{\Lambda}_S^1 + 2\mathbf{\Omega}_2\cdot\mathbf{X}_1]\mathbf{X}_{2,T}^{Inh}\right) = 0.\end{aligned} \tag{E.16}$$

After performing the integration in space involved in the inner product (*cf.* Eq. (E.4)), we get:

$$\begin{aligned}&-\overbrace{\overline{\mathbf{U}_T^\dagger}^{\mathrm{Tr}}\partial_{x_2}A_T\hat{\mathbf{\Lambda}}_S^1(k_T^c)\frac{\mathbf{U}_T}{2}}^{\mathbb{A}} + \overline{\mathbf{U}_T^\dagger}^{\mathrm{Tr}}[\partial_{t_2}A_T - \gamma_2^a A_T\mathbf{\Lambda}_{H,2} - \partial_{x_1}^2 A_T\hat{\mathbf{\Lambda}}_S^2(k_T^c)]\frac{\mathbf{U}_T}{2}\\ &\quad + |A_T|^2A_T\overline{\mathbf{U}_T^\dagger}^{\mathrm{Tr}}\mathbf{\Omega}_3\cdot\left[\frac{\overline{\mathbf{U}_T}}{2}\frac{\mathbf{U}_T}{2}\frac{\mathbf{U}_T}{2} + \frac{\mathbf{U}_T}{2}\frac{\overline{\mathbf{U}_T}}{2}\frac{\mathbf{U}_T}{2} + \frac{\mathbf{U}_T}{2}\frac{\mathbf{U}_T}{2}\frac{\overline{\mathbf{U}_T}}{2}\right]\\ &\quad - \Gamma\overbrace{\overline{\mathbf{U}_T^\dagger}^{\mathrm{Tr}}\partial_{x_1}A_T\hat{\mathbf{\Lambda}}_S^1(k_T^c)\frac{\mathbf{U}_T}{2}}^{\mathbb{B}} + \overline{\mathbf{U}_T^\dagger}^{\mathrm{Tr}}\partial_{x_1}^2 A_T\hat{\mathbf{\Lambda}}_S^1(k_T^c)\frac{\mathbf{V}_1^{Inh}}{2}\\ &\quad - \alpha\overline{A_T}A_T^2\overline{\mathbf{U}_T^\dagger}^{\mathrm{Tr}}\mathbf{\Omega}_2\cdot\frac{\overline{\mathbf{U}_T}}{2}\frac{\mathbf{V}_2^{Inh}}{2} - 2\alpha A_T|A_T|^2\overline{\mathbf{U}_T^\dagger}^{\mathrm{Tr}}\mathbf{\Omega}_2\cdot\frac{\mathbf{U}_T}{2}\frac{\mathbf{V}_0^{Inh}}{2} = 0.\end{aligned}$$

The terms inside braces $\mathbb{A}$ and $\mathbb{B}$ vanish because of the same reasons than Eq. (E.7).

This solvability condition leads us to the following partial differential equation:

$$\boxed{\partial_{t_2} A_T = \gamma_2^a \kappa_2^{a,T} A_T + d_T \partial_{x_1}^2 A_T - g_{TT} |A_T|^2 A_T, \qquad \text{(E.17)}}$$

where the coefficient are given by:

$$\kappa_2^{a,T} \stackrel{\text{def}}{=} \frac{\overline{\mathbf{U}_T^\dagger}^{\mathrm{Tr}} \mathbf{\Lambda}_{H,2} \mathbf{U}_T}{\overline{\mathbf{U}_T^\dagger}^{\mathrm{Tr}} \mathbf{U}_T} \quad , \quad d_T \stackrel{\text{def}}{=} \frac{\overline{\mathbf{U}_T^\dagger}^{\mathrm{Tr}} \hat{\mathbf{\Lambda}}_S^2(k_T^c) \mathbf{U}_T - \overline{\mathbf{U}_T^\dagger}^{\mathrm{Tr}} \hat{\mathbf{\Lambda}}_S^1(k_T^c) \mathbf{V}_1^{Inh}}{\overline{\mathbf{U}_T^\dagger}^{\mathrm{Tr}} \mathbf{U}_T}, \tag{E.18}$$

$$g_{TT} \stackrel{\text{def}}{=} \frac{1}{4\overline{\mathbf{U}_T^\dagger}^{\mathrm{Tr}} \mathbf{U}_T} \Bigg(3\beta + 2\alpha^2 \Big(\frac{\hat{\Lambda}_{22}(2k_T^c)}{det(\hat{\mathbf{\Lambda}}(2k_T^c))} + \frac{2\hat{\Lambda}_{22}(0)}{det(\hat{\mathbf{\Lambda}}(0))} \Big) \Bigg). \tag{E.19}$$

A discussion of Eq. (E.17) will be done in Section 4.3.2.D. The coefficients of this equation will be analysed in Section 4.4 and Chapter 5.

E.1.D Equation $\mathcal{O}(\varepsilon^2)$; wave case

Let us now address the wave instability case. Although the derivation of the amplitude equations in this case is conceptually similar to the Turing case, in practice it is more involved because now we have two critical eigenvectors becoming unstable simultaneously.

We need first to define an appropriated inner product for this case. It is easy to check that the following definition is suitable:

$$(\mathbf{Z}|\mathbf{Y}_j) \stackrel{\text{def}}{=} \int_0^{2\pi/k_W^c} dx_0 \int_0^{2\pi/\omega_c} dt_0 \quad \overline{\mathbf{Z}}^{\mathrm{Tr}} \mathbf{Y}_j. \tag{E.20}$$

We can now perform the solvability condition of $\mathcal{O}(\varepsilon^2)$, but before let us remark that there is *two* different critical solutions (see Eq. (3.17)). Therefore we should project over both[1] solutions:

$$\Big(\mathbf{X}_L^{c\,\dagger} \Big| [-\gamma_1^a \mathbf{\Lambda}_{H,1} + \partial_{t_1} - \partial_{x_1} \mathbf{\Lambda}_S^1 + \mathbf{\Omega}_2 \cdot \mathbf{X}_1] \mathbf{X}_1 \Big) = 0, \tag{E.21}$$

and:

$$\Big(\mathbf{X}_R^{c\,\dagger} \Big| [-\gamma_1^a \mathbf{\Lambda}_{H,1} + \partial_{t_1} - \partial_{x_1} \mathbf{\Lambda}_S^1 + \mathbf{\Omega}_2 \cdot \mathbf{X}_1] \mathbf{X}_1 \Big) = 0, \tag{E.22}$$

---

[1] Indeed there are *four* critical solutions, but two of them are nothing else than the complex conjugated of the other two. Consequently, the solvability conditions arising from them are identical to the complex conjugated of the two solvability conditions analysed in here (*i.e.* they provide redundant information).

where the solution $\mathbf{X}_1$ is given in Eq. (4.29) and the adjoint critical solutions are $\mathbf{X}_L^{c\,\dagger} \overset{\text{def}}{=} \mathbf{U}_W^\dagger e^{i(\omega_c t_0 + k_W^c x_0)}$ and $\mathbf{X}_R^{c\,\dagger} \overset{\text{def}}{=} \mathbf{U}_W^\dagger e^{i(\omega_c t_0 - k_W^c x_0)}$. After performing the integrations of the inner product given in Eq. (E.20), we get the following set of equations:

$$\overline{\mathbf{U}_W^\dagger}^{\mathrm{Tr}}[-\gamma_1^a A_L \mathbf{\Lambda}_{H,1} + \partial_{t_1} A_L - \partial_{x_1} A_L \hat{\mathbf{\Lambda}}_S^1(k_W^c)]\frac{\mathbf{U}_W}{2} = 0, \tag{E.23}$$

$$\overline{\mathbf{U}_W^\dagger}^{\mathrm{Tr}}[-\gamma_1^a A_R \mathbf{\Lambda}_{H,1} + \partial_{t_1} A_R - \partial_{x_1} A_R \hat{\mathbf{\Lambda}}_S^1(-k_W^c)]\frac{\mathbf{U}_W}{2} = 0. \tag{E.24}$$

In contrary to the Turing case, the quantities: $\overline{\mathbf{U}_W^\dagger}^{\mathrm{Tr}} \hat{\mathbf{\Lambda}}_S^1(k_W^c)\mathbf{U}_W$ and $\overline{\mathbf{U}_W^\dagger}^{\mathrm{Tr}} \hat{\mathbf{\Lambda}}_S^1(-k_W^c)\mathbf{U}_W$, do not vanish. Moreover, after some algebra is possible to see that:

$$\begin{aligned}
\frac{\overline{\mathbf{U}_W^\dagger}^{\mathrm{Tr}} \hat{\mathbf{\Lambda}}_S^1(k_W^c)\mathbf{U}_W}{\overline{\mathbf{U}_W^\dagger}^{\mathrm{Tr}} \mathbf{U}_W} &\equiv -\frac{\overline{\mathbf{U}_W^\dagger}^{\mathrm{Tr}} \hat{\mathbf{\Lambda}}_S^1(-k_W^c)\mathbf{U}_W}{\overline{\mathbf{U}_W^\dagger}^{\mathrm{Tr}} \mathbf{U}_W} \\
&= \left.\frac{\hat{\mathbf{\Lambda}}_{11}(k)\partial_k \hat{\mathbf{\Lambda}}_{22}(k)[\sqrt{det\hat{\mathbf{\Lambda}}(k)} - i\hat{\mathbf{\Lambda}}_{22}(k)]}{\sqrt{det\hat{\mathbf{\Lambda}}(k)}[\sqrt{det\hat{\mathbf{\Lambda}}(k)} + i\hat{\mathbf{\Lambda}}_{11}(k)]}\right|_{k=k_W^c, a=a_W^c} \\
&= \frac{1}{2}\left.\frac{\partial_k det\hat{\mathbf{\Lambda}}(k)}{\sqrt{det\hat{\mathbf{\Lambda}}(k)}}\right|_{k=k_W^c, a=a_W^c},
\end{aligned} \tag{E.25}$$

where we used the facts that $tr\hat{\mathbf{\Lambda}}(k_W^c) \equiv 0$, $\partial_k tr\hat{\mathbf{\Lambda}}(k)|_{k=k_W^c} \equiv 0$ and $\omega_c^2 = det\hat{\mathbf{\Lambda}}(k_W^c)$ (see Section 3.4.1). The last quantity in Eq. (E.25) is nothing else than the definition of the *group velocity* c_g of the waves at the criticality with opposite sing (see Eq. (3.40) in Section 3.5.4); hence:

$$c_g = \frac{\overline{\mathbf{U}_W^\dagger}^{\mathrm{Tr}} \hat{\mathbf{\Lambda}}_S^1(k_W^c)\mathbf{U}_W}{\overline{\mathbf{U}_W^\dagger}^{\mathrm{Tr}} \mathbf{U}_W}. \tag{E.26}$$

Introducing:

$$\kappa_1^{a,W} \overset{\text{def}}{=} \frac{\overline{\mathbf{U}_W^\dagger}^{\mathrm{Tr}} \mathbf{\Lambda}_{H,1}\mathbf{U}_W}{\overline{\mathbf{U}_W^\dagger}^{\mathrm{Tr}} \mathbf{U}_W}, \tag{E.27}$$

Eqs. (E.23,E.24) can be written as:

$$\partial_{t_1} A_L - c_g \partial_{x_1} A_L = \gamma_1^a \kappa_1^{a,W} A_L, \tag{E.28}$$

$$\partial_{t_1} A_R + c_g \partial_{x_1} A_R = \gamma_1^a \kappa_1^{a,W} A_R. \tag{E.29}$$

Eqs. (E.28) and (E.29) are a set of *two uncoupled linear PDEs*. Introducing two new pseudo-time variables: $\tau_L \overset{\text{def}}{=} x_1 - c_g t_1$ and $\tau_R \overset{\text{def}}{=} x_1 + c_g t_1$, corresponding to travelling frames with velocities $\pm c_g$, we get:

$$\partial_{\tau_L} A_L = \gamma_1^a \kappa_1^{a,W} A_L \quad \text{and} \quad \partial_{\tau_R} A_R = \gamma_1^a \kappa_1^{a,W} A_R. \tag{E.30}$$

These two equations we can be solved directly. Similarly than in the Turing case, if γ_1^a is nonzero then they predict that the amplitudes either run away to infinity or are equal to zero. Because none of these behaviours is consistent with the perturbative analysis, we are forced to choose:

$$\gamma_1^a \equiv 0.$$

Hence the two solvability conditions of the equation $\mathcal{O}(\varepsilon^2)$ lead to:

$$\boxed{\begin{aligned} \partial_{t_1} A_L - c_g \partial_{x_1} A_L &= 0, && \text{(E.31)} \\ \partial_{t_1} A_R + c_g \partial_{x_1} A_R &= 0. && \text{(E.32)} \end{aligned}}$$

We can now proceed to solve the equation $\mathcal{O}(\varepsilon^2)$ for $\mathbf{X}_2$. A general solution is given by:

$$\mathbf{X}_2 = \Gamma \mathbf{X}_1 + \mathbf{X}_{2,W}^{Inh}, \tag{E.33}$$

where, as in the Turing case, Γ is an arbitrary constant, $\mathbf{X}_1$ is given in Eq. (4.29) and the inhomogeneous solution $\mathbf{X}_{2,W}^{Inh}$ is given by:

$$\begin{aligned} \mathbf{X}_{2,W}^{Inh} = \frac{1}{2}\Big[& (\partial_{t_1} A_L \mathbf{W}_{1,1}^{Inh} - \partial_{x_1} A_L \mathbf{V}_{1,1}^{Inh}) e^{i(\omega_c t_0 + k_W^c x_0)} \\ & + (\partial_{t_1} A_R \mathbf{W}_{-1,1}^{Inh} - \partial_{x_1} A_R \mathbf{V}_{-1,1}^{Inh}) e^{i(\omega_c t_0 - k_W^c x_0)} \\ & - \frac{\alpha}{2}\Big(A_L^2 \mathbf{V}_{2,2}^{Inh} e^{i(2\omega_c t_0 + 2k_W^c x_0)} + A_R^2 \mathbf{V}_{-2,2}^{Inh} e^{i(2\omega_c t_0 - 2k_W^c x_0)} \\ & + 2A_L A_R \mathbf{V}_{0,2}^{Inh} e^{i(2\omega_c t_0)} + 2A_L \overline{A_R} \mathbf{V}_{2,0}^{Inh} e^{i(2k_W^c x_0)} \\ & + (|A_L|^2 + |A_R|^2) \mathbf{V}_{0,0}^{Inh} \Big) \Big] + c.c., \end{aligned} \tag{E.34}$$

where:

$$\mathbf{W}_{1,1}^{Inh} = \mathbf{W}_{-1,1}^{Inh} \overset{\text{def}}{=} \begin{pmatrix} \frac{1}{\hat{\mathbf{\Lambda}}_{11}(k_W^c) - i\omega_c} \\ 0 \end{pmatrix},$$

$$\mathbf{V}_{1,1}^{Inh} \overset{\text{def}}{=} \begin{pmatrix} \frac{\hat{\mathbf{\Lambda}}_{S_{11}}^1(k_W^c)}{\hat{\mathbf{\Lambda}}_{11}(k_W^c) - i\omega_c} \\ 0 \end{pmatrix}, \qquad \mathbf{V}_{-1,1}^{Inh} \overset{\text{def}}{=} \begin{pmatrix} \frac{\hat{\mathbf{\Lambda}}_{S_{11}}^1(-k_W^c)}{\hat{\mathbf{\Lambda}}_{11}(-k_W^c) - i\omega_c} \\ 0 \end{pmatrix},$$

and finally:

$$\mathbf{V}^{Inh}_{m,n} \stackrel{\text{def}}{=} \frac{1}{det(\hat{\boldsymbol{\Lambda}}(mk_W^c) - in\omega_c\mathbf{I})} \begin{pmatrix} \hat{\boldsymbol{\Lambda}}_{22}(mk_W^c) - in\omega_c \\ -\hat{\boldsymbol{\Lambda}}_{21}(mk_W^c) \end{pmatrix}.$$

where $\mathbf{I}$ is the 2x2 identity matrix and the indices m and n can be 0 or ± 2. Note that $\mathbf{V}^{Inh}_{1,1} = -\mathbf{V}^{Inh}_{-1,1}$.

E.1.E Equation $\mathcal{O}(\varepsilon^3)$; wave case

Now we can perform the solvability conditions for the next order. They are:

$$\begin{aligned}\Big(\mathbf{X}_L^{c\,\dagger}\Big|[-\partial_{x_2}\boldsymbol{\Lambda}_S^1 + \partial_{t_2} - \gamma_2^a\boldsymbol{\Lambda}_{H,2} - \partial^2_{x_1}\boldsymbol{\Lambda}_S^2 + \boldsymbol{\Omega}_3\cdot\mathbf{X}_1\mathbf{X}_1]\mathbf{X}_1\Big)&\\ +\Big(\mathbf{X}_L^{c\,\dagger}\Big|[-\partial_{x_1}\boldsymbol{\Lambda}_S^1 + \partial_{t_1} + 2\boldsymbol{\Omega}_2\cdot\mathbf{X}_1]\mathbf{X}_2\Big) &= 0,\end{aligned}$$

and

$$\begin{aligned}\Big(\mathbf{X}_R^{c\,\dagger}\Big|[-\partial_{x_2}\boldsymbol{\Lambda}_S^1 + \partial_{t_2} - \gamma_2^a\boldsymbol{\Lambda}_{H,2} - \partial^2_{x_1}\boldsymbol{\Lambda}_S^2 + \boldsymbol{\Omega}_3\cdot\mathbf{X}_1\mathbf{X}_1]\mathbf{X}_1\Big)&\\ +\Big(\mathbf{X}_R^{c\,\dagger}\Big|[-\partial_{x_1}\boldsymbol{\Lambda}_S^1 + \partial_{t_1} + 2\boldsymbol{\Omega}_2\cdot\mathbf{X}_1]\mathbf{X}_2\Big) &= 0.\end{aligned}$$

Inserting Eq. (E.33) in these two equations we get:

$$\begin{aligned}\Big(\mathbf{X}_L^{c\,\dagger}\Big|[-\partial_{x_2}\boldsymbol{\Lambda}_S^1 + \partial_{t_2} - \gamma_2^a\boldsymbol{\Lambda}_{H,2} - \partial^2_{x_1}\boldsymbol{\Lambda}_S^2 + \boldsymbol{\Omega}_3\cdot\mathbf{X}_1\mathbf{X}_1]\mathbf{X}_1\Big)&\\ +\Gamma\Big(\mathbf{X}_L^{c\,\dagger}\Big|[-\partial_{x_1}\boldsymbol{\Lambda}_S^1 + \partial_{t_1} + 2\boldsymbol{\Omega}_2\cdot\mathbf{X}_1]\mathbf{X}_1\Big)&\\ +\Big(\mathbf{X}_L^{c\,\dagger}\Big|[-\partial_{x_1}\boldsymbol{\Lambda}_S^1 + \partial_{t_1} + 2\boldsymbol{\Omega}_2\cdot\mathbf{X}_1]\mathbf{X}_{2,W}^{Inh}\Big) &= 0, \quad \text{(E.35)}\\ \Big(\mathbf{X}_R^{c\,\dagger}\Big|[-\partial_{x_2}\boldsymbol{\Lambda}_S^1 + \partial_{t_2} - \gamma_2^a\boldsymbol{\Lambda}_{H,2} - \partial^2_{x_1}\boldsymbol{\Lambda}_S^2 + \boldsymbol{\Omega}_3\cdot\mathbf{X}_1\mathbf{X}_1]\mathbf{X}_1\Big)&\\ +\Gamma\Big(\mathbf{X}_R^{c\,\dagger}\Big|[-\partial_{x_1}\boldsymbol{\Lambda}_S^1 + \partial_{t_1} + 2\boldsymbol{\Omega}_2\cdot\mathbf{X}_1]\mathbf{X}_1\Big)&\\ +\Big(\mathbf{X}_R^{c\,\dagger}\Big|[-\partial_{x_1}\boldsymbol{\Lambda}_S^1 + \partial_{t_1} + 2\boldsymbol{\Omega}_2\cdot\mathbf{X}_1]\mathbf{X}_{2,W}^{Inh}\Big) &= 0. \quad \text{(E.36)}\end{aligned}$$

The two terms multiplied by Γ are equivalent to Eqs. (E.21) and (E.22) and therefore they should vanish if Eqs. (E.31) and (E.32) are satisfied by the amplitudes A_L and A_R.

Implementing the integrations involved in the inner product, the solvability conditions of Eqs. (E.35,E.36) become:

$$-c_g\partial_{x_2}A_L + \partial_{t_2}A_L - \kappa_2^{a,W}\gamma_2^a A_L + \beta\frac{1}{4}(3|A_L|^2A_L + 6|A_R|^2A_L)$$

$$
\begin{aligned}
&-d_{L,1}\partial^2_{x_1}A_L - d_{L,2}\partial_{x_1}\partial_{t_1}A_L + d_{L,3}\partial^2_{t_1}A_L - d_{L,4}\partial_{t_1}\partial_{x_1}A_L\\
&-\frac{\alpha}{2}\overline{\mathbf{U}_W^{\dagger}}^{\mathrm{Tr}}\Big(|A_L|^2A_L(\boldsymbol{\Omega}_2\cdot\overline{\mathbf{U}_W}\mathbf{V}^{Inh}_{2,2}+2\boldsymbol{\Omega}_2\cdot\mathbf{U}_W\mathbf{V}^{Inh}_{0,0})\\
&+2|A_R|^2A_L(\boldsymbol{\Omega}_2\cdot\mathbf{U}_W\mathbf{V}^{Inh}_{0,0}+\boldsymbol{\Omega}_2\cdot\overline{\mathbf{U}_W}\mathbf{V}^{Inh}_{0,2}+\boldsymbol{\Omega}_2\cdot\mathbf{U}_W\mathbf{V}^{Inh}_{2,0})\Big)=0, \qquad \text{(E.37)}
\end{aligned}
$$

and:

$$
\begin{aligned}
&c_g\partial_{x_2}A_R + \partial_{t_2}A_R - \kappa_2^{a,W}\gamma_2^aA_R + \beta\frac{1}{4}(3|A_R|^2A_R + 6|A_L|^2A_R)\\
&-d_{R,1}\partial^2_{x_1}A_R - d_{R,2}\partial_{x_1}\partial_{t_1}A_R + d_{R,3}\partial^2_{t_1}A_R - d_{R,4}\partial_{t_1}\partial_{x_1}A_R\\
&-\frac{\alpha}{2}\overline{\mathbf{U}_W^{\dagger}}^{\mathrm{Tr}}\Big(|A_R|^2A_R(\boldsymbol{\Omega}_2\cdot\overline{\mathbf{U}_W}\mathbf{V}^{Inh}_{-2,2}+2\boldsymbol{\Omega}_2\cdot\mathbf{U}_W\mathbf{V}^{Inh}_{0,0})\\
&+2|A_L|^2A_R(\boldsymbol{\Omega}_2\cdot\mathbf{U}_W\mathbf{V}^{Inh}_{0,0}+\boldsymbol{\Omega}_2\cdot\overline{\mathbf{U}_W}\mathbf{V}^{Inh}_{0,2}+\boldsymbol{\Omega}_2\cdot\mathbf{U}_W\overline{\mathbf{V}^{Inh}_{2,0}})\Big)=0, \qquad \text{(E.38)}
\end{aligned}
$$

where:

$$
\kappa_2^{a,W} \overset{\text{def}}{=} \frac{\overline{\mathbf{U}_W^{\dagger}}^{\mathrm{Tr}}\boldsymbol{\Lambda}_{H,2}\mathbf{U}_W}{\overline{\mathbf{U}_W^{\dagger}}^{\mathrm{Tr}}\mathbf{U}_W}, \qquad \text{(E.39)}
$$

and the coefficients of the terms involving partial derivations are:

$$
d_{L,1} \overset{\text{def}}{=} \frac{\overline{\mathbf{U}_W^{\dagger}}^{\mathrm{Tr}}\hat{\boldsymbol{\Lambda}}^2_S(k^c_W)\mathbf{U}_W - \overline{\mathbf{U}_W^{\dagger}}^{\mathrm{Tr}}\hat{\boldsymbol{\Lambda}}^1_S(k^c_W)\mathbf{V}^{Inh}_{1,1}}{\overline{\mathbf{U}_W^{\dagger}}^{\mathrm{Tr}}\mathbf{U}_W}, \qquad \text{(E.40)}
$$

$$
d_{R,1} \overset{\text{def}}{=} \frac{\overline{\mathbf{U}_W^{\dagger}}^{\mathrm{Tr}}\hat{\boldsymbol{\Lambda}}^2_S(-k^c_W)\mathbf{U}_W - \overline{\mathbf{U}_W^{\dagger}}^{\mathrm{Tr}}\hat{\boldsymbol{\Lambda}}^1_S(-k^c_W)\mathbf{V}^{Inh}_{-1,1}}{\overline{\mathbf{U}_W^{\dagger}}^{\mathrm{Tr}}\mathbf{U}_W}, \qquad \text{(E.41)}
$$

$$
d_{L,2} \overset{\text{def}}{=} \frac{\overline{\mathbf{U}_W^{\dagger}}^{\mathrm{Tr}}\hat{\boldsymbol{\Lambda}}^1_S(k^c_W)\mathbf{W}^{Inh}_{1,1}}{\overline{\mathbf{U}_W^{\dagger}}^{\mathrm{Tr}}\mathbf{U}_W} \quad , \quad d_{R,2} \overset{\text{def}}{=} \frac{\overline{\mathbf{U}_W^{\dagger}}^{\mathrm{Tr}}\hat{\boldsymbol{\Lambda}}^1_S(-k^c_W)\mathbf{W}^{Inh}_{-1,1}}{\overline{\mathbf{U}_W^{\dagger}}^{\mathrm{Tr}}\mathbf{U}_W}, \qquad \text{(E.42)}
$$

$$
d_{L,3} \overset{\text{def}}{=} \frac{\overline{\mathbf{U}_W^{\dagger}}^{\mathrm{Tr}}\mathbf{W}^{Inh}_{1,1}}{\overline{\mathbf{U}_W^{\dagger}}^{\mathrm{Tr}}\mathbf{U}_W} \quad , \quad d_{L,4} \overset{\text{def}}{=} \frac{\overline{\mathbf{U}_W^{\dagger}}^{\mathrm{Tr}}\mathbf{V}^{Inh}_{1,1}}{\overline{\mathbf{U}_W^{\dagger}}^{\mathrm{Tr}}\mathbf{U}_W}, \qquad \text{(E.43)}
$$

$$
d_{R,3} \overset{\text{def}}{=} \frac{\overline{\mathbf{U}_W^{\dagger}}^{\mathrm{Tr}}\mathbf{W}^{Inh}_{-1,1}}{\overline{\mathbf{U}_W^{\dagger}}^{\mathrm{Tr}}\mathbf{U}_W} \quad \text{and} \quad d_{R,4} \overset{\text{def}}{=} \frac{\overline{\mathbf{U}_W^{\dagger}}^{\mathrm{Tr}}\mathbf{V}^{Inh}_{-1,1}}{\overline{\mathbf{U}_W^{\dagger}}^{\mathrm{Tr}}\mathbf{U}_W}. \qquad \text{(E.44)}
$$

After a close examination of these coefficients, the following symmetries can be recognised:

$$
d_{L,1} = d_{R,1} \quad , \quad d_{L,2} = -d_{R,2} \quad , \quad d_{L,3} = d_{R,3} \quad \text{and} \quad d_{L,4} = -d_{R,4}. \qquad \text{(E.45)}
$$

Rearranging Eqs. (E.37,E.38) we reach finally to the following set of two *coupled PDEs*:

$$\boxed{\begin{aligned}
\partial_{t_2}A_L - c_g\partial_{x_2}A_L &= \gamma_2^a\kappa_2^{a,W}A_L + \left[d_{L,1}\partial_{x_1}^2 + (d_{L,2}+d_{L,4})\partial_{x_1}\partial_{t_1} - d_{L,3}\partial_{t_1}^2\right]A_L \\
&\quad -g_{WW}|A_L|^2A_L - g_{RL}|A_R|^2A_L \qquad\qquad \text{(E.46)} \\
\partial_{t_2}A_R + c_g\partial_{x_2}A_R &= \gamma_2^a\kappa_2^{a,W}A_R + \left[d_{R,1}\partial_{x_1}^2 + (d_{R,2}+d_{R,4})\partial_{x_1}\partial_{t_1} - d_{R,3}\partial_{t_1}^2\right]A_R \\
&\quad -g_{WW}|A_R|^2A_R - g_{RL}|A_L|^2A_R \qquad\qquad \text{(E.47)}
\end{aligned}}$$

where the coefficients of the nonlinear terms are given by:

$$g_{WW} \stackrel{\text{def}}{=} \frac{1}{4\overline{\mathbf{U}_W^\dagger}^{\text{Tr}}\mathbf{U}_W}\left(3\beta + 2\alpha^2\Big(\frac{\hat{\Lambda}_{22}(2k_W^c) - i2\omega_c}{det(\hat{\mathbf{\Lambda}}(2k_W^c) - i2\omega_c\mathbf{I})} + 2\frac{\hat{\Lambda}_{22}(0)}{det(\hat{\mathbf{\Lambda}}(0))}\Big)\right), \tag{E.48}$$

$$\begin{aligned}
g_{RL} \stackrel{\text{def}}{=} \frac{1}{4\overline{\mathbf{U}_W^\dagger}^{\text{Tr}}\mathbf{U}_W}&\left(6\beta + 4\alpha^2\Big(\frac{\hat{\Lambda}_{22}(0) - i2\omega_c)}{det(\hat{\mathbf{\Lambda}}(0) - i2\omega_c\mathbf{I})} + \frac{\hat{\Lambda}_{22}(2k_W^c)}{det(\hat{\mathbf{\Lambda}}(2k_W^c))}\right. \\
&\left. + \frac{\hat{\Lambda}_{22}(0)}{det(\hat{\mathbf{\Lambda}}(0))}\Big)\right).
\end{aligned} \tag{E.49}$$

Eqs. (E.46,E.47) will be discussed in Section 4.3.2.E. In Section 4.4 and Chapter 5 we will analyse the coefficients of these equations.

E.2 Amplitude Equations near the Codimension-2 wave-Turing Point

Let us now discuss the derivation of amplitude equations near the codimension-2 wave-Turing instability. This derivation is, as we mentioned in Section 4.3.3, a combination of the derivations done in Section E.1 for the codimension-1 Turing and wave instabilities. In this section the differences between the codimension-2 and codimension-1 derivations will be explained in detail. The similarities, on the other hand, will be mentioned only very briefly.

In Section 4.3.3 we displayed the hierarchy of equations resulting from the insertion of the ε-expansions of Eqs. (4.15), (4.2), (4.20), (4.22) and (4.50,4.51,4.52) in the RDNC model (*cf.* Eq. (2.17)). The resulting hierarchy of Eq. (4.53) included an array of new operators (*cf.* Eqs. (4.50), (4.51) and (4.52)). As in the codimension-1 Turing and wave cases, it is useful to consider the action of these operators over a generic vector like: $\mathbf{V}(k) = \mathbf{U}e^{ikx_0}$. The matrices $\hat{\mathbf{\Lambda}}^0_{S,0}(k)$, $\hat{\mathbf{\Lambda}}^1_{S,0}(k)$ and $\hat{\mathbf{\Lambda}}^2_{S,0}(k)$ are equivalent (with $\delta \equiv \delta_c$) to the matrices $\hat{\mathbf{\Lambda}}^0_S(k)$, $\hat{\mathbf{\Lambda}}^1_S(k)$ and $\hat{\mathbf{\Lambda}}^2_S(k)$ given in Eqs. (E.1), (E.2) and (E.3) respectively and:

$$\hat{\mathbf{\Lambda}}^0_{S,1}(k) = \hat{\mathbf{\Lambda}}^0_{S,2}(k) = \begin{pmatrix} 0 & 0 \\ 0 & -k^2 \end{pmatrix} \quad \text{and} \quad \hat{\mathbf{\Lambda}}^1_{S,1}(k) = \begin{pmatrix} 0 & 0 \\ 0 & i2k \end{pmatrix}.$$

E.2.A Equation $\mathcal{O}(\varepsilon)$; codimension-2 wave-Turing case

The a general solution of the homogeneous equation $\mathcal{O}(\varepsilon)$ in the hierarchy of Eq. (4.53) is given in Eq. (4.54).

E.2.B Equation $\mathcal{O}(\varepsilon^2)$; codimension-2 wave-Turing case

The following definition of the inner product:

$$(\mathbf{Z}|\mathbf{Y}_j) \overset{\text{def}}{=} \int_0^{2\pi/k_W^c} dx_0 \int_0^{2\pi/\omega_c} dt_0 \quad \overline{\mathbf{Z}}^{\text{Tr}}\mathbf{Y}_j + \int_0^{2\pi/k_T^c} dx_0 \quad \overline{\mathbf{Z}}^{\text{Tr}}\mathbf{Y}_j, \tag{E.50}$$

assures the orthogonality between the critical solutions $\mathbf{X}_T^c$, $\mathbf{X}_L^c$ and $\mathbf{X}_R^c$ (and their complex conjugated solutions). Projecting over the adjoints of these three critical solutions we get the following set of solvability conditions:

$$\left(\mathbf{X}_T^{c\,\dagger}\middle|[-\gamma_1^a\mathbf{\Lambda}_{H,1} - \gamma_1^\delta\mathbf{\Lambda}_{S,1}^0 + \partial_{t_1} - \partial_{x_1}\mathbf{\Lambda}_{S,0}^1 + \mathbf{\Omega}_2\cdot\mathbf{X}_1]\mathbf{X}_1\right) = 0, \tag{E.51}$$
$$\left(\mathbf{X}_L^{c\,\dagger}\middle|[-\gamma_1^a\mathbf{\Lambda}_{H,1} - \gamma_1^\delta\mathbf{\Lambda}_{S,1}^0 + \partial_{t_1} - \partial_{x_1}\mathbf{\Lambda}_{S,0}^1 + \mathbf{\Omega}_2\cdot\mathbf{X}_1]\mathbf{X}_1\right) = 0, \tag{E.52}$$
$$\left(\mathbf{X}_R^{c\,\dagger}\middle|[-\gamma_1^a\mathbf{\Lambda}_{H,1} - \gamma_1^\delta\mathbf{\Lambda}_{S,1}^0 + \partial_{t_1} - \partial_{x_1}\mathbf{\Lambda}_{S,0}^1 + \mathbf{\Omega}_2\cdot\mathbf{X}_1]\mathbf{X}_1\right) = 0. \tag{E.53}$$

After performing the time and space integrations of the inner product, we get:

$$\overline{\mathbf{U}_T^\dagger}^{\text{Tr}}[-\gamma_1^a A_T\mathbf{\Lambda}_{H,1} - \gamma_1^\delta A_T\hat{\mathbf{\Lambda}}_{S,1}^0(k_T^c) + \partial_{t_1}A_T - \partial_{x_1}A_T\hat{\mathbf{\Lambda}}_{S,0}^1(k_T^c)]\frac{\mathbf{U}_T}{2} = 0, \tag{E.54}$$

$$\begin{aligned}\overline{\mathbf{U}_W^\dagger}^{\text{Tr}}[-\gamma_1^a A_L\mathbf{\Lambda}_{H,1} - \gamma_1^\delta A_L\hat{\mathbf{\Lambda}}_{S,1}^0(k_W^c) + \partial_{t_1}A_L \\ -\partial_{x_1}A_L\hat{\mathbf{\Lambda}}_{S,0}^1(k_W^c)]\frac{\mathbf{U}_W}{2} = 0,\end{aligned} \tag{E.55}$$

$$\begin{aligned}\overline{\mathbf{U}_W^\dagger}^{\text{Tr}}[-\gamma_1^a A_R\mathbf{\Lambda}_{H,1} - \gamma_1^\delta A_R\hat{\mathbf{\Lambda}}_{S,1}^0(-k_W^c) + \partial_{t_1}A_R \\ -\partial_{x_1}A_R\hat{\mathbf{\Lambda}}_{S,0}^1(-k_W^c)]\frac{\mathbf{U}_W}{2} = 0.,\end{aligned} \tag{E.56}$$

Note that the term $\overline{\mathbf{U}_T^\dagger}^{\text{Tr}}\hat{\mathbf{\Lambda}}_{S,0}^1(k_T^c)\mathbf{U}_T$, as we saw in the derivation of the Turing amplitude equation, vanishes (*cf.* Eq. (E.7)) and that $\overline{\mathbf{U}_W^\dagger}^{\text{Tr}}\hat{\mathbf{\Lambda}}_{S,0}^1(k_W^c)\mathbf{U}_W$ is proportional to the group velocity (*cf.* Eq. (E.26)). Hence:

$$\partial_{t_1}A_T = (\gamma_1^a\kappa_1^{a,T} + \gamma_1^\delta\kappa_1^{\delta,T})A_T, \tag{E.57}$$
$$\partial_{t_1}A_L - c_g\partial_{x_1}A_L = (\gamma_1^a\kappa_1^{a,W} + \gamma_1^\delta\kappa_1^{\delta,W})A_L, \tag{E.58}$$
$$\partial_{t_1}A_R + c_g\partial_{x_1}A_R = (\gamma_1^a\kappa_1^{a,W} + \gamma_1^\delta\kappa_1^{\delta,W})A_R, \tag{E.59}$$

where:

$$\kappa_1^{\delta,T} \overset{\text{def}}{=} \frac{\overline{\mathbf{U}_T^\dagger}^{\text{Tr}} \hat{\mathbf{\Lambda}}_{S,1}^0(k_T^c)\mathbf{U}_T}{\overline{\mathbf{U}_T^\dagger}^{\text{Tr}} \mathbf{U}_T} \quad \text{and} \quad \kappa_1^{\delta,W} \overset{\text{def}}{=} \frac{\overline{\mathbf{U}_W^\dagger}^{\text{Tr}} \hat{\mathbf{\Lambda}}_{S,1}^0(k_W^c)\mathbf{U}_W}{\overline{\mathbf{U}_W^\dagger}^{\text{Tr}} \mathbf{U}_W}, \tag{E.60}$$

and the coefficients $\kappa_1^{a,T}$ and $\kappa_1^{a,W}$ have been defined in Eqs (E.9) and (E.27) respectively.

Using the same arguments than in the derivation of Turing and wave amplitude equations, we conclude that γ_1^a and γ_1^δ should vanish (for more details see discussions in Sections E.1.B and E.1.D). Hence, the solvability conditions lead to:

$$\boxed{\begin{aligned} \partial_{t_1} A_T &= 0, && \text{(E.61)} \\ \partial_{t_1} A_L - c_g \partial_{x_1} A_L &= 0, && \text{(E.62)} \\ \partial_{t_1} A_R + c_g \partial_{x_1} A_R &= 0. && \text{(E.63)} \end{aligned}}$$

We can now solve the $\mathcal{O}(\varepsilon^2)$ inhomogeneous linear equation. A general solution of this equation is given by:

$$\mathbf{X}_2 = \Gamma \mathbf{X}_1 + \mathbf{X}_{2,T}^{Inh} + \mathbf{X}_{2,W}^{Inh} + \mathbf{X}_{2,WT}^{Inh}, \tag{E.64}$$

where $\mathbf{X}_{2,T}^{Inh}$ and $\mathbf{X}_{2,W}^{Inh}$ are given in Eqs. (E.13) and (E.34) respectively and:

$$\begin{aligned} \mathbf{X}_{2,WT}^{Inh} = -\frac{\alpha}{2}\Big[& A_L A_T \mathbf{V}_{1,1,1}^{Inh} e^{i(\omega_c t_0 + k_W^c x_0 + k_T^c x_0)} + A_L \overline{A_T} \mathbf{V}_{1,1,-1}^{Inh} e^{i(\omega_c t_0 + k_W^c x_0 - k_T^c x_0)} \\ & + A_R A_T \mathbf{V}_{1,-1,1}^{Inh} e^{i(\omega_c t_0 - k_W^c x_0 + k_T^c x_0)} + A_R \overline{A_T} \mathbf{V}_{1,-1,-1}^{Inh} e^{i(\omega_c t_0 - k_W^c x_0 - k_T^c x_0)}\Big] \\ & + c.c., \end{aligned} \tag{E.65}$$

where:

$$\mathbf{V}_{1,m,n}^{Inh} \overset{\text{def}}{=} \frac{1}{det(\hat{\mathbf{\Lambda}}(mk_W^c) + \hat{\mathbf{\Lambda}}(nk_T^c) - i\omega_c \mathbf{I})} \begin{pmatrix} \hat{\mathbf{\Lambda}}_{22}(mk_W^c) + \hat{\mathbf{\Lambda}}_{22}(nk_T^c) - i\omega_c \\ -\hat{\mathbf{\Lambda}}_{21}(mk_W^c) + \hat{\mathbf{\Lambda}}_{21}(nk_T^c) \end{pmatrix},$$

where the indices m and n can be ±1.

E.2.C Equation $\mathcal{O}(\varepsilon^3)$; codimension-2 wave-Turing case

We will not repeat here all calculations arising from the solvability conditions of the inhomogeneous equation $\mathcal{O}(\varepsilon^3)$ because they are very similar to the ones done for the Turing and wave cases. It is enough to mention that we should project the inhomogeneous term of this equation with respect to the adjoints of $\mathbf{X}_T^c$, $\mathbf{X}_L^c$ and $\mathbf{X}_R^c$. After integration and rearranging terms, we end up with the following set of *three coupled PDEs*:

$$\boxed{\begin{aligned}
\partial_{t_2}A_L - c_g\partial_{x_2}A_L &= (\gamma_2^a\kappa_2^{a,W}+\gamma_2^\delta\kappa_2^{\delta,W})A_L + d_W\partial_{x_1}^2 A_L \\
&\quad -g_{WW}|A_L|^2A_L - g_{RL}|A_R|^2A_L - g_{WT}|A_T|^2A_L, && \text{(E.66)}\\
\partial_{t_2}A_R + c_g\partial_{x_2}A_R &= (\gamma_2^a\kappa_2^{a,W}+\gamma_2^\delta\kappa_2^{\delta,W})A_R + d_W\partial_{x_1}^2 A_R \\
&\quad -g_{WW}|A_R|^2A_R - g_{RL}|A_L|^2A_R - g_{WT}|A_T|^2A_R, && \text{(E.67)}\\
\partial_{t_2}A_T &= (\gamma_2^a\kappa_2^{a,T}+\gamma_2^\delta\kappa_2^{\delta,T})A_T + d_T\partial_{x_1}^2 A_T \\
&\quad -g_{TT}|A_T|^2A_T - g_{TW}(|A_L|^2+|A_R|^2)A_T, && \text{(E.68)}
\end{aligned}}$$

where:

$$\kappa_2^{\delta,T} \overset{\text{def}}{=} \frac{\overline{\mathbf{U}_T^\dagger}^{\mathrm{Tr}}\,\hat{\mathbf{\Lambda}}_{S,2}^0(k_T^c)\mathbf{U}_T}{\overline{\mathbf{U}_T^\dagger}^{\mathrm{Tr}}\,\mathbf{U}_T} \quad \text{and} \quad \kappa_2^{\delta,W} \overset{\text{def}}{=} \frac{\overline{\mathbf{U}_W^\dagger}^{\mathrm{Tr}}\,\hat{\mathbf{\Lambda}}_{S,2}^0(k_W^c)\mathbf{U}_W}{\overline{\mathbf{U}_W^\dagger}^{\mathrm{Tr}}\,\mathbf{U}_W}, \tag{E.69}$$

and the coefficients $\kappa_2^{a,T}$ and $\kappa_2^{a,W}$ have been introduced previously in Eqs. (E.18) and (E.39) respectively.

The coefficient d_W was defined in Eq. (4.43), d_T in Eq. (E.18), and the nonlinear coefficients g_{WW}, g_{RL} and g_{TT} in Eqs. (E.48), (E.49) and (E.19) respectively. The new coefficients, corresponding to the nonlinear cross-coupling of wave and Turing modes, are given by:

$$\begin{aligned}
g_{WT} &\overset{\text{def}}{=} \frac{1}{4\overline{\mathbf{U}_W^\dagger}^{\mathrm{Tr}}\,\mathbf{U}_W}\Bigg(6\beta + 4\alpha^2\Big(2\frac{\hat{\mathbf{\Lambda}}_{22}(k_W^c)+\hat{\mathbf{\Lambda}}_{22}(k_T^c)-i\omega_c}{det(\hat{\mathbf{\Lambda}}(k_W^c)+\hat{\mathbf{\Lambda}}(k_T^c)-i\omega_c\mathbf{I})} \\
&\qquad + \frac{\hat{\mathbf{\Lambda}}_{22}(0)}{det(\hat{\mathbf{\Lambda}}(0))}\Big)\Bigg), \qquad \text{(E.70)}\\
g_{TW} &\overset{\text{def}}{=} \frac{1}{4\overline{\mathbf{U}_T^\dagger}^{\mathrm{Tr}}\,\mathbf{U}_T}\Bigg(6\beta + 4\alpha^2\Big(\frac{\hat{\mathbf{\Lambda}}_{22}(k_W^c)+\hat{\mathbf{\Lambda}}_{22}(k_T^c)-i\omega_c}{det(\hat{\mathbf{\Lambda}}(k_W^c)+\hat{\mathbf{\Lambda}}(k_T^c)-i\omega_c\mathbf{I})} \\
&\qquad + \frac{\hat{\mathbf{\Lambda}}_{22}(k_W^c)+\hat{\mathbf{\Lambda}}_{22}(k_T^c)+i\omega_c}{det(\hat{\mathbf{\Lambda}}(k_W^c)+\hat{\mathbf{\Lambda}}(k_T^c)+i\omega_c\mathbf{I})} + \frac{\hat{\mathbf{\Lambda}}_{22}(0)}{det(\hat{\mathbf{\Lambda}}(0))}\Big)\Bigg). \qquad \text{(E.71)}
\end{aligned}$$

The Eqs. (E.66,E.67,E.68) will be discussed in Section 4.3.3.C.

Appendix F

Introduction to Counting Arguments

In this appendix we will explain in detail how the counting arguments work, their limitations and interpretation.

- Setup

Let us consider the following dynamical system:

$$\partial_\xi \mathbf{X}(\xi) = \mathbf{F}(\mathbf{X}(\xi); p_1, \ldots, p_{n_F}), \tag{F.1}$$

where $\mathbf{F}$ is a nonlinear function of $\mathbf{X}(\xi) \in \mathbb{R}^d$ which depends on the n_F *free parameters*: $p_1, \ldots, p_{n_F}$. This dynamical system may consist of the ODEs (6.5,6.6) (*cf.* Section 6.4.3), or the ODEs (6.16,6.18,6.18) (*cf.* Section 6.4.5), or the ODEs (7.5-7.10) (*cf.* Section 7.3). In the first example $d = 2$ and $n_F = 1$ (*i.e.* $p_1 = v_{int}$), in the second example $d = 3$ and $n_F = 2$ (*i.e.* $p_1 = v_{int}$ and $p_2 = \omega$) and in the third example $d = 6$ and $n_F = 3$ (*i.e.* $p_1 = v_{int}$, $p_2 = \omega_W$ and $p_3 = \omega_T$).

- Heteroclinic orbit

Let us suppose that Eq. (F.1) has two hyperbolic [55] fixed points: $\mathbf{X}_O$ and $\mathbf{X}_I$. Any heteroclinic orbit going from $\mathbf{X}_O$ to $\mathbf{X}_I$ should belong to the intersection between the unstable manifold of $\mathbf{X}_O$ and the stable manifold of $\mathbf{X}_I$. Let us further suppose that Eq. (F.1) has, for $p_1 = p_1^s, \ldots, p_{n_F} = p_{n_F}^s$, a heteroclinic orbit Γ_s connecting $\mathbf{X}_O$, at $\xi \to -\infty$, and $\mathbf{X}_I$, at $\xi \to +\infty$. Let us denote the dimension of the unstable manifolds of $\mathbf{X}_O$ and $\mathbf{X}_I$ with n_O^+ and n_I^+ respectively. Since both fixed points are hyperbolic, their stable manifolds have dimensions $n_O^- = d - n_O^+$ and $n_I^- = d - n_I^+$ respectively.

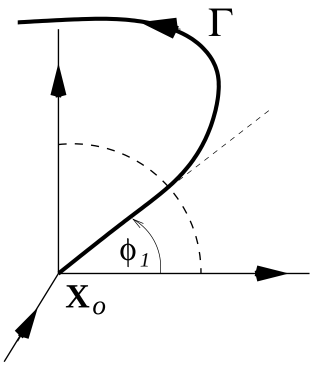

Figure F.1: Sketch of the phase space of a system with $d = 3$ and $n_O^+ = 2$ near the fixed point $\mathbf{X}_O$. The thick full line is a trajectory Γ starting at $\mathbf{X}_O$. Note the angle ϕ_1 parametrising the outgoing direction of the trajectory Γ.

- Multiplicity: necessary conditions

Let us now use the information about the manifold structure of each fixed point to study the likelihood of finding another heteroclinic orbits Γ near Γ_s, if we vary the values of the free parameters $p_1, \ldots, p_{n_F}$. In other words: let us study the *multiplicity* of Γ_s. To achieve this we will use the following counting arguments.

- Going out of $\mathbf{X}_O$

Note that there are $n_O^+ - 1$ (internal) free parameters characterising the flow of Eq. (F.1) out of the fixed point $\mathbf{X}_O$. These $n_O^+ - 1$ (internal) parameters can be interpreted as a set of angles $\phi_1, \ldots, \phi_{n_O^+ - 1}$ parametrising the direction in which the trajectory Γ flows out of $\mathbf{X}_O$. For example; if $n_O^+ = 1$, then the orbit should flow through the unique outgoing direction and therefore there is no free parameter. If $n_O^+ = 2$, then we have the possibility to choose the direction in a two dimensional plane. This direction is parameterised by one angle ϕ_1 (see Fig. F.1 for an illustration).

Additionally, we should take into account the n_F free parameters $p_1, \ldots, p_{n_F}$ of Eq. (F.1). Together we have $n_O^+ - 1 + n_F$ free parameters.

- Coming into $\mathbf{X}_I$

The trajectory Γ should flow into $\mathbf{X}_I$ through its stable manifold. For this to happen, the orbit should be orthogonal to the unstable manifold of $\mathbf{X}_I$. Let $\mathbf{E}_{I,1}^+, \ldots, \mathbf{E}_{I,n_I^+}^+$ be a set of orthogonal vectors spanning the unstable manifold of $\mathbf{X}_I$. Then, the orthogonality condition between the trajectory Γ and the stable manifold means that Γ should satisfy the following n_I^+ constraints for $\xi \to \infty$:

$$\begin{cases} \langle \Gamma(\xi; p_1, \ldots, p_{n_F}, \phi_1, \ldots, \phi_{n_O^+-1}), E_{I,1}^+ \rangle = 0, \\ \qquad\qquad\qquad\qquad\qquad\qquad\qquad\qquad \vdots \\ \langle \Gamma(\xi; p_1, \ldots, p_{n_F}, \phi_1, \ldots, \phi_{n_O^+-1}), E_{I,n_I^+}^+ \rangle = 0, \end{cases}$$

where $\langle \quad , \quad \rangle$ symbolises the standard scalar product in $\mathbb{R}^d$. Typically this will amount to the tuning of n_I^+ free parameters. Therefore we are left with

$$n = n_O^+ - 1 + n_F - n_I^+,$$

free parameters for the heteroclinic orbits.

- Remarks

If $n = 0$, then the counting arguments tell us that we should expect to find only a *discrete set* of heteroclinic orbits. In other words; if a heteroclinic orbit is known to exist for a particular value of the parameters and $n = 0$, then we expect not to find another heteroclinic orbit at nearby values of the parameters. On the other hand, if $n \geq 1$, then it is possible to find a *continuous family* of heteroclinic orbits.

The counting arguments described before consist in *necessary conditions* that the heteroclinic orbit should satisfy. Note that they provide a *upper bound* to the multiplicity of the orbits because we are assuming that the flow of the trajectory out of $\mathbf{X}_O$ is *independent* from the flow to $\mathbf{X}_I$. Typically the flow near the fixed points will be not independent if the Eq. (F.1) possesses some *symmetry* [85].

Appendix G

Interfaces in the real and complex Ginzburg-Landau equations

In this appendix we will analyse interfaces in the real and complex Ginzburg-Landau equations.

G.1 The real Ginzburg-Landau equation

In Chapter 5 we saw that the RGLE given by Eq. (4.72) has the following family of constant amplitude solutions (*cf.* Eq. (5.1)):

$$\widetilde{A}_T(x,t) = \rho_N e^{ip_T x} \quad \text{with} \quad \rho_N = \sqrt{\eta_T - d_T p_T^2}. \tag{G.1}$$

This family of solutions is parametrised by the wavenumber p_T.

Interfaces separating domains containing these types of solutions can be classified generically on three different classes: fronts, pulses and domain walls (see Fig. G.1).

- Coherent structure approach

In Section 6.4.3 we used a coherent structure approach to investigate interfaces (fronts) in the RGLE *with constant phase solutions.* This approach can be also used to investigate interfaces in the RGLE. However, some problems appear if we straightforwardly apply the ansatz of Eq. (6.2) to Eq. (4.72). To illustrate this, let us suppose:

$$\widetilde{A}_T(x,t) = \hat{A}(x - v_{int}t), \tag{G.2}$$

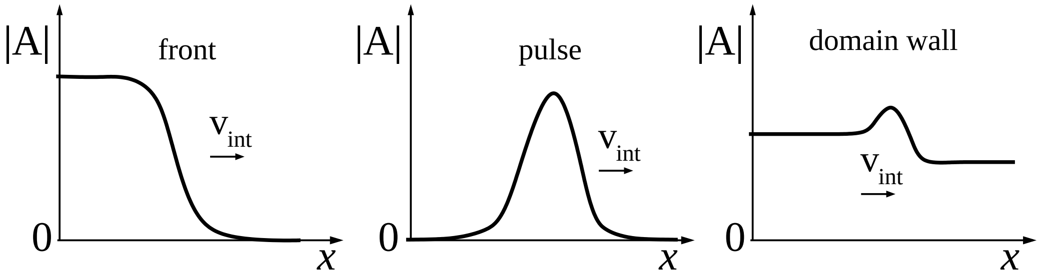

Figure G.1: Schematic sketch of typical interfaces in the single RGLE and CGLE. A *front* corresponds to a pattern with nonzero amplitude invading a zero amplitude unstable state. In a *pulse* the two asymptotic states joined by the interface have zero amplitude. Finally, in a *domain wall* both asymptotic states have nonzero amplitude.

where $\hat{A}(x - v_{int}t)$ is now a complex function and consequently it is convenient to write it as:

$$\hat{A}(\xi) = a(\xi)e^{i\phi(\xi)}, \tag{G.3}$$

where $\xi \overset{\text{def}}{=} x - v_{int}t$. Let us further suppose that on the left side of the interface (*i.e.* $\xi \to -\infty$) we have a constant amplitude solution $\widetilde{A}_T(x,t) \to \rho_N e^{ip_T x}$ with $p_T \neq 0$. Using the ansatz Eq. (G.2) we get that in the limit $\xi \to -\infty$ the amplitude $a(\xi) \to \rho_N$ and the phase:

$$\phi(x - v_{int}t) \to p_T x.$$

But, if $v_{int} \neq 0$, there is no function ϕ that can satisfy this limit. The solution to this is to introduce an extra phase into the ansatz:

$$\widetilde{A}_T(x,t) = e^{i\omega t}\hat{A}(x - v_{int}t). \tag{G.4}$$

This ansatz has *two free parameters*: v_{int} and ω!

Inserting Eq. (G.4) in the RGLE (4.72) and using Eq. (G.3) we get the following system of ordinary differential equations:

$$\partial_\xi a = \kappa a, \tag{G.5}$$

$$\partial_\xi \kappa = \mathcal{K}_T(a, q, \kappa), \tag{G.6}$$

$$\partial_\xi q = \mathcal{Q}_T(q, \kappa), \tag{G.7}$$

where we introduced two variables: $\kappa(\xi) \overset{\text{def}}{=} \partial_\xi a / a$ and $q(\xi) \overset{\text{def}}{=} \partial_\xi \phi$, and the functions $\mathcal{K}_T$ and $\mathcal{Q}_T$ are given by:

$$\mathcal{K}_T(a, q, \kappa) \overset{\text{def}}{=} \frac{1}{d_T}\Big[- v_{int}\kappa - \eta_T + a^2 \Big] - \kappa^2 + q^2, \tag{G.8}$$

$$\mathcal{Q}_T(q, \kappa) \overset{\text{def}}{=} \frac{1}{d_T}\Big[- \omega - v_{int} q \Big] - 2\kappa q. \tag{G.9}$$

As was explained in Section 6.4.3, $\kappa(\xi)$ is the decaying rate to $a = 0$ and the new variable $q(\xi)$ can be interpreted as a *local wavenumber*.

Eqs. (G.6,G.7) can be written in a simpler, more compact way, if we introduce the complex function:

$$z \overset{\text{def}}{=} \kappa + iq. \tag{G.10}$$

Eqs. (G.6,G.7) become:

$$\partial_\xi z = \frac{1}{d_T}\Big[- \eta_T - i\omega + a^2 - v_{int} z\Big] - z^2.$$

- Fixed points

The fixed points of Eqs. (G.5,G.6,G.7) are given by the conditions: $\partial_\xi a = 0$, $\partial_\xi q = 0$ and $\partial_\xi \kappa = 0$. Because of Eq. (G.5) they have either $a = 0$ or $\kappa = 0$ and, as in Section 6.4.3, we will call the first ones linear fixed points (**L**) and the second ones nonlinear fixed points (**N**).

The nonlinear fixed points exist only if $\eta_T \geq 0$ and fulfill the conditions: $\kappa_N = 0$ and $q_N \neq 0$. From Eq. (G.7) we get that they satisfy:

$$q_N = -\frac{\omega}{v_{int}}. \tag{G.11}$$

Therefore, given values of ω and v_{int}, the nonlinear fixed point is unique. Note that q_N is the wavenumber of the constant amplitude pattern far from the interface. This quantity is typically easy to measure. Therefore, given the direct relation of Eq. (G.11) between this wavenumber and ω, in the following we will choose the parameters q_N and v_{int}, instead of ω and v_{int}, to characterise the interface[1].

The coordinates κ_L and q_L of the linear fixed points are given by:

$$0 = v_{int}\kappa_L + \eta_T + d_T\kappa_L^2 - d_T q_L^2, \tag{G.12}$$

$$0 = \omega + v_{int} q_L + 2 d_T \kappa_L q_L. \tag{G.13}$$

These set of equations can be written in a compact way if we use z (*cf.* Eq. (G.10)):

$$z_L = \frac{-v_{int} \pm \sqrt{v_{int}^2 - 4d_T(\eta_T + i\omega)}}{2d_T}. \tag{G.14}$$

---

[1] Note that the substitution of q_N and v_{int} as free parameters of the interface, in place of ω and v_{int}, is *only meaningful if* $\eta_T > 0$! In this sense the free parameters ω and v_{int} are more general.

Consequently, there is always a pair of linear fixed points.

If $v_{int} = 0$, Eqs. (G.12,G.13) yield:

$$\kappa_L^2 = \frac{-\eta_T \pm \sqrt{\eta_T^2 + 4\omega^2}}{2d_T},$$

and consequently, whatever the sign of η_T, the sign of the decaying rate κ_L is positive for one of the fixed points and negative for the other (note that only real values of κ_L should be considered). In the other hand, for big velocities ($v_{int} \to \pm\infty$), we deduce from Eq. (G.14) that:

$$z_L \simeq \frac{-v_{int} \pm v_{int}(1 - \frac{2d_T(\eta_T + i\omega)}{v_{int}^2})}{2d_T}. \tag{G.15}$$

Hence, for $\eta_T < 0$, κ_L has still different signs for each fixed point. For $\eta_T > 0$ both fixed points have equal sign (this can be either positive or negative). As a consequence, in this last case and for some intermediate velocities v_{int}, we should have that $\kappa_L = 0$. From Eqs. (G.12,G.13) we deduce that in such a cases: $q_L = \pm\sqrt{\frac{\eta_T}{d_T}}$, and that the critical velocities are: $\pm v^c$, where:

$$v^c \overset{\text{def}}{=} \omega\sqrt{\frac{d_T}{\eta_T}}. \tag{G.16}$$

- Manifold structure of the fixed points

It is possible, with an easy but rather lengthy calculation, to determine the manifold structure of the linear and nonlinear fixed points. In the following table we summarise all the information about the fixed points of Eqs. (G.5, G.6,G.7) and their manifold structure:

$$\begin{array}{lll}
\eta_T < 0 \quad \text{for all } v_{int} & : & \mathbf{L}_1^-(+,+,-), \mathbf{L}_2^+(+,-,-) \\
\eta_T > 0 \begin{cases} v_{int} \geq v^c \\ |v_{int}| < v^c \\ v_{int} \leq -v^c \end{cases} & \begin{array}{l} : \\ : \\ : \end{array} & \begin{array}{l} \mathbf{L}_1^-(+,+,-), \mathbf{L}_2^-(-,-,-) \\ \mathbf{L}_1^-(+,+,-), \mathbf{L}_2^+(+,-,-) \\ \mathbf{L}_1^+(+,+,+), \mathbf{L}_2^+(+,-,-) \end{array} \\
\eta_T < 0 & : & \nexists \mathbf{N} \\
\eta_T > 0 \begin{cases} v_{int} > 0 \\ v_{int} < 0 \end{cases} & \begin{array}{l} : \\ : \end{array} & \begin{array}{l} \mathbf{N}^-(+,-,-) \\ \mathbf{N}^+(+,+,-) \end{array}
\end{array} \tag{G.17}$$

where $|\kappa_{L1}| < |\kappa_{L2}|$ and v^c was defined in Eq. (G.16).

- Front propagation: Counting arguments and marginal stability criterion

Let us consider the case of a front like in Fig. 6.4 with the addition that the pattern in the left side of the interface can have a wavenumber different from the critical (*i.e.* $q_N \neq 0$). Such a front corresponds to the heteroclinic orbit $\mathbf{N} \to \mathbf{L}^-$. If we keep on mind that there are two free parameters and using the manifold structures of Eq. (G.17) the counting arguments (see Appendix F) allow us to get the following multiplicities:

$$\left\{ \begin{array}{rll} v_{int} \geq v^c : & \mathbf{N}(+,-,-) \to \mathbf{L}_2^-(-,-,-) & \Longrightarrow \quad 2 \text{ PF} \\ v_{int} \geq 0 : & \mathbf{N}(+,-,-) \to \mathbf{L}_1^-(+,+,-) & \Longrightarrow \quad 0 \text{ PF} \\ 0 \geq v_{int} \geq -v^c : & \mathbf{N}(+,+,-) \to \mathbf{L}_1^-(+,+,-) & \Longrightarrow \quad 1 \text{ PF} \end{array} \right. \tag{G.18}$$

On the other hand, the leading edge approach and the marginal stability criterion give (see *e.g.* [85]):

$$v^* = 2\sqrt{\eta_T d_T} \quad , \quad \omega^* = 0 \quad \text{and} \quad \kappa_L^* = -\sqrt{\eta_T / d_T}. \tag{G.19}$$

Note that the marginal velocity is the same than for the RGLE with constant phase (*i.e.* $v^* \equiv v^m$) and that $v^* > v^c$. From Eq. (G.19) we can calculate $q_L^* = 0$ and the wavenumber selected by the front:

$$q_N^* = 0 \quad . \tag{G.20}$$

G.2 The complex Ginzburg-Landau equation

Let us finally address the case of the *single* CGLE given in Eq. (6.15). The analysis of this equation is very similar to the one done in the previous section for the RGLE. We will give here only a very brief discussion. For more details we refer to the literature (in particular, see [1, 85] and references therein).

In the context of the RDNC model, the CGLE (6.15) can arise in two different circumstances. The first is near a *homogeneous Hopf* instability (see Chapter 3) and the second is near a *travelling wave* instability (see section 5.3.1) in the particular case where, *either* waves travelling to the right *or* to the left, exist. Such a situation is possible whenever travelling waves are stable against standing waves (see section 5.3.1) and the system is initially prepared with waves travelling *only in one direction*. In this last case Eq. (5.9) can be reduced to Eq. (6.15) if we write it in the travelling frame: $x \to x - s v_g t$

- Coherent structure approach

As in the case of the RGLE, we will look for coherent solutions joining constant amplitude solutions. In Fig. G.1 different types of possible coherent structures are sketched.

Inserting the ansatz: $\widetilde{A}_H(x,t) = e^{i\omega t}\hat{A}(x - v_{int}t)$, in Eq. (6.15) and using Eq. (G.3) we get the following set of coupled ODEs:

$$\partial_\xi a = \kappa a, \tag{G.21}$$

$$\partial_\xi \kappa = \mathcal{K}_H(a,q,\kappa), \tag{G.22}$$

$$\partial_\xi q = \mathcal{Q}_H(a,q,\kappa), \tag{G.23}$$

where:

$$\begin{aligned}\mathcal{K}_H(a,q,\kappa) &\overset{\text{def}}{=} \frac{1}{1+c_1^2}\Big[-v_{int}(\kappa + c_1 q) - \eta'_W - c_1\omega + (1 - c_1c_3)a^2\Big] \\ &\quad -\kappa^2 + q^2, \qquad\qquad (G.24)\\ \mathcal{Q}_H(a,q,\kappa) &\overset{\text{def}}{=} \frac{1}{1+c_1^2}\Big[-\omega - v_{int}(q - c_1\kappa) + c_1\eta'_W - (c_1 + c_3)a^2\Big] \\ &\quad -2\kappa q. \qquad\qquad (G.25)\end{aligned}$$

If we make use of the variable z introduced in Eq. (G.10), then Eqs. (G.21,G.22,G.23) became:

$$\begin{aligned}\partial_\xi a &= \kappa a \\ \partial_\xi z &= \frac{1}{1+ic_1}\Big[-\eta'_W - i\omega + (1 - ic_3)a^2 - v_{int}z\Big] - z^2\end{aligned}$$

- Fixed points

The study of the linear and nonlinear fixed points of ODEs (G.21,G.22,G.23) goes in the same lines than what we did for the RGLE in the previous section. Consequently, here we will only give a brief overview of the most important facts about the fixed points and summarise their manifold structure. For a nice and extensive explanation of these topics see the appendix of [86].

As for the RGLE, the linear fixed points **L** came in pairs. If $\eta'_W > 0$, then there is also a pair of nonlinear fixed points **N** (remember that for the RGLE there was only one). They have coordinates:

$$a_N^2 = \eta'_W - q_N^2 \quad , \quad \kappa_N = 0,$$

and q_N is given by:

$$0 = (c_1 + c_3)q_N^2 - v_{int}q_N - \omega - c_3\eta'_W.$$

Each of these nonlinear fixed points correspond to a plane wave solutions of the form: $\widetilde{A}_H = a_N e^{-i(\Omega_H t - q_N x)}$, where $\Omega_H = \omega + v_{int} q_N$. Consequently, $\partial_{q_N}\omega$ is the group velocity of this travelling wave solution in a co-moving frame (*i.e.* $\partial_{q_N}\Omega_H - v_{int}$). The group velocity $\partial_{q_N}\omega$ has always different sign for each nonlinear fixed point. This fact let us further classify the nonlinear fixed points as $\mathbf{N}^+$ and $\mathbf{N}^-$ depending on the sing of this group velocity.

- Manifold structure

Let us summarise the manifold structure of the fixed points of the coupled ODEs (G.21,G.22,G.23):

$$\begin{array}{lll}
\eta'_W < 0 \quad \text{for all } v_{int} & : & \mathbf{L}_1^-(+,+,-), \mathbf{L}_2^+(+,-,-) \\
\eta'_W > 0 \begin{cases} v_{int} \geq v^c \\ |v_{int}| < v^c \\ v_{int} \leq -v^c \end{cases} & \begin{array}{c} : \\ : \\ : \end{array} & \begin{array}{l} \mathbf{L}_1^-(+,+,-), \mathbf{L}_2^-(-,-,-) \\ \mathbf{L}_1^-(+,+,-), \mathbf{L}_2^+(+,-,-) \\ \mathbf{L}_1^+(+,+,+), \mathbf{L}_2^+(+,-,-) \end{array} \\
\eta'_W < 0 & : & \nexists \mathbf{N} \\
\eta'_W > 0 \begin{cases} v_{int} > v^{cN} \\ |v_{int}| < v^{cN} \\ v_{int} < -v^{cN} \end{cases} & \begin{array}{c} : \\ : \\ : \end{array} & \begin{array}{l} \mathbf{N}^-(+,-,-), \mathbf{N}^+(-,-,-) \\ \mathbf{N}^-(+,-,-), \mathbf{N}^+(+,+,-) \\ \mathbf{N}^-(+,+,+), \mathbf{N}^+(+,+,-) \end{array}
\end{array} \tag{G.26}$$

with $|\kappa_{L1}| < |\kappa_{L2}|$ and where:

$$v^c \stackrel{\text{def}}{=} \frac{|c_1 \eta'_W - \omega|}{\sqrt{\eta'_W}}, \tag{G.27}$$

and v^{cN} is a complicated function of the free parameter ω that we will not need to calculate explicitly in this thesis (for the definition of v^{cN} see [86]).

Note that the manifold structures around the linear fixed points are the same than for the the RGLE (*cf.* Eq. (G.17)). Only the critical velocity v^c is different in both cases. On the other hand, there are now more nonlinear fixed points and their manifold structures are more complicated.

- Front propagation: Marginal stability criterion

The marginal stability criterion applied to the leading edge dynamics of Eq. (6.15) yields the following marginal velocity, frequency and decaying rate (see [85]):

$$v^* = 2\sqrt{\eta'_W(1 + c_1^2)} \quad , \quad \omega^* = -c_1 \eta'_W \quad \text{and} \quad \kappa_L^* = -\sqrt{\eta'_W/(1 + c_1^2)}. \tag{G.28}$$

These values alow to calculate: $q_L^* = -c_1 \kappa_L^*$, and the selected wavenumber:

$$q_N^* = \sqrt{\eta'_W}\Big(\frac{\sqrt{1+c_1^2} - \sqrt{1+c_3^2}}{c_1 + c_3}\Big). \tag{G.29}$$

Bibliography

[1] Cross, M.C., and P.C. Hohenberg, 1993, "Pattern Formation outside of equilibrium", Rev. Mod. Phys. **65**, 851-1112.

[2] Murray, J.D., 1989, *Mathematical Biology* (Springer-Verlag, Berlin).

[3] Mikhailov, A.S., 1991, *Foundations of Synergetics I: Distributed Active Systems* (Springer-Verlag, Berlin).

[4] Mikhailov, A.S., and I.V. Uporov, 1991, *Foundations of Synergetics II: Complex Patterns* (Springer-Verlag, Berlin).

[5] Nicolis, G., 1995, *Introduction to Nonlinear Sciences* (Cambridge University Press, Cambridge).

[6] Kuramoto, Y., 1984, *Chemical Oscillations, Waves, and Turbulence* (Springer-Verlag, Berlin).

[7] Manneville, P., 1990, *Dissipative Structures and Weak Turbulence* (Academic Press, San Diego).

[8] Mori, H., and Y. Kuramoto, 1998, *Dissipative Structures and Chaos* (Springer-Verlag, Berlin).

[9] Newell, A.C., Passot T. and J. Lega, 1993, "Order Parameter Equations for Patterns", Annu. Rev. Fluid Mech. **25**, 399-453.

[10] Aronson, I.S. and L. Kramer, 2001, "The world of Complex Ginzburg-Landau Equation", Rev. Mod. Phys. in press.

[11] Scott, S.K., 1994, *Oscillation, waves, and chaos in chemical kinetics* (Oxford University Press, Oxford).

[12] Kapral R. and K. Showalter, 1995, Ed., *Chemical waves and patterns* (Kluwer Academic Publishers, Dordrecht).

[13] Tyson, J.J. and J.P. Keener, 1988, "Singular Perturbation-Theory of Travelling Waves in Excitable Media (a Review)", Physica D **32**, 327-361.

[14] Walgraef, D., 1996, *Spatio-temporal pattern formation: with examples from physics, chemistry and materials science* (Springer-Verlag, New York).

[15] Yeargers, E.K., Shonkiwiler, R.W., and J.V. Herod, 1996, *An Introduction to the Mathematics of Biology* (Birkhäuser, Boston).

[16] Meinhardt, H., 1982, *Models of Biological Pattern Formation* (Academic Press, London).

[17] Zhabotinsky, A.M., Dolnik, M. and R. Epstein, 1995, "Pattern-Formation arising from Wave instability in a simple Reaction-Diffusion system", J. Chem. Phys. **103**, 10306-10314.

[18] Woesler, R., Schutz, P., Bode, M OrGuil, M., and H.G. Purwins, 1996, "Oscillations of fronts and front pairs in two- and three-component reaction-diffusion systems", Physica D **91**, 376-405.

[19] Schenk, C.P., OrGuil, M., Bode, M., and H.G. Purwins, 1997, "Interacting pulses in three-component reaction-diffusion systems on two-dimensional domains", Phys. Rev. Lett. **78**, 3781-3784.

[20] Niedernostheide, F.J., OrGuil, M., Kleinkes, M., and H.G. Purwins, 1997, "Dynamical behaviour of spots in a nonequilibrium distributive active medium", Phys. Rev. E **55**, 4107-4111.

[21] Or-Guil, M., Bode, M., Schenk, C.P., and H.G. Purwins, 1998, "Spot bifurcations in three-component reaction-diffusion systems: The onset of propagation", Phys. Rev. E **57**, 6432-6437.

[22] Meinhardt, H. and M. Klingler, 1987, "A model for pattern-formation on the shells of mollusks", J. Theor. Biol. **126**, 63-89.

[23] Meinhardt, H., 1999, "Orientation of chemotactic cells and growth cones: models and mechanisms", J. Cell Sci. **112**, 2867-2874.

[24] Brandtstädter, H., Braune, M., Schebesch, I. and H. Engel , 2000, "Experimental study of the dynamics of spiral pairs in light-sensitive Belousov-Zhabotinskii media using an open-gel reactor", Chem. Phys. Lett. **323**, 145-154.

[25] Brand, H.R., Hohenberg, P.C., and V. Steinberg, 1983, "Amplitude equation near a ploycritical point for the convective instability of a binary fluid mixture in a porous-medium", Phys. Rev. A **27**, 591-593.

[26] Brand, H.R., Hohenberg, P.C., and V. Steinberg, 1984, "Codimension-2 bifurcation for convection in binary fluid mixtures", Phys. Rev. A **30**, 2548-2561.

[27] Schöpf W. and W. Zimmermann, 1993, "Convection in binary fluids - Amplitude equations, codimension-2 bifurcation and thermal fluctuations", Phys. Rev. E **47**, 1739-1764.

[28] Martinez-Mardones, J., Tiemann, R., Zeller, W., and C. Perez-Garcia, 1994, "Amplitude equations in polymeric fluid convection", Int. J. Bifurcation Chaos **4**, 1347-1351.

[29] De Wit, A., 1999, "Spatial patterns and spatiotemporal dynamics in chemical systems", Adv. Chem. Phys. **109** , 435-513.

[30] Walgraef, D., 1997, "Pattern selection and the effect of velocity on interacting oscillatory and stationary instabilities", Phys. Rev. E **55**, 6887-6897.

[31] Willebrand H., Matthiessen K., Niedernostheide F.J., Dohmen R. and H.G. Purwins, 1992, "Experimental observation of simultaneously existing moving and standing patterns in a gas-discharge system", Contrib. Plasma Phys. **32**, 57-68.

[32] Malomed, B.A., 1994, "Domain wall between travelling waves", Phys. Rev. E **50**, R3310-R3313.

[33] Malomed, B.A., Nepomnyashchy, A.A. and M.I. Tribelsky, 1990, "Domain boundaries in convection patterns", Phys. Rev. A **42**, 7244-7263.

[34] Pomeau, Y., 1986, "Front motion, metastability and subcritical bifurcations in hydrodynamics", Physica D **23**, 3-11.

[35] Bär, Markus, 1993, *Räumliche Strukturbildung bie einer Oberflächenreaktion: Chemische Wellen und Turbulenz in der CO-Oxidation auf Platin-Einkristall-Oberflächen*, (PhD Thesis, Freie Universität Berlin).

[36] Meron, E., 1992, "Pattern formation in excitable media", Phys. Rep. **281**, 1-66.

[37] Winfree, A.T., 1991, "Varieties of spiral wave behaviour: An experimentalist's approach to the theory of excitable media", Chaos **1**, 303-334.

[38] FitzHugh, R., 1961, "Impulses and physiological states in theoretical models of nerve membrane", Biophys. J. **1**, 445-466.

[39] Nagumo, J.S., Arimoto, S. and S. Yoshizawa, 1962, "An active pulse transmission line simulating nerve axon", Proc. IRE **50**, 2061-2071.

[40] Ermentrout, B. and M. Lewis, 1997, "Pattern formation in systems with one spatially distributed species", Bul. Math Biol. **59**, 533-549.

[41] Sheintuch, M., and O. Nekhamikina, 1997, "Reaction-diffusion patterns on a disk or a square in a model with long-range interactions", J. Chem. Phys. **107**, 8165-8174.

[42] Nekhamikina, O., and M. Sheintuch, 1998, "On the breakup of target and spiral waves on a disk, in a reaction-diffusion system with long-range interactions", —Physica A **249**, 134-140.

[43] Levine, H., and X. Zou, 1992, "Standing Waves in Catalysis at Single-Crystal Surfaces", Phys. Rev. Lett. **69**, 204-207.

[44] Levine, H., and X. Zou, 1993, "Catalysis at single-crystal Pt(110) surfaces: Global coupling and standing waves", Phys. Rev. E **48**, 50-64.

[45] Sheintuch, M., 1997, "Pattern selection in a general model of convection, diffusion and catalytic reaction", Physica D **102**, 125-146.

[46] Graham, M.D., Middaya, U., and D. Luss, 1993, "Pulses and global bifurcations in a nonlocal reaction-diffusion system", Phys. Rev. E **48**, 2917-2923.

[47] Bär, M., Falcke, M., Hildebrand, M., Neufeld, M., Engel, H. and M. Eiswirth, 1994, "Chemical turbulence and standing waves in a surface reaction model: The influence of global coupling and wave instabilities", Intern. Journ. Bifur. Chaos **4**, 499-508.

[48] Falcke, M. and H. Engel, 1994, "Influence of global coupling through the gas phase on pattern formation during CO oxidation on Pt(110)", Phys. Rev. E **50**, 1353-1359.

[49] Falcke, M. and H. Engel, 1994, "Pattern formation during the CO oxidation on Pt(110) surfaces under global coupling", J. Chem. Phys. **101**, 6255-6263.

[50] Falcke, M., Engel, H., and M. Neufeld, 1995, "Cluster formation, standing waves, and stripe patterns in oscillatory active media with local and global coupling", Phys. Rev. E **52**, 763-771; 1996, **53**, 6589 [Errata].

[51] Kuhnert, L., 1986, "A new optical photochemical memory device in a light-sensitive chemical active medium", Nature **319**, 393-394.

[52] Krug, H.-J., Pohlmann, L. and L. Kuhnert, 1990, "Analysis of the Modified Complete Oregonator (MCO) Accounting for Oxygen- and Photosensitivity of Belousov-Zhabotinsky Systems", J. Phys. Chem. **94**, 4862-4866.

[53] Braune, M. and H. Engel, 2000, "Feedback-controlled forcing of meandering spiral waves in an open gel reactor", Phys. Rev. E **62**, 5986-5988.

[54] Hildebrand, M., Skodt H. and K. Showalter, 2001, "Spatial Symmetry Breaking in the Belusov-Zhabotinsky Reaction with Light-Induced Remote Communication", Phys. Rev. Lett. **87**, 88303.

[55] Kusnetsov, Y.A., 1995, *Elements of Applied Bifurcation Theory* (Springer-Verlag, Berlin).

[56] Guckenheimer, J., and P. Holmes, 1983, *Nonlinear Oscillations, Dynamical Systems and Bifurcations of Vector Fields* (Springer-Verlag, New York).

[57] Wiggins, S., 1990, *Introduction to Applied Non-linear Dynamical Systems and Chaos* (Springer-Verlag, New York).

[58] Crawford, J.D., 1991, "Introduction to bifurcation theory", Rev. Mod. Phys. **63**, 991-1037.

[59] Iooss, G., and D.D. Joseph, 1997, *Elementary Stability and Bifurcation Theory;* 2^{nd} *Ed.* (Springer-Verlag, New York).

[60] Turing, A.M., 1952, "The chemical basis of morphogenesis", Phil. Trans. R. Soc. London B **237**, 37.

[61] Perraud, J.J., De Wit, A., Dulos, E., Dekepper, P., Dewel, G. and P. Borckmans, 1993, "One-dimensional spirals - Novel asynchronous chemical wave sources", Phys. Rev. Lett. **71**, 1272-1275.

[62] Dewel, G., Borckmans, P., De Wit, A., Rudovics, B., Perraud, J.J., Dulos, E., Boissonade, J. and P. Dekepper, 1995, "Pattern selection and localised structures in reaction-diffusion systems", Physica A **213**, 181-198.

[63] Logvin, Y.A. and T. Ackemann, 1998, "Interaction between Hopf and static instabilities in a pattern-forming optical system", Phys. Rev. E **58**, 1654-1661.

[64] Tlidi, M., Mandel, P. and M. Haelterman, 1997, "Spatiotemporal patterns and localised structures in nonlinear optics", Phys. Rev. E **56**, 6524-6530.

[65] Borckmans, P., Dewel, G., De Wit, A. and D Walgraef, 1995, "Turing Bifurcations and Pattern Selection", in *Chemical Waves and Patterns*, edited by R. Kapral and K. Showalter (Kluwer, Dordrecht), p. 323-363.

[66] De Wit, A., Lima, D., Dewel, G. and P. Borckmans, 1996, "Spatiotemporal dynamics near a codimension-two point", Phys. Rev. E **54**, 261-271.

[67] Dewel, G., De Wit, A., Metens, S., Verdasca, J. and P. Borckmans, 1996, "Pattern selection in reaction-diffusion systems with competing bifurcations", Phys. Scripta **T67**, 51-57.

[68] Lima, D., De Wit, A., Dewel, G. and P. Borckmans, 1996, "Chaotic spatially subharmonic oscillations", Phys. Rev. E **53**, R1305-R1308.

[69] Meixner, M., De Wit, A., Bose, S. and E. Scholl, 1997, "Generic spatiotemporal dynamics near codimension-two Turing-Hopf bifurcations", Phys. Rev. E **55**, 6690-6697.

[70] Meixner, M., Bose, S. and E. Scholl, 1997, "Analysis of complex and chaotic patterns near a codimension-2 Turing-Hopf point in a reaction-diffusion model", Physica D **109**, 128-138.

[71] Heidemann, G., Bode, M. and H.-G. Purwins, 1993, "Fronts between hopf- and turing-type domains in a two-component reaction-diffusion system", Phys. Lett. A **177**, 225-230.

[72] Or-Guil, M. and M. Bode, 1998, "Propagation or turing-hopf fronts", Physica A **249**, 174-178.

[73] Walgraef, D., 1997, “Pattern selection and the effect of group velocity on interacting oscillatory and stationary instabilities”, Phys. Rev. E **55**, 6887-6897.

[74] Hildebrand M., and A.S. Mikhailov, 2000, “Nanoscale wave patterns in reactive adsorbates with attractive lateral interactions”, J. Stat. Phys. **101**, 599-620.

[75] Zimmermann, W., 1994, “Srukturbildung”, in *Komplexe Systeme; zwischen Atom und Festkörper*, edited by R. Hölzle (Forschungszentrum Jülich GmbH, Jülich, Germany), p. 32.1-32.80.

[76] Zwillinger, D., 1992, *Handbook of differential equations - 2^{nd} Edition* (Academic Press, San Diego).

[77] Keworkian, J. and J. Cole, 1981, *Perturbation methods in applied mathematics* (Springer-Verlag, Berlin).

[78] Murray, J.D., 1984, *Asymptotic Analysis, 2nd edn.* (Springer-Verlag, Berlin).

[79] Holmes, M.H., 1995, *Introduction to Perturbation Methods* (Springer-Verlag, New York).

[80] Holmes, P., Lumley, J.L., and G. Berkooz, 1996, *Turbulence, coherent structures, dynamical systems and symmetry* (Cambridge, Univ. Pr., Cambridge).

[81] Knobloch, E., 1995, “Remarks on the use and misuse of the Ginzburg-Landau Equation”, in *Nonlinear Dynamics and Pattern Formation in the Natural Environment*, edited by A. Doelman and A. van Harten (Pitman Research Notes in Mathematics;Longman).

[82] Stuart, J.T., and R.C. DiPrima, 1978, “The Eckhaus and Benjamin-Feir resonance mechanisms”, Proc. R. Soc. Lond. A **362**, 27-41.

[83] Kramer, L., and W. Zimmermann, 1985, “On the Eckhaus instability for spatially periodic patterns”, Physica D **16**, 221-231.

[84] Janiaud, B., Pumir, A., Bensimon, D., Croquette, V., Richter, H. and L. Kramer, 1992, “The Eckhaus instability for travelling waves”, Physica D **55**, 269-286.

[85] van Saarloos, W., and P.C. Hohenberg, 1992, "Fronts, pulses, sources and sinks in generalised complex Ginzburg-Landau equations", Physica D **56**, 303-367; 1993, **69**, 209 [Errata].

[86] van Hecke, M., Storm, C., and W. van Saarloos, 1999, "Sources, sinks and wavenumber selection in coupled CGL equations and experimental implications for counter-propagating waves system", Physica D **134**, 1-47.

[87] Landman, M.J., 1987, "Solutions of the Ginzburg-Landau equation of interest in shear flow transitions", Studies Appl. Math. **76**, 187-237.

[88] Cross, M.C., and E. Kuo, 1992, "One-dimensional spatial structure near a Hopf bifurcation at finite wavenumber", Physica D **59**, 90-120.

[89] van Saarloos, W., 1988, "Front propagation into unstable states: marginal stability as a dynamical mechanism for velocity selection", Phys. Rev. A **37**, 211.

[90] van Saarloos, W., 1989, "Front propagation into unstable states II. linear versus nonlinear marginal stability and rate of convergence", Phys. Rev. A **39**, 6367.

[91] Ben-Jacob, E., Brand, H., Dee, G., Kramer, L. and J.S. Langer, 1985, "Pattern propagation in nonlinear dissipative systems", Physica D **14**, 348-364.

[92] Dee, G.T., and J.S. Langer, 1983, "Propagating pattern selection", Phys. Rev. Lett. **50**, 383-387.

[93] Aronson, D.G., and H.F. Weinberger, 1978, "Multidimensional nonlinear diffusion arising in population genetics", Adv. Math. **30**, 33.

[94] Flesselles, J.-M., Simon, A.J., and A.J. Libchaber, 1991, "Dynamics of one-dimensional interfaces: an experimentalist's view", Adv. in Phys. **40**, 1-49.

[95] Counillon, C., Daudet, L., Podgorski, T., and L. Limat, 1998,"Dynamics of a liquid column array under periodic boundary conditions", Phys. Rev. Lett. **80**, 2117-2120.

[96] Coullet, P., and G. Iooss, 1990, "Instabilities of One-Dimensional Cellular Patterns", Phys. Rev. Lett. **64**, 866-869.

[97] Goldstein, R.E., and G.H. Gunaratne, 1990, "Defects and travelling-wave states in nonequilibrium patterns with broken parity", Phys. Rev. A **41**, 5731-5734.

[98] Coullet, P., Goldstein, R.E., and G.H. Gunaratne, 1989, "Parity-Breaking Transitions of Modulated Patterns in Hydrodynamic Systems", Phys. Rev. Lett. **63**, 1954-1957; Fauve, S., Douady, S., and O. Thual, 1990, Comment on "Parity-Breaking Transitions of Modulated Patterns in Hydrodynamic Systems", Phys. Rev. Lett. **65**, 385.

[99] Goldstein, R.E.,Gunaratne, G.H., Gil, L., and P. Coullet, 1991, "Hydrodynamic and interfacial patterns with broken space-time symmetry", Phys. Rev. A **43**, 6700-6721.

[100] Alvarez, R., van Hecke, M. and W. van Saarloos, 1997, "Sources and sinks separating domains of left- and right-travelling waves: experiment versus amplitude equations", Phys. Rev. E **56**, R1306-R1309.

[101] Dubois, M., Davidaud, F., Ronsin, O. and P. Berge, 1992, "Travelling waves in pure fluids locally heated along wires", Physica D **61**, 140-146.

[102] Vince, J.M. and M. Dubois, 1992, "Hot-wire below the free-surface of a liquid - Structural and dynamic properties of a secondary instability", Europhys. Lett. **20**, 505-510.

[103] Vince, J.M. and M. Dubois, 1997, "Critical properties of convective waves in a one-dimensional system", Physica D **102**, 93-100.

Versicherung

Hiermit versichere ich, daß ich die vorliegende Arbeit ohne unzulässige Hilfe Dritter und ohne Benutzung anderer als der angegebenen Hilfsmittel angefertigt habe; die aus fremden Quellen direkt oder indirekt übernommenen Gedanken sind als solche kenntlich gemacht. Die Arbeit wurde bisher weder im Inland noch im Ausland in gleicher oder ähnlicher Form einer anderen Prüfungsbehörde vorgelegt.

Die vorliegende Doktorarbeit wurde in der Nachwuchsgruppe "Musterbildung in Reaktions-Diffusions-Systemen" der Max-Planck-Institutes für Physik komplexer Systeme in Dresden angefertigt und vom Leiter der Nachwuchsgruppe Dr. M. Bär betreut.

Die Promotionsordnung der Technischen Universität Dresden wird anerkannt.

Ernesto Nicola